Une contribution a l'étude de quelques problèmes de rhéologie des suspensions

François Peters

▶ **To cite this version:**

François Peters. Une contribution a l'étude de quelques problèmes de rhéologie des suspensions. Mécanique des fluides [physics.class-ph]. Université Nice Sophia Antipolis, 2012. tel-00716822
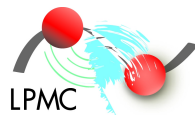
HAL Id: tel-00716822
https://theses.hal.science/tel-00716822

Submitted on 11 Jul 2012

Université de Nice - Sophia Antipolis

Une contribution à l'étude de quelques problèmes de rhéologie des suspensions

Mémoire présenté pour l'obtention de

L'Habilitation à Diriger les Recherches

par

François PETERS
Laboratoire de Physique de la Matière Condensée

soutenu le mercredi 22 février 2011 à 14h devant le jury composé de

Mme Laurence BERGOUGNOUX	*Rapporteur*
M Georges BOSSIS	
M Philippe GONDRET	*Rapporteur*
M Alberto T. PÉREZ	*Rapporteur*
M Bernard POULIGNY	

Table des matières

Préambule

Je mène depuis une quinzaine d'années une activité de recherche dans le domaine des milieux divisés. Pendant la préparation de mon doctorat au Laboratoire de Physique de la Matière Condensée (LPMC) à Nice, je me suis d'abord intéressé à la propagation des ondes ultrasonores dans des suspensions concentrées de particules solides dans un régime où les fractions volumiques élevées et la diffusion résonnante des ondes par les particules conduisent à des effets de diffusion multiple. Dans ce régime, l'onde dite « cohérente » , c'est-à-dire la composante qui se propage comme dans un milieu homogène, s'atténue très vite au cours de sa propagation. Cette onde cohérente est caractérisée par une vitesse de phase et un coefficient d'atténuation qui varient très vite avec la fréquence, et ce à cause des résonances de diffusion par les particules. J'ai dans un premier temps utilisé pour le traitement des signaux une méthode spectrale, donnant des valeurs absolues de la vitesse de phase et de l'atténuation sur une large bande de fréquences [1]. J'ai pu expliquer la dépendance de la vitesse et du coefficient d'atténuation en fonction de la fréquence et de la fraction volumique de particules dans la suspension grâce à un modèle prenant en compte la diffusion de l'onde par les particules [2]. D'autre part, une deuxième méthode d'analyse des données a été mise à profit, qui est fondée sur une analyse temps-fréquence utilisant le spectrogramme des signaux. Il est possible d'en déduire une vitesse de groupe, qui est cohérente avec celle que l'on peut calculer à partir de la vitesse de phase précédente, excepté aux fréquences où la diffusion est résonante.

A la suite de mon doctorat, j'ai été nommé PRAG à l'Université de Nice en 2000, ce qui impliquait une charge d'enseignement assez lourde. Malgré cela, j'ai pu poursuivre mon activité de recherche au LPMC, en l'élargissant à l'étude des milieux granulaires. Je me suis ainsi intéressé aux propriétés mécaniques d'un milieu granulaire magnétique. Je ne développerai pas cette partie de mon activité dans ce document, c'est pourquoi je le résume maintenant. Ce travail a donné lieu à une publication [3] qui est reproduite dans l'annexe A.1.

La mécanique des mileux granulaires a connu depuis une vingtaine d'années un intérêt renouvelé de la part des physiciens, notamment à cause des nombreuses questions posées dans le cadre de problèmatiques industrielles ou de la mécanique des sols. En particulier, les granulaires cohésifs, au sein desquels existent des interactions attractives entre grains, constituent un champ de recherche à part entière. En fonction de la taille des grains, les interactions pertinentes sont des forces électrostatiques, de Van der Waals ou des forces capillaires dues à la présence de liquide interstitiel. Si ces interactions ont de très fortes implications dans la mécanique des matériaux considérés, il est en revanche difficile de les faire varier à volonté sans changer la nature même du matériau.

Forts de l'expertise existant au laboratoire dans le domaine de l'électromagnétisme des mi-

lieux divisés, Elisabeth Lemaire et moi-même avons décidé de mettre en place une expérience permettant de faire varier les interactions entre grains par l'intermédiaire d'un champ magnétique tournant. Les granulaires étudiés étaient constitués de billes d'acier de taille millimétrique dont la distribution était assez monodisperse. Nous avons appliqué soit un champ statique, soit un champ tournant, afin de nous affranchir au maximum, dans ce dernier cas, de l'anisotropie inhérente aux interactions magnétiques entre particules. Le matériau granulaire a été caractérisé d'un point de vue mécanique par l'angle maximum de stabilité d'une part, par l'angle de repos après avalanche d'autre part. A cause des intensités du champ magnétique relativement faibles qu'il nous a été possible de générer, nous nous sommes limités au domaine des faibles cohésions comparées à la gravité.

Nous avons pu montrer que, pour un champ statique, les angles mesurés dépendaient assez largement de l'orientation du champ magnétique, ce qui justifiait l'utilisation d'un champ tournant. Dans ce dernier cas, il est apparu que l'angle maximum de stabilité variait proportionnellement au carré de l'intensité du champ magnétique et donc à la force entre grains, mais ne dépendait pas de la hauteur initiale du tas. Nous avons montré que ce comportement était compatible avec un modèle où l'avalanche est décrite comme un phénomène de surface. D'autre part, nous avons également pu montrer que la différence entre angle de repos et angle maximum de stabilité, faible pour un matériau non cohésif, augmentait avec les forces d'interaction.

Par la suite, j'ai été recruté comme maître de conférences à l'Université de Nice, toujours au LPMC. Je me suis alors intéressé à la rotation de Quincke, et à ses applications à la rhéologie des suspensions de particules diélectriques. La rotation de Quincke désigne la mise en rotation spontanée d'un objet diélectrique plongé dans un liquide faiblement conducteur et soumis à un champ électrique continu. Cette activité avait été initiée au LPMC par Elisabeth Lemaire et Laurent Lobry quelques années auparavant. Comme je le développerai dans la suite du document, je me suis intéressé d'une part à la dynamique d'un rotor macroscopique, d'autre part aux conséquences de la rotation de Quincke de particules au sein d'une suspension en écoulement.

Toujours dans le domaine de l'électromagnétisme des supensions, dans le cadre d'une collaboration avec le professeur Alberto T. Perez et son doctorant Manuel Medrano-Munoz de l'Université de Séville, j'ai participé avec Laurent Lobry à une activité expérimentale concernant l'électrophorèse de particules en milieu semi-dilué. Nous avons encadré Manuel Medrano-Munoz pendant plusieurs séjours au cours desquels il a pu concevoir une expérience de diffusion de lumière et obtenir des résultats concernant non seulement la mobilité électrophorétique moyenne, mais également la dispersion de cette mobilité dans une suspension colloïdale semi-diluée.

Enfin, depuis 2008, notre équipe a entamé une activité dans le domaine de la rhéologie des suspensions concentrées, qui a beaucoup bénéficié d'une ANR que nous avons obtenue en collaboration avec le Groupe Ecoulements de Particules de l'IUSTI (Marseille) et le laboratoire J.A. Dieudonné (Nice). Nous avons pu recruter un doctorant, Frédéric Blanc, que j'ai co-encadré, avec Elisabeth Lemaire, durant sa thèse. Il a mis en place des expériences de rhéométrie locale par imagerie de particules (P.I.V.), et de suivi de particules qui nous ont permis de clarifier le lien entre la rhéologie de suspensions concentrées et leur microstructure induite par le cisaillement.

Dans la suite de ce mémoire, je décrirai dans une première partie l'essentiel de mon activité en électrorhéologie. La deuxième partie sera consacrée à la rhéologie des suspensions concentrées. J'y aborderai les principaux résultats que Frédéric Blanc a obtenus durant sa thèse.

Première partie

Electrorhéologie

Chapitre 1

La rotation de Quincke et les suspensions

1.1 Introduction

La rotation de Quincke est la rotation spontanée d'un objet immergé dans un liquide peu conducteur et soumis à un champ électrique continu. La modélisation précise de cette instabilité sera développée dans la section 1.2. En voici tout de suite l'explication pour un objet sphérique soumis à un champ uniforme : lorsque les temps caractéristiques de relaxation de la charge électrique $\frac{\epsilon}{\sigma}$ (ϵ est la permittivité diélectrique, σ la conductivité électrique) dans les milieux liquides et solides sont différents, une couche de charge électrique se forme à la surface de la particule. Si la charge relaxe plus vite dans le liquide que dans le solide, le moment dipolaire de cette distribution de charge est opposé au champ électrique extérieur (figure 1.1(a)). Lorsque l'intensité
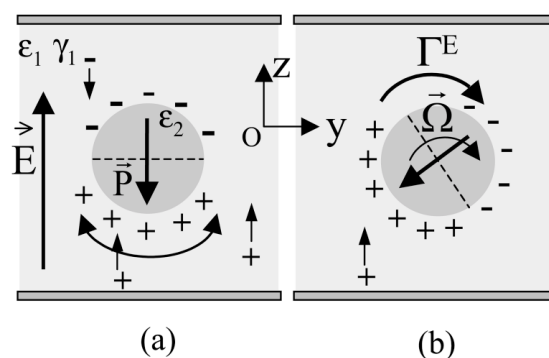
FIGURE 1.1 – Rotation de Quincke d'un cylindre. (a) Equilibre instable (b) Rotation

du champ électrique excède une valeur critique, cette situation devient instable et l'objet se met spontanément en rotation (figure 1.1(b)). Il atteint une vitesse angulaire constante, caractérisée par l'équilibre du couple électrique sur la distribution de charge et du couple visqueux sur la particule. En pratique, la faible conductivité de l'objet en rotation (typiquement 10^{-14} S.m^{-1} pour du PMMA) permet de le considérer comme isolant du point de vue électrique. Comme on le rappellera dans la section 1.2, le champ seuil est proportionnel à la racine carrée de la

conductivité du liquide et le temps caractéristique inversement proportionnel à cette conductivité. Puisque le champ seuil doit être largement inférieur au champ de claquage dans le liquide (au maximum une dizaine de kV.mm^{-1}), cela impose de travailler avec des huiles peu polaires ($\epsilon_1 \approx 1 - 4 \; \epsilon_0$) rendues conductrices grâce à un surfactant ionique. En pratique et en ordre de grandeur, la conductivité du liquide varie de quelques 10^{-10} à quelques 10^{-8} S.m^{-1}, le champ seuil de quelques centaines de V.mm^{-1} à quelques milliers de V.mm^{-1} et le temps caractéristique de relaxation du dipôle, qui fixe toutes les échelles de temps dans les différents problèmes que nous envisagerons, de quelques millisecondes à quelques centaines de millisecondes.

La mise en évidence expérimentale de la rotation de Quincke a été réalisée par le scientifique qui lui a donné son nom en 1896 [4], mais il a fallu près d'un siècle pour que le phénomène soit compris théoriquement [5, 6]. Plus récemment, Elisabeth Lemaire et Laurent Lobry (LPMC Nice), réalisant que l'inverse du temps de relaxation du dipôle était dans la pratique du même ordre de grandeur que les taux de cisaillement qu'ils avaient l'habitude de manipuler en rhéologie, se sont intéressés à l'électrorotation en vue de l'appliquer aux suspensions de particules solides dans un liquide [7, 8, 9, 10, 11, 12, 13]. Une autre propriété importante a motivé cette décision : la rotation d'un objet ne dépend pas, dans une certaine mesure qui sera clarifiée à la section 1.4, de la taille de cet objet, mais seulement de sa forme et des caractéristiques électriques et mécaniques des matériaux utilisés. Elle peut donc avoir lieu pour des objets macroscopiques (chapitre 2) comme pour des particules microscopiques (section 1.3). Du point de vue de la rhéologie des suspensions, l'électrorotation permet de diminuer la viscosité effective du matériau. En effet, la rotation induite par le champ a lieu dans ce cas dans la même direction que la rotation locale du fluide ambiant, et les particules mues par le champ électrique entrainent à leur tour le liquide [7, 8, 9, 11, 12]. Des diminutions de la viscosité d'un facteur 5 ont ainsi pu être mises en évidences pour des suspensions de fraction volumique jusqu'à 20%. On peut remarquer qu'il s'agit d'un effet inverse à celui qui prévaut dans les suspensions électrorhéologiques classiques, pour lesquelles le champ induit une structuration, en chaine notamment, qui a tendance à rigidifier le milieu [14].

Dans la suite de ce chapitre, je vais tout d'abord, pour fixer les idées, rappeler rapidement la description théorique de la rotation d'une particule sphérique sous l'action d'un champ électrique uniforme, ainsi que les résultats importants pour la suite. Je décrirai ensuite le modèle qui permet d'interpréter la diminution de la viscosité d'une suspension dont les particules sont entrainées par le champ électrique. Ce modèle a été confronté à des mesures issues de différentes expériences. Notamment, nous avons réalisé des mesures de profils de vitesse dans un tube rectangulaire par une technique de Vélocimétrie Ultrasonore Doppler Pulsée. Je décrirai le dispositif expérimental ainsi que les principaux résultats. Enfin, si le modèle classique de la rotation de Quincke prévoit que le comportement de l'objet en rotation est indépendant de sa taille, c'est essentiellement une conséquence de l'hypothèse que la couche d'ions libres qui entoure la particule est infiniment fine. Dés lors, il convient de se demander si, lorsqu'on diminue la taille de l'objet, cette hypothèse est encore légitime. Nous nous sommes intéressés à ce problème de façon numérique pour un cylindre de longueur grande devant son rayon et soumis à un champ orthogonal à son axe. J'exposerai les conclusions de cette étude à la fin du chapitre.

1.2 La rotation de Quincke d'une particule isolée

1.2.1 Equations fondamentales

Equations électriques

On considère une particule sphérique de rayon a isolée (milieu noté 2) immergée dans un liquide peu conducteur (noté 1) soumise à un champ électrique extérieur uniforme $\vec{E_0} = E_0\vec{e}_z$. Les conductivités électriques sont notées σ_1 et σ_2, les permittivités ϵ_1 et ϵ_2. Sous l'action du champ électrique extérieur, une couche de charges électriques, supposée pour le moment infiniment fine, se développe à la surface de la particule. Chaque milieu reste en revanche localement neutre du point de vue électrique. Le champ électrique total obéit aux équations suivantes :

$$\begin{aligned} \vec{\nabla} \cdot (\epsilon_{1,2}\vec{E}_T) &= 0 \\ \vec{\nabla} \times \vec{E}_T &= \vec{0} \quad (\vec{E}_T = -\vec{\nabla}V_T) \end{aligned} \tag{1.1}$$

Avec les conditions limites :

$$\begin{aligned} r \to +\infty \qquad & \vec{E}_T \to \vec{E}_0 \\ r = a \qquad & (\epsilon_1\vec{E}_{T1} - \epsilon_2\vec{E}_{T2}) \cdot \vec{e}_r = \sigma_S \\ & (\vec{E}_{T1} - \vec{E}_{T1}) \times \vec{e}_r = \vec{0} \end{aligned} \tag{1.2}$$

où la densité surfacique de charge électrique est notée σ_S. D'autre part, la particule est supposée en rotation à la vitesse angulaire $\vec{\omega}$. La dynamique de σ_S est donnée par la loi habituelle de conservation de la charge de toute portion (S) de la surface de la sphère :

$$\frac{d}{dt}\iint_{(S)} \sigma_S \, dS = \oint_{(L)} \sigma_S(a\vec{\omega} \times \vec{e}_r) \cdot (\vec{e}_r \times \vec{dr}) + \iint_{(S)} (\sigma_2\vec{E}_{T2} - \sigma_1\vec{E}_{T1}) \cdot \vec{e}_r \, dS \tag{1.3}$$
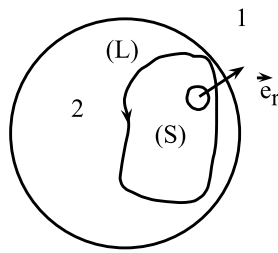
FIGURE 1.2 – Bilan de charge sur une sphére

Le premier terme du membre de droite est le flux convectif tangentiel à travers le contour (L) de la surface (S), où la vitesse des charges de la couche en un point de la surface de vecteur position $\vec{r}$ est supposée égale à la vitesse de la sphère en ce point $\vec{\omega} \times \vec{r}$. Ceci résulte de l'hypothèse d'une couche infiniment fine, c'est à dire très petite devant le rayon a de la sphère. Le second terme est le flux conductif de charges dû à la migration vers l'interface sous l'effet du champ électrique. A l'aide théorème de Green, l'équation (1.3) devient :

$$\iint_{(S)} [\frac{\partial \sigma_S}{\partial t} - (a\vec{\omega} \times \vec{\nabla}_t \sigma_S) \cdot \vec{e}_r - (\sigma_2 \vec{E}_{T2} - \sigma_1 \vec{E}_{T1}) \cdot \vec{e}_r] \, dS = 0 \qquad (1.4)$$

où l'opérateur $\vec{\nabla}_t$ est le gradient tangentiel à la surface, qui s'écrit dans la base sphérique $(\vec{e}_r, \vec{e}_\theta, \vec{e}_\phi)$:

$$\vec{\nabla}_t = \begin{pmatrix} 0 \\ \frac{1}{a} \frac{\partial}{\partial \theta} \\ \frac{1}{a \sin \theta} \frac{\partial}{\partial \phi} \end{pmatrix}$$

Puisque la surface (S) est quelconque sur la sphère, la relation (1.4) s'écrit localement en r=a :

$$\frac{\partial \sigma_S}{\partial t} = (a\vec{\omega} \times \vec{\nabla}_t \sigma_S) \cdot \vec{e}_r + (\sigma_2 \vec{E}_{T2} - \sigma_1 \vec{E}_{T1}) \cdot \vec{e}_r \qquad (1.5)$$

Equation mécanique

La rotation de la particule est régie par le théorème du moment cinétique qui s'écrit :

$$I \frac{d\vec{\omega}}{dt} = -\alpha \vec{\omega} + \vec{\Gamma}_E \qquad (1.6)$$

où le premier terme du second membre est le couple de friction visqueuse et le second terme est le couple électrique exercé sur la particule dont l'expression sera déterminée dans la section suivante. Dans le cas d'une particule sphérique homogène, le moment d'inertie I et le coefficient de friction sont donnés en fonction de la viscosité η du liquide et de la masse volumique ρ_s de la particule par :

$$\begin{aligned} I &= \frac{8}{15} \pi \rho_s a^5 \\ \alpha &= 8\pi \eta a^3 \end{aligned} \qquad (1.7)$$

1.2.2 Solution dipolaire

Champ électrique

Compte tenu du caractère sphérique de la particule et de la linéarité de l'équation (1.5) vis à vis du champ électrique, le champ électrique créé ainsi que la distribution surfacique de charge sont dipolaires. Plus précisément, le potentiel électrique total $V_T(\vec{r})$ est la somme du potentiel créé par les charges libres sur les électrodes $-\mathrm{E}_0 r \cos \theta + V_\infty(\vec{r})$ et du potentiel créé par les charges libres de surface $V(\vec{r})$. Le premier est le potentiel qui existe dans le cas de milieux diélectriques non conducteurs, c'est-à-dire en l'absence de charges libres de surface :

$$\begin{aligned} V_\infty(\vec{r}) &= \frac{\vec{P}_\infty \cdot \vec{r}}{4\pi\epsilon_1 \, r^3} \qquad r > a \\ V_\infty(\vec{r}) &= \frac{\vec{P}_\infty \cdot \vec{r}}{4\pi\epsilon_1 \, a^3} \qquad r < a \end{aligned} \qquad (1.8)$$

où le moment dipolaire $\vec{P}_\infty$ est proportionnel au champ extérieur :

$$\vec{P}_\infty(\vec{r}) = 4\pi\epsilon_1 a^3 \frac{\epsilon_2 - \epsilon_1}{2\epsilon_1 + \epsilon_2} \vec{E}_0 \tag{1.9}$$

D'autre part, la distribution surfacique de charges libres, également dipolaire, est caractérisée par un moment dipolaire $\vec{P}$:

$$\sigma_S(\vec{e}_r) = \frac{2\epsilon_1 + \epsilon_2}{4\pi\epsilon_1 a^3} \vec{P} \cdot \vec{e}_r \tag{1.10}$$

Cette distribution de charge crée le potentiel électrique $V(\vec{r})$:

$$\begin{aligned} V(\vec{r}) &= \frac{\vec{P} \cdot \vec{r}}{4\pi\epsilon_1 \, r^3} \qquad r > a \\ V(\vec{r}) &= \frac{\vec{P} \cdot \vec{r}}{4\pi\epsilon_1 \, a^3} \qquad r < a \end{aligned} \tag{1.11}$$

qui, compte tenu de la relation (1.10), vérifie bien les deux dernières relations de l'équation (1.2).

Equation de relaxation

L'expression du potentiel total $V_T = -E_0 r \cos\theta + V_\infty + V$ permet de réécrire l'équation dynamique (1.5) sous la forme :

$$\forall \vec{e}_r, \ \frac{\partial \vec{P}}{\partial t} \cdot \vec{e}_r = \vec{\omega} \times \vec{P} \cdot \vec{e}_r - \frac{1}{\tau}(\vec{P} - (\chi_0 - \chi_\infty)\vec{E}_0) \cdot \vec{e}_r \tag{1.12}$$

soit

$$\frac{\partial \vec{P}}{\partial t} = \vec{\omega} \times \vec{P} - \frac{1}{\tau}(\vec{P} - (\chi_0 - \chi_\infty)\vec{E}_0) \tag{1.13}$$

où le temps de relaxation de la polarisation τ et les coefficients de polarisation à fréquence nulle χ_0 et à fréquence infinie χ_∞ sont donnés par :

$$\begin{aligned} \tau &= \frac{2\epsilon_1 + \epsilon_2}{2\sigma_1 + \sigma_2} \\ \chi_0 &= 4\pi\epsilon_1 a^3 \frac{\sigma_2 - \sigma_1}{2\sigma_1 + \sigma_2} \\ \chi_\infty &= 4\pi\epsilon_1 a^3 \frac{\epsilon_2 - \epsilon_1}{2\epsilon_1 + \epsilon_2} \end{aligned} \tag{1.14}$$

Couple électrique

A cause de la symétrie sphérique de l'objet, le couple exercé par le champ électrique sur la particule se réduit au couple exercé par le champ extérieur $\vec{E}_0$ sur la densité de charge surfacique, qui s'écrit :

$$\vec{\Gamma}_E = \vec{P} \times \vec{E}_0 \tag{1.15}$$

Un couple existe donc dés que le moment dipolaire de la distribution de charges n'est pas aligné avec le champ électrique.

De façon générale la dynamique de la particule sphérique en rotation est régie par les équations (1.6), (1.13) et (1.15).

1.2.3 Rotation en régime permanent

On peut s'intéresser au régime permanent pour lequel la particule tourne avec une vitesse angulaire constante $\vec{\omega}$, avec un moment dipolaire $\vec{P}$ constant. Dans ce cas, le couple visqueux équilibre le couple électrique. En particulier, les équations (1.6) et (1.15) montrent que le vecteur vitesse angulaire a pour direction celle du couple, orthogonal au champ externe $\vec{E}_0$. La symétrie du problème indique que l'axe de rotation peut être quelconque dans le plan orthogonal à $\vec{E}_0$. On peut poursuivre en remarquant qu'alors, l'équation de relaxation donne le moment dipolaire et donc le couple électrique en fonction de la vitesse de rotation :

$$\vec{\Gamma}_E = -(\chi_0 - \chi_\infty)\frac{\vec{\omega}\tau}{1 + (\omega\tau)^2}E_0^2 \tag{1.16}$$

En comparant cette dernière expression à l'équation (1.6), il apparaît immédiatement que la rotation spontanée n'est possible que si $\chi_0 - \chi_\infty < 0$, qui est la condition pour que le couple électrique soit moteur. D'après l'équation (1.13), c'est également la condition pour que le dipôle associé à une sphère maintenue immobile soit opposé au champ extérieur $\vec{E}_0$. La vitesse angulaire stationnaire est alors donnée par (1.6) et (1.16) :

$$
\begin{aligned}
\omega_s &= \frac{1}{\tau}\sqrt{\left(\frac{E}{E_c}\right)^2 - 1} \\
E_c &= \sqrt{-\frac{\alpha}{(\chi_0 - \chi_\infty)\tau}} = \sqrt{\frac{2}{3}\frac{\eta}{\epsilon_1}\frac{(2\sigma_1 + \sigma_2)^2}{\sigma_1\sigma_2}\frac{1}{\frac{\epsilon_2}{\sigma_2} - \frac{\epsilon_1}{\sigma_1}}}
\end{aligned}
\tag{1.17}
$$

Des résultats similaires peuvent être montrés pour un cylindre infini en rotation autour de son axe et soumis à un champ orthogonal. Ils sont rappelés dans l'annexe 1.A.

Quelques commentaires sont ici nécessaires :

1. La condition sur les polarisabilités est importante : l'état immobile ne peut être instable que si le dipôle dans ce cas est opposé au champ extérieur, ou de façon équivalente si le temps caractéristique de relaxation de la charge dans la particule est supérieur à celui dans le liquide.

2. La situation d'une particule libre immobile devient instable lorsque l'intensité du champ électrique dépasse une valeur critique. Ceci s'explique bien en étudiant l'allure de la variation du couple électrique stationnaire (1.16) d'une part, et du couple visqueux d'autre part, avec la vitesse angulaire de la particule, tous deux représentés sur la figure 1.3. Ainsi, le couple électrique est tout d'abord une fonction croissante de la vitesse angulaire ($\omega\tau << 1$), puisque c'est la rotation de la particule qui incline la distribution de charge et donc le dipôle par rapport au dipôle d'une particule immobile $\vec{P}_0$. A grande vitesse, en revanche ($\omega\tau >> 1$), la distribution de charge est convectée trop vite pour que le flux de charge puisse la reconstruire efficacement, et la norme du dipôle, pratiquement orthogonal à $\vec{E}_0$, est de plus en plus faible, ce qui induit une diminution du couple. Ceci apparaît
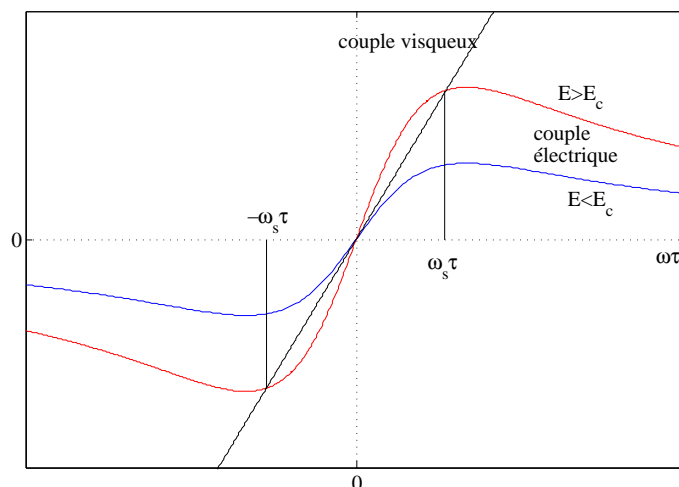
FIGURE 1.3 – Allure du couple électrique stationnaire et du couple visqueux en fonction de la vitesse angulaire pour deux valeurs de l'intensité du champ électrique

de façon semi-quantitative sur le schéma de la figure 1.4, où les extrémités des vecteurs $\vec{P}$ et $\vec{P_0}$ sont cocycliques. Le couple atteint donc un maximum pour une vitesse angu-
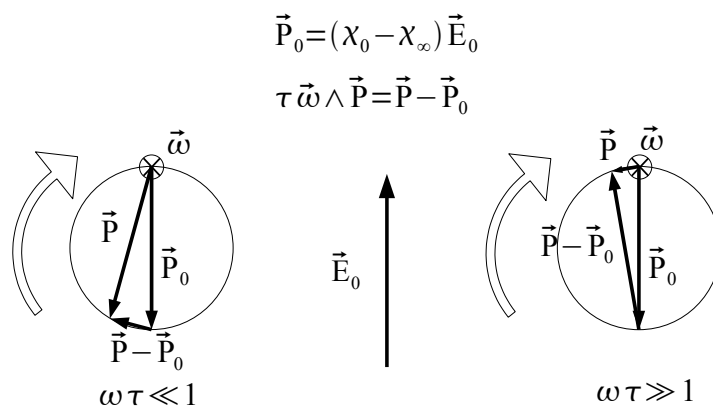
FIGURE 1.4 – Explication qualitative des limites $\omega\tau << 1$ et $\omega\tau >> 1$

laire intermédiaire, précisément pour $\omega\tau = 1$. D'autre part, le couple est proportionnel au carré de l'intensité du champ. Il est donc clair que lorsque l'intensité du champ est trop faible, aucune solution non nulle de l'équation (1.6) n'existe (cf. figure 1.3). En revanche, lorsque l'intensité du champ est supérieure à E_c, deux solutions existent, correspondant à des vitesses de rotation opposées, ce qui traduit bien la symétrie du problème par rotation

autour de la direction du champ appliqué. Une étude élémentaire confirme la stabilité de ces solutions.

3. Enfin, il convient de remarquer ici une propriété importante : les couples visqueux et électriques sont tous deux proportionnels au cube du rayon a de la particule, si bien que le champ critique et la vitesse de rotation des particules sont indépendantes du rayon a. Cette propriété remarquable permet de mettre en évidence l'électrorotation sur des objets macroscopiques [10, 15] aussi bien que dans le domaine de suspensions de particules microscopiques [7, 8, 9, 11, 12]. Comme on le verra dans l'étude numérique de la section 1.4, la taille de la particule redevient un paramètre important lorsqu'elle n'est plus très grande devant l'épaisseur de la couche superficielle de charge électrique.

1.2.4 Quelques ordres de grandeur

En pratique nous avons utilisé des particules isolantes ($\sigma_2 < 10^{-12}$ S/m) et de faible permittivité ($\epsilon_2 < 5\epsilon_0$), principalement des polymères (PMMA). Le choix des liquides est lui fortement dicté par l'existence du champ seuil E_c et par sa dépendance vis à vis de la conductivité du liquide suspendant. En effet, en supposant que la conductivité de la particule est très inférieure à celle du liquide suspendant, le champ seuil varie comme la racine carrée de la conductivité du liquide. Celle-ci devra donc être assez petite pour que les champs critiques correspondants aient des valeurs raisonnables, accessibles expérimentalement avec les sources de tension dont nous disposons et surtout inférieurs aux champs de claquage diélectrique. Ainsi, si nous souhaitons nous contenter d'appliquer des champs de quelques kilovolts par millimètre, nous serons conduits à travailler avec des liquides dont la conductivité sera typiquement comprise entre 10^{-10} et 10^{-8} S/m. Les liquides ayant des conductivités aussi faibles sont généralement peu polaires avec des constantes diélectriques inférieures à $10\epsilon_0$. Dans ces conditions, le champ seuil sera typiquement compris entre 1 et 2 kV/mm, le temps de Maxwell sera de l'ordre de quelques millisecondes et les vitesses de rotation de quelques centaines de radians par seconde. Ce dernier chiffre est très important pour la raison suivante : la vitesse de rotation induite par le champ étant du même ordre de grandeur que celle d'une particule dans une expérience de rhéologique typique, la rotation de Quincke peut conduire à une modification notable du comportement rhéologique d'une suspension soumise à un champ électrique. C'est le sujet de la section suivante.

1.3 Application aux suspensions

1.3.1 Introduction

Dans la section précédente, nous avons rappelé ce qu'est la rotation de Quincke d'un objet unique dans un fluide au repos. Nous allons maintenant nous intéresser aux propriétés rhéologiques particulières d'une suspension cisaillée dont les particules sont mises en électrorotation. La problématique principale consiste à déterminer comment le cisaillement modifie la rotation des particules, et comment en retour la viscosité de la suspension en est modifiée. Comme on l'a remarqué précédemment, dans un fluide au repos, la direction de rotation d'une particule isolée est quelconque dans le plan orthogonal au champ électrique. Dans une suspension au repos, on s'attend donc à ce que les particules tournent dans des directions aléatoires, avec pour

conséquence une vitesse de rotation moyenne nulle (Fig. 1.5.a.). Ce n'est plus le cas dans une suspension cisaillée. En effet, même en l'absence de champ électrique, les particules d'une suspension cisaillée sont en rotation à une vitesse angulaire moyenne égale à la vitesse de rotation locale du fluide, soit la moitié de la vorticité moyenne. Dans le cas d'un cisaillement simple, lorsqu'on applique un champ électrique dans la direction du gradient de vitesse (Fig. 1.5.a.), la rotation a lieu préférentiellement dans la direction de la vorticité. Dans ce cas, le couple moyen exercé par le champ électrique, non nul, entraîne les particules en rotation dans la direction de la vorticité, ainsi que l'ensemble du milieu par friction visqueuse. La viscosité apparente diminue donc.
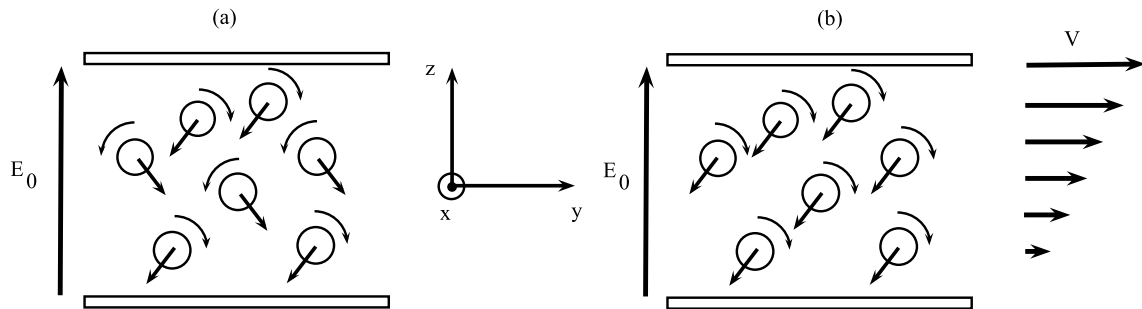
FIGURE 1.5 – (a) Electrorotation dans une suspension non cisaillée. La vitesse angulaire moyenne est nulle. (b) Suspension cisaillée. La vitesse angulaire moyenne est non nulle.

On peut noter ici que le champ électromagnétique a des effets inverses à ceux qu'on trouve dans les fluides électrorhéologiques ou magnétorhéologiques habituels [16], pour lesquels les interactions électriques ou magnétiques entre particules mènent à la formation de chaînes qui ont tendance à rigidifier le milieu.

Cette baisse de viscosité a été prévue en 1980 par Cebers [17], mais aucune confirmation expérimentale n'a eu lieu jusqu'au travaux réalisés par Elisabeth Lemaire et Laurent Lobry au LPMC à Nice [7, 8, 9, 11, 12, 13]. Le modèle complet permettant de prévoir la viscosité apparente a été publié pour la première fois dans l'article reproduit à la fin du manuscrit [18] (annexe B.1 p.85). Je le décrirai rapidement dans la section 1.3.2. Ce modèle a été comparé à des mesures rhéométriques réalisées par N. Pannacci pendant sa thèse [18] (annexe B.1 p.85 et section 1.3.3) ainsi qu'à des mesures de profils de vitesse dans un tube à section rectangulaire que j'ai moi-même réalisées et sur lesquelles je reviendrai dans la section 1.3.4.

1.3.2 Loi constitutive : fluide micropolaire

Généralités

Il s'agit ici comme souvent en rhéologie des milieux diphasiques, de décrire la suspension comme un milieu homogène doté de propriétés mécaniques. En ce qui concerne les suspensions non-soumises à un champ électromagnétique, de nombreux travaux ont été réalisés depuis les articles fondateurs d'Einstein [19] et Batchelor [20, 21], notamment en vue de décrire des domaines de concentration croissante. Le couple exercé par le champ électrique sur les particules qui a été évoqué plus haut ajoute à la suspension des propriétés mécaniques particulières, que l'on peut

décrire sous la forme d'une composante antisymétrique du tenseur de contrainte dépendant du champ électrique. C'est cette composante qui est à l'origine de la baisse de viscosité effective qui nous occupe.

La modélisation macroscopique des fluides à couples (ou fluide micropolaire) est décrite avec précision dans [22]. On peut cependant établir le lien qui existe entre le couple sur les particules et la partie antisymétrique du tenseur de contrainte à l'aide d'un raisonnement simplifié. Il suffit de reprendre le bilan habituel des moments de force sur un élément de volume infinitésimal cubique de côté b, moments calculés au centre de l'élément de volume (figure 1.6). Le moment
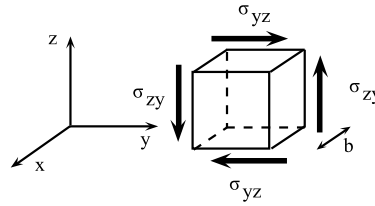
FIGURE 1.6 –

suivant l'axe x des forces visqueuses de surface s'écrit en fonction des composantes du tenseur de contrainte σ_{ij} au centre du cube à l'ordre le plus bas en b :

$$d\Gamma_x = b^3(\sigma_{zy} - \sigma_{yz}) \tag{1.18}$$

Notons $\vec{\gamma}^E$ la densité volumique de couple électrique sur le milieu. Le moment cinétique de l'élément de volume est la somme de deux termes : le moment cinétique habituel d'un élément de volume de milieu continu, d'ordre b^5 et le moment cinétique propre des particules solides en rotation, proportionnel au nombre de particules, d'ordre b^3. Ce dernier terme est négligé dans le domaine des petits nombres de Reynolds qui nous occupe et le premier terme disparaît dans la limite b→0. L'équilibre des moments s'écrit donc :

$$\frac{\sigma_{zy} - \sigma_{yz}}{2} = -\frac{\gamma_x^E}{2} \tag{1.19}$$

et de même pour les autres composantes. On retrouve évidemment la symétrie du tenseur de contrainte lorsque le couple extérieur est nul. Dans le cas contraire, le pseudo-vecteur associé à la partie antisymétrique du tenseur est l'opposé de la densité de couple : le couple extérieur est contrebalancé par le couple des forces de surfaces. Dans le cas du cisaillement simple de la figure 1.5, le couple sur les particules est dirigé suivant $-\vec{e}_x$ et la composante antisymétrique σ_{yz}^A est négative d'après (1.19), ce qui revient à diminuer la contrainte nécessaire à l'écoulement.

Modèle microrhéologique

Le raisonnement précédent ne donne évidemment pas l'expression de la partie symétrique de la contrainte, non plus que celle du couple électrique moyen sur l'élément de volume. Pour aller plus loin, nous avons utilisé dans l'article de l'annexe B.1 p.85 un modèle de microrhéologie valable pour les suspension diluées [23]. A noter qu'une première version incomplète du modèle –

un groupe de solution manquait – avait déjà été publiée par Elisabeth Lemaire et Laurent Lobry [7, 12]. Je vais maintenant rappeler les principaux résultats du modèle complet [18] (annexe B.1).

L'idée consiste à calculer les grandeurs macroscopiques caractérisant le milieu moyen (contraintes, vitesse, gradient de vitesse) comme les valeurs moyennes des grandeurs associées à l'échelle de la particule. Comme toujours en milieu dilué, on se ramène à l'étude d'une particule unique. Dans ce cadre, la contrainte moyenne est finalement mise sous la forme suivante [23] [1] :

$$\overline{\overline{\sigma}} = -P\overline{\overline{I}} + \eta(\phi)\left(\vec{\nabla}\vec{v} + \vec{\nabla}\vec{v}^{\dagger}\right) - \frac{1}{2}\zeta\,\boldsymbol{\epsilon}\boldsymbol{\cdot}\left(\frac{1}{2}\vec{\nabla}\times\vec{v} - \vec{\omega}\right) \tag{1.20a}$$

$$\eta(\phi) = \eta_0\frac{1 + 3/2\phi}{1 - \phi} \tag{1.20b}$$

$$\zeta = 6\eta_0\frac{\phi}{1 - \phi} \tag{1.20c}$$

où η_0 est la viscosité du fluide suspendant, $\vec{v}$, P, ϕ sont respectivement le champ de vitesse, la pression et la fraction volumique solide macroscopiques, $\overline{\overline{I}}$ le tenseur unité et $\boldsymbol{\epsilon}$ le tenseur de permutation d'ordre 3. $\vec{\omega}$ définit la vitesse de rotation moyenne (locale) des particules de la suspension.

D'autre part, il apparaît au cours du calcul une vitesse de rotation $\vec{\omega}_0$, qui représente la vitesse de rotation du fluide de viscosité η_0 vue par une particule. La vitesse de rotation locale du milieu macroscopique s'écrit alors :

$$\frac{1}{2}\vec{\nabla}\times\vec{v} = \phi\vec{\omega} + (1 - \phi)\vec{\omega}_0 \tag{1.21}$$

Le deuxième terme de l'équation (1.20a) représente la contrainte visqueuse habituelle, avec une viscosité moyenne η (1.20b) en accord avec la loi d'Einstein. Le troisième terme est la partie antisymétrique du tenseur de contrainte, qui existe seulement si la vitesse de rotation moyenne des particules est différente de la vitesse de rotation locale du fluide. En régime stationnaire, ou si l'on peut négliger l'inertie en rotation des particules, ce dernier terme s'exprime bien en fonction de la densité volumique de couple sur les particules. En effet, l'équilibre des moments sur une particule s'écrit :

$$8\pi\eta_0 a^3(\vec{\omega} - \vec{\omega}_0) = \vec{P}\times\vec{E}_0 \tag{1.22}$$

et la densité volumique de couple électrique pour une suspension de fraction volumique Φ s'écrit donc avec l'aide de l'équation (1.21) :

$$\vec{\gamma}_E = \frac{\phi}{4/3\pi a^3}\vec{P}\times\vec{E}_0 = 6\eta_0\frac{\phi}{1 - \phi}\left(\vec{\omega} - \frac{1}{2}\vec{\nabla}\times\vec{v}\right) \tag{1.23}$$

---

1. Le signe - devant le dernier terme de la relation (1.20a), et non + comme dans [23] et [18], provient de la convention différente pour la relation entre la normale à un élément de surface et la contrainte. Ici : $\vec{\sigma} = \overline{\overline{\sigma}}\vec{n}$. Dans [23] et [18] : $\vec{\sigma} = \vec{n}\,\overline{\overline{\sigma}}$.

ce qui permet de déduire de l'équation (1.20a) :

$$\overline{\overline{\sigma}} = -P\overline{\overline{I}} + \eta_0 \frac{1 + 3/2\phi}{1 - \phi} \left(\vec{\nabla}\vec{v} + \vec{\nabla}\vec{v}^\dagger \right) - \boldsymbol{\epsilon} \boldsymbol{\cdot} \left(-\frac{\vec{\gamma}^E}{2} \right) \tag{1.24}$$

en accord avec l'expression (1.19). Dans le cas du cisaillement simple $\vec{v} = \dot{\gamma}z \, \vec{e}_y$ de la figure 1.5, la contrainte tangentielle s'écrit en fonction du moment dipolaire, ou de la vitesse de rotation des particules :

$$\begin{aligned} \sigma_{yz} &= \eta_0 \frac{1 + 3/2\phi}{1 - \phi}\dot{\gamma} + \frac{\phi}{\frac{4}{3}\pi a^3}\frac{P_y E_0}{2} \\ \sigma_{yz} &= \eta_0 \frac{1 + 3/2\phi}{1 - \phi}\dot{\gamma} + 3\eta_0 \frac{\phi}{1 - \phi} \left(\frac{\dot{\gamma}}{2} + \omega_x \right) \end{aligned} \tag{1.25}$$

et l'on peut définir la viscosité apparente de la suspension comme le rapport $\sigma_{yz}/\dot{\gamma}$:

$$\begin{aligned} \eta_{app} &= \eta(\phi) + \frac{\phi}{\frac{4}{3}\pi a^3}\frac{P_y E_0}{2\dot{\gamma}} \\ \eta_{app} &= \eta(\phi) + \frac{3}{2}\eta_0 \frac{\phi}{1 - \phi}\frac{\frac{\dot{\gamma}}{2} + \omega_x}{\frac{\dot{\gamma}}{2}} \\ \eta(\phi) &= \eta_0 \frac{1 + 3/2\phi}{1 - \phi} \end{aligned} \tag{1.26}$$

Ainsi, la composante P_y du moment dipolaire moyen des particules, ou de façon équivalente la composante ω_x de la vitesse angulaire moyenne des particules, donnent la viscosité apparente de la suspension.

Rotation de Quincke dans un liquide cisaillé

Il reste donc à déterminer la vitesse moyenne des particules dans la suspension cisaillée. Pour ce faire, on considère une particule isolée dans un cisaillement simple uniforme soumise à un champ électrique $\vec{E}_0$ (figure 1.7). La particule possède la même vitesse de translation que l'écoulement ambiant à cette position. On ne la considérera donc pas, puisqu'aucune force nette n'est appliquée à la particule. Du fait que la couche de charges électriques à la surface de la
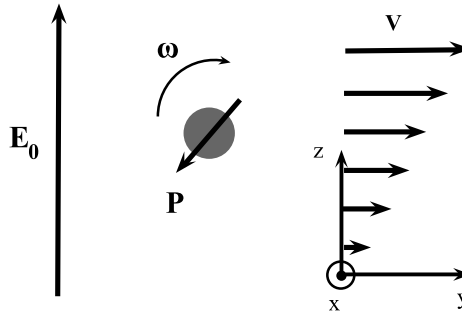

FIGURE 1.7 –

particule est supposée infiniment fine, les équations qui définissent le champ électrique, ainsi que les conditions à la surface de la particule et loin de celle-ci restent inchangées. L'équation de relaxation (1.13) est donc toujours valide. Le théorème du moment cinétique est adapté pour prendre en compte la vitesse angulaire locale du fluide vue par la particule $\vec{\omega}_0 = \omega_0 \vec{e}_x$. On a ici imposé la direction de $\vec{\omega}_0$ pour des raisons de symétrie. On doit donc résoudre le système suivant :

$$\frac{d\vec{P}}{dt} = \vec{\omega} \times \vec{P} - \frac{1}{\tau}(\vec{P} - (\chi_0 - \chi_\infty)\vec{E}_0)$$
$$I\frac{d\vec{\omega}}{dt} = -\alpha(\vec{\omega} - \vec{\omega}_0) + \vec{P} \times \vec{E}_0 \qquad (1.27)$$
$$-\frac{\dot{\gamma}}{2} = \phi\omega_x + (1-\phi)\omega_0$$

Ces équations sont résolues numériquement en régime stationnaire et leur stabilité étudiée dans l'article de l'annexe B.1 p.85. On peut ensuite en déduire la viscosité grâce à l'une des expressions de l'équation (1.26). La figure 1.8 représente la viscosité normalisée en fonction de $r = (E_0/E_c)^2$.
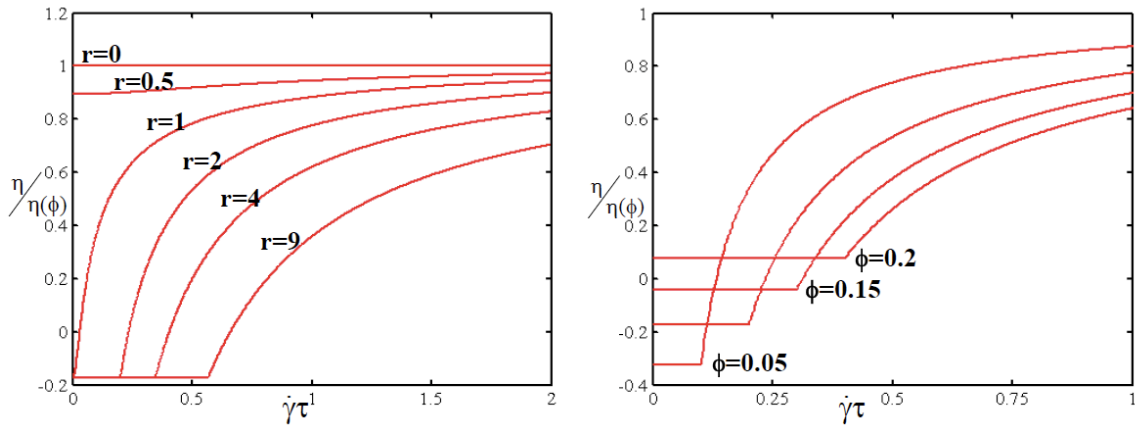
FIGURE 1.8 – Viscosité apparente calculée numériquement. $r = \left(\frac{E_0}{E_c}\right)^2$. $\tau = \frac{2\epsilon_1 + \epsilon_2}{2\sigma_1 + \sigma_2}$. **Gauche :** Φ=0.1 . **Droite :** r=2.

La partie croissante d'une part et le palier horizontal d'autre part sont caractéristiques de deux groupes de solution des équations (1.27) :

1. Le premier groupe compte une ou trois solutions en fonction de la valeur de l'intensité du champ électrique. Le vecteur vitesse angulaire est dirigé suivant la vorticité $\vec{\omega} = \omega_x \vec{e}_x$ et X=$\omega_x\tau$ est solution de l'équation :

$$X^3 + \frac{\dot{\gamma}\tau}{2}X^2 + [1 - (1 - \Phi)\,r]X + \frac{\dot{\gamma}\tau}{2} = 0 \qquad (1.28)$$

Lorsque $\dot{\gamma}\tau > \dot{\gamma}^*\tau = 2\Phi\sqrt{r-1}$, une seule de ces solutions est stable. Il s'agit de celle qui correspond à un rotation dans le même sens que la vorticité $-\frac{\dot{\gamma}}{2}\vec{e}_x$, alors que les deux autres, lorsqu'elles existent, correspondent à une rotation dans le sens inverse.

2. Lorsque $\dot{\gamma}\tau < \dot{\gamma}^*\tau$ la précédente solution n'est plus stable, mais une autre solution apparaît,

toujours stable. Cette solution peu intuitive correspond à une vitesse angulaire du liquide ambiant nulle, $\vec{\omega}_0 = \vec{0}$. Les équations (1.27) se ramènent donc à celles de la rotation de Quincke d'une particule dans un liquide au repos, mais à laquelle on aurait imposé une vitesse de rotation suivant la vorticité $\omega_x = -\frac{\dot{\gamma}}{2\Phi}$. Naturellement, puisque cette vitesse n'est pas forcément celle du rotor libre $\frac{1}{\tau}\sqrt{r-1}$ (relation (1.17)), une vitesse angulaire apparaît dans la direction de la vitesse du milieu moyen, $\vec{e}_y$, telle que $\sqrt{\omega_x^2 + \omega_y^2} = \frac{1}{\tau}\sqrt{r-1}$. Le signe de la rotation suivant $\vec{e}_y$ étant indéterminé, celle-ci n'intervient pas sur la vitesse de rotation moyenne des particules et du milieu effectif. Finalement, puisque la vitesse angulaire de rotation suivant la vorticité est imposée, indépendante de l'intensité du champ électrique et proportionnelle à $\dot{\gamma}$, cette solution correspond bien aux paliers de viscosité représentés sur la figure 1.8.

La valeur du palier de viscosité constante peut, pour des fractions volumiques assez faibles, devenir négative. Dans ce cas, la suspension continuerait à s'écouler dans la même direction, disons y>0, alors que la contrainte σ_{yz} deviendrait négative : dans une expérience de rhéométrie, le fluide serait entraîné complètement par les particules et il faudrait freiner la géométrie du rhéomètre.

1.3.3 Vérification expérimentale

Des expériences ont été réalisées pendant la thèse de Nicolas Pannacci et ont été comparées au modèle précédent dans l'article de l'annexe B.1. La figure 1.9 représente des courbes obtenues en géométrie de Couette cylindrique à entrefer étroit. Les particules sont en PMMA de diamètre 60 μm, le liquide suspendant est constitué d'un mélange d'huile permettant d'ajuster sa masse volumique à celle des particules.

L'accord qualitatif est manifestement très bon, en particulier en ce qui concerne l'apparition du plateau pour les valeurs du champ électrique importantes, ce qui corrobore l'existence du deuxième groupe de solutions des équations (1.27) évoqué plus haut. En revanche, la décroissance de viscosité due au champ électrique est surestimée par le modèle. Notamment, il n'a pas été possible de mettre en évidence une viscosité apparente négative. Il est probable que cela découle des interactions électriques et hydrodynamiques entre particules, négligées dans le modèle de suspensions diluées que nous avons utilisé. Les premières ont tendance à structurer les particules et donc à rigidifier le milieu, tandis que les secondes pourraient être à l'origine d'une dispersion des vitesses angulaires des particules. D'autre part, la structuration est responsable de l'apparition d'une contrainte seuil qui se traduit par une divergence de la viscosité dans la limite des faibles taux de cisaillement pour les faibles champs [12].

1.3.4 Ecoulement dans un tube à section rectangulaire

Objectifs de l'expérience

Nous avons voulu mesurer l'influence de la rotation de Quincke dans une suspension subissant un écoulement plus complexe que le cisaillement simple caractéristique de la géométrie de Couette cylindrique. Des mesures de débit d'un écoulement de type Poiseuille dans un tube rectangulaire [11] avaient déjà été réalisées pour deux valeurs de la fraction volumique de particules ($\phi = 5\%$, 10%), et s'étaient traduites par un bon accord avec les valeurs prévues par le modèle
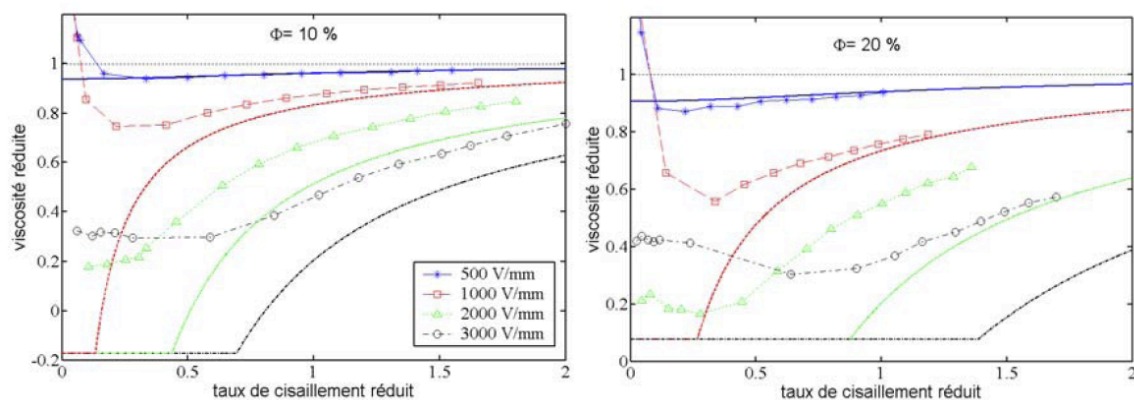
FIGURE 1.9 – Variations de la viscosité apparente d'une suspension (rapportée à la viscosité en absence de champ) contenant respectivement 10 et 20% de particules de PMMA, supposé isolant, en suspension dans un mélange dielec/ugilec, pour différentes valeurs du champ appliqué. Les caractéristiques de la suspension sont les suivantes : ϵ_1=3.7ϵ_0, σ_1=1.5 10^{-8} S/m, η_0=13.7 mPa.s, ϵ_2 =2.6ϵ_0, 2a=60μm. Ceci donne : E_c=950V/mm et τ=3ms.

pour la plus faible fraction volumique. A la fraction volumique ϕ=10%, l'accord était moins bon, vraisemblablement à cause d'interactions hydrodynamiques et électrostatiques entre particules. Nous avons par la suite décidé d'approfondir la description expérimentale de l'écoulement considéré par des mesures de profil de vitesse. En particulier, le modèle que nous utilisons prévoit l'apparition d'un point anguleux dans le profil de vitesse au centre du tube, lié à l'annulation de la viscosité apparente pour un taux de cisaillement non nul (figure 1.8).
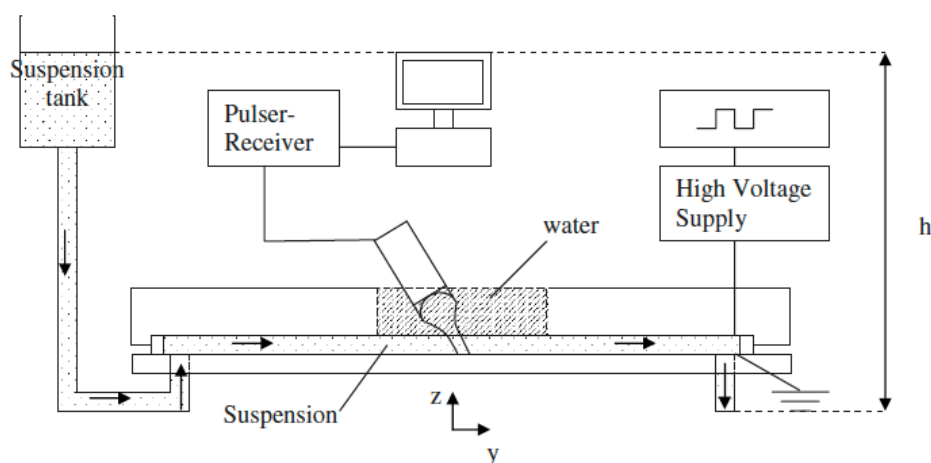
FIGURE 1.10 – Vélocimétrie par diffusion ultrasonore : dispositif expérimental

Vélocimétrie par diffusion ultrasonore

Pour mesurer les profils de vitesse, nous avons utilisé la méthode de Vélocimétrie Ultrasonore Doppler Pulsée (figure 1.10). Il s'agit d'une méthode comparable à la diffusion dynamique de la lumière, mais utilisant des ondes ultrasonores, et non lumineuses. Le principe est décrit en détail dans la référence [24] et rappelé dans l'article de l'annexe B.2 p. 101. On envoie deux trains d'onde séparés par un intervalle de temps Δt, et on compare les ondes rétrodiffusées. Puisque les particules diffusantes sont en mouvement, les ondes diffusées sont légèrement différentes. Pour être plus précis, l'onde émise est de largeur temporelle restreinte – quelques périodes– alors que l'onde diffusée est beaucoup plus longue (figure 1.11). Cela correspond à la diffusion par l'ensemble des particules situées sur le trajet de l'onde incidente. On peut donc sélectionner la position d'un certain volume diffusant en sélectionnant un intervalle de l'onde diffusée autour d'un instant donné compté à partir de l'émission du train d'onde excitateur, ainsi que la figure 1.11 le représente schématiquement. Pour chaque position dans le canal, on compare les portions de signal diffusé correspondant aux deux trains d'onde incidents consécutifs. Le décalage temporel, relativement à l'émission, entre ces deux portions de trains d'onde donne le déplacement pendant le temps Δt de la suspension à la position considérée. Ceci répété pour chaque position dans le canal fournit le profil de vitesse. L'intérêt des ondes ultrasonores (de fréquence f) est
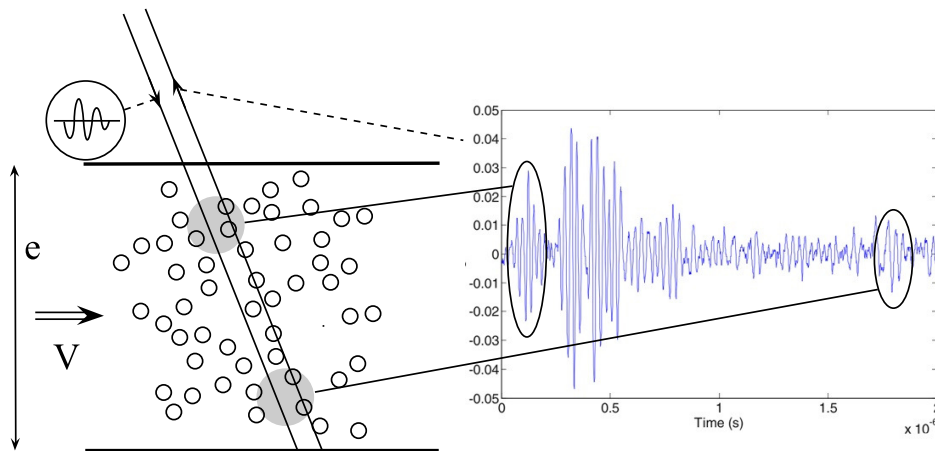
FIGURE 1.11 – Diffusion d'un pulse par la suspension en écoulement dans un tube rectangulaire

leur grande longueur d'onde λ=c/f relativement aux ondes lumineuses, leur permettant ainsi de sonder des suspensions de particules non colloïdales en s'affranchissant dans une certaine mesure des effets de la diffusion multiple. Pour cela, la longueur d'onde doit être suffisamment grande devant la taille des particules. En revanche, la résolution spatiale du dispositif est de l'ordre de la longueur du train d'onde émis λ. Il faut donc que l'épaisseur e du canal rectangulaire soit suffisamment grande devant λ. L'épaisseur du canal a été fixée à e = 1mm, afin de minimiser la longueur d'entrée de l'écoulement à l'extrémité du tube. La fréquence centrale imposée par l'émetteur acoustique est d'environ f=36 MHz, donnant une longueur d'onde $\lambda \approx 40\mu$m<<e.

Quelques ordres de grandeur

La suspension étudiée est constituée de particules de PMMA de diamètre 6μm, de masse volumique ρ_p=1.18x10^3 kg.m^{-3}, de permittivité relative ϵ_2=2.4ϵ_0 et de conductivité électrique inférieure à 10^{-14} S.m^{-1}. La taille des particules est choisie pour minimiser les effets colloïdaux tout en restant suffisamment petite pour que les effets de diffusion multiple ne soient pas trop gênants (6μm$<<40\mu$m). Le fluide suspendant est un mélange d'huiles Ugilec-Dielec rendu conducteur (γ_1=5.4x10^{-8} S.m^{-1}) par l'adjonction d'un surfactant ionique (AOT). Sa permittivité relative, sa viscosité et sa densité valent respectivement ϵ_1=3.7ϵ_0, η_1=16.5 mPa.s et ρ_l=1.14x10^3 kg.m^{-3}. On en tire l'intensité du champ électrique critique E$_c$ $\approx$1800 V.mm^{-1}. Enfin la largeur du canal (1.5 cm) est suffisamment importante devant son épaisseur e pour que l'on puisse négliger au centre du canal l'effet de largeur finie.

Discussion

La figure 1.12 représente les profils mesurés par la méthode acoustique ainsi que les profils calculés, pour un tube de largeur et de longueur infinies, à partir des mesures rhéométriques réalisées en géométrie de Couette cylindrique. Ces deux types de profils sont tout à fait comparables
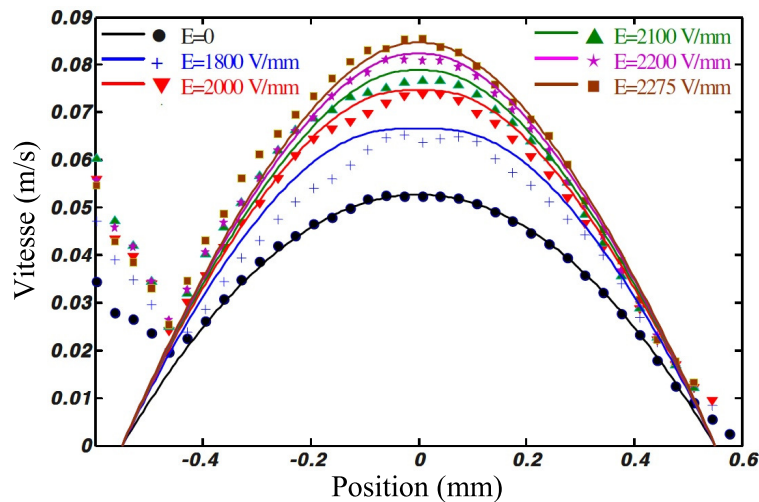
FIGURE 1.12 – Profils de vitesse pour différentes valeurs de l'intensité du champ électrique. Les symboles correspondent aux mesures acoustiques, les lignes aux courbes calculées à partir des mesures rhéologiques. Φ=5%.

d'un point de vue quantitatif. Au lieu du point anguleux prévu par le modèle au centre du tube, on observe au contraire un aplatissement, tout à fait cohérent avec l'augmentation de viscosité apparente lorsque $\dot{\gamma} \to 0$, bien visible sur la figure 1.13 représentant les mesures rhéométriques classiques réalisées sur la même suspension.

D'un point de vue plus général, la mesure d'une éventuelle viscosité nulle est problématique, car elle se produirait à faible contrainte de cisaillement. Cette dernière est alors difficilement contrôlable par un rhéomètre classique, ce qui rend très attractif la rhéométrie locale par vélocimétrie ultrasonore. D'autre part, il semble exister dans les fluides à couples tels que les ferrofluides
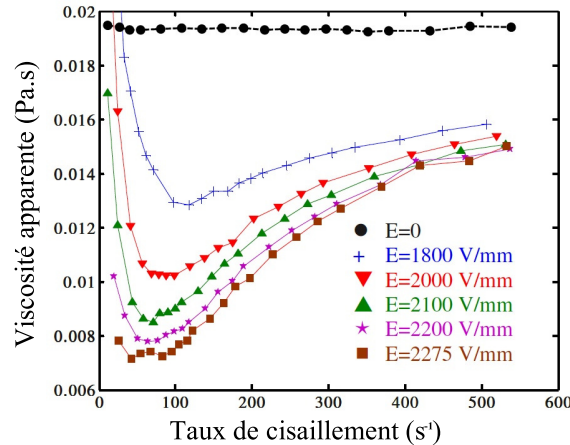
FIGURE 1.13 – Rhéogrammes de la suspension de la figure 1.12. Φ=5%

un couplage entre le moment cinétique interne du fluide, proportionnel à $\vec{\omega}$, et la quantité de mouvement du milieu macroscopique [22]. Ceci est habituellement décrit par un tenseur analogue au tenseur de contrainte et qui définit une densité surfacique de couple. De nombreuses questions se posent au sujet de cette densité de couple, notamment en ce qui concerne les conditions aux limites qu'elle doit vérifier. Dans notre expérience, cet effet devrait être faible (annexe B.2) et nécessiterait pour être perceptible une meilleure sensibilité de la mesure ultrasonore et un meilleur contrôle des gradients de pression dans le tube.

1.4 Influence de la taille des particules

1.4.1 Position du problème

Ainsi que l'on a pu le remarquer à la section 1.2.3, la rotation de Quincke d'un objet sphérique, ne dépend pas, dans le cadre du modèle classique, de la taille des particules. Rappelons que la principale hypothèse de ce modèle revient à considérer la couche de charges libres à la surface de la particule comme infiniment fine, ce qui lui impose de se déplacer en bloc avec la particule. D'un point de vue macroscopique, cela revient à négliger tous les phénomènes de transport de charges à l'intérieur de la couche. Ceci n'est évidemment pas universel, témoin le domaine bien connu des colloïdes (voir par exemple [25]). En effet, une particule chargée immergée dans un liquide conducteur est entourée par une couche d'ions dont l'ordre de grandeur de l'épaisseur peut s'écrire $\sqrt{D\tau_1}$ en fonction du coefficient de diffusion des ions dans le liquide D et du temps de relaxation de la charge dans le liquide τ_1. Dans les fluides non polaires que nous étudions, D$\approx$2.5 10^{-11}m^2.s^{-1} et τ_1=ϵ_1/σ_1 $\approx$1-100 ms. L'épaisseur typique de la couche varie donc entre 0.1 et 10 μm. Il est donc légitime de supposer que pour des tailles inférieures à une dizaine de microns, le modèle doive être réexploré.

Considérons une particule unique sphérique de rayon a, indéformable, plongée dans un liquide conducteur et soumise à un champ électrique uniforme $\vec{E}_0$. Il faut donc repartir des équations de transport en volume habituelles. Pour plus de simplicité, la particule est supposée complètement isolante, non chargée, et de même permittivité diélectrique ϵ que le liquide suspendant. Le

potentiel électrique est noté Φ. On suppose que les ions libres du liquide sont de deux types seulement, monovalents de surcroît, et qu'ils peuvent s'associer pour former une paire d'ions liés. Les constantes de dissociation et de recombinaison des ions sont notées k_d et k_r. Les densités numériques respectives des ions positifs, négatifs et des paires d'ions sont notées n_+, n_- et c. $e_0 > 0$ est la charge d'un électron. Les mobilités électrophorétiques des ions positifs et négatifs sont supposées identiques, leur valeur est notée K. Le mouvement du liquide environnant (masse volumique ρ_f) est caractérisé par le champ de vitesse $\vec{v}$ et le champ de pression P. Dans ces conditions, les équations de transport des ions dans le liquide, de la quantité de mouvement dans le liquide, l'équation d'incompressibilité du liquide et l'équation régissant le champ électrique s'écrivent respectivement (1.29a), (1.29b), (1.29c) et (1.29d).

$$\frac{\partial n_\pm}{\partial t} + \vec{\nabla} \cdot \left[n_\pm \left(\vec{v} \mp K\vec{\nabla}\Phi \right) - D\vec{\nabla}n_\pm \right] = k_d c - k_r n_+ n_- \tag{1.29a}$$

$$\rho_f \left[\frac{\partial \vec{v}}{\partial t} + \left(\vec{v} \cdot \vec{\nabla} \right) \vec{v} \right] = -\vec{\nabla}P + \eta \vec{\nabla}^2 \vec{v} - e_0(n_+ + n_-)\vec{\nabla}\Phi \tag{1.29b}$$

$$\vec{\nabla} \cdot \vec{v} = 0 \tag{1.29c}$$

$$\vec{\nabla} \cdot \left(\epsilon \vec{\nabla}\Phi \right) = \begin{cases} -e_0(n_+ + n_-) & \text{liquide} \\ 0 & \text{particule} \end{cases} \tag{1.29d}$$

Notons qu'à cause de la faible dissociation des ions en liquide peu polaire, la concentration c=c_0 est supposée constante dans l'équation (1.29a). Les conditions limites sont explicitées dans l'article de l'annexe B.3 p. 117.

A partir des équations précédentes, il est possible de dégager les temps caractéristiques pertinents :

– $\tau_1 = \epsilon/\sigma_1$ est le temps de relaxation de la charge dans le liquide, avec $\sigma_1 = 2K\sqrt{k_d/k_r\ c_0}$
– $\tau_m = a/(KE_0)$ est le temps de migration d'un ion à l'échelle de la particule.
– $\tau_D = a^2/D$ est le temps de diffusion d'un ion à l'échelle de la particule (donc tangentiellement à sa surface).

Rappelons qu'un phénomène physique est ici d'autant plus efficace que le temps caractéristique qui lui est associé est court. Dans le domaine des liquides peu polaires qui nous occupe, les ordres de grandeur des paramètres physiques sont les suivants : $\epsilon \approx 2\epsilon_0$, $\sigma_1 \approx 10^{-8}$ S.m^{-1}, $\eta \approx 10^{-2}$ Pa.s, K$\approx 10^{-9}$ m^{2}V^{-1}s^{-1}, D$\approx 2.5\times10^{-11}$m^{2}s^{-1} et E$_0 \approx$ E$_c \sim 600$V/mm. Dans ces conditions on peut calculer l'ordre de grandeur des temps caractéristiques pour différentes valeurs du rayon a de la particule. L'examen du tableau de la figure 1.14 montre que pour des valeurs de a comprises entre 1 μm et 100 μm, le temps de diffusion reste toujours plus grand que les deux autres. Lorsque le rayon a est abaissé jusqu'à la valeur de 1 μm, le temps d'électromigration devient du même ordre de grandeur que le temps de relaxation, et le temps de diffusion est environ 40 fois plus grand. On s'attend donc à ce que la migration tangentielle à la surface de la particule commence à jouer un rôle pour des tailles inférieures à quelques microns, tandis que la diffusion tangentielle à la surface n'interviendrait que pour des taille inférieures à quelques dizièmes de microns.

Rayon a (micron)	1	2.5	10	100
$\tau_r = \dfrac{\varepsilon}{\sigma}(s)$	1.8×10^{-3}	1.8×10^{-3}	1.8×10^{-3}	1.8×10^{-3}
$\tau_m = \dfrac{a}{KE_0}(s)$	10^{-3}	2.5×10^{-3}	10^{-2}	10^{-1}
$\tau_D = \dfrac{a^2}{D}(s)$	4×10^{-2}	0.25	4	400

FIGURE 1.14 – Temps caractéristiques pertinents du problème en fonction du rayon du cylindre

1.4.2 Traitement numérique

Nous ne connaissons pas de solution analytique à ce système d'équation non-linéaires, si bien que nous nous sommes orientés vers une résolution numérique. Pour simplifier encore et par soucis de rapidité de calcul, nous nous sommes limités au cas bidimensionnel d'un cylindre infini en rotation autour de son axe et soumis à un champ électrique orthogonal à celui-ci. Comme le rappelle l'article de l'annexe B.3 [26], dans le modèle classique de Quincke, le rotor se comporte de façon analogue à une sphère. Le champ seuil dépend des même paramètres, et ne diffère du cas de la sphère que par des facteurs géométriques indépendants de la taille du cylindre (voir aussi le chapitre suivant). Du point de vue du traitement numérique, le système d'équations (1.29) a été résolu dans le cas stationnaire de façon approchée par une méthode d'éléments finis via le logiciel commercial Comsol. Les détails numériques sont rassemblés dans l'article de l'annexe B.3 [26].

Nous avons fait d'abord varier les deux rapports pertinents τ_D/τ_r entre 20 et 2000 et τ_m/τ_r entre 0.8 et 20, indépendamment des paramètres physiques (figure 1.15). Comme prévu, lorsque les deux temps τ_D et τ_m sont très grands devant le temps de relaxation de la charge, nous avons constaté que la loi de variation de la vitesse angulaire du cylindre Ω en fonction de l'intensité du champ électrique réduite au carré r=$(E_0/E_c)^2$ était conforme à la description classique du rotor de Quincke bidimensionnel. En revanche, lorsqu'un de ces temps diminue, le champ seuil de rotation augmente, et la vitesse de rotation à champ électrique donné diminue. Ces variations sont significatives pour $\tau_D/\tau_r \leqslant 20$ ou $\tau_m/\tau_r \leqslant 2$.

Pour revenir au cas concret des liquides peu polaires, nous avons choisi de reprendre les paramètres physiques donnés dans la section précédente, et de faire varier le rayon a du cylindre : a=2.5, 3, 5, 10 μm. Les résultats sont rassemblés sur la figure 1.16. Là encore, plus a est petit, plus la rotation est rendue difficile. Il est également remarquable que la loi qui lie la vitesse angulaire du rotor à l'intensité du champ électrique semble adopter la même forme que dans le cadre du modèle de Quincke classique :

$$\Omega = \frac{1}{\tau_{MW}^*} \sqrt{\left(\frac{E_0}{E_c^*}\right)^2 - 1} \tag{1.30}$$

où les paramètres τ_{MW}^* et E_c^* dépendent des paramètres – constants sur chaque courbe – τ_D et

FIGURE 1.15 – Carré de la vitesse de rotation normalisée en fonction du carré de l'intensité du champ normalisée. $\tau_{MW}=\tau_{MW}/2$. E_c est l'intensité du champ électrique critique dans le cadre du modèle classique de Quincke.

rτ_m^2.

1.4.3 Modèle de conductivité de surface

Compte tenu que pour toutes les valeurs de a considérées, le rapport τ_D/τ_r est grand devant 1, alors que τ_m/τ_r est de l'ordre de l'unité, nous avons bâti un modèle prenant en compte l'électromigration tangentielle à l'intérieur de la couche, par le biais d'une conductivité de surface σ_Σ équivalente à une conductivité de volume du cylindre $\sigma_2=\sigma_\Sigma/a$. Les détails du modèle se trouvent dans l'article de l'annexe B.3. On trouve une loi semblable à l'expression de la vitesse de rotation d'un cylindre conducteur dans l'approximation de Quincke (voir l'annexe 1.A) avec :

$$\frac{\sigma_2}{\sigma_1} = \frac{1}{r\left(\frac{\tau_m}{\tau_r}\right)^2} \left(\sqrt{1 + 2r\left(\frac{\tau_m}{\tau_r}\right)^2} - 1 \right) \tag{1.31}$$

La conductivité équivalente σ_2 ne dépend donc que de $r\left(\frac{\tau_m}{\tau_r}\right)^2 = \frac{a^2\sigma_1}{K^2\eta}$ (il y a une erreur typographique dans l'article [26] de l'annexe B.3) en accord avec ce qui est trouvé numériquement dans la section précédente. Notamment, la conductivité équivalente ne dépend pas du champ électrique, ce qui explique la forme des courbes de la figure 1.16. Ajoutons que le temps de diffusion, absent de la modélisation, ne joue évidemment plus aucun rôle.

Comme le montre la figure 1.16, ce modèle décrit assez bien les calculs numériques pour les rayons a=10 μm et a=5 μm. En revanche, pour des rayons plus petits, des différences croissantes entre modèle et calculs numériques apparaissent. Pour l'expliquer, nous avons mis en évidence qu'en plus d'une couche ionique très fine à la surface existait une couche de charge diffuse, dont l'extension augmentait avec la diminution du rayon du cylindre. L'ordre de grandeur de
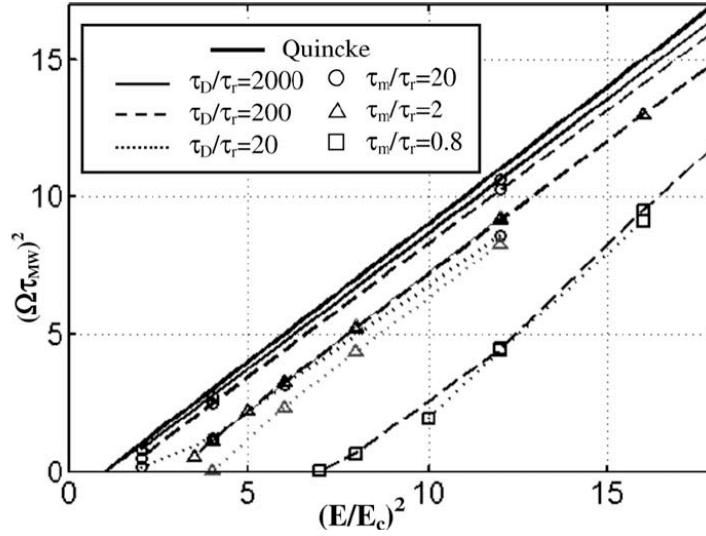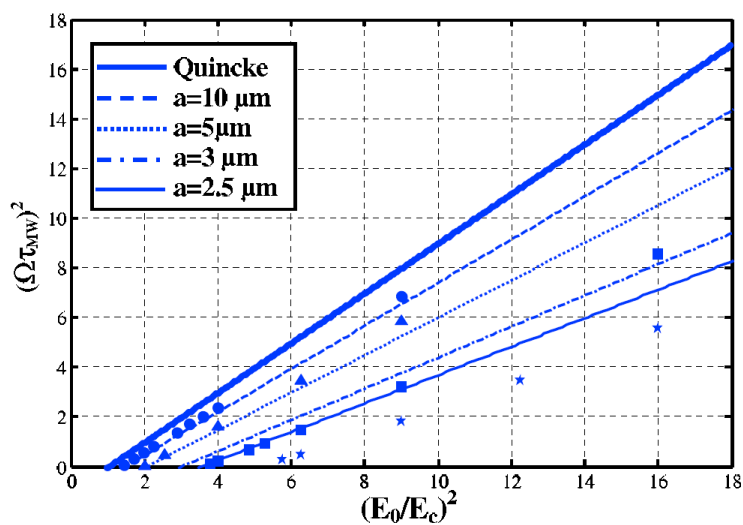
FIGURE 1.16 – Carré de la vitesse de rotation normalisée en fonction du carré de l'intensité du champ normalisée. Ligne épaisse : rotor de Quincke classique. Symboles : calcul numérique. Lignes : modèle. ● a=10 μm ; ▲ a=5 μm ; ■ a=3 μm ; ★ a=2.5 μm ;

l'épaisseur de la couche δ s'obtient en égalant le flux dû à l'électromigration des charges au flux diffusif à l'échelle de la couche $Kn_{\pm}E_0 \approx Dn_{\pm}/\delta$, ce qui donne :

$$\frac{\delta}{a} \approx \frac{\tau_m}{\tau_D} \qquad (1.32)$$

Lorsque δ/a devient de l'ordre de 1, le modèle de conductivité de surface n'est plus pertinent et il faut avoir recours au calcul numérique.

Annexe 1.A Grandeurs caractéristiques de la rotation de Quincke en géométries sphérique et cylindrique

Equation de relaxation

$$\frac{\partial \vec{P}}{\partial t} = \vec{\omega} \times \vec{P} - \frac{1}{\tau}(\vec{P} - (\chi_0 - \chi_\infty)\vec{E}_0)$$

Vitesse angulaire stationnaire

$$\omega_s = \frac{1}{\tau}\sqrt{\left(\frac{E}{E_c}\right)^2 - 1}$$

Champ seuil

$$E_c = \sqrt{-\frac{\alpha}{(\chi_0 - \chi_\infty)\tau}}$$

Géométrie sphérique	**Géométrie cylindrique**

Grandeurs géométriques

Rayon de la particule : a	Rayon du cylindre : a Longueur L

Coefficient de friction visqueuse

$\alpha = 8\pi\eta a^3$	$\alpha = 4\pi\eta a^2 L$

Polarisabilités

$\chi_0 = 4\pi\epsilon_1 a^3 \dfrac{\sigma_2 - \sigma_1}{2\sigma_1 + \sigma_2}$	$\chi_0 = 2\pi\epsilon_1 a^2 L \dfrac{\sigma_2 - \sigma_1}{\sigma_1 + \sigma_2}$
$\chi_\infty = 4\pi\epsilon_1 a^3 \dfrac{\epsilon_2 - \epsilon_1}{2\epsilon_1 + \epsilon_2}$	$\chi_\infty = 2\pi\epsilon_1 a^2 L \dfrac{\epsilon_2 - \epsilon_1}{\epsilon_1 + \epsilon_2}$

**Temps caractéristique
de relaxation du dipole**

$\tau = \dfrac{2\epsilon_1 + \epsilon_2}{2\sigma_1 + \sigma_2}$	$\tau = \dfrac{\epsilon_1 + \epsilon_2}{\sigma_1 + \sigma_2}$

Champ seuil

$$E_c = \sqrt{\frac{2}{3}\frac{\eta}{\epsilon_1}\frac{(2\sigma_1+\sigma_2)^2}{\sigma_1\sigma_2}\frac{1}{\frac{\epsilon_2}{\sigma_2}-\frac{\epsilon_1}{\sigma_1}}}$$
$$= \sqrt{\frac{8}{3}\frac{\eta\sigma_1}{\epsilon_1\epsilon_2}} \quad \text{si } \sigma_2 = 0$$

$$E_c = \sqrt{\frac{\eta}{\epsilon_1}\frac{(\sigma_1+\sigma_2)^2}{\sigma_1\sigma_2}\frac{1}{\frac{\epsilon_2}{\sigma_2}-\frac{\epsilon_1}{\sigma_1}}}$$
$$= \sqrt{\frac{\eta\sigma_1}{\epsilon_1\epsilon_2}} \quad \text{si } \sigma_2 = 0$$

Chapitre 2

Un peu de chaos dans l'électrorotation

2.1   Introduction

Jusqu'ici nous n'avons envisagé que le comportement stationnaire d'un objet en rotation. Ceci est tout à fait justifié lorsque l'inertie du système peut être négligée. Dans le cas contraire, en plus du temps de relaxation de la polarisation, un deuxième temps caractéristique intervient dans la dynamique en rotation de l'objet, qui devient donc plus complexe. Dans le cas d'un cylindre de section circulaire en rotation autour de son axe, Elisabeth Lemaire et Laurent Lobry ont montré [10] que les équations de la dynamique étaient équivalentes sans approximation aux célèbres équations de Lorenz, prévoyant notamment une dynamique chaotique lorsque l'inertie du cylindre n'est pas trop importante et que l'intensité du champ électrique est suffisante. Ils ont également dans le même article présenté une expérience qui le montrait de façon qualitative. Nous avons alors pensé que la mise au point d'une expérience quantitative s'imposait. En effet, du point de vue de la rotation de Quincke, aucune étude instationnaire n'avait jusqu'ici été menée. D'autre part, les systèmes obéissant aux équations de Lorenz, qui sont emblématiques du chaos déterministe, ne sont pas légions. Une démonstration expérimentale d'un nouveau système avait donc tout son intérêt. Elle a été publiée dans l'article de l'annexe B.4.

2.2   Système d'équation de Lorenz pour un rotor cylindrique

Le modèle classique de la rotation de Quincke d'un cylindre de rayon a et de longueur L soumis à un champ électrique uniforme orthogonal à son axe est décrit par les équations suivantes (voir l'annexe 1.A) :

$$\frac{d\vec{P}}{dt} = \Omega \ \vec{n} \times \vec{P} - \frac{1}{\tau_M}(\vec{P} - (\chi_0 - \chi_\infty)\vec{E})$$

$$I\frac{d\Omega}{dt}\vec{n} = -\alpha \ \Omega\vec{n} + \vec{P} \times \vec{E} \tag{2.1}$$

où $\vec{P}$ est le moment dipolaire du cylindre, situé dans le plan orthogonal à l'axe du cylindre repéré par $\vec{n}$, Ω est la vitesse de rotation du cylindre autour de son axe, I son moment d'inertie et $\vec{E}$ est le champ électrique uniforme appliqué orthogonalement à l'axe du cylindre. Rappelons également l'expression des coefficients de polarisabilité en fonction des conductivités σ_i et des permittivités ϵ_i : $\chi_0 = 2\pi\epsilon_1 a^2 L(\sigma_2 - \sigma_1)/(\sigma_1 + \sigma_2)$ et $\chi_\infty = 2\pi\epsilon_1 a^2 L(\epsilon_2 - \epsilon_1)/(\epsilon_1 + \epsilon_2)$, ainsi que le temps caractéristique de relaxation du dipôle dans le cas du cylindre $\tau_M = (\epsilon_2 + \epsilon_1)/(\sigma_1 + \sigma_2)$. La géométrie du problème est définie sur la figure 2.1. On peut introduire les variables
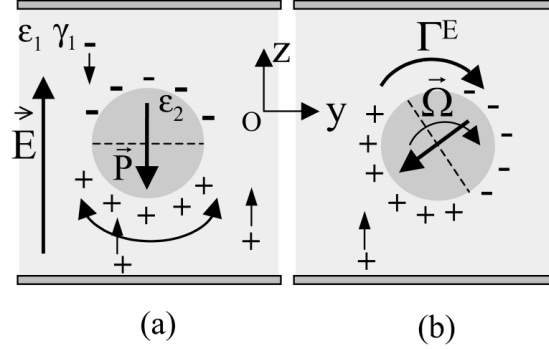
FIGURE 2.1 – Rotation de Quincke d'un cylindre. (a) Equilibre instable (b) Rotation

adimensionnées suivantes :

$$t^* = t/\tau_M; \ X = \Omega\tau_M; \ Y = \frac{\tau_M}{\alpha}P_y E$$
$$Z = \frac{\tau_M}{\alpha}(P_z - (\chi_0 - \chi_\infty)E)E \tag{2.2}$$

Les équations (2.1) se réduisent à :

$$\frac{dX}{dt^*} = P_r(Y - X)$$
$$\frac{dY}{dt^*} = -XZ + rX - Y \tag{2.3}$$
$$\frac{dZ}{dt^*} = XY - Z$$

On reconnaît les équations de Lorenz mettant en jeu deux paramètres de contrôle. Le premier, $P_r = \alpha\tau_M/I$, mesure le temps de relaxation du dipôle par rapport au temps mécanique de relaxation du cylindre. Le second est le paramètre habituel de la rotation de Quincke $r = (E/E_c)^2$. Comme on le sait, ces équations exhibent divers types de dynamiques, stationnaires, chaotiques, périodiques, intermittentes, séparées par des bifurcations. On pourra consulter par exemple [27] pour plus de précisions. Toutefois, voici les informations les plus importantes pour la suite. Lorsqu'on fait croître r à partir de 0, la solution stationnaire (X,Y,Z)=(0,0,0) se déstabilise en r=1, en une bifurcation fourche où deux solutions stationnaires symétriques apparaissent. Elle sont représentées par les deux points de la figure 2.2. Si Pr>2, une nouvelle bifurcation a lieu pour une valeur de r donnée par $r_b = P_r(P_r+4)/(P_r-2)$. Lors de cette bifurcation de Hopf sous-critique, les solutions stationnaires deviennent instables et les trajectoires du système, chaotiques,

sont confinées à une région de l'espace appelée attracteur étrange. Une telle trajectoire est représentée sur la figure 2.2. Elle oscille alternativement autour des deux solutions stationnaires non nulles instables. Nous allons nous tourner maintenant vers l'étude expérimentale.
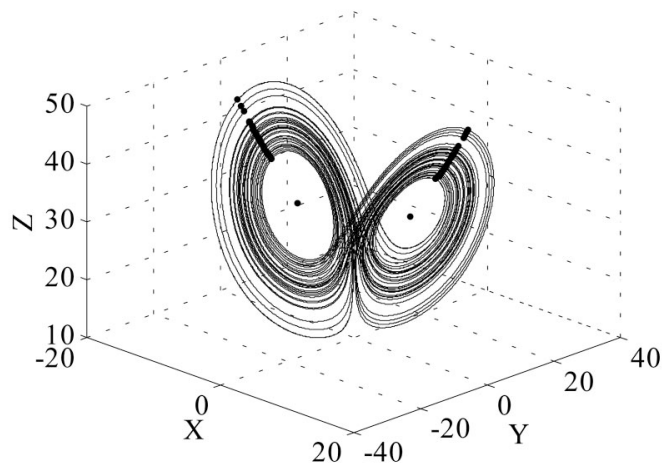
FIGURE 2.2 – Trajectoire chaotique du système de Lorenz dans l'espace des phases. Pr=2.5, r=33.

2.3 Etude expérimentale

2.3.1 Dispositif expérimental

Le dispositif expérimental est précisément décrit dans l'article de l'annexe B.4 [15]. En plus des contraintes habituelles sur les conductivités, les conditions pour observer le chaos résultent d'un compromis : l'inertie ne doit pas être trop grande, car le chaos ne peut apparaître pour des valeurs du paramètre P_r plus petites que 2. Cependant, elle ne doit pas être trop faible car la bifurcation vers le chaos a lieu pour une valeur de r critique $r_b = P_r(P_r + 4)/(P_r - 2)$ qui est une fonction croissante de P_r pour $P_r \gtrsim 5.5$. Or il est impossible d'augmenter l'intensité du champ électrique au-delà de l'intensité de claquage, qui est au maximum d'une dizaine de kV/mm. Nous avons donc choisi un capillaire en verre de diamètre extérieur 1 mm et de longueur 5 cm, monté sur des mécaniques d'horlogerie destinées à limiter au maximum le frottement solide. Le rotor, isolant, est plongé dans de l'huile rendue faiblement conductrice. Après mesure du temps de relaxation mécanique I/α et connaissant les permittivités du liquide et du rotor, et la conductivité de l'huile, le paramètre P_r est estimé, $P_r \approx 2.5$, de même que le champ seuil, $E_c \approx$ 1kV/cm.

Le dispositif expérimental est schématisé sur la figure 2.3. La vitesse de rotation du capillaire est mesurée grâce à un encodeur conçu ad hoc. Il s'agit d'un disque comportant 16 secteurs noirs et blancs, sur lequel convergent deux faisceaux laser. L'image des deux points laser sur deux photodiodes produit deux signaux binaires permettant de remonter à la position angulaire et au sens de rotation du capillaire, et donc après traitement à la vitesse de rotation, c'est-à-dire la variable X des équations (2.3). Remarquons que les deux autres variables Y et Z, correspondant
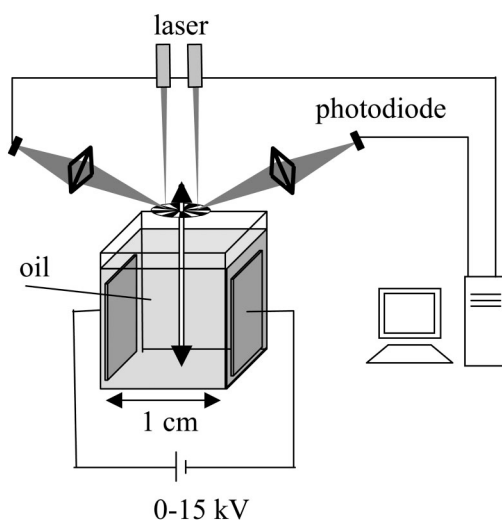
FIGURE 2.3 – Dispositif expérimental

aux composantes du dipôle, ne sont pas accessibles à la mesure.

2.3.2 Résultats expérimentaux

Dans un premier temps, la vitesse de rotation est enregistrée pour des valeurs croissantes de l'intensité du champ électrique. On obtient le diagramme de bifurcation représenté sur la figure 2.4. La première bifurcation a déjà été décrite dans le chapitre 1. Pour une intensité du
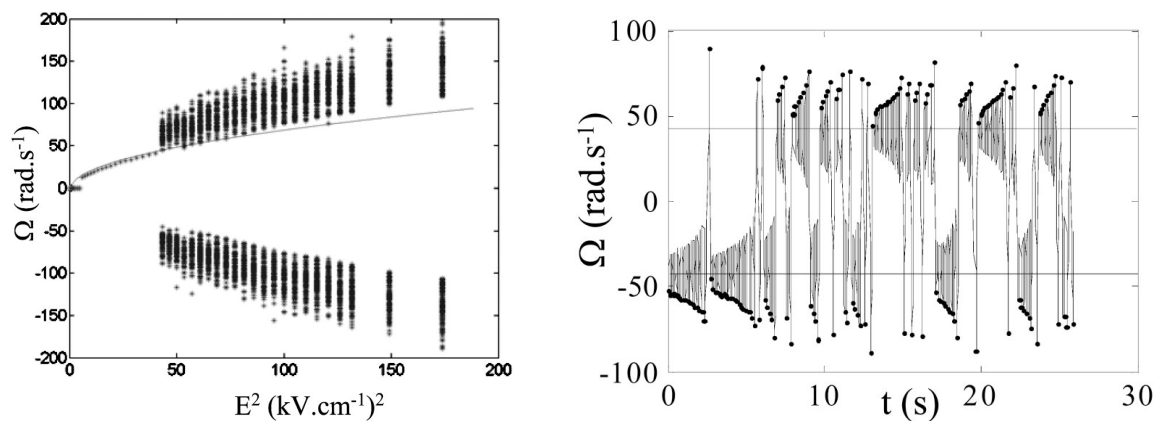
FIGURE 2.4 – Gauche : diagramme de bifurcation expérimental du rotor de Quincke. La ligne est un ajustement par la courbe théorique. Droite : dynamique de la vitesse angulaire dans le régime chaotique.

champ supérieure à E_c (r>1), le capillaire se met en rotation de façon spontanée. Il s'agit d'une bifurcation fourche, où l'état immobile devient instable, et où deux états caractérisés par des vitesses constantes et opposées apparaissent. Sur le diagramme, seules les vitesses positives sont représentées.

Au-delà de la deuxième bifurcation ($E^2 > 45kV^2.cm^{-2}$), la solution stationnaire n'est plus stable, et on obtient une évolution semblable à celle qui apparaît sur la figure 2.4. Le système oscille autour d'une solution instable, puis bascule et oscille autour de l'autre solution instable. Sur le diagramme de bifurcation de la figure 2.4, pour un champ donné, on a représenté l'ensemble des extrema de la vitesse, matérialisés par des points sur la courbe de droite. Les intensités critiques du champ pour les deux bifurcations sont en bon accord avec les valeurs prévues théoriquement.

Il reste à caractériser le régime chaotique. Comme je l'ai rappelé plus haut, nous n'avons accès expérimentalement qu'à une variable, $\Omega(t)$. Nous ne pouvons donc représenter la trajectoire du système dans l'espace (X,Y,Z). Cependant, il est possible d'utiliser une technique classique dans l'étude du chaos déterministe : il s'agit d'étudier les intersections $\{M_k\}_{k=1...}$ d'une trajectoire avec une surface bien choisie (voir la figure 2.5). On parle de la section de Poincaré associée à la
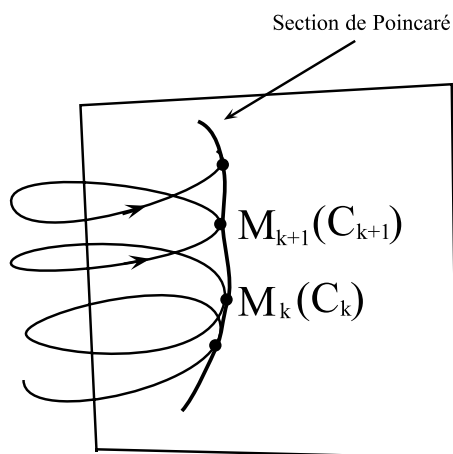
FIGURE 2.5 – Schématisation d'une section de Poincaré

trajectoire. Les points obtenus, qui appartiennent à une même surface, peuvent donc être décrits par deux coordonnées. Or il est connu que dans le cas des équations de Lorenz, les points d'une section de Poincaré se rassemblent quasiment sur une courbe, et peuvent donc en pratique être repérés par une seule coordonnée C_k. Enfin, une des caractéristiques du système de Lorenz est que la k+1^{ieme} intersection peut se déduire dans une certaine mesure de la précédente : si on représente C_{k+1} en fonction de C_k, tous les points se rassemblent sur une même quasi-courbe, appelée application de premier retour. Ceci est évidemment lié à la notion de chaos déterministe.

Nous avons choisi de repérer les intersections de la trajectoire avec le plan X=Y. Comme le montre les équations 2.3, ceci correspond aux extrema de la variable X, c'est-à-dire de la vitesse angulaire. La coordonnée C_k choisie est la valeur absolue de la vitesse de rotation au moment du passage par l'extremum. La représentation de l'application de premier retour consiste donc en l'ensemble des points de coordonnées ($|\Omega_k|, |\Omega_{k+1}|$). Une telle application apparaît sur la figure 2.6. Cette application de premier retour est en excellent accord qualitatif avec le comportement théorique attendu, compte tenu notamment de la friction solide résiduelle au niveau des pivots.

En conclusion, nous avons montré que le rotor de Quincke est un des rares systèmes modèles qui obéissent aux équations de Lorenz sans approximation notable. Nous avons en particulier
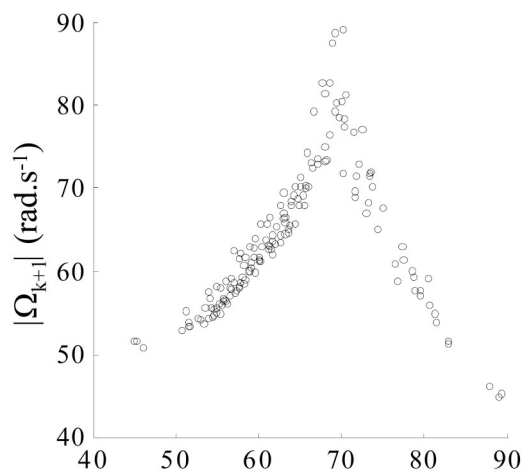
FIGURE 2.6 – Application de premier retour expérimentale correspondant à la trajectoire de la figure 2.4

caractérisé quantitativement le régime chaotique et l'attracteur étrange qui lui est associé. Cela nous a permis également de vérifier pour la première fois que le modèle classique du rotor de Quincke était tout à fait valide dans le cas instationnaire.

Chapitre 3

Electrophorèse dans une suspension semi-diluée

3.1   Introduction

Principe de l'électrophorèse

L'électrophorèse est la mise en mouvement de particules chargées en suspension dans un liquide sous l'action d'un champ électrique (voir [25] pour une introduction). Elle se traduit essentiellement par l'existence d'un coefficient de proportionnalité entre la vitesse moyenne des particules et le champ électrique imposé, qu'on appelle mobilité électrophorétique :

$$\vec{v} = \mu \vec{E} \tag{3.1}$$

Comme nous allons le rappeler par la suite, ce phénomène met en jeu les propriétés électrochimiques de l'interface des particules avec le liquide, et particulièrement la distribution de charges électriques au voisinage de la surface. Ces propriétés interviennent également dans la description des mécanismes de stabilisation des suspensions, qui sont évidemment d'une très grande importance pratique. De ce point de vue, l'électrophorèse apparaît donc comme une méthode de mesure, dont l'utilisation est subordonnée à une compréhension fine des liens entre la mobilité et les propriétés électrochimiques de l'interface solide-liquide.

Pour fixer les idées, le modèle le plus simple d'une particule isolante chargée dans un liquide conducteur est schématisé sur la figure 3.1. La particule est entourée d'une couche diffuse d'ions
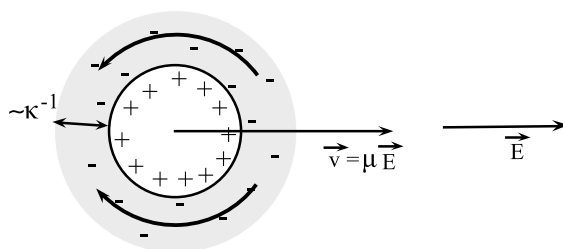
FIGURE 3.1 –

de charge opposée à la sienne. Deux paramètres jouent des rôles prépondérants dans la description du phénomène : la longueur de Debye κ^{-1} et le potentiel zeta ζ. Le premier est l'épaisseur typique de la couche ionique qui se développe au voisinage de l'interface, tandis que le potentiel zeta est le potentiel électrique à la position où le liquide commence à être cisaillé si la particule se déplace par rapport au liquide [1]. Dans le cas d'un électrolyte constitué de deux types d'ion de charges opposées $\pm ze$, où e est la charge élémentaire d'un électron, et de densité volumique n_0, la longueur de Debye a pour expression :

$$\kappa^{-1} = \sqrt{\frac{\epsilon_r \epsilon_0 k_B T}{2e^2 z^2 n_0}} \tag{3.2}$$

De façon générale, le mouvement de la particule est le résultat de l'action du champ électrique sur la distribution de charge liée à la particule, à laquelle s'oppose la force de résistance visqueuse du liquide (figure 3.1). On peut remarquer que cette force visqueuse n'est pas donnée par les lois habituelles pour un corps en mouvement en l'absence de champ électrique, puisque ce dernier entraîne le liquide de la couche diffuse et crée donc un gradient de vitesse supplémentaire qui freine la particule (figure 3.1). La mobilité est étroitement dépendante de la structure de la couche diffuse, et notamment du rapport de son épaisseur donnée par la relation (3.2) à la taille de la particule. Dans le cas de liquides polaires comme l'eau, la densité d'ions est importante et la longueur de Debye est généralement faible (quelques nanomètres). En revanche, dans le cas des liquides peu polaires qui nous intéressent, la couche s'épaissit et peut avoisiner quelques centaines de nanomètres et donc se trouver du même ordre de grandeur que la taille de particules colloïdales.

Influence de la concentration

Les suspensions très diluées ont reçu beaucoup d'attention depuis les travaux fondateurs de Smoluchowski [28]. Du point de vue théorique, cela revient à s'intéresser à une particule unique. Le cas le plus étudié, celui d'une sphère dont le potentiel zeta est uniforme, a été le sujet de traitements numériques [29], ou analytiques dans le cadre de différentes approximations – essentiellement $\kappa a \ll 1$ ou faible potentiel zeta. A l'heure actuelle, la mobilité électrophorétique d'une suspension très diluée est assez bien comprise, parfois au prix d'une description fine des propriétés électrochimiques de l'interface (couche de Stern, conduction de surface). D'autre part, de nombreuses méthodes d'investigation existent (optique, acoustique) qui en permettent la mesure de façon tout à fait standard.

Ce n'est pas le cas lorsque on augmente la fraction volumique, même en restant dans le régime semi-dilué ($\phi \approx 5\% - 10\%$). D'un point de vue expérimental, les méthodes optiques sont plus difficiles à mettre en oeuvre du fait de l'opacité introduite par l'absorption ou la diffusion multiple de la lumière. Des méthodes acoustiques existent, mais qui fonctionnent à haute fréquence. Les appareils disponibles commercialement sont d'autre part parfois difficiles à adapter aux besoins d'une expérience particulière. Enfin il est souvent délicat de diluer une suspension si l'on veut garder ses propriétés électrochimiques inchangées.

D'un point de vue théorique, la description de l'évolution de la mobilité avec la fraction

---

1. Il peut y avoir une différence entre cette position et la surface de la particule dans le cas d'éventuels ions ou molécules adsorbés à la surface (couche de Stern).

volumique de particules dans une suspension semi-diluée passe par la prise en compte des interactions électriques et hydrodynamiques entre particules. Nous y reviendrons à la section 3.3. Qualitativement, dans le régime semi-dilué, lorsque la taille des particules n'est pas très grande devant l'épaisseur de la couche ionique, on s'attend à ce que la mobilité décroisse avec la fraction volumique Φ, en suivant une loi du type :

$$\mu_E = \mu_0(1 - S\Phi) \tag{3.3}$$

où la constante S peut-être supérieure à 5.

3.2 Dispositif expérimental

Nous nous sommes intéressés à la mobilité électrophorétique de particules de silice dans un mélange de toluène et d'éthanol. Les particules fabriquées au laboratoire étaient assez monodisperses, de diamètre 2a=88±8 nm. Le liquide a été choisi pour sa faible permittivité relative ($\epsilon_r \approx 6.8$) et parce que son indice optique était le même que celui des particules. De cette façon, les suspensions étaient suffisamment transparentes et nous avons pu mesurer la mobilité jusqu'à une fraction volumique Φ=5.5%.

Nous avons utilisé une méthode de diffusion de lumière hétérodyne pour mesurer la mobilité. La méthode générale est décrite dans la référence [30], et le détail de notre dispositif, représenté sur la figure 3.2, est expliqué dans l'article de l'annexe C.1 [31]. La suspension est éclairée par un faisceau laser, et la lumière diffusée, mélangée à une fraction de la lumière incidente, est détectée par un photomultiplicateur. Un corrélateur calcule la fonction d'autocorrélation temporelle de
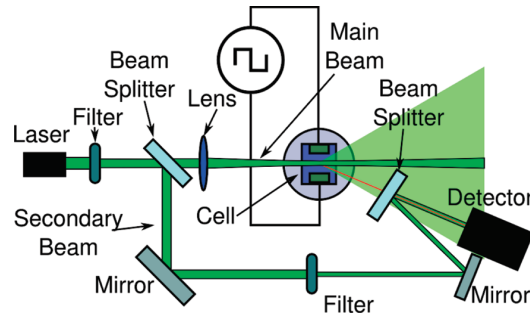
FIGURE 3.2 – Dispositif expérimental

l'intensité $C(\tau) = \langle I(t)I(t + \tau)\rangle_t$. Pour une suspension très diluée dont les particules sont en mouvement à la vitesse $\vec{v}$, la fonction d'autocorrélation s'écrit (voir [31]) :

$$C(\tau) = 1 + \alpha_2 \ e^{-\Gamma\tau}cos(\omega_D\tau) \tag{3.4}$$

La fréquence de l'oscillation donne la vitesse dans la direction du vecteur d'onde de diffusion $\vec{q}$, tandis que la modulation exponentielle est liée à la diffusion brownienne des particules, caracté-

risée par le coefficient de diffusion D :

$$\omega_D = \vec{q}.\vec{v}$$
$$\Gamma = Dq^2 \tag{3.5}$$

3.3   Résultats expérimentaux

La figure 3.3 représente la fonction d'autocorrélation de l'intensité lumineuse pour différentes valeurs de l'intensité du champ électrique pour une concentration $\Phi = 4.5\%$. La fréquence augmente linéairement avec le champ, comme le suggèrent les relations (3.1) et (3.5). En faisant
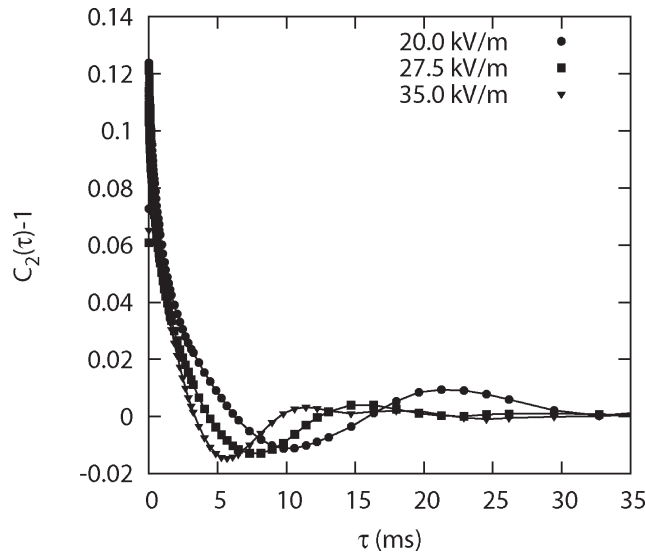
FIGURE 3.3 – Fonction d'autocorrélation de l'intensité lumineuse pour différentes valeurs de l'intensité du champ électrique. $\Phi = 4.5\%$.

varier la fraction volumique, on retrouve bien une dépendance linéaire pour la mobilité, avec un coefficient :

$$S = -8 \pm 2 \tag{3.6}$$

D'autre part, contrairement à ce qu'exprime la relation (3.5), la largeur de la fonction d'autocorrélation varie avec le champ électrique. Pour les plus faibles intensités électriques, la largeur de la fonction est due à la diffusion brownienne. Pour des intensités électriques plus fortes, elle diminue de sorte que le nombre d'oscillations visibles reste approximativement constant (figure 3.3), c'est-à-dire qu'elle devient proportionnelle à l'inverse de l'intensité du champ électrique. Nous avons interprété ces dernières mesures comme résultant de l'influence de la dispersion de la vitesse électrophorétique autour de la vitesse moyenne. La variance de la mobilité a été évaluée pour la fraction $\Phi=4.5\%$:

$$\Delta\mu_E \approx 0.6\mu_E \tag{3.7}$$

Pour comprendre ces résultats, nous avons fait appel à un modèle prenant en compte les inter-

actions hydrodynamiques et électriques entre particules.

3.4 Dispersion de la mobilité et interactions hydrodynamiques

Ainsi que nous l'avons rappelé à la section 3.1, une augmentation de la concentration induit des interactions hydrodynamiques et électriques entre particules. Ces interactions sont fortement influencées par le paramètre κa qui mesure le rayon d'une particule ramené à l'épaisseur de la couche diffuse. Ainsi, dans la limite $\kappa a >> 1$, pour des particules de même potentiel zeta, il apparaît que les interactions hydrodynamiques et les interactions électriques se neutralisent [32]. On peut le comprendre en remarquant que la charge de l'ensemble particule/couche diffuse est nulle, et que ce dernier n'est donc soumis à aucune force électrique. Dans ce cas, l'écoulement induit est potentiel dipolaire, proportionnel à l'inverse du cube de la distance, et adopte la même forme que le champ électrique induit à cause du caractère isolant de la particule, mais avec un effet opposé comme on l'a représenté de façon schématique sur le figure 3.4. Dans ce cas, la
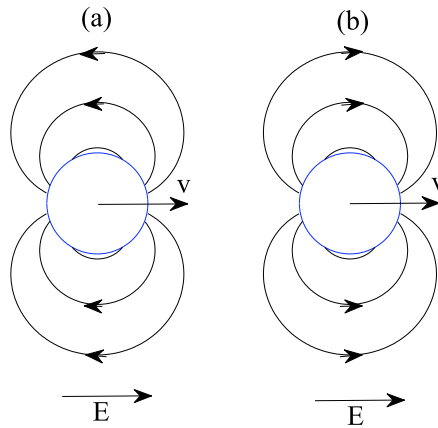
FIGURE 3.4 – Perturbation due au mouvement électrophorétique d'une particule chargée. (a) champ de vitesse (b) champ électrique.

mobilité moyenne dépend de la fraction volumique, sous la forme :

$$\mu_E = \mu_0(1 - 3/2\ \Phi)$$

En effet, sur le coefficient -3/2 Φ, une partie (-Φ) provient du fait que les particules déplacent du fluide dans la direction inverse de leur mouvement, puisque le système est limité par des parois imperméables, ce qui freine la particule d'autant. Le reste (-1/2 Φ) provient du champ électrique local ressenti par une particule à cause de la présence des autres. On peut noter que même si les potentiels zeta de deux particules en interaction ne sont pas identiques, la perturbation du champ décroît rapidement avec la distance, et les interactions sont faibles.

Ce n'est plus le cas lorsque $\kappa a \approx 1$. Nous avons évalué la longueur de Debye et le potentiel zeta des particules à partir des données expérimentales : $\kappa^{-1}a \approx 0.44$ et $\zeta \approx 50mV$. Dans ces conditions, des travaux numériques portant sur les interactions entre particules [33] ont montré

que l'on pouvait s'attendre à un coefficient S de l'ordre de -6 qui est en bon accord qualitatif avec nos résultats expérimentaux (3.6).

D'autre part, le même article présente un calcul de la dispersion des mobilités due à la variation de la vitesse d'une paire de particules en fonction de l'orientation de cette paire par rapport au champ électrique. Encore une fois, la mesure (3.7) est tout à fait compatible avec ces calculs numériques.

Naturellement, d'autres sources de dispersion de la mobilité existent, dont les plus évidentes sont la dispersion des charges portées par les particules, et celle des tailles de particules. D'autre part, la physico-chimie de la surface des particules joue évidemment un rôle très important, qui n'apparaît pas dans le modèle. Cependant, nous avons pu montrer que la méthode expérimentale que nous avons choisie, d'utilisation commune dans les suspensions très diluées, permet d'accéder à la fois à la mobilité et à sa dispersion dans les suspensions semi-diluées modèles. Même si la dispersion des mobilités a reçu peu d'attention pour le moment du point de vue expérimental, cette propriété constitue un paramètre supplémentaire de contrôle des modélisations du transport électrophorétique.

Deuxième partie

Rhéologie et microstructure des suspensions concentrées

Introduction

Rhéologie des suspensions : quelques idées fortes

Les suspensions concentrées de particules solides représentent une importante partie des matériaux naturels (fluides biologiques, boues) et industriels (bétons, polymères chargés, boues de forage, produits alimentaires et cosmétiques), et il est souvent primordial de comprendre leur propriétés rhéologiques. De par la diversité des particules considérées (distribution de taille, forme, densité, nature physico-chimique des surfaces), des fluides (newtoniens, viscoélastiques), des écoulements (influence du mouvement brownien, écoulement inertiel ou non), le champ d'investigation est extrêmement large, et les propriétés mécaniques d'une grande diversité. Comme souvent, il intéressant de restreindre le nombre de paramètres afin d'identifier ceux qui imposent des propriétés génériques. De ce point de vue, l'étude de suspensions modèles, si elle ne suffit naturellement pas à décrire tel ou tel matériau particulier d'intérêt industriel ou autre, a pourtant toute sa place dans une démarche plus globale.

Ainsi, les suspensions de particules sphériques non-browniennes, isodenses, dans un fluide newtonien en écoulement non-inertiel, présentent des propriétés non triviales communes à beaucoup de suspensions. Dans des écoulements de cisaillement stationnaires, il est possible de définir une viscosité qui ne dépend que de la fraction volumique et du taux de cisaillement [34]. D'autre part, cette viscosité diverge au voisinage d'une fraction volumique maximale Φ^*. Différentes lois d'ajustement ont été ainsi utilisées pour représenter la viscosité normalisée par celle du liquide suspendant :

$$\eta_r = \left(1 - \frac{\Phi}{\Phi^*}\right)^{-2} \text{ [35]}$$

$$\eta_r = \left(1 - \frac{\Phi}{\Phi^*}\right)^{-2.5\Phi^*} \text{ [36]} \tag{3.8}$$

$$\eta_r = e^{-2.34\Phi}\left(1 - \frac{\Phi}{\Phi^*}\right)^{-3} \text{ [37]}$$

La valeur de Φ^* observée expérimentalement est variable et se situe autour de 0.6.

D'autre part, dans des écoulements de cisaillement, des différences de contraintes normales ont été mises en évidence, d'autant plus importantes que la fraction volumique est grande [37, 38, 39, 40]. Ces différences de contraintes normales sont proportionnelles à la valeur absolue du taux de cisaillement, contrairement à ce qu'on peut observer dans les écoulements de polymères. De plus, sous l'action du cisaillement, les particules sont susceptibles de migrer vers certaines

zones de l'écoulement [41, 42]. Cette migration est d'ailleurs imputée par certains modèles à l'existence des contraintes normales [43, 44, 45]. Elle est liée à l'échelle des particules à un mouvement erratique, à l'instar de ce qu'on observe dans les suspensions browniennes, alors même que le mouvement brownien est négligeable [46, 47].

D'un point de vue théorique et numérique, de nombreuses études ont été menées depuis les travaux fondateurs d'Einstein [19] en vue de relier ces propriétés aux caractéristiques des particules et de l'écoulement à leur échelle, au prix de difficultés croissantes à mesure que les fortes fractions volumiques étaient appréhendées. Il est utile de rappeler quelques idées importantes à ce sujet. Tout d'abord, les interactions hydrodynamiques entre particules, de longue portée, sont omniprésentes à partir de fractions volumiques de quelques pour cent [21]. Pour les faibles distances interparticulaires, les forces d'interaction sont dominées par les forces de lubrification qui divergent au contact [48]. D'autre part, les interactions non-hydrodynamiques comme les forces de contact entre particules rugueuses, jouent de toute évidence un rôle très important. On peut remarquer d'abord qu'à l'échelle de l'interaction de deux particules, la présence de telles interactions brise la réversibilité des trajectoires des particules par inversion du cisaillement [49]. En ce qui concerne la rhéologie, les interactions non-hydrodynamiques influencent profondément à la fois la viscosité et les différences de contraintes normales [50, 51], mais également les coefficients d'auto-diffusion [49, 52].

Naturellement, si les interactions entre particules influencent les contraintes dans la suspension, la répartition spatiale des particules doit être prise en compte. Il est ainsi apparu qu'une suspension développait sous l'action d'un cisaillement une microstructure, c'est-à-dire un arrangement spatial relatif des particules, et que cette microstructure déterminait en retour, par le biais de la distribution des interactions entre particules, le comportement des suspensions (contraintes, diffusion induite par le cisaillement). Les travaux théoriques de Batchelor [20, 21] ont montré l'importance de cette microstructure, même pour des particules supposées lisses, dès que la fraction volumique est suffisamment importante pour que les interactions hydrodynamiques interviennent. D'autre part, des simulations [53, 54, 55] ainsi que des modèles théoriques [51, 56, 57, 58] ont permis de mieux comprendre l'influence des forces non hydrodynamiques sur la microstructure. Une des propriétés les plus frappantes est la brisure de symétrie amont-aval de la microstructure lorsque de telles forces sont prises en compte. Le lien direct entre les différences de contraintes normales dans le plan de cisaillement et cette brisure de symétrie a pu être mis en évidence [58]. Tout ceci est d'autant plus marqué que la fraction volumique est importante [55]. Finalement, il est utile de rappeler que, si les études concernant des suspensions concentrées relatées dans les deux derniers paragraphes mettent clairement en jeu des interactions non hydrodynamiques, vraisemblablement des interactions de contact entre particules rugueuses, il s'agit essentiellement d'études numériques. Même si d'énormes progrès ont été réalisés depuis une trentaine d'années, tant en ce qui concerne la puissance des ordinateurs que les techniques numériques, il n'en reste pas moins que les simulations de suspensions concentrées sont d'une mise en oeuvre assez lourde et d'une mise au point subtile, surtout lorsqu'on s'approche du blocage. De ce fait, certaines questions même qualitatives concernant les liens entre interactions et comportement mécanique macroscopique – la rhéofluidification des suspensions non browniennes par exemple, ou l'influence de la friction entre particules ou de leur élasticité – restent assez ouvertes.

Du point de vue expérimental, cette microstructure a d'abord été mise en évidence indi-

rectement en rhéométrie classique au travers d'expériences d'inversion de cisaillement [59]. Les auteurs ont pu montrer un régime transitoire à partir de l'inversion de cisaillement, constitué d'une diminution rapide de la viscosité avant un retour vers la viscosité stationnaire. Ces expériences les ont amenés à envisager une structure microscopique induite par l'écoulement, non invariante par inversion du taux de cisaillement. Le même type de régime transitoire, cette fois pour les contraintes normales, a été également mis en évidence par la suite [60, 61]. Ces études ont montré non seulement l'existence d'une microstructure, mais également que cette dernière pouvait changer en fonction des conditions d'écoulement, stationnaire ou transitoire. Ceci a donc débouché sur l'inclusion dans les lois de comportement de la suspension d'un paramètre supplémentaire, en plus du taux de cisaillement et de la fraction volumique. Ce paramètre décrivant l'état de structure locale a pu prendre plusieurs formes en fonction des modèles considérés [62, 63, 64].

En ce qui concerne la visualisation directe de la microstructure à l'échelle de la particule, peu d'expériences ont été reportées, et la plupart d'entre elles sont relativement qualitatives [65, 66] ou limitées aux faibles fractions volumiques [67].

A la suite de cet état de l'art, on peut définir quelques idées générales pour répondre aux questions expérimentales posées dans ce domaine. Tout d'abord, certains phénomènes inhérents aux suspensions, comme la migration induite par l'écoulement, que l'on a déjà évoquée, ou le glissement aux parois [68] ont mis en évidence les insuffisances dans ce domaine des expériences de rhéométrie classique, fondées sur l'hypothèse de matériaux homogènes et invariant au cours du temps. La réponse naturelle, quoique parfois difficile à mettre en oeuvre, réside dans la rhéologie locale, qui consiste à observer l'écoulement, et si possible la composition de la suspension, localement. Parmi les méthodes expérimentales, l'une est particulièrement attractive, à savoir l'imagerie par résonance magnétique (IRM). Elle peut notamment s'appliquer à un grand nombre de fluides complexes sans considération de transparence lumineuse et donc de concentration. D'ores et déjà, elle a permis d'éclaircir d'importantes questions [41, 34]. Outre le coût important associé à une méthode assez lourde à mettre en oeuvre, on peut regretter la difficulté de réaliser simultanément des mesures de profils de vitesse et de contraintes. En effet, il est difficile à l'heure actuelle d'intégrer un rhéomètre à un dispositif d'IRM.

Nous nous sommes tournés vers les méthodes optiques, plus exactement des techniques de vélocimétrie par image de particules (PIV), ainsi que de suivi de particules (ou Particle Tracking, PT). Ces méthodes, plus légères que l'IRM, peuvent être mises en oeuvre directement sur un rhéomètre, ce qui autorise simultanément les mesures de couple (donc de contrainte) et l'acquisition d'image. La principale difficulté réside dans l'ajustement des indices des particules et du liquide suspendant, obligatoirement très fin si l'on veut sonder des suspensions concentrées. Enfin, dans notre cas, contrairement aux méthodes ponctuelles comme la vélocimétrie laser Doppler, un plan entier de la suspension est sondé en bloc, ce qui permet d'étudier les régimes transitoires.

La fin de ce document sera consacré à la description de deux types d'expériences réalisées au laboratoire par Frédéric Blanc pendant sa thèse. L'ensemble des résultats présentés ici se trouve plus détaillé dans son manuscrit [69]. La première expérience, fondée sur la PIV, nous a permis de revisiter les expériences historiques de Gadala Maria et Acrivos [59] concernant l'inversion d'un cisaillement en géométrie de Couette. La comparaison de nos résultats expérimentaux avec des simulations numériques en dynamique stokésienne [70] a contribué à éclaircir le lien entre

chacune des phases du régime transitoire et l'évolution de la microstructure. En particulier, il a été possible d'identifier une contribution de la microstructure à la viscosité de la suspension, qui semble directement reliée aux différences de contraintes normales.

Nous nous intéresserons ensuite à des expériences de suivi de particules, au cours desquelles les positions de toutes les particules d'un plan de cisaillement en géométrie de Couette sont déterminées. En plus de donner accès au profil de vitesse des particules, cette méthode permet de calculer la fonction de distribution de paire (PDF) des particules dans le plan de cisaillement, qui est une mesure de la microstructure induite par l'écoulement. En particulier, pour des suspensions diluées, nous avons pu dégager une signature de la rugosité des particules sur la PDF [71] qui est à l'origine de la brisure de symétrie amont-aval de cette dernière. D'autre part, nous avons pu mesurer l'influence de la concentration en particules sur la microstructure pour une gamme de fraction volumique s'étendant de 5% à 56%, en portant une attention particulière à la structuration spatiale de la suspension au voisinage des parois de la cellule de Couette. Enfin, en régime transitoire, l'évolution de la microstructure a pu être corrélée à la réponse rhéologique de la suspension.

Chapitre 4

Rhéométrie locale par PIV

4.1 Dispositif expérimental

La description précise du dispositif expérimental et sa validation ont fait l'objet d'une publication [72] qui est reproduite dans l'annexe D.1.

Suspensions

Le choix du liquide et des particules constituant nos suspensions modèles non browniennes a été dicté essentiellement par le type de mesure que nous désirions entreprendre. L'indice optique autant que la densité des particules et du liquide devaient être ajustées au mieux. Nous avons donc opté pour des particules de PMMA de diamètre 2a=31±4μm fournies par la société Microbeads, de masse volumique évaluée à 1.178$kg.m^{-3}$ et d'indice optique environ 1.49. Le liquide suspendant nous a été fourni par la société Cargille. Il s'agit d'une huile de mêmes masse volumique et indice optique que les particules. Pour améliorer l'adaptation d'indice, la température est fixée à θ=34°C. Pour les besoins de la PIV, une petite quantité de particules, qui représente une fraction volumique de 0.25%, est marquée à l'aide d'un colorant fluorescent (nile blue A).

Dans toutes les expériences présentées par la suite, le nombre de Reynolds $Re_p = \rho\dot{\gamma}a^2/\eta_0$ est inférieur à 10^{-7}, ce qui permet de négliger l'inertie dans l'écoulement à l'échelle des particules. De même, les grandes valeurs du nombre de Péclet, $Pe = 6\pi\eta_0 a^3\dot{\gamma}/k_B T$, toujours supérieures à 10^5, rendent négligeable l'influence du mouvement brownien sur l'écoulement à cette échelle.

Dispositif de mesure

Nous avons adapté le dispositif de PIV sur un rhéomètre à contrainte imposée ThermoFisher Mars 2 (voir l'article en annexe D.1). Il s'agit d'une cellule de Couette transparente en PMMA, d'entrefer 10 mm et de hauteur 60 mm. Les rayons intérieurs et extérieurs de la géométrie sont respectivement notés R_i et R_e. Une nappe laser éclaire un plan de cisaillement, si bien que toutes les particules marquées de ce plan sont visibles. Une caméra enregistre les images de ce plan à intervalle régulier.

Le principe de la PIV est rappelé dans l'annexe D.1. Sur chaque image est défini un réseau de points. Le logiciel de PIV calcule le déplacement moyen entre deux images des particules

marquées situées dans une fenêtre de taille B autour de chaque point. On obtient donc à partir de deux images successives un champ de vitesse, dont on peut tirer la vitesse orthoradiale moyenne et donc le taux de cisaillement $\dot{\gamma}(r, t)$, ainsi que le cisaillement total $\gamma(r, t) = \int \dot{\gamma}(r, t')dt'$. D'autre part, la mesure du couple sur la géométrie permet d'accéder à la contrainte $\sigma(r, t)$, et donc au profil de viscosité $\eta(r, t) = \sigma(r, t)/\dot{\gamma}(r, t)$. La validation du dispositif, y compris les corrections de couple rendues nécessaire par la hauteur finie de la cellule, est détaillée dans l'annexe D.1.

La résolution spatiale est liée à la taille de la fenêtre de corrélation B, et vaut 200 microns environ. La résolution temporelle est l'intervalle entre deux images, 100ms.

4.2   Rhéométrie locale des suspensions concentrées

4.2.1   Influence de la migration

Il est bien connu que dans une géométrie de Couette, les particules ont tendance à migrer vers la paroi extérieure [42, 44]. Bien que cette propriété ne constitue pas le coeur de notre étude, nous avons voulu nous assurer que la migration ne perturberait pas nos mesures. Nous avons donc réalisé des expériences sur de grandes déformations. Il faut noter que, vraisemblablement à cause de la faible fraction de particules marquées, il est impossible de mesurer directement le profil de fraction volumique de particules. Pour pallier à cette difficulté, nous nous sommes intéressés à l'évolution du profil de viscosité, qui est liée de façon univoque à la fraction volumique [34]. La figure 4.1 résume une telle expérience pour une suspension de fraction volumique Φ=44.4%. La viscosité évolue avec un nombre de révolution caractéristique de quelques centaines
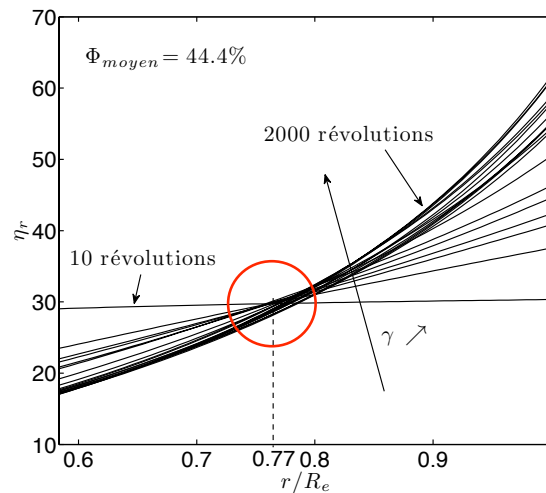
FIGURE 4.1 – Evolution du profils de viscosité réduite à grande déformation. Fraction volumique de départ : Φ=44.4%. L'intervalle entre deux courbes est de 100 tours.

de tours ; elle augmente au voisinage du cylindre extérieur, ce qui traduit un enrichissement en particules à cet endroit. Deux points sont importants ici : en dessous d'une dizaine de tours, les variations de viscosité, et donc de fraction volumique, sont très faibles. D'autre part, il existe une position particulière r=$r_c \approx 0.77 \times$R$_e$ au voisinage de laquelle la fraction volumique évolue

peu. L'existence d'une telle position n'a rien d'évident, mais elle est bien décrite par les deux principaux modèles qui traitent de la migration [73, 44].

Afin de s'affranchir au mieux de l'influence de la migration, toutes les mesures présentées par la suite ont été réalisées au voisinage de r_c, et pour des déformations totales équivalentes à 4 tours au maximum.

4.2.2 Etude du régime transitoire consécutif à une inversion de cisaillement

Comme je l'ai rappelé au cours de l'introduction, l'idée d'une microstructure induite par le cisaillement a été conçue comme une explication des variations de viscosité à partir d'une inversion de cisaillement [59]. Nous avons reproduit une expérience similaire en rhéométrie locale. Le principe est le suivant : une contrainte de cisaillement constante est imposée jusqu'à ce que la vitesse de rotation du cylindre se stabilise. On annule alors la contrainte, et à un instant pris comme origine, on impose un cisaillement opposé. On mesure alors la viscosité au cours du temps. On obtient une évolution comme celle qui est représentée sur la figure 4.2 pour une fraction volumique de 44.4%. Il s'agit d'une courbe maîtresse, c'est-à-dire que la viscosité
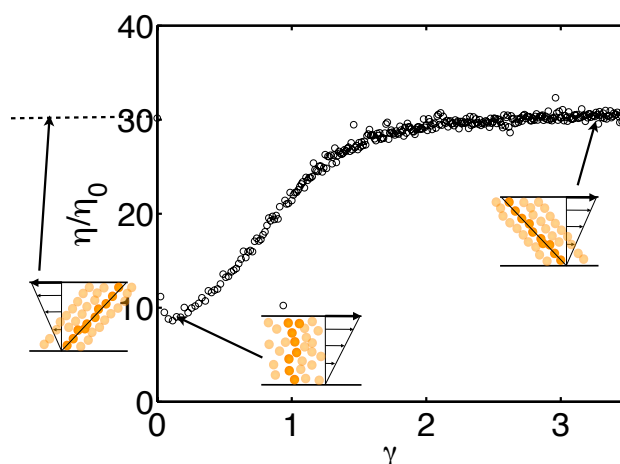
FIGURE 4.2 – Viscosité transitoire après inversion de cisaillement. $\Phi = 44.4\%$

réduite dépend essentiellement du cisaillement total γ à partir de l'inversion, et peu du taux de cisaillement auquel la courbe est parcourue. Seule la valeur du plateau change faiblement, ce qui est en accord avec le comportement légèrement rhéofluidifiant qui a été mis en évidence par ailleurs en écoulement stationnaire (voir l'annexe D.1).

L'interprétation est la suivante : le cisaillement induit une microstructure, schématisée sur la figure 4.2, ne présentant pas la symétrie amont-aval. Lors de l'inversion du cisaillement, la microstructure ne correspond donc plus à son état stationnaire. La diminution brutale de viscosité et le retour à la valeur stationnaire du plateau est attribuée à la destruction de cette microstructure et à la reconstruction de la microstructure symétrique.

La répétition de la même expérience pour différentes fractions volumiques mène à la figure 4.3. Ainsi, une augmentation de la fraction volumique induit une augmentation de la viscosité de plateau, qui est aussi la viscosité stationnaire, une augmentation de la viscosité minimale et

FIGURE 4.3 – Viscosité transitoire après inversion de cisaillement pour différentes fractions volumiques

une diminution de la déformation caractéristique du régime transitoire. Tout ceci avait été mis en évidence précédemment [59], mais seulement qualitativement en ce q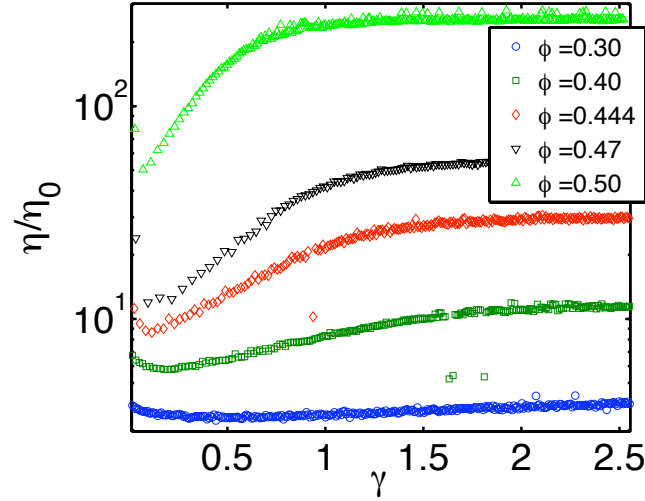ui concerne la viscosité minimale. Plus précisément, on peut représenter l'évolution de ces trois quantités en fonction de la fraction volumique (figure 4.4). Ainsi, la viscosité de plateau et la viscosité minimale ne dépendent pas de la même façon de la fraction volumique.

Les deux quantités divergent à approximativement la même fraction volumique $\Phi^* \approx 0.54$, mais avec des exposants différents :

$$
\begin{aligned}
\eta_{plateau} &\sim (1 - \frac{\Phi}{\Phi^*})^{-2} \\
\eta_{min} &\sim (1 - \frac{\Phi}{\Phi^*})^{-1}
\end{aligned}
\tag{4.1}
$$

On peut définir la déformation caractéristique telle que $\eta_r(\gamma_c) = \eta_{min} + (\eta_{plateau} - \eta_{min})/2$ et la représenter en fonction de la fraction volumique (figure 4.4). On obtient encore une loi simple mettant en jeu la même fraction volumique maximale Φ^* :

$$
\gamma_c \sim (1 - \frac{\Phi}{\Phi^*})
\tag{4.2}
$$

La première relation de l'équation (4.1) traduit une loi de corrélation classique pour la viscosité stationnaire d'une suspension non brownienne [34], même si la fraction volumique maximale $\Phi^* \approx 0.54$ que nous obtenons est un peu plus faible que les valeurs classiquement mesurées, proches de 0.6. Nous avons attribué cela à de possibles interactions colloïdales résiduelles entre particules, dont l'origine serait une couche de surfactant à la surface des particules provenant du processus de fabrication. Ceci est corroboré par une certaine relaxation élastique de la suspension, visible dans des tests de recouvrance que nous avons réalisés. On pourra consulter l'annexe
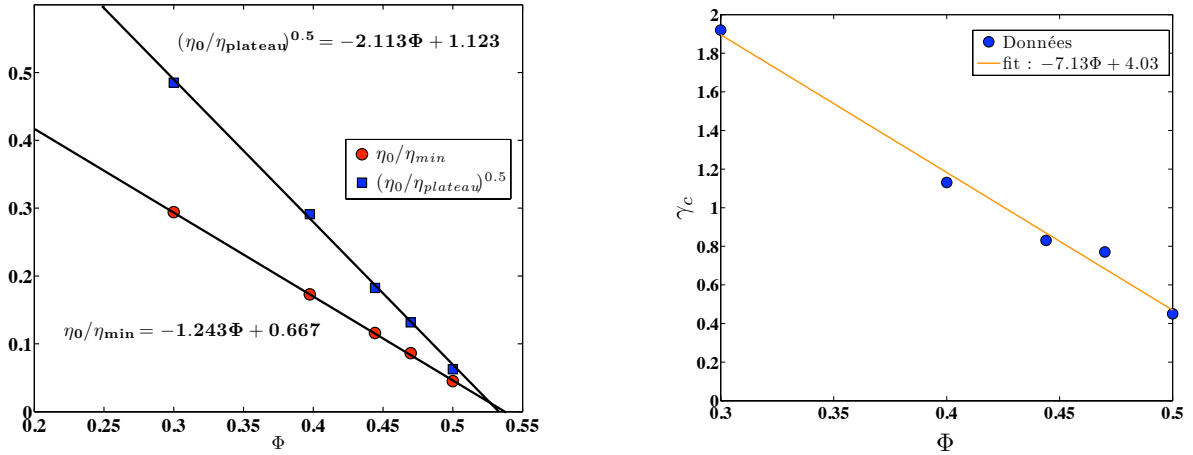
FIGURE 4.4 – **Gauche** : lois d'échelle pour la viscosité minimale et la viscosité de plateau. **Droite** : déformation totale caractéristique du régime transitoire

D.1 pour plus de détails.

La loi donnant la déformation critique γ_c (4.2), sans être classique, avait déjà été qualitativement mise en évidence [59]. Elle exprime simplement que le changement de microstructure se passe à une échelle de déformation telle que deux particules doivent parcourir une distance relative correspondant au volume libre disponible.

La deuxième relation de la corrélation (4.1) est plus nouvelle et plus éclairante quant à l'influence de la microstructure sur la rhéologie. Les deux comportements des viscosités stationnaire et minimale sont suffisamment différents pour représenter des mécanismes physiques distincts. Ainsi, on peut mieux comprendre l'origine de cette viscosité minimale en la comparant à des simulations numériques en dynamique stokésienne concernant des suspensions non browniennes aléatoires réalisées par Sierou et Brady [70]. Dans cette étude, les particules sont placées aléatoirement à chaque pas de calcul, et ne sont donc pas structurées par l'écoulement. Une telle simulation décrit bien par ailleurs la viscosité à fréquence infinie des suspensions colloïdales [74], pour lesquelles l'excitation est suffisamment rapide pour que la suspension ne se structure pas. La figure 4.5 permet de comparer la viscosité minimale avec les simulations numériques. On a représenté également des données expérimentales pour la viscosité à fréquence infinie de suspensions colloïdales de rayon 76nm [74]. L'accord entre nos mesures et les simulations est très bon, ce qui suggère que le minimum de viscosité correspond à un état de la suspension où la microstructure, si elle existe, a peu d'influence sur la rhéologie. Ceci est également en bon accord avec le modèle que proposent Mills et Snabre [75], qui prévoit une contribution purement hydrodynamique à la viscosité au voisinage du blocage proportionnelle à $\Phi^{4/3}(\Phi^* - \Phi)^{-1}$.

Tout cela est bien cohérent avec les mesures de contraintes normales après inversion de cisaillement publiées dans la littérature. En effet, il a été montré que la force normale sur une géométrie annulaire plan-plan s'annulait approximativement pour la déformation à laquelle le minimum de viscosité avait lieu [61], comme on peut le voir sur la figure 4.6. Or ces différences de contraintes normales seraient dues à la répartition anisotrope des interactions entre particules proches du contact [51]. Ainsi, à la déformation à laquelle la viscosité passe par un minimum, cette répartition de forces interparticulaires disparaît. Comme on le verra lors des mesures di-
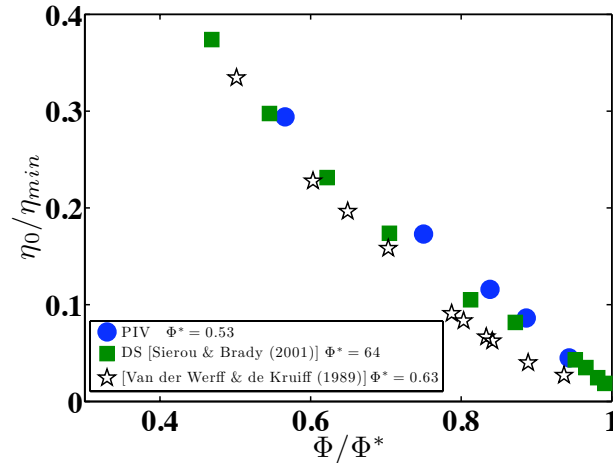
FIGURE 4.5 – Inverse de la viscosité réduite. ● Viscosité minimale par PIV. ■ Simulation numérique en dynamique stokésienne. ☆ Viscosité à fréquence infinie expérimentale (particule de rayon 76nm) [74]

rectes de microstructure, et en accord avec les simulations numériques [76], cela signifie que les particules initialement proches du contact ou au contact se sont éloignées les unes des autres.

Il semblerait donc que, de même que les différences de contraintes normales sont dues à la microstructure, on puisse définir une viscosité structurale due à la présence d'une microstructure :

$$\eta_{struct} = \eta_{plateau} - \eta_{min} \tag{4.3}$$

En fait, une telle viscosité ("excess viscosity") a déjà été définie à partir de la viscosité station-naire et de la viscosité à fréquence infinie [53]. Puisque cette viscosité η_{struct} semble avoir les mêmes origines que les différences de contraintes normales, on peut s'attendre à ce que ces deux quantités aient des dépendances assez similaires en fonction de la fraction volumique. Et en effet on peut s'en rendre compte en comparant les figures 4.7 et 4.8. Sur la première apparaissent les mesures de la viscosité structurale normalisée par la viscosité au plateau en fonction de la frac-tion volumique, en PIV et en PTV (chapitre 5) ainsi que les calculs par dynamique stokésienne évoqués plus haut. Une droite est ajustée à la deuxième partie de la courbe expérimentale en PIV. Sur la figure 4.8, nous avons représenté des mesures de différences de contraintes normales normalisées par la contrainte de cisaillement, réalisées par Dbouk [77] sur des suspensions non browniennes. Il est évidemment difficile de comparer quantitativement ces mesures qui corres-pondent à des systèmes différents. Cependant, les comportements au voisinage de $\Phi = 0$ et $\Phi = \Phi^*$ sont qualitativement les mêmes pour les deux quantités. Et en effet, une modélisation des contraintes de cisaillement et de la pression particulaire a été proposée récemment [78], qui semble donner à la viscosité structurale et à la pression particulaire des dépendances très proches.
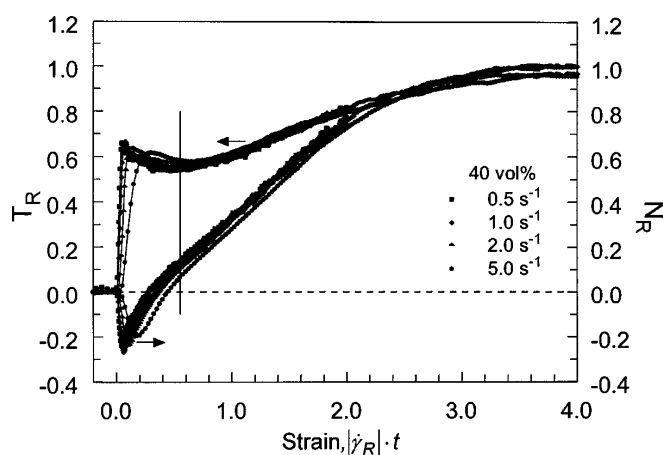
FIGURE 4.6 – Couple et force normale normalisés par leur valeur au plateau en fonction de la déformation moyenne d'après Kolli et al. [61]. Mesures réalisées dans un anneau plan-plan sur une suspension de 40% de sphères de diamètres 38-75μm dans du polyéthylène glycol. La ligne verticale correspond à la déformation pour laquelle le couple est minimal.

4.3 Conclusion

L' exploitation en rhéométrie locale d'expériences d'inversion de cisaillement a donc permis de mieux comprendre chaque étape du régime transitoire. La dépendance de la viscosité minimale associe de façon claire l'état de la suspension à cette étape à une distribution de particules peu structurée, où les contacts directs jouent un rôle peu important. Une viscosité structurale peut être définie, qui décrit l'influence de la microstructure sur la viscosité de la suspension. La dépendance en fonction de la fraction volumique de cette viscosité structurale, similaire à celle des différences de contraintes normales, confirme que l'origine physique de ces deux quantités se trouvent dans la microstructure induite par le cisaillement. D'autre part, à mesure que la fraction volumique s'approche de sa valeur de blocage, la viscosité stationnaire est dominée de plus en plus par la microstructure, comme le montrent les dépendances différentes de la viscosité au minimum et de la viscosité stationnaire.

Finalement, si l'interprétation de ces expériences de rhéométrie locale est plus claire à la lumière de considération microscopique – microstructure, interactions entre particules – tirées essentiellement de modèles et de simulations numériques, il n'en reste pas moins que ni la microstructure, ni les conséquences des interactions de contact n'ont été pour le moment mesurées dans notre étude. C'est l'objet du chapitre suivant.
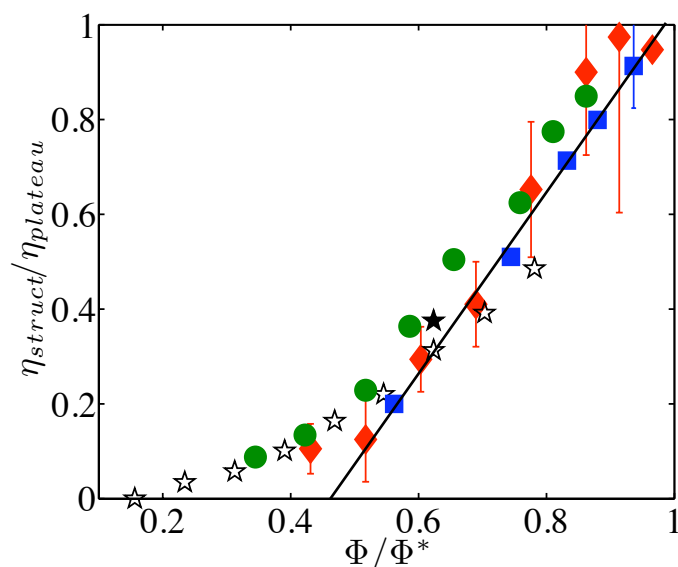
FIGURE 4.7 – Viscosité structurale normalisée par la viscosité de plateau en fonction de Φ/Φ^*.($\blacksquare$) Mesures en PIV - Φ^*=0.534 - a=15.5 μm. ($\blacklozenge$) Mesures en PTV (chap. 5) - Φ^*=0.58 - a=85 μm. ($\bullet$) Mesures en Couette cylindrique entrefer étroit.- Φ^*=0.58 - a=70 μm. d'après Dbouk [77]. Calculs en dynamique stokésienne :[53] ($\star$) Sans friction Φ^*=64. ($\bigstar$) Avec friction. (-) Régression linéaire sur les données en PIV : $1.9\times(\Phi/\Phi^*\text{-}0.47)$.
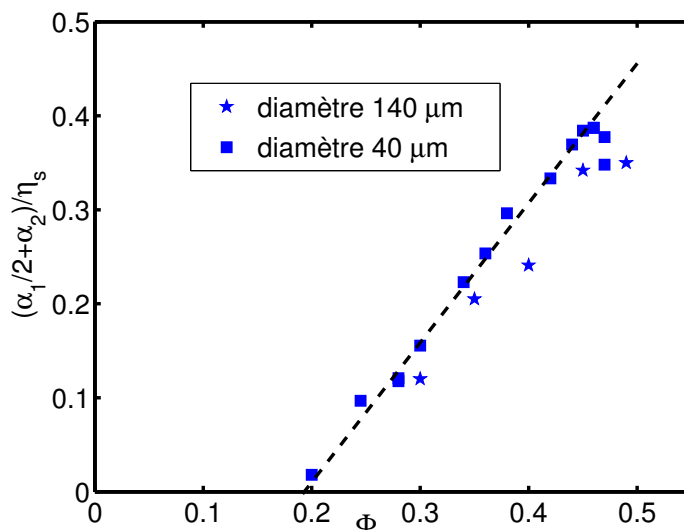
FIGURE 4.8 – Combinaison des coefficients de différences de contraintes normales normalisées par la contrainte de cisaillement. $\alpha_1 = -(\Sigma_{11} - \Sigma_{22})/\dot{\gamma}$; $\alpha_2 = -(\Sigma_{22} - \Sigma_{33})/\dot{\gamma}$. D'après Dbouk [77]. (- -) ajustement linéaire.

Chapitre 5

Mesure directe de la microstructure d'une suspension cisaillée

5.1   Introduction

Ce chapitre est consacré à la mesure directe de la microstructure d'une suspension non brownienne dans le plan de cisaillement. Comme on l'a déjà rappelé précédemment, des études théoriques et numériques ont montré l'importance de la microstructure dans le passage d'une description microscopique de la suspension à son comportement rhéologique macroscopique [21, 51, 57, 53]. En effet, l'arrangement spatial des particules détermine la distribution de forces interparticulaires, d'origine hydrodynamique ou autre, qui en retour est à l'origine des contraintes à l'échelle macroscopique. D'autre part, des études numériques ont montré le lien direct entre les interactions non hydrodynamiques et la brisure de symétrie amont-aval de la microstructure [54, 55], qui est, rappelons-le, à l'origine du régime transitoire observé dans le chapitre précédent. Enfin, à mesure que la fraction volumique augmente, on s'attend à ce que les effets de la microstructure s'accentuent [55], avec une probabilité de contact, ou de particules très proches selon les modèles d'interaction, en forte augmentation, menant à des interactions plus intenses. Pour toutes ces raisons, la mesure expérimentale de la microstructure d'une suspension cisaillée est d'un très grand intérêt, et notamment pour la validation de modèles théoriques ou de simulations numériques très complexes à forte fraction volumique.

La microstructure est caractérisée en première approximation par la fonction de distribution de paires (PDF). Pour la mesurer, nous avons utilisé le dispositif de PIV, mis en oeuvre cependant de façon un peu différente. Après une brève description de la méthode de mesure et de calcul de la PDF (on pourra se reporter à l'annexe D.3 pour une description plus détaillée), je montrerai d'abord les mesures que nous avons obtenues à basse fraction volumique. En les comparant à un calcul numérique fondé sur les trajectoires de deux particules rugueuses en interaction, nous pourrons identifier la signature de la rugosité sur la PDF et obtenir une mesure de la taille caractéristique des rugosités.

Nous étudierons ensuite l'influence de la fraction volumique sur la microstructure, ainsi que l'influence du confinement, c'est-à-dire de la taille finie de l'entrefer de la cellule de Couette. Enfin, nous reviendrons aux régimes transitoires du chapitre précédent, observés cette fois du point de vue de la microstructure.

5.2 Mise en oeuvre de la mesure de la microstructure

Dispositif expérimental

Nous avons réutilisé le dispositif expérimental présenté au chapitre 4, en diminuant le gap de moitié (0.5 cm) afin d'obtenir une meilleure définition des particules. Nous avons choisi d'autre part des particules plus grosses, de diamètre $170\pm12\ \mu$m, toujours en PMMA. L'entrefer, mesuré relativement à la taille d'une particule, correspond donc à 30 diamètres de particules, et 1 pixel sur le plan de l'image correspond à 5.5 μm. Cette fois, le colorant fluorescent est dissous dans le même liquide suspendant que précédemment, si bien que toutes les particules traversées par le plan laser, d'épaisseur approximative 30 μm, sonts visibles en négatif, sous la forme de disques noirs de différentes tailles (figure 5.1).
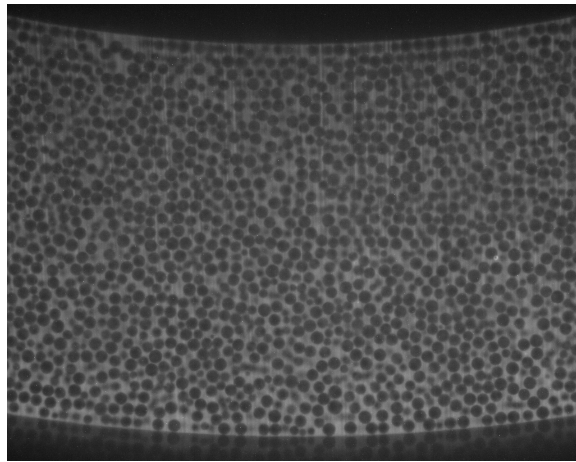
FIGURE 5.1 – Image typique d'une suspension. Φ=0.56

Détection des particules

Après une extraction des bords des particules, une procédure de détection de cercle fondée sur la transformée de Hough circulaire (voir [69] et les références incluses) permet d'obtenir la position des centres des particules avec une résolution d'une fraction de pixel (environ 0.1 px soit environ 0.5 μm), et les rayons avec une résolution de 1 pixel. Nous avons vérifié que la distribution de rayon était compatible avec celle que l'on attend pour des particules monodisperses traversées par un plan infiniment fin.

Extraction de la fonction de distribution de paires

La fonction de distribution de paires est liée à la densité de probabilité de présence d'une particule en une position $\vec{r}$ étant donné qu'une particule se trouve à l'origine $P(\vec{r}|\vec{0})$. Puisque deux particules très éloignées sont complètement décorrélées, on normalise $P(\vec{r}|\vec{0})$ par la densité moyenne de particules n_0, ce qui définit la fonction de distribution de paires :

$$g(\vec{r}) = \frac{P(\vec{r}|\vec{0})}{n_0} \tag{5.1}$$

On s'attend donc à ce que g($\vec{r}$) tende vers 1 loin de l'origine.

Naturellement, on n'a accès qu'à une fonction de distribution surfacique que l'on construit en comptant les paires de particules pour un vecteur $\vec{r}$ donné dans le plan de la figure, relativement aux axes de cisaillement. Ce vecteur position est en fait la projection du vecteur joignant les centres des particules dans le plan. La probabilité est alors normalisée par la densité surfacique de particules détectées. On montre que, pourvu que l'on ne prenne en compte dans le calcul que les particules de plus gros diamètres, c'est-à-dire centrées au mieux sur la nappe dans la direction orthogonale au plan, on mesure alors avec une bonne approximation la véritable PDF dans le plan de cisaillement [69, 71]. D'autre part, le plan est échantillonné en coordonnées cylindriques, et la taille de l'échantillon ($\Delta\rho, \Delta\theta$) fixe la résolution de la mesure. Nous avons choisi $\Delta\rho = 1$ px $\approx 1/15 \times$a et $\Delta\theta = 2\pi/80$ rad $= 4.5°$. Cela signifie que l'on mesure la valeur moyenne de la PDF sur chaque échantillon. Cette résolution est bien meilleure que les quelques mesures qui sont publiées dans la littérature, ce qui explique l'originalité de nos résultats. Cependant, il faut garder à l'esprit que les simulations prévoient qu'à forte fraction volumique, les interactions importantes se passent au contact, c'est à dire à des échelles encore inférieures à la résolution radiale de notre dispositif. Nous n'obtiendrons donc qu'une partie de l'information pertinente, comme cela apparaîtra dans la section 5.5.

5.3 Microstructure d'une suspension diluée

Le travail décrit dans cette section a fait l'objet d'une publication [71] reproduite dans l'annexe D.3. La figure 5.2 représente la PDF d'une suspension de fraction volumique 5% mesurée grâce au traitement de 50000 images. Le nombre de Reynolds et le nombre de Péclet valent respectivement Re $\approx 4.10^{-6}$ et Pe $\approx 6.10^{7}$. La direction de la vitesse est le vecteur de base $\vec{e}_x$, et les quadrants de compression du tenseur de taux de déformation sont définis par xy<0.

Les caractéristiques principales sont les suivantes. Tout d'abord, dés qu'on considère des positions un peu éloignées de la particules centrale (r/a > 2.5), la PDF est isotrope, excepté au voisinage d'un axe proche de la direction de la vitesse dans le quadrant de dilatation. Cet axe se caractérise par une déplétion de particules. Dans les autres directions, on observe une zone de surconcentration de paires de particules au contact (r/a ≈ 2), qui se décolle dans le quadrant de dilatation. Ainsi, la PDF est anisotrope, et non invariante par la symétrie par rapport au plan ($\vec{\nabla}v, \vec{\nabla} \times \vec{v}$), symétrie qui correspond à une inversion du cisaillement. On peut noter que cette anisotropie de la PDF, avec une déplétion de particules dans une direction proche de celle de la vitesse, avait déjà été mesurée auparavant [67]. Cependant, le décollement de la zone de surconcentration en forme de traînée est ici mise en évidence pour la première fois. Il est important puisqu'il traduit une interaction non hydrodynamique entre particules, comme nous allons le comprendre maintenant.

Pour bien saisir la portée de la figure 5.2, on peut revenir au premier calcul de la fonction de distribution de paires réalisé par Batchelor et Green en prenant en compte seulement les interactions entre paires de particules [21] :

$$g_{BG}(r) = \frac{1}{1 - A(r)} exp \left(\int_r^\infty \frac{3}{s} \frac{B(s) - A(s)}{1 - A(s)} ds \right) \qquad (5.2)$$
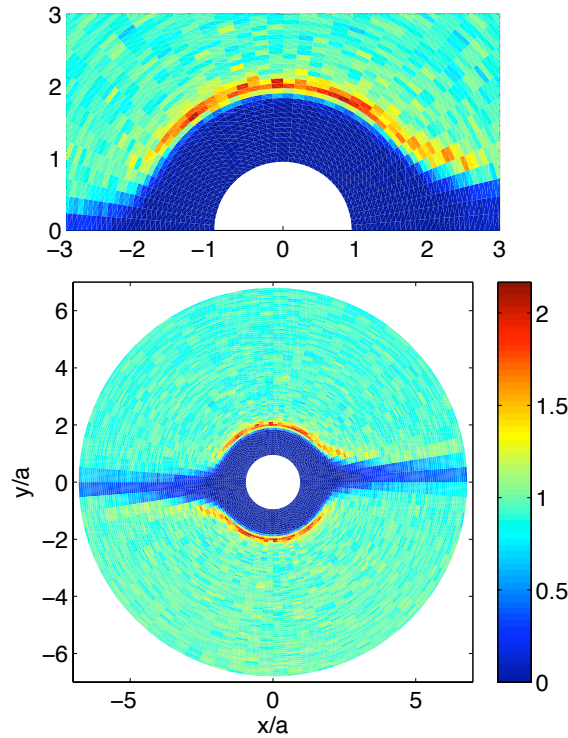
FIGURE 5.2 – Fonction de distribution de paires dans le plan $(\vec{v}, \vec{\nabla}\, v)$. Φ=0.05. Les quadrants de compression sont définis par xy<0. En haut : agrandissement de la région centrale avec la traînée de forte concentration.

Les fonctions de mobilité 1-A(r) et B(r) donnent les vitesses relatives respectivement radiale et tangentielle de deux particules dans un écoulement linéaire. Cette fonction g_{BG}(r) est isotrope. Cependant, elle a été déterminée à partir des trajectoires relatives de deux particules en supposant que ces trajectoires provenaient toutes de l'infini où la PDF vaut 1. Ce n'est cependant pas le cas pour un écoulement de cisaillement simple tel que le nôtre où la rotation locale de l'écoulement induit l'existence de trajectoires fermées, situées au voisinage de r/a≈2 dans le plan de cisaillement (figure 5.3.a). Il est théoriquement difficile de prédire la valeur de la PDF dans cette zone, qui dépend en tout état de cause de la distribution initiale des particules. Notons que ces trajectoires fermées, lorsqu'elles se trouvent dans le plan de cisaillement, amènent les particules à une distance obligatoirement inférieure à r/a ≈ 2.00004 (voir [71] et références incluses).

Pour expliquer leurs résultats, Rampall et al. [67] utilisent l'argument suivant : la rugosité des particules, pourvu qu'elle excède 4.10^{-5}a, supprime les orbites fermées dans le plan de cisaillement. En effet, une façon de modéliser la rugosité consiste à supposer une distance ϵa, telle que les surfaces des particules ne puissent pas s'approcher à une distance inférieure à celle-ci [49]. Pour ce faire, on annule la vitesse relative radiale des particules. Ceci permet donc d'expliquer la déplétion des particules dans la zone des orbites fermées représentée schématiquement sur la figure 5.3. Cela a été prévu théoriquement [57] et mis en évidence dans des simulations en dynamique stokésienne [55]. D'autre part, cette rugosité brise la symétrie des trajectoires provenant de l'infini : les particules dans le quadrant de compression sont empêchées de s'approcher,
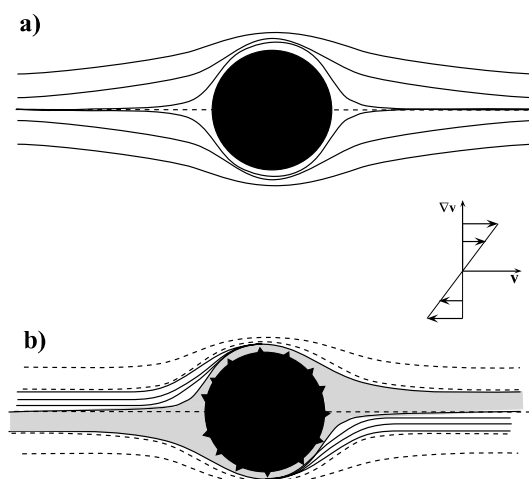
FIGURE 5.3 – Explication qualitative de la PDF à partir des trajectoires. (a) Rugosité nulle. Les trajectoires sont symétriques avec une zone d'orbites fermées peuplée éventuellement. (b) Rugosité non nulle. La rugosité élimine les orbites fermées et dissymétrise les trajectoires. D'après [69].

mais peuvent se séparer dés que la ligne des centres dépasse l'axe du gradient de vitesse. Les particules qui entrent en contact subissent donc un décalage de leur trajectoire relative [49, 71]. Ce décalage élargit la zone de déplétion dans le quadrant de dilatation (figure 5.3). D'autre part, si l'on considère une unique taille de rugosité, toutes les trajectoires de particules qui subissent un contact se rassemblent sur la même trajectoire dans le quadrant de dilatation, ce qui induit le décollement de la zone de surconcentration [57]. Cette zone constitue donc une mesure de la rugosité.

Pour préciser ce dernier point, nous avons calculé la PDF à partir des trajectoires de deux particules dans un cisaillement simple, modifiées pour tenir compte de la rugosité [49, 71]. La figure 5.4 reproduit la PDF calculée pour une rugosité $\epsilon a = 3.10^{-3}a$. La résolution spatiale est sensiblement la même que dans l'étude expérimentale. On a aussi représenté une trajectoire au cours de laquelle un contact a lieu. Cette trajectoire définit de façon très claire la traînée de forte concentration. L'accord qualitatif avec les résultats expérimentaux de la figure 5.2 est évidemment très bon. Une comparaison plus quantitative est proposée sur la figure 5.5. L'accord est encore une fois très bon, notamment en ce qui concerne la position de la traînée matérialisée par le pic sur les figures 5.5.a et b. On peut donc évaluer la rugosité à environ $3.10^{-3}a \approx 255$nm. Des mesures réalisées par ailleurs en microscopie à force atomique font état d'une rugosité généralement faible (20nm) avec des pics isolés mais réguliers d'environ 200nm. Ces dernières mesures confirment donc à la fois l'influence de la rugosité et des contacts entre particules sur la microstructure d'une suspension diluée et la pertinence du modèle de rugosité que nous avons utilisé.
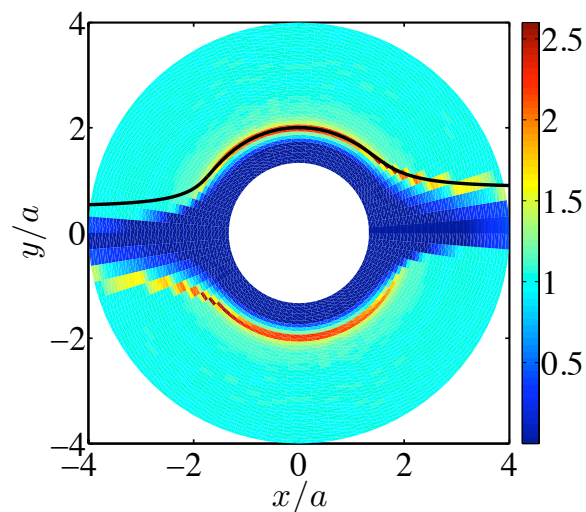
FIGURE 5.4 – PDF calculée numériquement à partir des trajectoires de deux particules rugueuses. $\epsilon a = 3.10^{-3}a$. Une trajectoire, au cours de laquelle un contact a lieu, est représentée. Quadrant de dilatation :xy>0.
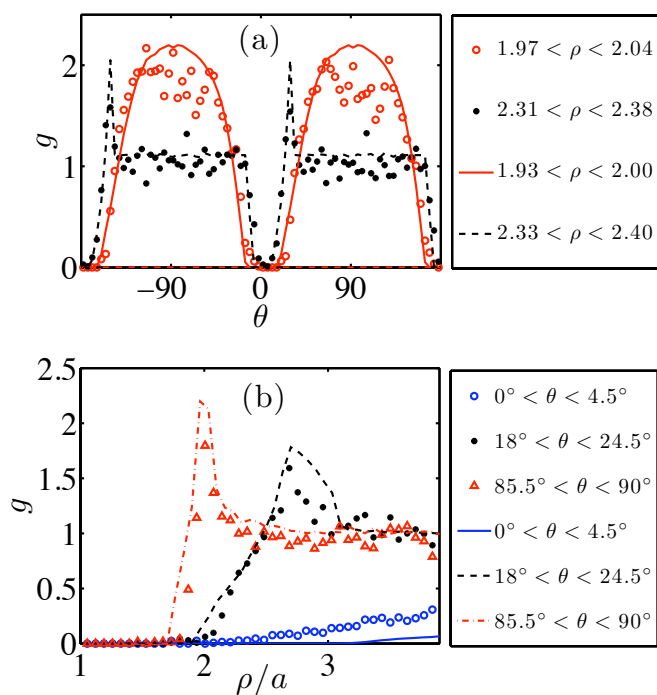
FIGURE 5.5 – Comparaison entre les PDF mesurée et calculée. (a) En fonction de l'angle à partir de la direction de la vitesse, au contact et pour r/a≈2.3. (b) En fonction de la distance interparticulaire, pour différentes valeurs de l'angle. Quadrant de dilatation : $0 < \theta < 90°$.

5.4 Influence de la fraction volumique sur la microstructure

Résultats expérimentaux

La bonne qualité des images que nous avons obtenues nous a permis de mesurer les PDF jusqu'à des fractions volumiques de 56%. Pour limiter l'influence des bords de la cellule sur le

calcul de la PDF, une zone d'exclusion est définie, dont les bords se situent à 3a des bords de la cellule de Couette (figure 5.6). Aucune particule ne peut être choisie dans cette zone d'exclusion.
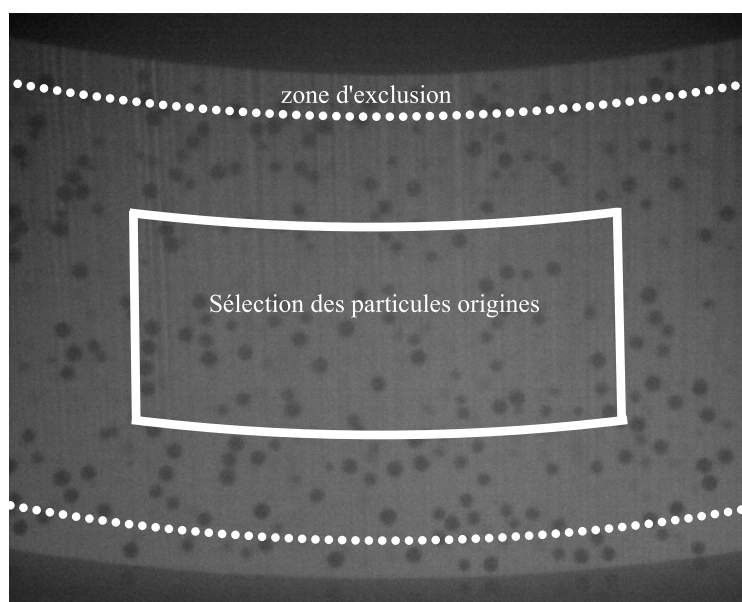
FIGURE 5.6 – Définition des zones pour la sélection des particules

On impose en outre une distance minimale de 8a entre une particule origine de la paire et la zone d'exclusion.

L'ensemble des PDF mesurées est représenté sur les figures 5.15 et 5.16 de l'annexe 5.A p.68. Le nombre d'images disponibles pour le calcul de chaque fonction est variable, ce qui explique la qualité inégale des PDF. Pour les plus basses fractions volumiques, typiquement jusqu'à $\Phi=0.1$, on retrouve l'allure générale de la PDF à $\Phi=0.05$, avec une couche de concentration importante au voisinage du contact, et une zone de déplétion dans une direction proche de celle de la vitesse. Le décollement de la couche dans le quadrant de dilatation n'est plus visible dés $\Phi=0.1$, mais il faut noter que le nombre de particules entrant dans le calcul est de 1000 seulement, ce qui traduit une statistique moins précise avec plus de bruit. Une caractéristique importante est l'inclinaison croissante avec la fraction volumique de la direction de déplétion. A partir de $\Phi=0.4$, l'allure de la PDF change : une surintensité dans la direction proche de celle de la vitesse apparaît, avec une zone de déplétion secondaire dans le quadrant de compression. Finalement, on peut remarquer que la PDF ne s'éloigne significativement de 1 qu'au voisinage des plus proches voisins – $\rho/\mathrm{a} \approx 2$ – et que la seconde couronne de voisins – $\rho/\mathrm{a} \approx 4$ – apparaît faiblement, et ce seulement pour les plus hautes fractions volumiques. Ceci marque donc l'absence d'un ordre à longue portée.

On peut adopter une autre point de vue en intégrant la PDF sur une fine couche radiale correspondant à la forte concentration au contact. La variation angulaire de cette quantité, g(θ), est représentée sur les figures 5.7 et 5.8. Il apparaît sur la figure 5.7 que pour les fractions volumiques de 0.1 à 0.15, g(θ) évolue peu, notamment en ce qui concerne l'angle du minimum. En revanche, la figure 5.8 montre qu'à partir de $\Phi=0.2$, l'angle caractéristique de la déplétion (matérialisé par une des lignes pointillées) augmente jusqu'à avoisiner l'axe de dilatation $\theta=45°$. D'autre part, à partir d'une fraction volumique de 0.4, le pic de surintensité est clairement visible

FIGURE 5.7 – PDF intégrée sur une couche $\rho/a \in [1.87, 2.14]$. Quadrant de dilatation $\theta > 0$. Direction de la vitesse : $\theta = 0$. D'après [69].
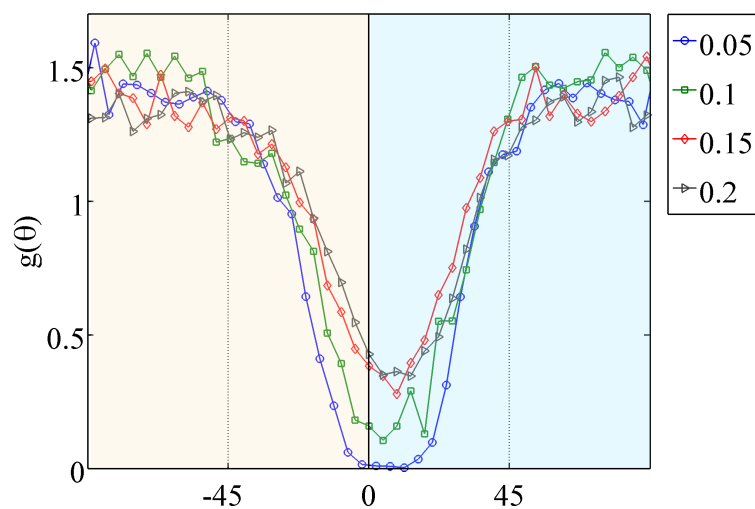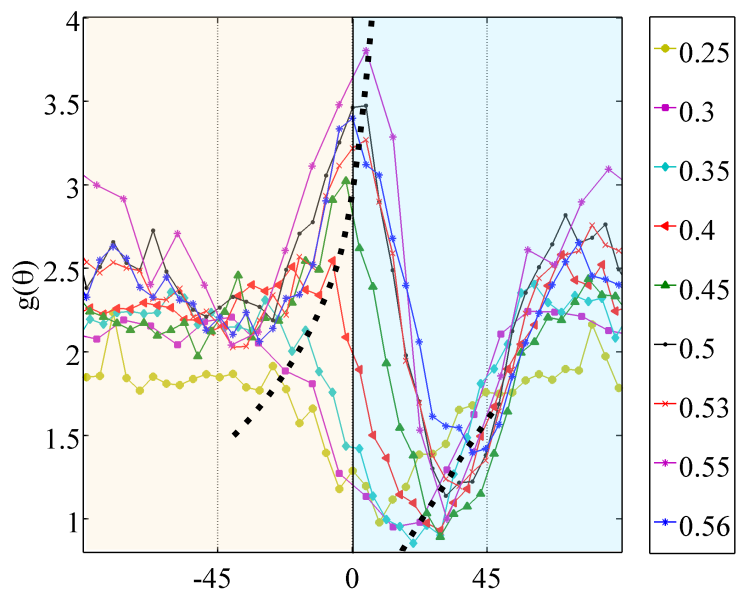

FIGURE 5.8 – PDF intégrée sur une couche $\rho/a \in [1.87, 2.14]$. Quadrant de dilatation : $\theta > 0$. Direction de la vitesse : $\theta = 0$. Les lignes pointillées matérialisent les positions du pic de surintensité proche de la direction de la vitesse d'une part, les positions du centre de la zone déplétée d'autre part. D'après [69].

au voisinage de la direction de la vitesse $\theta=0$°, de plus en plus intense à mesure que la fraction volumique augmente.

Finalement, nous avons estimé la valeur de l'angle correspondant à la déplétion, θ^*, par un ajustement d'une fonction quadratique sur le minimum de g(θ). La figure 5.9 représente l'évolution de θ^* en fonction de la fraction volumique. Jusqu'à $\Phi=0.15$, θ^* est approximativement
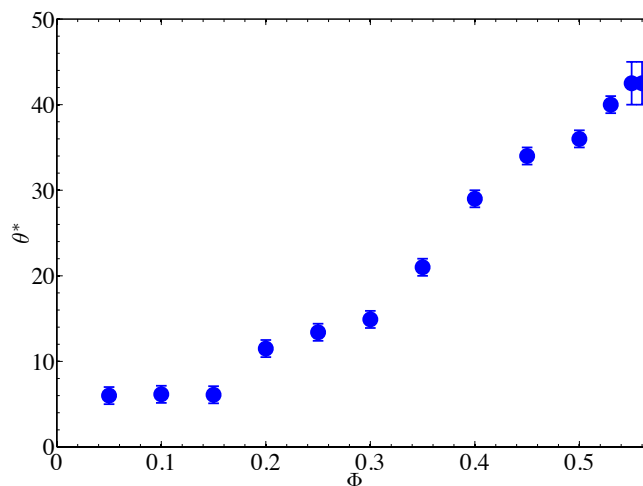
FIGURE 5.9 – Angle caractéristique de la zone de déplétion (°).

constant et vaut 6°. Au delà d'une fraction volumique d'environ 0.2, cet angle augmente plus ou moins linéairement pour s'approcher de 45°à $\Phi=0.56$.

Discussion

Comme cela a été rappelé précédemment, les modèles théoriques et les simulations numériques montrent un lien étroit entre la microstructure et les propriétés rhéologiques des suspensions cisaillées. De ce point de vue, la position angulaire de la zone de déplétion, θ^*, semble un paramètre important. Comme nous l'avons montré à la section 5.3, dans la limite des petites fractions volumiques, la PDF est déterminée par la rugosité des particules, ce qui fixe la limite de θ^* lorsque $\Phi \rightarrow 0$. Ceci a d'ailleurs été montré dans des simulations numériques [54], dans lesquelles la rugosité a été modélisée par un potentiel d'interaction répulsif. A basse fraction volumique (0.1), les auteurs on montré que la portée r_c de ce potentiel d'interaction, équivalent à une taille de rugosité, contrôlait la taille et donc l'angle de la zone déplétée.

Au cours d'une autre étude [55], les mêmes auteurs ont fait varier la fraction volumique et ont obtenu pour une portée $r_c=10^{-4}$a – a est le rayon d'une particule – les courbes de la figure 5.10. Pour la plus basse fraction volumique (0.01), la PDF n'est pas tout à fait symétrique, avec une valeur de θ^* faible dans le quadrant de dilatation. C'est bien ce qu'on pouvait attendre, puisque la portée r_c est à peine supérieure à la distance minimale d'approche de deux sphères dans un cisaillement (section 5.3). D'autre part, lorsque la fraction volumique augmente, la PDF est peu modifiée jusqu'à $\Phi=0.05$, puis l'angle θ^* augmente, de même que ce que nous observons expérimentalement.

FIGURE 5.10 – Fonctions de distribution de paires normalisées pour différentes fractions volumiques de particules obtenues par simulation numérique en Dynamique Stokésienne. La portée du potentiel d'interaction est ici $r_c = 10^{-4}$a. D'après [55]
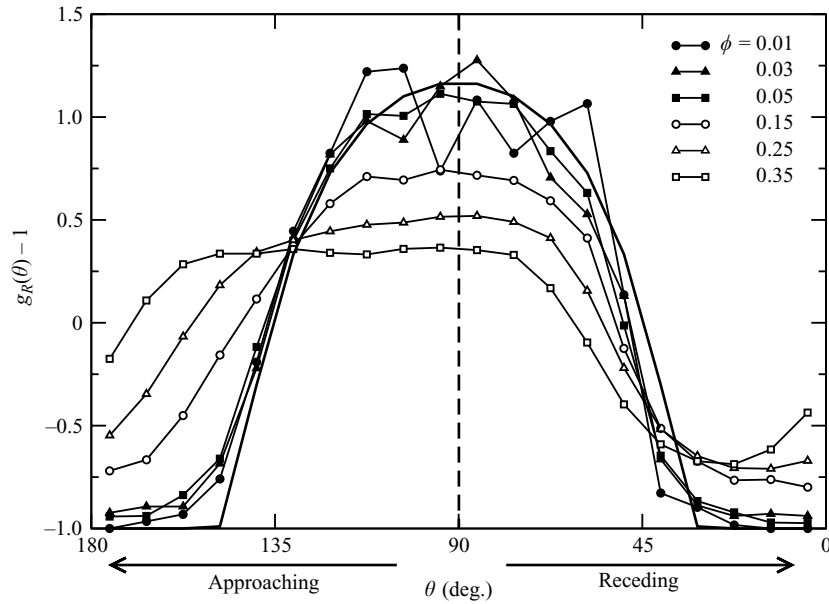
Du point de vue de la rhéologie, on peut comparer l'évolution de l'angle θ^* (figure 5.9) aux figures 4.7 et 4.8 représentant respectivement la viscosité structurale et les différences de contraintes normales mesurées expérimentalement. Ces trois courbes mettent en évidence ce qui apparaît comme un changement de régime à une fraction volumique de l'ordre de 0.2. A basse fraction volumique, la PDF reste assez semblable à sa limite en dilution infinie, les interactions induites par la microstructure restent peu importantes. Les fractions volumiques supérieures sont caractéristiques d'une augmentation rapide de l'influence des contacts et des forces de lubrification, couplée à une évolution importante de la microstructure.

L'apparition d'une surintensité dans la direction de la vitesse révèle la forte augmentation de la probabilité de paires de particules approximativement alignées avec la vitesse. Ceci, de même que l'apparition concomitante d'une déplétion secondaire dans le quadrant de compression, appelle naturellement des questions. De tels comportements ont rarement été décrits dans la littérature théorique et numérique. Cependant, à l'aide de simulations en dynamique stokésienne concernant des particules peu browniennes (Pe=1000), Morris et Katyal [79] ont reporté l'apparition d'un tel pic . De même, Yeo et Maxey [80], au travers de simulation de suspensions de particules non browniennes dans une cellule de couette, ont mis en évidence des variations de $g(\theta)$ qualitativement proche de la figure 5.8. Une des questions qui se posent concerne l'influence de l'entrefer fini de la cellule sur l'apparition de paires alignées avec la vitesse, qui serait pris en compte dans cette dernière simulation. Cette hypothèse serait en accord avec une constatation expérimentale que nous avons faite [69], selon laquelle une structuration très nette de la suspension apparaît près des parois aux mêmes fractions volumiques que le pic de probabilité dans la direction de la vitesse. En ce qui concerne le travail de Morris et Katyal, si les simulations en dy-

namique stokésienne visent à modéliser un milieu infini, la taille finie de la cellule représentative pourrait être à l'origine d'un pseudo-confinement ayant le même type de conséquences que des parois. Le problème semble donc encore ouvert, et il sera donc intéressant dans des expériences futures de faire varier le confinement.

5.5 Microstructure et inversion de cisaillement

Les résultats du chapitre 4 ont permis de supposer que l'état de la suspension s'apparentait, lors du passage au minimum de viscosité, à une microstructure sinon isotrope, du moins qui avait peu d'influence sur la rhéologie. Nous avons donc essayé de vérifier ce point. Pour ce faire, nous avons réalisé le même type d'inversion de cisaillement qu'au cours des expériences décrites dans le chapitre 4. Le suivi de particules nous a permis d'obtenir la viscosité en régime transitoire, dont un exemple est représenté sur la figure 5.11. L'allure du régime transitoire est tout à
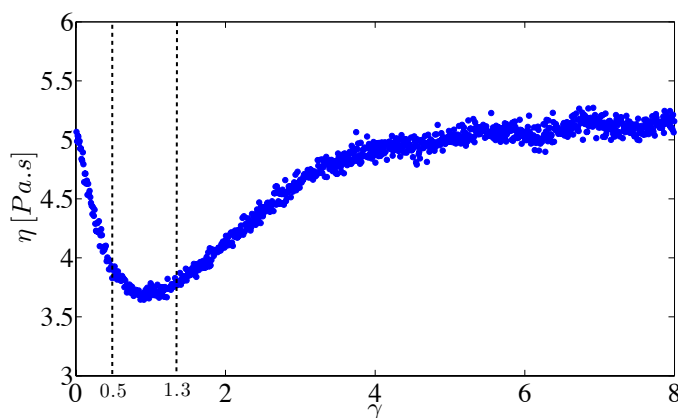
FIGURE 5.11 – Réponse transitoire de la viscosité réduite locale (r/R$_e$=0.88) après une inversion de contrainte de cisaillement (le couple passe en γ=0 de 50 μN.m à -50 μN.m). $\Phi = 0.35$. D'après [69].

fait similaire à ce qui a été mesuré en PIV. Cependant, la résolution en déformation est bien meilleure, ce qui s'explique par la meilleure résolution des déplacements des centres des particules ramenés à la valeur du rayon. Il apparaît que la viscosité ne subit aucune discontinuité lors de l'inversion de cisaillement. Ce résultat préliminaire reste à confirmer. Cependant, la question semble importante du point de vue de l'interprétation microscopique des forces de contact : les particules qui sont en contact avant l'inversion sont majoritairement orientées dans le quadrant de compression, et l'écoulement est donc fortement contraint par l'impossibilité de ces particules de se rapprocher. A l'inversion, ce degré de liberté étant libéré, puisque les particules considérées peuvent se séparer, on s'attend intuitivement à une discontinuité des contraintes. Ainsi, les contraintes normales, au lieu de simplement changer de signe, s'annulent pratiquement [61, 60]. On peut cependant incriminer les capteurs de force normale sur les rhéomètres, habituellement bien moins performants que les capteurs de couple. Finalement, ce point reste à éclaircir, et une étude est en cours dans ce but.

Les PDF avant inversion et sur le plateau après inversion sont représentées sur la figure 5.12. Elles sont manifestement symétriques par rapport au plan $(\vec{\nabla} v, \vec{\nabla} \times \vec{v})$, comme on s'y attendait.
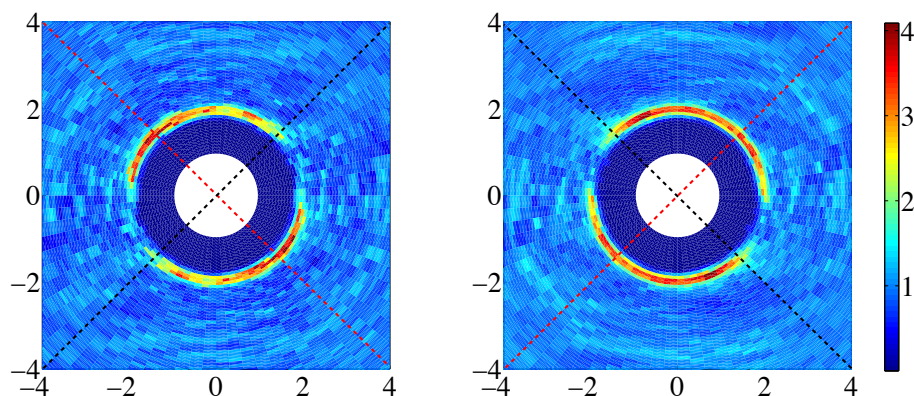
FIGURE 5.12 – Fonctions de distributions de paires dans le plan (x/a , y/a) calculées en cisaillement stationnaire avant et après l'inversion de la figure 5.11. D'après [69].

La fonction de distribution de paires au minimum de viscosité est évaluée en calculant la moyenne des PDF instantanées sur un intervalle de déformation représenté sur la figure 5.11 entre 0.5 et 1.3. Ceci permet un meilleur échantillonnage statistique. La PDF obtenue apparaît sur la figure 5.13. Sa qualité est moins bonne, car elle a été calculée à partir d'un nombre réduit d'images.
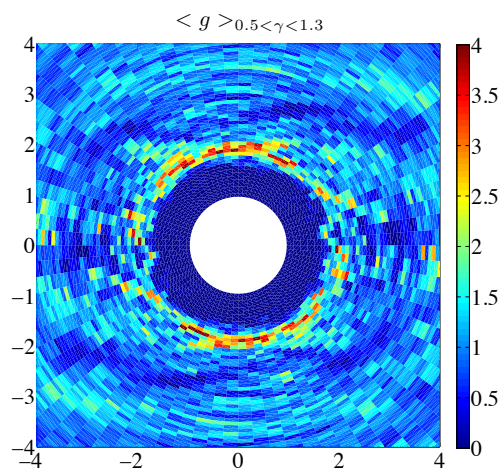
FIGURE 5.13 – Fonction de distribution de paires dans le plan (x/a , y/a) au minimum de viscosité (0.5<γ<1.3). D'après [69].

Elle paraît cependant symétrique par rapport au plan $(\vec{\nabla} v, \vec{\nabla} \times \vec{v})$. Pour s'en convaincre, on peut observer la figure 5.14 qui représente l'intégrale de la PDF sur une fine couche radiale 1.8<ρ/a<2.1 en fonction de l'angle θ compté à partir de la direction de la vitesse. Là encore, les deux fonctions stationnaires sont symétriques l'une de l'autre, et la fonction au minimum de viscosité est elle-même symétrique. On remarque donc qu'une microstructure existe, mais qu'elle
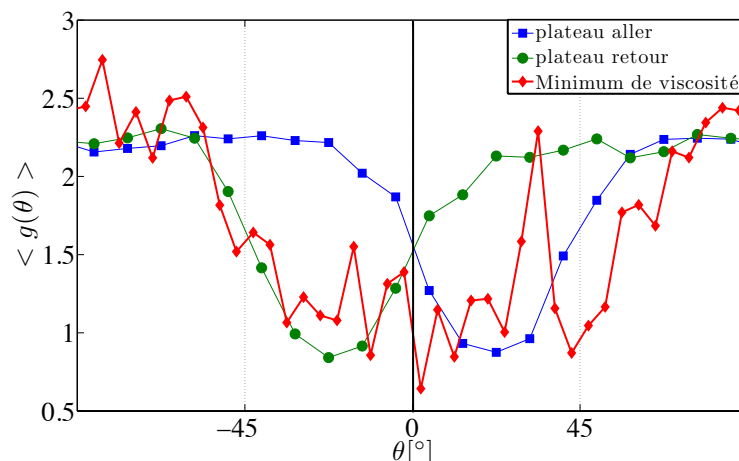
FIGURE 5.14 – Fonction de distribution de paires intégrée sur une couche $1.8 < \rho/\text{a} < 2.1$. $\theta = 0$: direction de la vitesse. D'après [69].

est symétrique.

Ce résultat appelle un commentaire, puisque le chapitre 4 concluait sur une microstructure plutôt isotrope au minimum de viscosité. Ceci semble en contradiction avec le résultat de la figure 5.14 où une probabilité nettement plus importante est visible dans la direction du gradient de vitesse. Il est cependant utile de se rappeler que les simulations numériques [53] et les modèles théoriques [51] suggèrent que les propriétés rhéologiques sont liées aux caractéristiques de la fonction de distribution de paires à très petite échelle, c'est-à-dire pour des particules au contact. D'autre part, des simulations numériques de suspensions (monocouche de particules) après inversion de cisaillement ont permis de calculer la fonction de distribution de paires au cours du régime transitoire [76]. Les auteurs ont pu montrer que lorsque la viscosité atteint le minimum, la probabilité que des particules se trouvent à des distances relatives aussi faibles que durant le cisaillement stationnaire est quasiment nulle dans toutes les directions Ceci signifie qu'au minimum, les particules se sont fort éloignées les unes des autres, et cela confirme que l'influence de la microstructure sur les propriétés rhéologiques s'exerce essentiellement via des particules très proches les unes des autres ("au contact"). Ce résultat donne également une explication à notre paradoxe : malgré une bonne résolution, notre dispositif ne parvient pas à résoudre la distribution à l'échelle des rugosités. Il est donc probable que, dans le cas de l'inversion du cisaillement, la microstructure à notre échelle de mesure ne soit pas l'image exacte de la microstructure au contact. Ce dernier résultat a toutefois le mérite de mettre une fois de plus en exergue l'importance des distances interparticulaires et du contact dans la rhéologie des suspensions.

Annexe 5.A   Fonction de distribution de paire pour différentes valeurs de la fraction volumique

FIGURE 5.15 – PDF mesurées pour différentes fractions volumiques. Quadrant de compression : xy<0

FIGURE 5.16 – PDF mesurées pour différentes fractions volumiques. Quadrant de compression : xy<0

Conclusion et perspectives

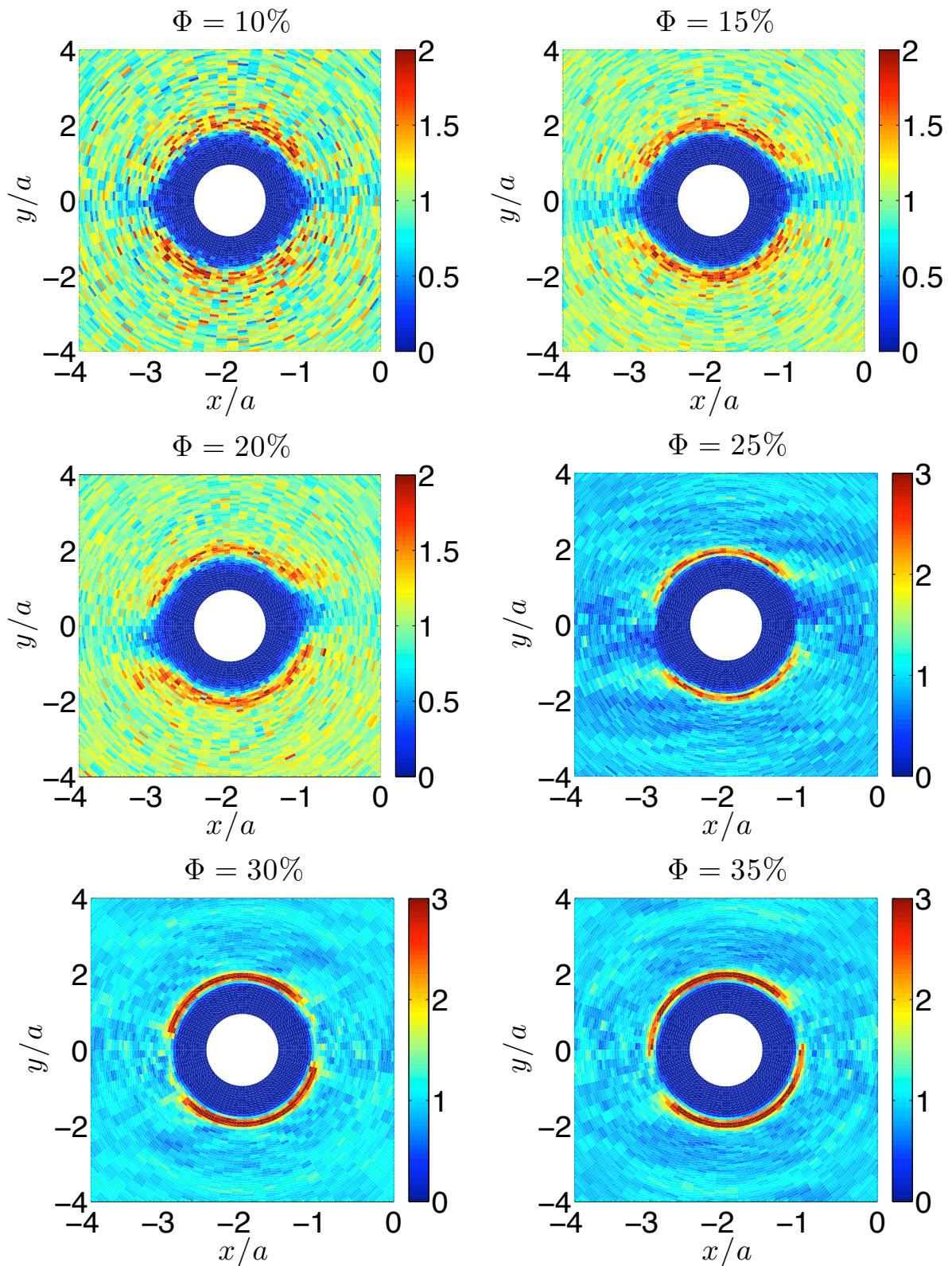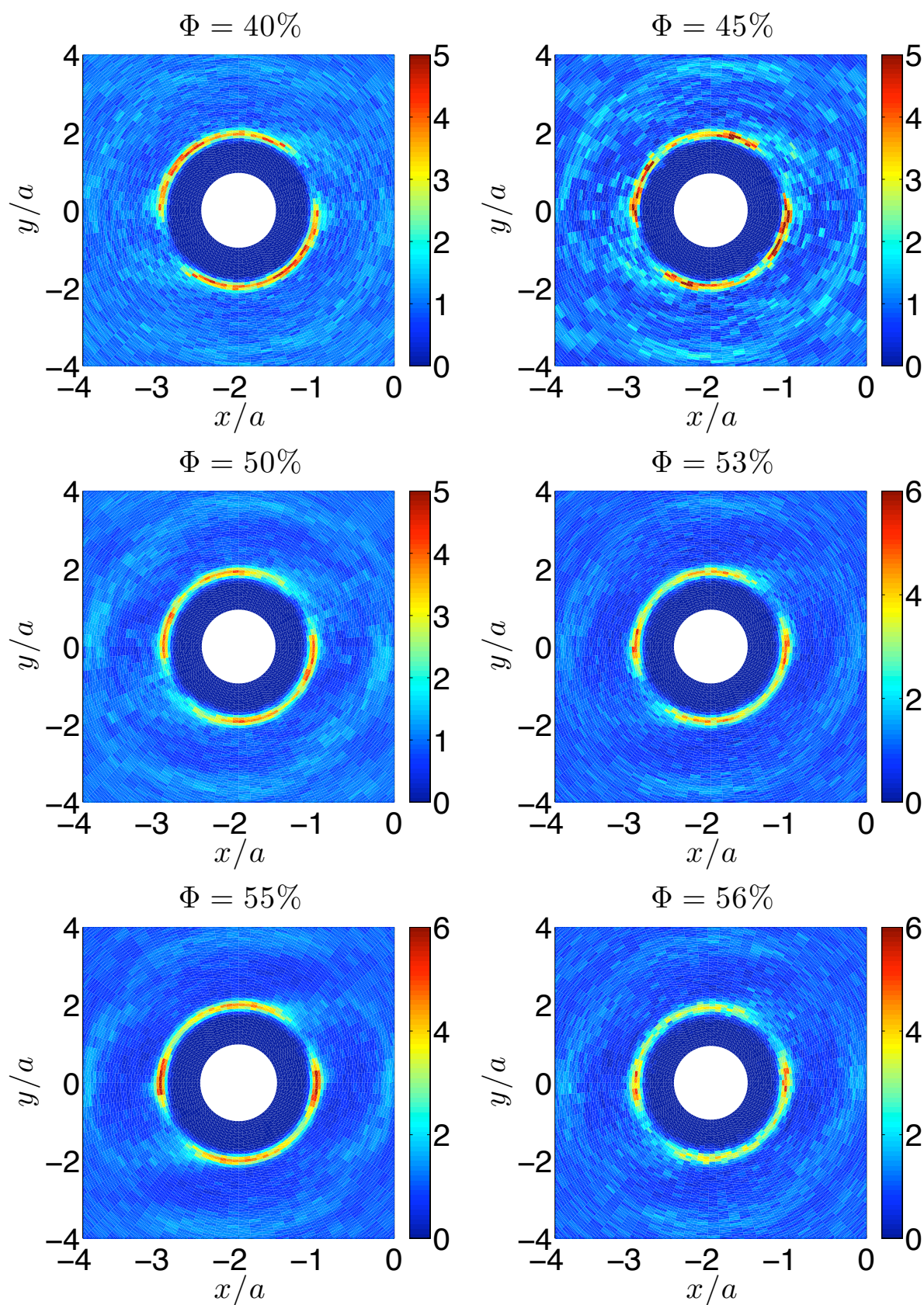Ce manuscrit présente de façon synthétique l'activité de recherche concernant la rhéologie des suspensions, au sens large, à laquelle j'ai participé depuis la fin de ma thèse. Le domaine exploré est relativement large, allant de suspensions colloïdales semi-diluées soumises à des forces électriques jusqu'à des suspensions non-browniennes concentrées cisaillées, soumises ou non à un couple extérieur, avec une brève incursion dans le domaine des milieux granulaires cohésifs. La constante dans ce travail me semble, assez classiquement, le soucis de comprendre les comportements d'ensemble, macroscopiques, à la lumière de la physique à l'échelle des particules. Ceci passe naturellement par un aller et retour permanent entre les expériences et la modélisation microscopique. Notre équipe essaie de ce point de vue de développer les outils nécessaires, expérimentaux, mais aussi de modélisation et de calcul numérique. Un des paramètres importants est évidemment la conception d'expériences capables de fournir des mesures pertinentes. De ce point de vue, les mesures macroscopiques, telles que celles qu'un rhéomètre classique peut réaliser, ont évidemment un grand intérêt, ne serait-ce que parce que le tels outils sont extrêmement répandus, donnant lieu à un très grand nombre de résultats de la littérature. Il en est de même de beaucoup de dispositifs du commerce (mesure de potentiel zeta...) bien adaptés à la caractérisation systématique des matériaux et donc très utilisés, notamment dans un contexte industriel. Cependant, les données fournies par de tels appareils – très utiles en première approximation – sont parfois très difficiles à interpréter en profondeur, ou offrent une vision partielle des grandeurs pertinentes. Nous avons donc tenté de concevoir des dispositifs expérimentaux capable de fournir des données plus précises. Ainsi, l'utilisation que nous avons faite d'une expérience de " diffusion de lumière électrophorétique" conçue au laboratoire nous a permis d'accéder aux fluctuations de vitesse électrophorétique, qui permet de mieux comprendre l'origine de la dépendance de la mobilité en fonction de la fraction volumique.

Dans le domaines des suspensions, la rhéologie macroscopique se heurte à certaines hypothèses, de continuité de la vitesse aux parois, ou d'homogénéité du matériau qui rendent les mesures pour le moins difficiles à interpréter. La solution la plus attractive est évidemment d'aller voir directement dans la suspension. Nous avons donc monté une première expérience de vélocimétrie ultrasonore, qui, en donnant accès aux profils de vitesse dans une suspension semi-diluée soumise à un couple, nous a permis de bien contrôler la loi constitutive prévue par notre modèle. En ce qui concerne les suspensions concentrées, l'apport de la rhéométrie locale est encore plus important, puisqu'elle permet seule des mesures quantitatives de la loi de comportement visqueuse nécessaires à la compréhension du minimum de viscosité.

Pour aller plus loin dans la description à l'échelle des particules, la dernière expérience de suivi de particules a déjà fourni des résultats originaux concernant la microstructure et la

rhéologie des suspensions sur une large gamme de fractions volumiques. En plus des mesures de la fonction de distribution de paires décrites dans ce mémoire, nous avons pu mettre en évidence une structuration de la suspension en couches au voisinage des parois, qui semble avoir une influence sur la microstructure plus loin des parois. Ce point reste cependant à éclaircir.

Ces derniers résultats sont prometteurs, et nous nous proposons de poursuivre nos investigations dans cette direction. Une des questions qui se pose, naturellement, est l'influence de la rugosité sur la rhéologie et la microstructure dans des suspensions concentrées. Dans le domaine dilué, on s'attend à ce que la microstructure soit simplement décrite par le modèle que nous avons utilisé, avec une zone de déplétion directement influencée par la taille des rugosités. Dans le domaine concentré, il n'en est pas de même. Il sera intéressant de mesurer l'influence de la rugosité sur la fraction volumique qui sépare le domaine semi-dilué où les contacts ont peu d'influence sur la rhéologie (mais pas sur la microstructure) du domaine concentré où la microstructure et les contacts ont une influence déterminante sur la viscosité et les différences de contraintes normales.

Une autre question importante concerne l'existence et la taille des agrégats transitoires souvent évoqués dans la littérature numérique [81] et théorique [75]. On a ainsi parlé de percolation pour expliquer le changement de régime, décrit dans les deux derniers chapitres, qui apparaît sur les mesures de contraintes normales mais aussi sur celles de viscosité [82, 39]. Notre dispositif de suivi de particules semble adapté pour détecter de tels agrégats, ce que nous prévoyons de vérifier à très court terme.

Enfin, le domaine des suspensions de fibres, dont les champs d'application sont très vastes, a jusqu'ici été peu sondé par des expériences de rhéométrie locale et de suivi de particules, alors même que les questions d'homogénéité et de structure sont vraisemblablement de la même importance que dans le domaine des suspensions de particules sphériques. Nous allons donc d'ici peu nous intéresser à ces problèmes.

Recueil d'articles

Annexe A

Milieux granulaires cohésifs

A.1 Cohesion induced by a rotating magnetic field in a granular material

Cohesion induced by a rotating magnetic field in a granular material

F. Peters and E. Lemaire

Laboratoire de Physique de la Matière Condensée, CNRS UMR6622, Université de Nice–Sophia Antipolis,
Parc Valrose, 06108 Nice cedex 2, France

We report experiments on a magnetic cohesive granular material made of steel spheres in the millimeter range. A magnetic field magnetizes the spheres, so that an interaction force between grains appears. A rotating magnetic field is applied parallel to plane of the quasi-two-dimensional cell containing the spheres so that only the time averaged force between two particles will be considered. Both maximum angle of stability and angles of repose are measured. The maximum angle of stability is found to depend linearly on the interaction force. Another noticeable feature is the lack of dependence of the maximum angle of stability on the initial height of the heap. We show that the angle of repose is less sensitive to the magnetic interaction force than the maximum of stability. At last, we discuss the importance of using a rotating field rather than a constant one. In particular, we report some measurements of both the maximum angle of stability and the angle of repose in constant field, which show a strong dependence of the angles of avalanche on the direction of the field.

I. INTRODUCTION

Granular materials are present in various contexts including industrial processes, food technology, the pharmaceutical industry, or geophysics. At first, in the 1980's, physicists' attention focused on dry granular materials where, if the grains are sufficiently large, they interact only through contact forces. The mechanical behavior of a granular material is characterized by numerous variables among which the maximum angle of stability (MAS) and the angle of repose are of primordial importance. The MAS is measured by slowly tilting a container filled with the granular material, thereby increasing the angle between the top free surface of the grains and a horizontal plane. When this angle reaches the MAS, an avalanche of grains occurs and the angle of the pile relaxes to a lower angle which is the angle of repose. There exist several methods to measure the angle of repose of a granular material which do not necessarily give exactly the same results. One can pour the grains on a horizontal plane and measure the angle between the top surface of the heap and the horizontal plane. Another method consists of filling a flat bottomed box with the granular material and allowing the grains to flow out through a hole in the bottom of the container, until an equilibrium is reached. The top surface of the grains is no longer horizontal but makes an angle (the angle of repose) with the horizontal plane. In this paper we will use this so-called draining crater method.

The MAS and the angle of repose has been shown to depend drastically on the roughness of the surface of the grains. They are also extremely sensitive to any other interaction forces between grains and will increase as the cohesion between grains is enhanced. The most famous and common example of such interaction force is the adhesive force induced by moisture through capillarity in granular media. It has been observed and measured that even a small amount of liquid added to a granular medium drastically changes its mechanical properties [1–7]. But these changes are not completely understood. In particular, the increase of the MAS cannot be explained by considering simple liquid bridges between ideally smooth particles. Many other questions remain unanswered such as the consequences of the plastic deformation of the particles or the effects of humidity induced ageing [4–7]. Beside the difficulties of the theoretical approaches, the experiments are rather tricky. It is, for instance, difficult to control exactly the degree of humidity in the granular heap and to be sure that it is uniform over the whole volume [3].

Another example of cohesive granular materials is the fine dry cohesive powders [8,9]. Since the surface forces, usually van der Waals forces, scale with the diameter of the particles while the gravitational forces depend on the volume of the particles, reducing the size of the particles is a way to increase the ratio of the cohesion to the weight. Nevertheless, the behavior of such fine powders is made rather complicated by the no longer negligible interaction between the particles and the surrounding gas during the settling of the grains.

Forsyth *et al.* [10] have proposed another method to modify the interparticle forces in a granular media, by applying a vertical magnetic field on a pile of iron particles. The degree of cohesion of this granular media is thus readily tuned by changing the magnetic field strength. They obtained interesting results concerning the dependence of both static and dynamic angles of repose of the pile on the ratio of the magnetic force to the particle weight. Concerning the static experiment, they measure the angle of repose for different values of the constant magnetic field. The force between two particles inside the heap is evaluated by measuring for the same magnetic field the force between an isolated pair of touching spheres aligned in the field direction. The main result they obtain is that the angle of repose increases linearly with the interparticle force. It should be noted, however, that the interactions between the iron particles are highly anisotropic. For instance, the interaction between two adjacent particles is attractive and maximum when the particles are aligned along the field direction while the same adjacent particles repel each other if they are in a plane perpendicular to the field direction. Consequently, the angle of avalanche of
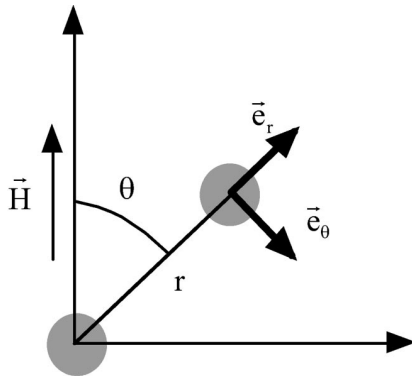
F. PETERS AND E. LEMAIRE

FIG. 1. Two particles in a magnetic field $\vec{H}$. The force in Eq. (2) is exerted on the particle lying at the origin.

such a magnetic granular material should depend on the direction of the field.

In this paper, we present a study of such cohesive magnetic material where, in order to limit the anisotropy of the interaction between grains, we apply a rotating magnetic field. The iron beads are contained in a quasi-two-dimensional (quasi-2D) box (five bead diameters in width), and a rotating magnetic field is applied parallel to the plane of the cell [plane (x, z) in Fig. 6].

In Sec. II, we briefly recall the expression of the magnetic force between two magnetic particles and we present the very simple model used to predict the dependence of the MAS on the intensity of the magnetic field. In Sec. III, we present the experimental device and the main characteristics of the particles. Sec. IV is devoted to the experimental results dealing with the dependence of the MAS and the static angle of repose on the magnetic field strength and the role played by cohesion will be discussed.

II. COHESION INDUCED BY A ROTATING MAGNETIC FIELD

A. The magnetic interaction between two spheres

When a ferromagnetic particle is placed into a uniform magnetic field $\vec{H}$ it becomes magnetized with a dipole moment $\vec{p}$ given by

$$\vec{p} = 4\pi a^3 \mu_f \beta \vec{H} \quad \text{with} \quad \beta = \frac{\mu_p - \mu_f}{\mu_p + 2\mu_f}, \qquad (1)$$

where a is the radius of a spherical particle, μ_p its relative magnetic permeability, and μ_f the relative magnetic permeability of the interstitial fluid. In the following, we consider particles in air, so that $\mu_f = 1$. As long as the magnetic field is constant, the particle experiences no magnetic force. When a second particle is introduced at coordinates (r, α) (Fig. 1), its magnetic dipole interact with that of the first particle which experiences, in dipolar approximation, the force $\vec{F}_{\text{dip}}$:

$$\vec{F}_{\text{dip}} = 12\pi\mu_0\mu_f a^2 \beta^2 H^2 \vec{f}_{\text{dip}},$$

$$\vec{f}_{\text{dip}} = \left(\frac{a}{r}\right)^4 [(2\cos^2\alpha - \sin^2\alpha)\vec{e}_r + \sin 2\alpha\vec{e}_\alpha]. \qquad (2)$$

This approximation holds as long as the particles are sufficiently far apart or if their relative permeability is close to one so that the secondary field created by the magnetization of one sphere will not significantly affect the magnetization of the other sphere. Even when these conditions are not met, expression (2) shows an important qualitative characteristic of the magnetic interaction force between two particles: it strongly depends on their position with respect to the field direction. For example, when the spheres are aligned in the direction of the field, they attract each other while they repel when they are in the plane perpendicular to the field direction. This is the reason we proposed to use in our experiment a magnetic rotating field to try to avoid this angular dependence.

As we will see in Sec. III, a direct measurement of the interaction force between two spheres shows that the dipolar approximation is not valid in our case, so that we have to use a multipole expansion of the field to calculate the interaction force. Furthermore if the magnetic permeability depends on the magnetic field, the problem is rather complicated. But, in the following section, we will show that, in the magnetic field range we used, μ_p can be regarded as a constant. In this case, the problem of magnetic particles in a magnetic field is analog to the problem of dielectric particles in an electric field. Using a multipole expansion, Klingenberg proposed in 1989 [11] a method to calculate the exact force between dielectric particles in a uniform electric field. He obtained the following expression for the interaction force:

$$\vec{F} = 12\pi\mu_0\mu_f a^2 \beta^2 H^2 \vec{f},$$

$$\vec{f} = \left(\frac{a}{r}\right)^4 [(2f_{/\!/}\cos^2\alpha - f_\perp\sin^2\alpha)\vec{e}_r + f_\Gamma\sin 2\alpha\vec{e}_\alpha]. \qquad (3)$$

The functions $f_{/\!/}$, $f_\perp$, and f_Γ depend on the distance between the particles and on their magnetic permeability (dielectric permittivity in the case of dielectric particles submitted to an electric field). They are positive and approach one in the limits: $r/a \to \infty$ and $\mu_p/\mu_f \to 1$.

With the method proposed by Klingenberg, it is impossible to study the interaction force between touching spheres for high values of μ_p/μ_f. In 1993, Clercx and Bossis [12] proposed a more efficient method which allows us to calculate the force up to touching spheres for $\mu_p/\mu_f \lesssim 100$. In the following, we will use the results of Clercx and Bossis for the values of the force functions $f_{/\!/}$, $f_\perp$, and f_Γ.

B. The magnetic force exerted on a particle at surface of the heap

In a granular media, when an avalanche takes place, a slip surface appears in the material. If a constant magnetic field is applied to vary the interaction forces between grains, the angle between the slip surface and the direction of the field would play a role. And finally the values of the angle of repose and of the maximum angle of stability should depend on the direction of the field. To avoid this dependence, we
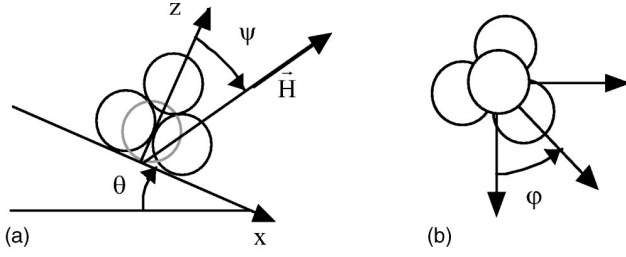
FIG. 2. A particle at the surface of the heap is supposed to be supported by three particles in the layer below. θ is the angle between the surface of the heap and the horizontal plane. The four particles form a regular tetrahedron. The angle Ψ defines the field orientation, and the angle φ defines the orientation of the triangular base.

propose to apply a rotating field in the vertical plane parallel to the quasi-2D box containing the steel beads:

$$\vec{H} = H_0[\sin(\psi)\vec{e}_x + \cos(\psi)\vec{e}_z], \quad (4)$$

ψ being the angle between the normal of the surface of the heap and the direction of the field. We will assume that the avalanche is a superficial model. This hypothesis is supported by visual evidence and, as we will see in Sec. IV, this assumption allows us to explain the main experimental results. Thus, in the following, we will examine the stability of the top layer of particles of the heap interacting with the layer below. Due to the $(a/r)^4$ dependence of the magnetic force, this amounts to studying the interaction between a given particle of the top layer and three adjacent spheres in the layer just below [Fig. 2(a)]. This pyramidal structure is of course a local structure and the orientation of the base triangle defined by φ [Fig. 2(b)] is random. Consequently, to calculate the magnetic force exerted on the top sphere, we have to average the force over all the possible values of φ. The sum of the three interaction forces averaged on φ yields the following expression for the force exerted on the top sphere:

$$\langle \vec{F} \rangle_\varphi = \frac{1}{2}\sqrt{\frac{3}{2}}\pi\mu_0\mu_f a^2\beta^2 H_0{}^2(f_x\vec{e}_x + f_z\vec{e}_z),$$

$$f_x = -(2f_{//} + f_\perp - 4f_\Gamma)\cos\psi\sin\psi, \quad (5)$$

$$f_z = -(1 + 3\cos^2\psi)f_{//} - \frac{1}{2}(3\cos^2\psi - 5)f_\perp + (3\cos^2\Psi - 1)f_\Gamma.$$

Furthermore, if the magnetic field is rotating in the plane (x,z), we have to average the force over the possible directions of $\vec{H}$ (i.e., over ψ), and we obtain a force that is normal to the surface of the heap:

$$\langle \vec{F} \rangle_{\varphi,\psi} = \frac{1}{4}\sqrt{\frac{3}{2}}\pi\mu_0\mu_f a^2\beta^2 H_0{}^2\left(-5f_{//} + \frac{7}{2}f_\perp + f_\Gamma\right)\vec{e}_z. \quad (6)$$

At last, it should be noted that the condition to consider only the average force over ψ is that the frequency of the field is sufficiently high for the particles to be at rest during a half period of rotation of the magnetic field. Namely, the

half period of the field has to be smaller than the characteristic time for a particle to move on a distance equal to its diameter under gravity:

$$T < 4\sqrt{\frac{a}{g}}. \quad (7)$$

C. The dependence of the MAS on the magnetic interaction force

To link the MAS to the average interaction force, we use a very simple model based on a stability criterion of a single layer of particles lying on the surface of the heap. The choice of such a surface model will be justified by the experimental results presented in Sec. IV. We write the equilibrium of one particle under the contact forces exerted by the particles in the layer below, the magnetic force (6) and the gravity. The contact force is the sum of the component parallel, $\vec{T}$, and normal, $\vec{N}$, to the surface. The projection of the different forces on the axes x and z [Fig. 2(a)] leads to

$$-T + mg\sin\theta = 0,$$

$$N - mg\cos\theta - F_{\text{magn}} = 0, \quad (8)$$

where m is the mass of the particle and F_{magn} is taken positive. The measurement of the MAS of the granular material in the absence of a magnetic field, θ_0, allows us to define the internal friction coefficient μ,

$$\mu = \frac{T}{N} = \tan\theta_0, \quad (9)$$

and, in the presence of a magnetic interaction between particles, the MAS of the heap will be given by the following relation:

$$\tan(\theta) = \mu + \frac{\mu F_{\text{magn}}}{mg\cos(\theta)}, \quad (10)$$

which can also be written as

$$\theta = \theta_0 + a\sin\left(\frac{\mu F_{\text{magn}}}{mg}\cos(\theta_0)\right) = \theta_0 + a\sin\left(\frac{F_{\text{magn}}}{mg}\sin(\theta_0)\right). \quad (11)$$

III. EXPERIMENT

A. The particles

We use monodisperse steel ball bearing particles (diameter 1 mm$\pm$1%), with density 7.9×10^3 kg m^{-3}. In order to measure the average permeability of the granular material, we have subjected an ensemble of densely packed spheres (ϕ=0.61) to a magnetic field gradient. A long cylindrical tube (length 4 cm, radius 0.45 cm) is filled with the particles and suspended under the tray of a sensitive laboratory balance, in order to measure the magnetic force exerted on the sample (Fig. 3). The magnetic field is supplied by a coil, positioned below the sample. In this configuration, since the
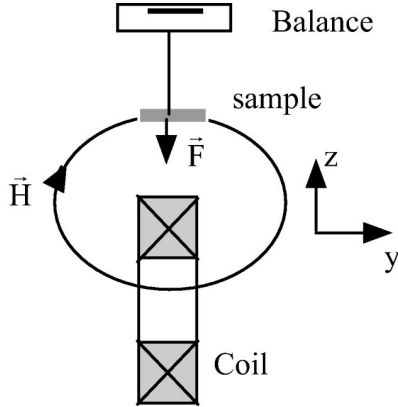
FIG. 3. Measurement of the bulk permeability of the granular material. The magnetic field gradient is normal to the field, and the cylindrical sample is parallel to the field.

long axis of the sample is parallel to the field, the demagnetizing field is low: the demagnetizing factor is evaluated to $N \approx 0.04$ [13]. The magnetic energy may be written as

$$E_{\mathrm{m}} = -\frac{1}{2}\mu_0 V \frac{(\mu_{\mathrm{b}} - 1)}{1 + N(\mu_{\mathrm{b}} - 1)} H_{\mathrm{y}}^2, \qquad (12)$$

where μ_{b} is the bulk relative permeability of the sample, V is its volume, and H_{y} is the external magnetic field. The force is thus

$$\vec{F} = -\vec{\nabla} E_{\mathrm{m}} = \mu_0 V \frac{(\mu_{\mathrm{b}} - 1)}{1 + N(\mu_{\mathrm{b}} - 1)} H_{\mathrm{y}} \frac{dH_{\mathrm{y}}}{dz} \vec{e}_{\mathrm{z}}. \qquad (13)$$

Figure 4 shows the variation of the magnetization ($M = \|\vec{F}\| / \mu_0 V dH_{\mathrm{y}}/dz$) with H_{y}. As it can be seen, the granular sample can be considered as a linear magnetic material and the slope of the curve gives the average permeability of the granular material: $\mu_{\mathrm{b}} \approx 6.2$.

The permeability of the steel particles has been estimated by measuring the interaction force between two touching
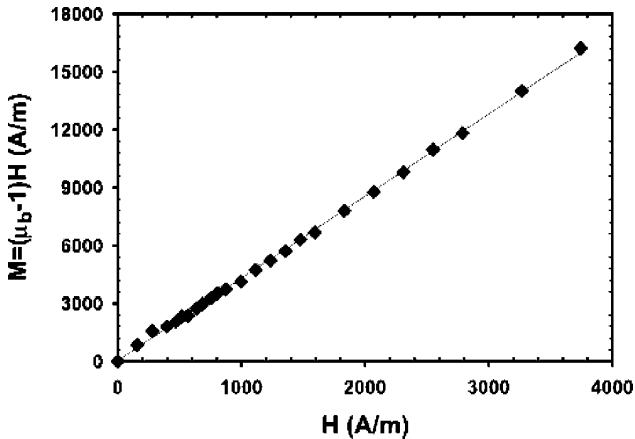

FIG. 4. Measured bulk magnetization vs magnetic field intensity. The granular material can be considered as a linear magnetic material with bulk relative permeability $\mu_{\mathrm{b}} = 6.2$.
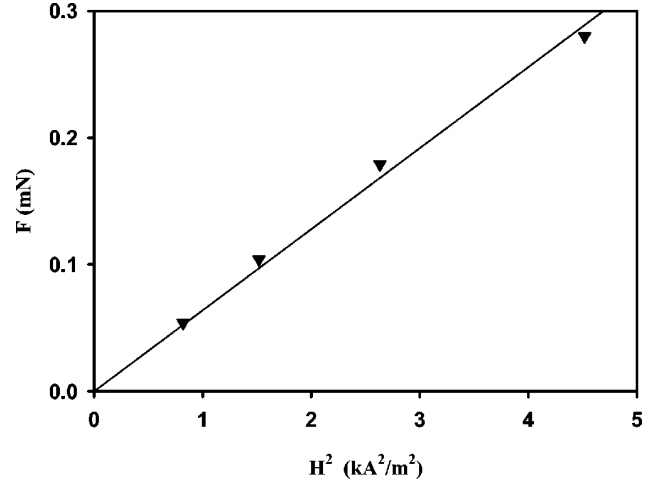

FIG. 5. Magnetic interaction force between two steel spheres (diameter 1 mm) aligned along the field direction vs magnetic intensity squared.

spheres aligned in the direction of a magnetic field. Following Forsyth *et al.* [10], we place two particles in a vertical magnetic field, the top one being fixed, the bottom one holding under the effect of the magnetic interaction. The field is then decreased, until the second particle falls. The weight of the particle gives the magnetic interaction force for this field intensity. To obtain the magnetic force for different field intensities, we glue some additional nonmagnetic masses to the suspended particle. In order to avoid residual magnetization effects, we use an ac magnetic field at the same frequency as in the case of the rotating field (50 Hz). The measured force is displayed versus the square of the field intensity in Fig. 5. A linear regression of the curve gives $F(N) \approx 6.4 \times 10^{-11} H^2 (\mathrm{A}^2/\mathrm{m}^2)$, i.e., from Eq. (3) $\beta^2 f_{//} \approx 43.2$. Volkova [14] gives a polynomial expression for the coefficient $f_{//}$,

$$f_{//} = 0.058 + 0.596\mu_{\mathrm{p}} + 0.015\mu_{\mathrm{p}}^2$$
$$- (2.78 \times 10^{-5})\mu_{\mathrm{p}}^3 \quad \text{for } 10 < \mu_{\mathrm{p}} < 100. \qquad (14)$$

From this expression and the value of the slope of the curve $F(H^2)$, we deduce the permeability of the particles: $\mu_{\mathrm{p}} = 42.1$ and $f_{//} = 49.7$. We have to mention that this determination of the particles permeability is valid only if the magnetic material is linear, i.e., if the permeability does not depend on the magnetic field intensity. This seems to be the case since the force has a quadratic dependence with the field. So in the following, we will use this value for the sphere permeability.

This value of μ_{p} should be compared to the one obtained from the measured mean permeability of the ensemble of packed spheres using an effective medium theory such as Bruggeman's model [15]:

$$\phi \frac{\mu_{\mathrm{p}} - \mu_{\mathrm{b}}}{2\mu_{\mathrm{b}} + \mu_{\mathrm{p}}} + (1 - \phi) \frac{1 - \mu_{\mathrm{b}}}{2\mu_{\mathrm{b}} + 1} = 0. \qquad (15)$$

This model gives $\mu_{\mathrm{p}} \approx 12.3$. This value is much smaller than the one obtained from the measurement of the interaction force between two spheres. This discrepancy is not surpris-
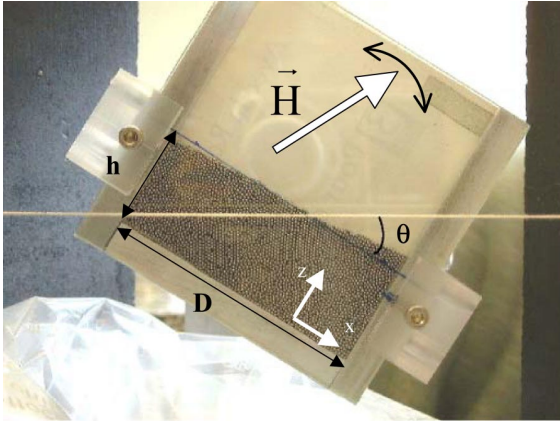
FIG. 6. To measure the MAS, the cell is rotated slowly until the avalanche occurs. The magnetic field is either constant or rotates in the plane (x, z).

FIG. 7. After the plug has been removed, the grains flow out until the angle of repose is reached. The magnetic field is either constant or rotates in the plane (x, z).

ing since the Bruggeman's model is known to underestimate the value of the permeability of the particles [16]. In the following, we will take the value deduced from the measurement of the magnetic force, $\mu_p \approx 42.1$.

B. Experimental device

A narrow rectangular box is filled with the granular material with a controlled volume fraction $\phi = 0.61$. It is positioned at the center of two perpendicular pairs of coils. The inner and outer diameters of the coils are, respectively, 24 cm and 29 cm and their width is 5 cm. Our work mostly deals with the measurement of the MAS or of the angle of repose when the applied magnetic field is rotating. We also make few measurements in the case of a constant field, to show the importance of using a rotating field, and to compare our results with earlier works described in the literature [10].

To create a rotating magnetic field, the two pairs of coils are run in quadrature phase. The electric current in the coils is supplied by a function generator and amplified by two bipolar amplifiers (Kepco). The resulting magnetic field rotates in the vertical plane perpendicular to the width of the cell containing the beads. Its maximum amplitude is 1430 A m^{-1}. Due to the large impedance of each pair of coils, the field frequency is limited to a quite low value, namely, 50 Hz. The value of the characteristic time defined in inequality (7) is $4\sqrt{a/g} \approx 2.8 \times 10^{-2}$ s, which is slightly larger than the period of the field. Finally, the width of the cell is chosen small enough compared to its length and to its height for the demagnetizing field to be much lower than the external field.

We make two different types of measurement, i.e., we measure either the MAS or the angle of repose. In the first case (Fig. 6), we use a box whose width is 5 mm, its length 80 mm, and its height 80 mm. The cell is manually tilted with a low gear. The angular velocity of the cell has been estimated to 6°/min. The rotation is stopped when the avalanche occurs and the angular position of the cell gives the angle before the avalanche, i.e., the MAS.

To measure the angle of repose, a fixed cell (width 5 mm, length 60 mm, height 60 mm) with a 15 mm long hole in its
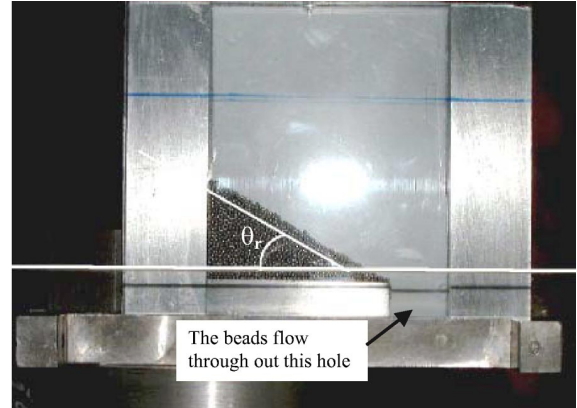
bottom is used (Fig. 7). A plug is adjusted in the hole and the cell is filled with the steel particles and placed in the magnetic field. When the plug is removed, the beads start flowing out, until the angle of repose is reached. A picture of the cell is recorded by a digital camera and downloaded to a PC. The surface of the heap is fitted to a straight line. The angle between this line and the horizontal plane gives the angle of repose.

For each value of the magnetic field, six independent measurements were made, yielding a measurement uncertainty of ±1.5°.

IV. RESULTS AND DISCUSSION

A. Constant field

Figure 8 displays the angle of repose versus the square of the magnetic field, in the case of a vertical magnetic field. The best fit shows that the angle of repose scales as $H_0^{1.38}$, i.e., as $F_{magn}^{0.69}$. In their experiment, Forsyth *et al.* [10] also
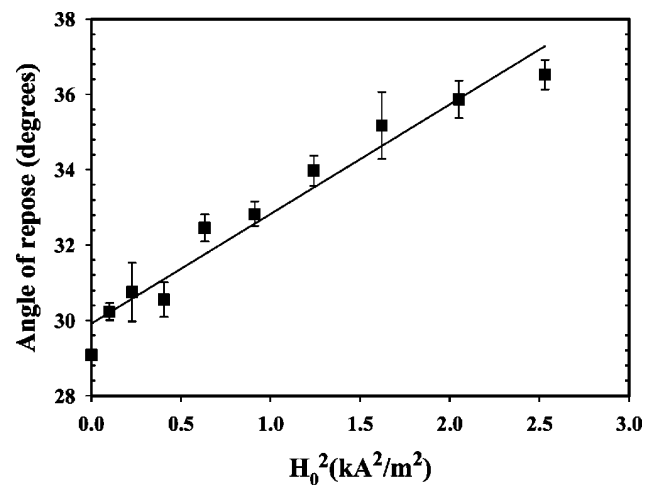
FIG. 8. Angle of repose vs the square of the magnetic field intensity. The magnetic field is vertical and constant. The solid line is a linear regression of the data $\theta_r = 29.9 + 2.91 H^2 (\text{kA}^2/\text{m}^2)$.

TABLE I. MAS and angle of repose obtained for a constant field $H_0 = 800$ A m^{-1}. The reference axis is the vertical axis. The angle defining the field direction is taken positive clockwise, such as the avalanche angle. So, $+45°$ defines a field roughly normal to the surface of the heap when avalanche occurs and $-45°$ defines a field roughly parallel to the surface.

	Vertical	Horizontal	$+45°$	$-45°$
Maximum angle of stability	38.6	38.8	34.4	40.8
Angle of repose	32.3	34	31.3	34.5

apply a vertical magnetic field to the steel beads and they find a linear dependence of the angle of repose on the magnetic force. The main difference between their work and ours is that they apply stronger magnetic fields so that the cohesion is much higher in their experiments than in ours. Nevertheless, the curves they show include few points in the low cohesion regime and a careful look of this part of their results seems to reveal a sublinear dependence of the angle of repose on H_0^2.

Moreover, we have measured the MAS and the angle of repose obtained for one magnetic field intensity ($H_0 = 800$ A m^{-1}) and various directions of the magnetic field. Table I shows the results. As expected, the values of the angles are strongly dependent on the field direction. This observation emphasizes the importance of applying a rotating field rather than a constant field.

B. Rotating field

Figure 9 displays the MAS together with the angle of repose versus the rotating magnetic field amplitude H_0. The experimental results are fitted by the following expression:

$$\theta - \theta_0 = a \sin(A H_0^n). \quad (16)$$

The best fit, which is shown in Fig. 9 together with the experimental values, gives $A = 1.7 \times 10^{-7}$ and $n_{\text{expt}} = 1.95$. As

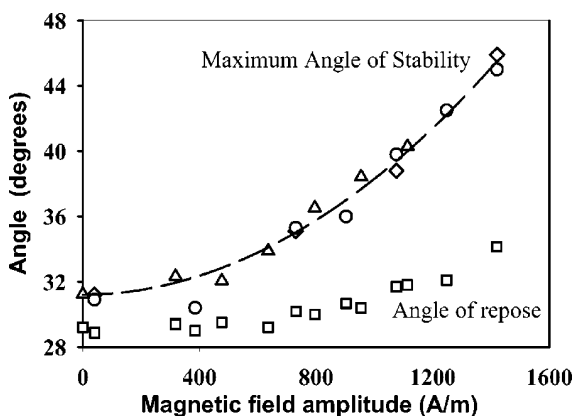

FIG. 9. Measured maximum angle of stability vs rotating magnetic field amplitude for three initial values of the height of the heap. ($\diamondsuit$) 2.75 cm; ($\bigcirc$) 3.2 cm; ($\triangle$) 4.4 cm. Dashed line— best fit of the MAS curve to the relation (16); $n_{\text{expt}} = 1.95$; $A_{\text{expt}} = 1.7 \times 10^{-7}$; ($\blacksquare$)—angle of repose vs rotating field intensity.

expected from Eq. (11), the MAS variation is quadratic with the magnetic field amplitude.

Our model is of course oversimplified but the qualitative agreement is rather good. Concerning the quantitative comparison, the theoretical coefficient A in Eq. (16) can be calculated using Eqs. (6) and (11). In Eq. (6), $f_{//} = 49.7$ and $f_\perp$ and f_Γ are taken equal to zero since, for high permeability materials, they are much smaller than $f_{//}$ (see, for instance, Refs. [11,14]) and we obtain $A_{\text{th}} = 4.1 \times 10^{-7}(A/m)^{-2}$, whereas the fit of the experimental data gives $A_{\text{expt}} = 1.3 \times 10^{-7}(A/m)^{-2}$. The calculated value of A is three times larger than the measured one. This discrepancy may have different origins. Evaluating the magnetic force, we consider that the force exerted by each particle on the top particle is the same than the force that would exist if the other two base particles were not there. Clercx and Bossis [12] have shown that this assumption is a rather crude approximation. For instance, they obtained that, in a cluster of three particles laid on an equilateral triangle, the two-particle approach led to a strong overestimation (about twice) of the interaction force. The overestimation of A_{th} could also originate in the existence of a demagnetizing field in the pile. This field is rather small since the applied field rotates perpendicularly to the narrow cell width. Nevertheless, it may not be negligible: a rough order of magnitude of the demagnetizing field can be obtained by evaluating the demagnetizing field in an ellipsoid whose polar axis is 5 mm and equatorial axis 80 mm. For such an ellipsoid, the demagnetizing factor in the direction of the polar axis is about 0.9 and so 0.05 in the other two directions. This leads to an internal magnetic field 25% lower than the external applied field.

At last, our model does not take into account the influence of the wall of the cell. Indeed, previous works on dry [18] or immersed [19] granular media without cohesion showed that the maximum angle of stability strongly depends on the ratio of the gap between the walls over the diameter of the beads. It appears that the maximum angle of stability decreases when the gap increases with a characteristic length $B_m \approx 4d$ for glass beads ($d = 1$ mm). Hence wall effects may not be negligible in our case.

We find another noticeable feature of this granular system: we have made several measurements of the MAS for different initial heights of the heap (2.75 cm, 3.2 cm, and 4.4 cm). It clearly appears in Fig. 8 that the MAS do not depend on the height. This observation is the reason we used a surface model to calculate the MAS.

The dependence of the MAS on the height of the pile is still controversial and several models exist that predict different behaviors concerning this precise point. Using the analysis due to Mohr and Coulomb, Halsey and Levine have calculated an upper bound for the MAS [7], which depends on the height h of the granular heap, namely,

$$\tan \theta = \mu + \frac{c}{\rho g h \cos \theta}, \quad (17)$$

where μ and c define the criterion for failure in the heap, i.e.,

$$\tau < \mu\sigma + c, \qquad (18)$$

where τ is the tangential stress along the slipping plane and σ the normal stress. μ is a phenomenological friction coefficient of the material and c its cohesion.

However, other models exist, which do not predict the same dependence of the MAS on the height of the heap. Albert *et al.* [2] propose a model that takes into account only the surface mechanisms, yielding avalanche angles independent of the heap size. They predict a variation of the MAS linear with the interaction force between grains. Actually, our model is a very simplified version of the model of Albert *et al.* leading to identical qualitative behaviors. In an experimental work dealing with the measurement of the angle of repose in wet granular media, Tegzes *et al.* [1] have shown that in a strong cohesion regime, the angle of repose depends on the height of the heap, whereas in a weak cohesion regime (as in our case), such a dependence does not exist. We believe that in this last regime, due to the weakness of the cohesion, the avalanche is a surface phenomenon, and that, consequently, the angles of avalanche are independent of the height of the pile, as it is the case for noncohesive materials.

In the experiments of Valverde *et al.* [9] on fine granular powders, the avalanche angle depends on the size of the heap, but in this case, the important dimension seems to be the length D of the cell (see Fig. 5) rather than the height. They compare their experimental data to the so-called wedge model [9,17] that they generalize to take into account the cohesion of the material and different shapes of the slipping wedge. They show that this model is appropriate in the high cohesion regime exhibited by the fine powders they use (contrarily to our experimental system where the cohesion is weak). However, such an analysis is difficult to be performed in our case since the predictions of the dependence of the angle versus the cohesion depends on the choice of the wedge shape.

Concerning the angle of repose, the measured angle at zero field is slightly lower than the MAS (2° lower), which is usual for dry granular media. The magnetic interaction leads to an increase of the angle of repose, but the influence of the cohesion induced by the field on the angle of repose is less pronounced than in the case of the MAS. The experimental results seem to indicate that the dependence of the angle of repose on the magnetic field is quadratic but the variation range of the angle is too small for us to be more affirmative. Unfortunately, at present, we are not able to create a larger rotating magnetic field. It should be interesting to make further experiments with higher field intensities using a device such as the one proposed by Martin *et al.* [20]. Another way

could be to perform a similar experiment on smaller grains, such as iron powders. The ratio of the magnetic force over weight should be greater in this case, leading to higher cohesion regime.

V. CONCLUSION

In this paper, we have presented some results on the measurement of the maximum angle of stability and of the angle of repose for a cohesive granular material. The cohesion between grains (millimeter steel spheres) is induced by a magnetic field.

Measurement of both the MAS and the angle of repose in static magnetic field exhibits a strong dependence of the values of these angles on the direction of the field. Thus, we emphasized the importance of applying a rotating magnetic field rather than a constant one. This may be especially important for the measurement of the maximum stability angle, since in the case of a static field, the particles are submitted to a variable interaction depending on the varying angular position of the cell before avalanche.

Concerning the experiments made in the presence of a rotating magnetic field, due to the low range of the field intensities, the cohesion is weak (the magnetic interaction force is always lower than the weight of a particle). In this low cohesion regime we have been able to bring out a few characteristics of the behavior of a cohesive granular material. The measured angles have been shown to depend linearly on the interaction force between grains. No variation of the maximum angle of stability of the pile has been noticed when its initial height is changed. A very simple model based on a stability criterion of a single particle lying at the surface of the heap shows a good qualitative agreement with experimental data.

In the presence of a rotating magnetic field, we have also measured the angle of repose. We show that the difference between MAS and angle of repose, which is small for dry granular media, grows up with the interaction between grains.

Finally, we plan to make further measurements in a higher cohesion regime to determine if the dependence of the MAS remains linear with the interaction force between particles and if the independence of the MAS with the height of the pile holds.

[1] P. Tegzes, R. Albert, M. Paskvan, A.-L. Barabasi, T. Vicsek, and P. Schiffer, Phys. Rev. E **60**, 5823 (1999).

[2] R. Albert, I. Albert, D. Hornbaker, P. Schiffer, and A.-L. Barabasi, Phys. Rev. E **56**, R6271 (1997).

[3] N. Fraysse, H. Thomé, and L. Petit, Eur. Phys. J. B **11**, 615

(1999).

[4] L. Bocquet, E. Charlaix, S. Ciliberto, and J. Crassous, Nature (London) **396**, 735 (1998).

[5] F. Restagno, C. Ursini, H. Gayvallet, and E. Charlaix, Phys. Rev. E **66**, 021304 (2002).

[6] T. G. Mason, A. J. Levine, D. Ertas, and T. C. Halsey, Phys. Rev. E **60**, R5044 (1999).

[7] T. C. Halsey and A. J. Levine, Phys. Rev. Lett. **80**, 3141 (1998).

[8] A. Castellanos, J. M. Valverde, A. T. Pérez, A. Ramos, and P. K. Watson, Phys. Rev. Lett. **82**, 1156 (1999).

[9] R. M. Valverde, A. Castellanos, and A. Ramos, Phys. Rev. E **62**, 6851 (2000).

[10] A. J. Forsyth, S. R. Hutton, M. J. Rhodes, and C. F. Osborne, Phys. Rev. E **63**, 031302 (2001).

[11] D. J. Klingenberg, Ph.D. thesis, University of Illinois, 1989 (unpublished).

[12] H. Clercx and G. Bossis, Phys. Rev. E **48**, 2721 (1993).

[13] R. M. Bozorth, *Ferromagnetism* (Van Nostrand, Princeton, NJ, 1964).

[14] O. Volkova, Ph.D. thesis, Université de Nice-Sophia Antipolis, 1998 (unpublished).

[15] D. A.G. Bruggeman, Ann. Phys. (Leipzig) **24**, 636 (1935).

[16] S. S. Dukhin, in *Surface and Colloid Science*, edited by E. Matijevic (Wiley-Interscience, New York, 1971), Vol. 3, 83–165.

[17] R. Nedderman, *Statics and Kinematics of Granular Materials* (Cambridge University Press, Cambridge, 1992).

[18] P. Boltenhagen, Eur. Phys. J. B **12**, 75 (1999).

[19] S. Courrech du Pont, P. Gondret, B. Perrin, and M. Rabaud, Europhys. Lett. **61**, 492 (2003).

[20] J. Martin, R. Anderson, and R. Willamson, J. Chem. Phys. **1183**, 1557 (2003).

Annexe B

Rotation de Quincke

B.1 Viscosity of an electro-rheological suspension with internal rotations

Viscosity of an electro-rheological suspension with internal rotations

E. Lemaire, L. Lobry, N. Pannacci, and F. Peters

Laboratoire de Physique de la Matière Condensée, CNRS, Université de Nice, Parc Valrose, 06108 Nice cedex 2, France

Synopsis

The rheological behavior of a suspension of insulating particles dispersed in a slightly conducting liquid under the action of a DC electric field is studied. The polarization of the particles induced by the field is shown to be responsible for a rotation of the particles (Quincke rotation) which, in turn, leads to a drastic decrease of the apparent viscosity of the suspension. The purpose of the paper is to provide a relation between the apparent viscosity of the suspension and the electric (E) field intensity. First, the steady-state solutions are searched for the angular velocity of a particle subjected to both DC E field and simple shear flow. Since the solutions are multivalued, their stability is studied using a linear stability analysis. Then the stable solution for the particle angular velocity is used to deduce the value of the apparent viscosity of the suspension. The predictions of the model are compared to experimental data which have been obtained on a suspension of polymethylmethacrylate particles dispersed in a low polar dielectric liquid. The agreement between experiments and theory is rather good even if the model overestimates the viscosity decrease induced by the field. © *2008 The Society of Rheology.* [DOI: 10.1122/1.2903546]

I. INTRODUCTION

The control of the viscosity of a suspension by the application of an electric field has attracted considerable attention these last years because it can be used in various kinds of industrial devices such as active dampers, clutches, or brakes [Phani and Venkatraman (2005); Lim *et al.* (2005); Tan *et al.* (2006)]. Usually, the so-called electrorheological (ER) fluids are made of relatively polarizable particles dispersed in a nonconducting liquid.

When the suspension is subject to an electric field, the particles group together in elongated aggregates aligned in the direction of the external field. This structuring of the suspension leads, in the rheology of the ER fluids, to the fast and reversible change from a liquid to a solid state. Most of ER fluids are used with an AC electric field; in this case, it is the permittivity mismatch between the particles and the liquid which is responsible for the polarization of the particles [Marshall *et al.* (1989)]. DC electric fields are more rarely employed and, when they are, the polarization of the particles comes from the conductivity difference between the solid and the liquid phases. If the conductivity of the particles is higher than that of the suspending liquid, the dipole moments of the particles are collinear to the electric (E) field direction and a particle-chaining happens, exactly as in the ac case [Atten *et al.* (1997)]. However, if the particles are less conducting than the suspending liquid, the dipole moments of the particles lie in a direction opposite to the field and, if the E field intensity is high enough, this orientation is unstable and can give

rise to a rotation of the particles. This particles' spinning is known as Quincke rotation [Quincke (1896)]. In such a case, the particles behave like colloidal motors which drive the suspending liquid and the viscosity of the suspension is lessened by the application of the field so that we can speak about "negative ER effect" [Lobry and Lemaire (1999)].

A negative ER effect has already been reported in the literature, but the involved mechanism is quite different: Boissy *et al.* (1995) showed that it was possible to decrease the viscosity of a suspension of electrically charged particles upon the application of a DC electric field. Indeed, the charged particles group together on the electrode of opposite charge. The suspension is, therefore, composed of two phases: the first one has a high-particle concentration and its volume fraction is close to that of the packing while the second phase is only constituted of the suspending liquid. The resulting mean apparent viscosity was shown to be lower than that of the homogeneous suspension (its value is comprised between that of the suspending liquid and that of the suspension).

The possibility of decreasing the viscosity of a suspension by exerting a torque on its particles has been demonstrated on ferrofluids subject to AC or rotating magnetic fields [Bacri *et al.* (1995)]. The ferrofluids are suspensions of rigid dipoles so that a time-varying external magnetic field is able to exert a torque which results in the particles rotation. Recently, Rinaldi *et al.* (2005) demonstrated the possibility of obtaining "negative viscosity" when the ferrofluid is placed in a cylindrical Couette geometry and subject to a uniform rotating field.

In the present paper, we develop a model to predict the viscosity reduction induced by the application of a DC electric field to a suspension. This work is an extension of a previous study [Cebers *et al.* (2000)] where the direction of the axis of rotation of the particles was assumed fixed. This assumption was responsible for a divergence of the apparent "negative viscosity" of the suspension at low shear rate. Here we show that, if the direction of the rotation axis of the particles *is* not necessarily chosen along the vorticity direction, the "negative viscosity" divergence disappears and the model is able to fit the experimental data. The paper begins with a presentation of the model which allows the prediction of the viscosity as a function of the applied electric field (Sec. II). Section II A is dedicated to a discussion of the mechanisms involved in Quincke rotation and of the conditions for such a DC electro-rotation to take place. In Sec. II B, the Quincke rotation of particles in the presence of a shear flow is analyzed and, at last, we state how the electro-rotation of the particles modifies the apparent viscosity of the suspension. The following section (Sec. III) is experimental, both the samples and the experimental procedure are described. Section IV is devoted to the presentation of the results and to their analysis.

II. THEORY

A. Mechanism of Quincke rotation

Even though the rotation of small particles dispersed in a dielectric liquid and subject to a dc electric field, $\mathbf{E_0}$, was observed as early as 1896, it was only at the end of the 20th century that a correct analysis of the phenomenon was proposed. The analysis proposed by Melcher (1974) is based on the role played by the free electrical charges on the particle surface and the necessary condition for the Quincke rotation to appear deals with the relative magnitude of the charge relaxation times in the liquid and in the particle. The charge relaxation time is given by the ratio of the dielectric permittivity to the conductivity: $\tau_i = \varepsilon_i / \gamma_i$, $i = l, p$, refers to the liquid and the particle respectively. Indeed, if the charge relaxation time is shorter in the liquid than in the particles when the E field is applied, the superficial charge which builds at the interface between the particle and the
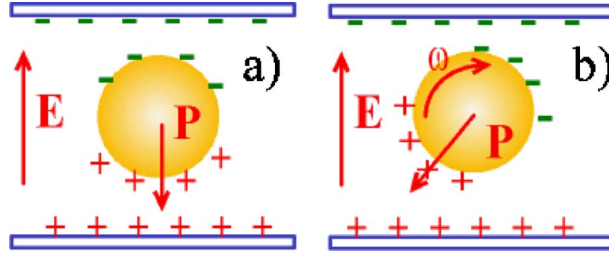
FIG. 1. Representation of the particle dipole, **P**, coming from the interfacial charge distribution. If the charge relaxation time is higher in the particle than in the host liquid ($\tau_1 \tau_2$), **P** is anticollinear to the field direction (a). If the E field intensity is high enough, this situation is unstable and the particle rotates either in a clockwise or a counter-clockwise direction. In such a case, the rotation of the particle at constant velocity and the tilt of P correspond the stationary equilibrium of the system.

liquid is equivalent to that of a dipole moment, **P**, which is in the direction opposite to the dc field [Fig. 1(a)]. Any angular deviation of the particle produces a torque, $\mathbf{\Gamma^E} = \mathbf{P} \times \mathbf{E_0}$, which tends to increase its rotation further and the particle begins to rotate with an angular velocity $\boldsymbol{\omega}$.

The dipole moment **P** is named "retarded dipole moment" and is given by a relaxation equation [Pannacci *et al.* (2007a)],

$$\frac{\partial \mathbf{P}}{\partial t} = (\boldsymbol{\omega} \times \mathbf{P}) - \frac{1}{\tau}(\mathbf{P} - (\chi^0 - \chi^\infty)\mathbf{E_0}), \tag{1}$$

where the characteristic relaxation time for the polarization to relax is the Maxwell–Wagner time,

$$\tau = \frac{\varepsilon_p + 2\varepsilon_l}{\gamma_p + 2\gamma_l}, \tag{2}$$

and χ^0 and χ^∞ are the polarizability factors of the particle (radius a) at low and high frequencies, respectively,

$$\chi^0 = 4\pi\varepsilon_l a^3 \frac{\gamma_p - \gamma_l}{\gamma_p + 2\gamma_l} \quad \text{and} \quad \chi^\infty = 4\pi\varepsilon_l a^3 \frac{\varepsilon_p - \varepsilon_l}{\varepsilon_p + 2\varepsilon_l}. \tag{3}$$

When the particle is rotating at angular velocity $\boldsymbol{\omega}$, it undergoes a viscous resistant torque, $\mathbf{\Gamma^\eta}$,

$$\mathbf{\Gamma^\eta} = -\alpha(\boldsymbol{\omega} - \boldsymbol{\omega_0}), \tag{4}$$

where $\boldsymbol{\omega_0}$ is the angular velocity of the surrounding fluid (half the vorticity) and $\alpha = 8\pi\eta a^3$, the rotational friction coefficient of the spherical particle, η being the viscosity of the liquid.

The dynamics of the particle is, therefore, determined upon solving Eq. (1) coupled with the angular momentum principle,

$$I\frac{d\boldsymbol{\omega}}{dt} = \mathbf{P} \times \mathbf{E_0} - \alpha(\boldsymbol{\omega} - \boldsymbol{\omega_0}), \tag{5}$$

where I is the moment of inertia of the particle. In a previous paper, we have shown both experimentally and theoretically that a particle undergoing Quincke rotation in a quiescent fluid could exhibit a complex dynamical behavior. In particular, when the field
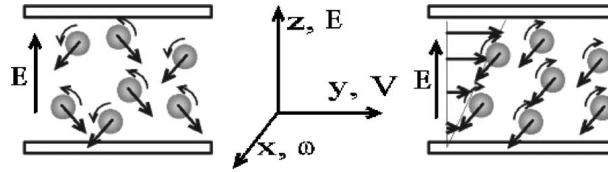
FIG. 2. Representation of the suspension subject to a DC E field. If the suspension is quiescent, the particles rotate around themselves with any axis perpendicular to the field so that the average spin rate is zero. When a shear flow is applied, all the particle rotation axes may be aligned in the direction of the mean vorticity of the suspension and the collective movement of the particles drives the suspending liquid in such a way that the apparent viscosity of the suspension is lessened.

intensity is sufficiently high, the rotor can exhibit a chaotic behavior which is exactly described by the Lorenz equations [Peters (2005)].

The stationary behavior of a particle undergoing Quincke rotation in a quiescent liquid ($\boldsymbol{\omega_0}=\mathbf{0}$) has been studied in detail [Jones (1984)] and it is well known that the particle rotation depends on a threshold value of the field E_c and that, above this critical field, the particle rotates around itself with an axis pointing in any direction perpendicular to the DC field. The modulus of its angular velocity is given by

$$\omega = \frac{1}{\tau}\sqrt{\left(\frac{E_0}{E_c}\right)^2 - 1} \quad \text{with } E_c = \sqrt{\frac{-\alpha}{(\chi^0 - \chi^\infty)\tau}}. \tag{6}$$

If the liquid vorticity is nonzero, the resolution of Eqs. (1) and (5), even in the stationary case, is much more complicated. This problem is solved in the following subsection.

B. Quincke rotation in the presence of a simple shear flow

Let us consider a suspension of spheres (volume fraction ϕ) subject to a dc electric field applied in z-direction. If the liquid is at rest, the particles start rotating around themselves in any direction perpendicular to the field and so the average spin rate of the suspension is zero [Fig. 2(a)]. However, when a velocity gradient is applied along the E field direction, the particles rotation axes will be favored in the vorticity direction (x-direction). Therefore, the degeneracy of the rotation direction will be lifted giving rise to a nonzero spin rate of the ensemble of particles [Fig. 2(b)].

The angular velocity of the suspension, $\boldsymbol{\omega_s}$, viewed like a macrocontinuum, is given by the volume average of the angular velocity over the particles and the suspending liquid [Brenner (1970)],

$$\boldsymbol{\omega_s} = \frac{1}{2}\boldsymbol{\nabla}\times\mathbf{v} = -\frac{\dot{\gamma}}{2}\mathbf{e_x} = \phi\boldsymbol{\omega} + (1-\phi)\boldsymbol{\omega_0}, \tag{7}$$

where $\mathbf{v}=\mathrm{v}(z)\mathbf{e_y}$ is the suspension velocity field and $\dot{\gamma}$ is the the macroscopic shear rate. For the following, we have to keep in mind that $\dot{\gamma}$ is the only external parameter of Eq. (7) while ω and ω_0 are coupled variables.

Upon using Eq. (7) to express the suspending fluid angular velocity, $\boldsymbol{\omega_0}$, in terms of $\dot{\gamma}$ and $\boldsymbol{\omega}$, the projections of Eqs. (1) and (5) on the axes Ox, Oy, and Oz (see Fig. 2) give rise to a system of five scalar equations:

$$\frac{dX}{dt^*} = \Pr\left(Y - \frac{X + \dfrac{\dot{\gamma}\tau}{2}}{1-\phi}\right),$$

$$\frac{dY}{dt^*} = -X(Z - r) - Y,$$

$$\frac{dZ}{dt^*} = XY - Z - \psi\xi,$$

$$\frac{d\xi}{dt^*} = \psi(Z - r) - \xi,$$

$$\frac{d\psi}{dt^*} = -Pr(\psi + \xi), \tag{8}$$

where the variables are dimensionless,

$$X = \omega_x\tau; \quad \psi = \omega_y\tau; \quad t^* = \frac{t}{\tau},$$

$$\xi = P_x\frac{E\tau}{\alpha}; \quad Y = P_y\frac{E\tau}{\alpha}; \quad Z = P_z\frac{E\tau}{\alpha} + r,$$

and where we have introduced the ratio of the electric field intensity to the threshold value,

$$r = \left(\frac{E}{E_c}\right)^2,$$

and the ratio of the Maxwell–Wagner time to the characteristic mechanical time,

$$Pr = \frac{\alpha\tau}{I}.$$

In stationary state, this system of equations admits five solutions which can be divided into two groups. The solutions of the first group correspond to a rotation of the particles in x-direction while the few intuitive solutions of the second group correspond to zero-vorticity of the suspending liquid ($\boldsymbol{\omega_0=0}$) and a nonzero value for the y-component of the angular velocity. Let us give some details about these five solutions:

First group of solutions: $\boldsymbol{\omega=\omega e_x}$, $X=X_{1,2,3}$, $\psi=\xi=0$, and the variables Y, Z can be expressed as a function of X which is the solution of the following third order equation:

$$X^3 + \frac{\dot{\gamma}\tau}{2}X^2 + [1 - (1 - \phi)r]X + \frac{\dot{\gamma}\tau}{2} = 0. \tag{9}$$

When the shear rate tends toward zero, the particles rotate only if the E field intensity is higher than a critical value, E*,

$$E^* = \frac{E_c}{\sqrt{1 - \phi}}. \tag{10}$$

When the electrical field intensity is lower than E*, Eq. (9) admits only one solution which corresponds to a rotation of the particles in the direction of the vorticity (X_1 in Fig. 3). For higher field intensities, there exist either one or three solutions to Eq. (9) (see Fig.
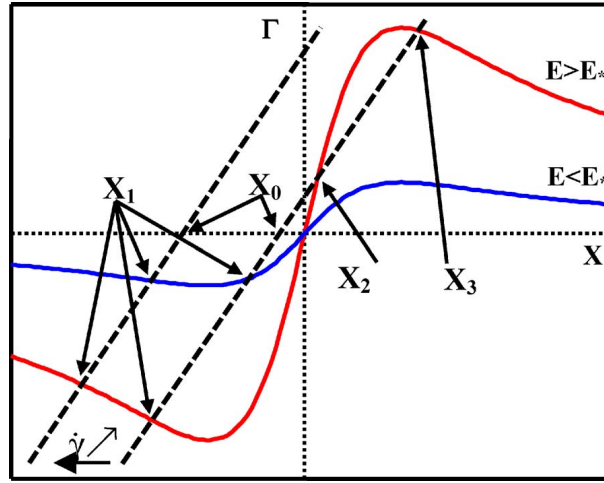
FIG. 3. Variation of the driving electric torque (solid lines) and of the opposite of the viscous resistant torque (dashed lines) exerted on a particle with its angular velocity. The electric torque has been drawn for two intensities of the electric field and the viscous one for two values of the average shear rate in the suspension. Depending both on the values of the field intensity and of the mean shear rate, there exists either one or three solutions for the angular velocity of the particle.

3), depending on the value of $\dot{\gamma}$. X_1, which is always a solution, corresponds to a rotation of the particles in the vorticity direction while the other two possible solutions represent a rotation in the opposite direction (X_2 and X_3 in Fig. 3).

Second group of solutions: $\omega_y \neq 0$, $X = X_4$,

$$X = Y = -\frac{\dot{\gamma}\tau}{2\phi},$$

$$Z = r - 1,$$

$$\psi = -\xi = \pm \sqrt{-\left(\frac{\dot{\gamma}\tau}{2\phi}\right)^2 + r - 1}. \tag{11}$$

For ψ and ξ to be real, this double solution exists only if

$$\dot{\gamma}\tau < \dot{\gamma}^*\tau = 2\phi\sqrt{r-1}. \tag{12}$$

The x-component of the angular velocity of the particles does not depend on the E field intensity and, according to Eq. (7), this nonintuitive solution corresponds to a zero vorticity of the suspending liquid ($X_0 = \omega_0\tau = 0$). Then the modulus of the particles' angular velocity is equal to the value we have defined previously when there was no shear flow [Eq. (6)]. At last, it should be stressed that this solution is compatible with the flow geometry wherein the y-component of the velocity gradient is zero. This requirement is achieved if the y-component of the angular velocity corresponds to clockwise rotation ($\psi < 0$) for half of the particles and counter-clockwise ($\psi > 0$) for the other half.

All the X-solutions of the system of Eqs. (8) are plotted in Figs. 4(a) and 4(b). In Appendix A, we study the stability of these solutions and we show that the solution X_4 is always a stable solution. When the shear rate is higher than the critical value $\dot{\gamma}^*$, X_4 does not exist any more but X_1 becomes stable. In Figs. 4(a) and 4(b), the thick lines represent the stable solutions.
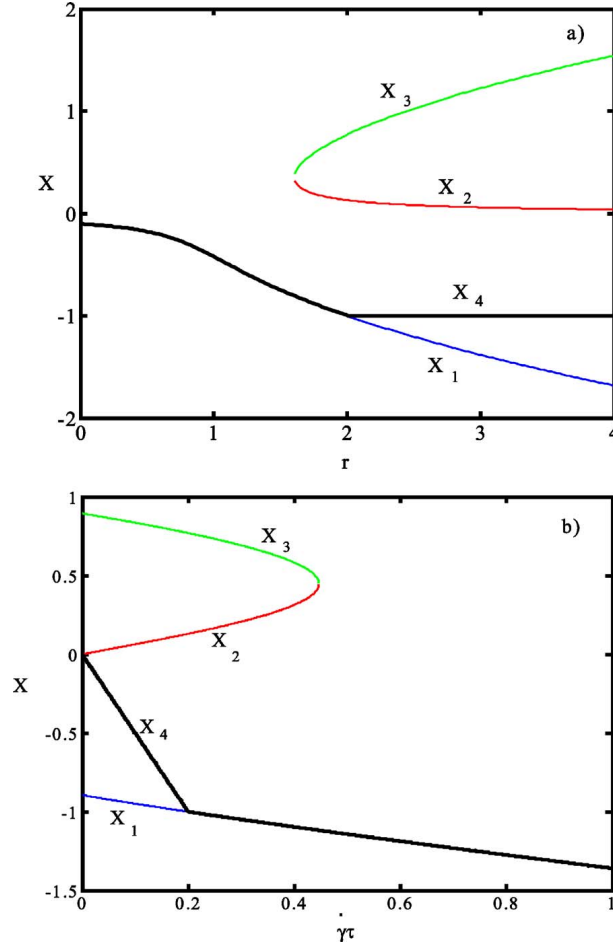
FIG. 4. Normalized average angular velocity of the particles of a suspension ($\phi=10\%$). (a) variation with the square of the normalized field intensity for an average normalized shear rate of 0.2. (b) variation with the normalized shear rate for r=2. The thick lines represent the stable values of the angular velocity.

C. Influence of electric driving torque on the value of the apparent viscosity of the suspension

The zy-component of the total stress tensor in the suspension σ_{zy} is obtained upon adding its symmetric and anti-symmetric parts. Its symmetric part is the viscous stress while its anti-symmetric part is equal to the half of the x-component of the volume torque exerted on the suspension, γ^{E}:

$$\sigma_{zy}^{T} = \eta(\phi)\,\dot{\gamma} + \tfrac{1}{2}\,\gamma_{x}^{E}, \tag{13}$$

where $\eta(\phi)$ is the viscosity of the suspension in the absence of an electric field.

In the following, we shall use the expression of the viscosity proposed by Brenner (1970) since, as it can be seen in Fig. 5, for rather low volume fractions of particles, it captures the variation of the viscosity with the particles' concentration,

$$\eta(\phi) = \eta \frac{1 + (3/2)\,\phi}{1 - \phi}. \tag{14}$$
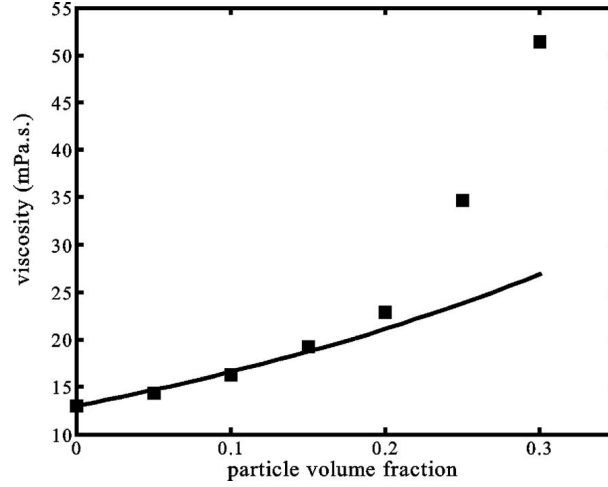
FIG. 5. Variation of the viscosity of a suspension of PMMA particles dispersed in neutrally buoyant mixture of dielec S and Ugilec with the particle volume fraction. The solid line represents the values of the viscosity predicted by Brenner (1970).

The volume torque is given by adding the torques, Γ^E, exerted on each particle contained in a unit volume,

$$\gamma_x^E = \frac{\phi}{(4/3)\pi a^3}\Gamma_x^E = \frac{\phi}{(4/3)\pi a^3}P_y E. \tag{15}$$

The apparent viscosity of the suspension is then given by the ratio of the total tangential stress in the suspension to the mean shear rate,

$$\eta_{app} = \frac{\sigma_{zy}^T}{\dot{\gamma}} = \eta(\phi) + \frac{\phi}{(8/3)\pi a^3}\frac{P_y E}{\dot{\gamma}}, \tag{16}$$

and the apparent viscosity normalized by the viscosity of the suspension when no field is applied is given by

$$\eta_{app}^* = \frac{\eta_{app}}{\eta(\phi)} = 1 + \frac{3\phi}{1+(3/2)\phi}(1-\phi)\frac{Y}{\dot{\gamma}\tau}. \tag{17}$$

Since the y-component of **P** [see Fig. 2(b)] is negative, it appears clear that the apparent viscosity is lowered by the application of a DC electric field. It should be stressed that expressing P_y in terms of ω_x, Eq. (17) is formally equivalent to the expression for the viscosity of a suspension of rotating spheres proposed by Brenner (1970),

$$\eta_{app} = \eta(\phi) + \eta_r(\phi)$$

with

$$\eta(\phi) = \eta\frac{1+(3/2)\phi}{1-\phi}; \quad \eta_r(\phi) = \eta\frac{(3/2)\phi}{1-\phi}\frac{(\dot{\gamma}/2)+\omega_x}{(\dot{\gamma}/2)}, \tag{18}$$

where η is the suspending liquid viscosity.

The variation of η_{app}^* with normalized shear rate is shown in Figs. 6(a) and 6(b) for various volume concentrations and field intensities. As mentioned before, the value of the
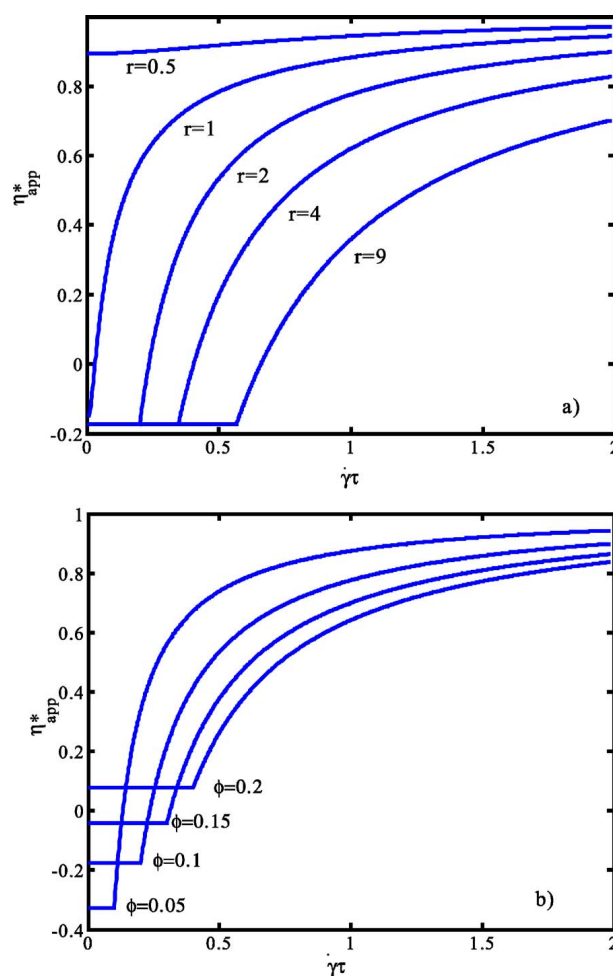
FIG. 6. Variation of the normalized apparent viscosity of the suspension with the average normalized shear rate. (a) for different values of the E field intensity and for $\phi=10\%$. (b) for different particle volume fractions and r=2.

low shear rate viscosity plateau does not depend on the field intensity but only on the particle volume fraction. In particular, when ϕ is lower than $\frac{1}{6}$, the value of the plateau is negative.

III. EXPERIMENTS

A. Materials

We studied the rheological behavior of a suspension of PMMA particles (polymethylmethacrylate, ICI Acrylics, grade 2041) dispersed into a mixture of transformer oil (dielec S, Hafa, France) and Ugilec (Elf Atochem). The resulting suspending liquid is such that its density is the same as that of the particles, $\rho=1.18\times10^3$ kg/m^3, and its viscosity at 25 °C is 13 mPa s. Its dielectric constant was measured to be 3.69 ε_0 and its conductivity has been raised to 1.5×10^{-8} S/m upon addition of AOT salt (Sigma Aldrich, sodium dioctylsulfosuccinate). Although Quincke rotation effect is not expected to depend on the particle size, the particles were sieved between 50 and 63 μm. Their dielectric constant is 2.6 ε_0 and their conductivity is about 10^{-14} S/m so that, compared

to the suspending liquid, they are regarded as insulating. The volume fraction is varied between 5% and 20%. All these physical properties give the following values for the parameters introduced previously: $\tau = 3$ ms; $E_c = 830$ V/mm; Pr$=720$.

B. Rheological measurements

The rheological measurements were carried out with a controlled stress rheometer, Carrimed CSL 100, in Couette flow geometry. The coaxial cylinders also serve as electrodes so that the E field is applied along the velocity gradient direction (radial direction). A high voltage is applied to the outer stator (radius R_1) while the inner rotor (radius R_2) is grounded to the earth through an electrode dipping in a mercury reservoir situated at the top of the rotation axis of the rheometer. The gap between the two cylinders (1 mm) is narrow compared to their radii ($R_2 = 14.5$ and $R_1 = 15.5$ mm) so that the flow can be approximated by a simple shear flow, $\dot{\gamma}$, where the shear rate is related to the angular velocity of the inner cylinder Ω by

$$\dot{\gamma} = \frac{\Omega R_1}{R_2 - R_1}.$$ (19)

Furthermore, since the gap is narrow, the shear stress, σ, can be considered as homogeneous in the suspension and given by

$$\sigma = \frac{M}{4\pi h} \frac{R_1^2 + R_2^2}{R_1^2 R_2^2},$$ (20)

where M is the mechanical torque exerted on the inner cylinder. Then from the measurement of the variation of Ω with M, using relations (19) and (20), the experimental value of the viscosity is determined. The rheological measurements are made at equilibrium: first, in the absence of an electric field, a constant shear stress is applied as long as necessary (≈ 10 s) to record a constant viscosity value, $\eta(\phi)$. Then the E field is applied and the value of η_{app} is estimated when the shear rate has become constant. After that, the viscosity in the absence of the electric field is again measured to verify that the suspension has not been heated by the electric current which passes through the suspension when the electric field is present.

## IV. RESULTS AND DISCUSSION

The variation of η_{app}^* with the normalized shear rate is shown in Figs. 7(a)–7(c), for three volume fractions, 5%, 10%, and 20%, respectively. The solid symbols and dashed lines correspond to the experimental results while the open symbols and the solid lines represent the theoretical predictions given by Eq. (18), wherein Y has been substituted by its stable stationary value. The qualitative agreement between model and experiment is quite good since there is no free parameter. In particular, for the highest fields and the highest volume fractions, the data display a clear viscosity plateau at low shear rates. Whatever the field intensity, the concordance between experimental data and theoretical values of the viscosity is satisfactory at high shear rates. A discrepancy appears for low values of the shear rate, especially in the case of low field intensities for which the experiments show that the field is responsible for an increase of the viscosity ($\eta_{app}^* > 1$) while the theory predicts a decrease. In a previous paper [Pannacci (2007b)], we have attributed this discrepancy to a structuring of the suspension which occurs at low shear rates and for moderate E field intensities. We have shown in this paper that the E field had two opposite effects on the structure of a suspension. Indeed, it induces dipole-dipole
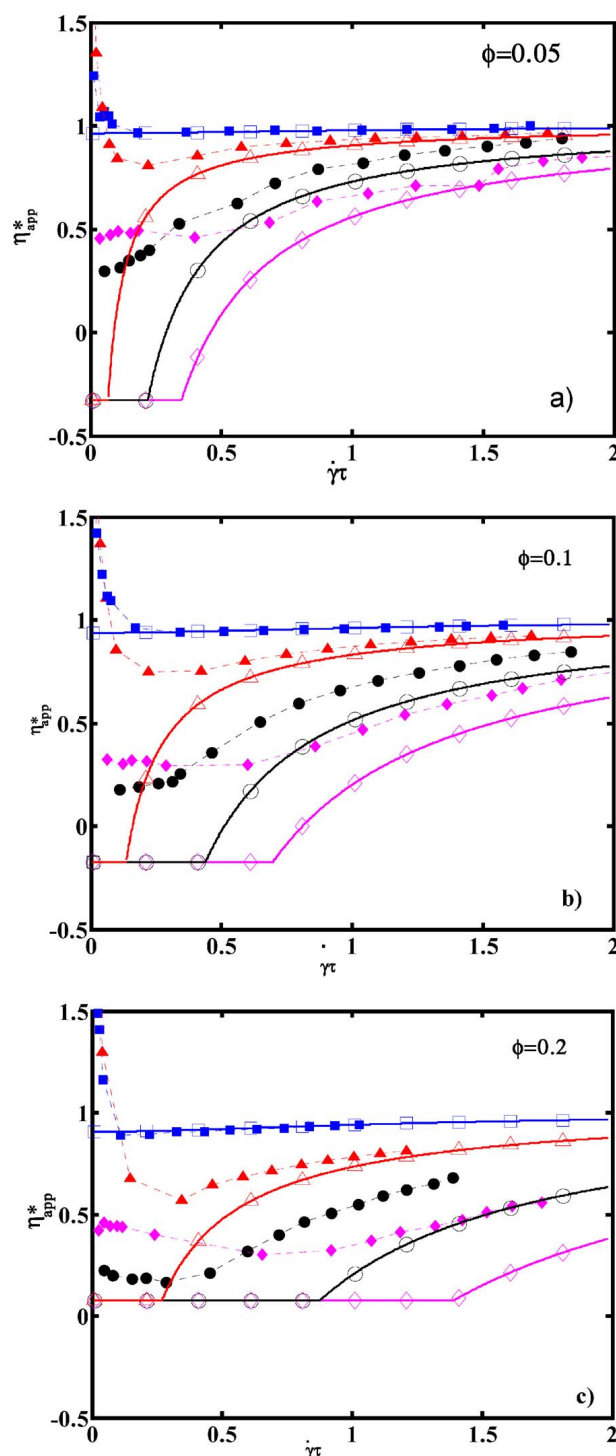
FIG. 7. Comparison between experimental (solid symbols and dotted lines) and theoretical results (open symbols and solid lines) for the variation of the apparent viscosity of a suspension of PMMA particles dispersed in a neutrally buoyant mixture of dielec S and Ugilec with the shear rate for different E field intensities: (squares) 500 V/mm, (triangles) 1000 V/mm, (circles) 2000 V/mm, (diamonds) 3000 V/mm. (a) $\phi=5\%$, (b) $\phi=10\%$, (c) $\phi=20\%$.
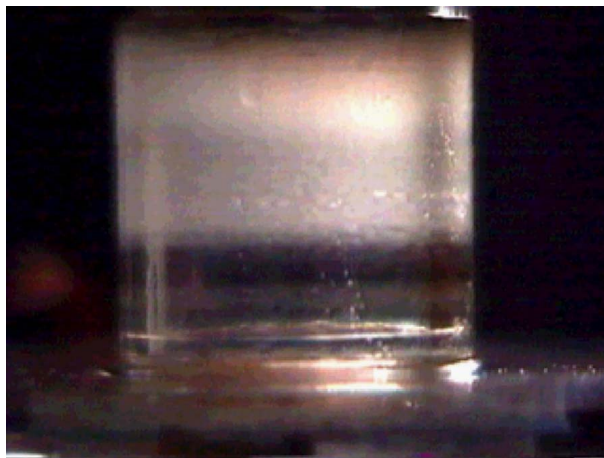
FIG. 8. Phase separation in the Couette geometry. The suspension has been subject to a shear stress of 10 Pa and to a DC electric field of 2000 V/mm for 5 min.

interactions between particles, which tend to structure the suspension but, because of particles' spinning, the E field also gives rise to hydrodynamic forces which tend to break the structures. These two antagonistic actions of the E field explain why no structuring of the suspension takes place for the highest field intensities, contrary to what would have happened in a classical ER fluid. These theoretical predictions have been confirmed by experimental observations of the suspension structuring carried out with semi-transparent cylinders mounted on the rheometer which allow the observation of the structure of the suspension when an electric field is applied.

For the highest field intensities, the low shear rate viscosity plateau is observed as expected from the model and that is an important point since the presence of this plateau substantiates the existence of the solution X_4 (and associated values of X_0, Y, Z, ψ, and ξ). The model presented in Sec. II and the stability analysis reported in Appendix A predicts that the solution X_4 is stable and so is observable for shear rates lower than a critical value, $\dot{\gamma}^*$, which is an increasing function of the particle volume fraction, and of the field intensity [Eq. (12)]. Even though it is difficult to determine an accurate value for $\dot{\gamma}^*$ from the experimental rheological curves, the low shear rate plateau seems to be longer the higher the field intensity and the particle volume fraction are. Despite this rather good qualitative agreement, it is worth noting that the viscosity decrease is over-estimated by the theory. This disagreement could originate, as already said, in the dipolar forces but also in the hydrodynamic interactions between particles which could lead to a dispersion in their spin velocities. There exists a third possible source of the discrepancy which lies in a tendency of the suspension to separate into two phases, one constituted by only the suspending liquid while the other contains a high concentration of particles. This kind of phase separation is illustrated by the picture in Fig. 8 which represents the Couette cell filled with a suspension containing 10% of particles after application of an electric field of 2000 V/mm and of a shear stress of 5 Pa for 5 min. Since the value of the viscosity plateau is an increasing function of the spinning particle concentration, the phase separation of the suspension is responsible for an increase of the measured apparent viscosity. We have observed that the demixing was the most pronounced for the most diluted suspension so that the discrepancy of the experimental and theoretical values of the viscosity plateau is the greatest in the case of the less concentrated suspensions.

V. CONCLUSION

The study of the rheological behavior of a suspension of insulating particles suspended in a slightly conducting liquid submitted to a DC electric has shown that it was possible to drastically reduce the apparent viscosity. The model we use to predict the viscosity reduction is based on the calculation of the angular velocity of the particles subject to a DC field in a shear flow. We have been able to qualitatively explain the viscosity decrease and to derive a model which captures the essential variation of the suspension viscosity with the E field intensity and with the shear rate. In particular, we have shown that, if the direction of the axis of rotation of the particles is not fixed, the low shear rate viscosity is expected to be constant and independent of the electric field intensity. These predictions are corroborated by the experimental observation of a low shear rate viscosity plateau.

From an application point of view, this electric field-induced viscosity reduction should develop in an interesting way since it is easy to achieve and the viscosity changes are quite important. We have already demonstrated the possibility of using DC electrorotation to increase the flow rate in a capillary [Cebers (2002)]. Besides these applications in microfluidics, these fluids should be used as smart fluids in a variety of applications, including damping or vibration control.

APPENDIX A: STABILITY ANALYSIS OF THE SOLUTIONS

A linear stability analysis of system of Eqs. (8) is conducted to discriminate the stable solution from the unstable ones. All the five variables, v, of the system (8) are perturbed around their stationary values,

$$X = X_S + \delta X e^{\lambda t^*}, \quad Y = Y_S + \delta Y e^{\lambda t^*}, \quad Z = Z_S + \delta Z e^{\lambda t^*},$$

$$\psi = \psi_S + \delta\psi e^{\lambda t^*}, \quad \xi = \xi_S + \delta\xi e^{\lambda t^*},$$

where v_S represents the equilibrium values [solutions of Eq. (9) and associated values of the other variables and Eq. (10)] and $\delta v e^{\lambda t^*}$ the first order perturbation with λ, the normalized growth rate of the perturbation.

Around v_S, the system of Eqs. (8) is written:

$$(\lambda + \mathrm{Pr}/(1 - \phi))\delta X - \mathrm{Pr}\,\delta Y = 0,$$

$$(Z_S - r)\delta X + (\lambda + 1)\delta Y + X_S \delta Z = 0,$$

$$-Y_S \delta X - X_S \delta Y + (\lambda + 1)\delta Z = 0,$$

$$(\lambda + 1)\delta\xi - (Z_S - r)\delta\psi = 0,$$

$$\mathrm{Pr}\,\delta\xi + (\lambda + \mathrm{Pr})\delta\psi = 0. \tag{A1}$$

To have nontrivial solutions, the determinant of the system of five equations has to be zero or

$$\{(\lambda + \mathrm{Pr})(\lambda + 1) + \mathrm{Pr}(Z_S - r)\}\left\{\left(\lambda + \frac{\mathrm{Pr}}{1 - \phi}\right)[X_S^2 + (\lambda + 1)^2] + \frac{\mathrm{Pr}}{1 - \phi}\left[-\frac{X_S + \dot\gamma\tau/2}{X_S}(\lambda + 1)\right.\right.$$

$$\left.\left. + X_S\left(X_S + \frac{\dot\gamma\tau}{2}\right)\right]\right\} = 0. \tag{A2}$$

In particular, the determinant is zero if the first factor of the left-hand side of Eq. (A2) is zero,

$$\lambda_{1,2} = \frac{-(Pr+1) \pm \sqrt{(Pr+1)^2 - 4\,Pr(Z_S - r + 1)}}{2}. \tag{A3}$$

So, if $Z_S - r + 1 < 0$, or equivalently from Eq. (7) and the first two equations of Eq. (8) if $X_0/X < 0$, there exists a positive real solution for λ and the perturbation grows. As a result, if the directions of the angular velocity of the particles and of the vorticity of the suspending liquid are opposite, the solution cannot be stable. Therefore, X_2 and X_3 are always unstable solutions. Now let us find a condition for which X_1 and X_0 have opposite signs. The instability criterion implies that X_1 becomes unstable when X_0 changes its sign. Cancelling X_0 and expressing X_1 in terms of $\dot{\gamma}$ in Eqs. (8), we obtain that X_1 is unstable if $\dot{\gamma}\tau < \dot{\gamma}^*\tau = 2\phi\sqrt{r-1}$.

A numerical study of the second term of the determinant shows that, for the experimental system which will be described hereafter ($Pr \approx 700$, $0 \lesssim r \lesssim 20$, $0 \lesssim \dot{\gamma}\tau \lesssim 2$), the values of λ which cancel this term are always negative if $X_0/X > 0$ so that the stability criterion defined before is still valid.

As a summary, the stable solutions are X_4 for $\dot{\gamma} < \dot{\gamma}^*$ and X_1 for $\dot{\gamma} > \dot{\gamma}^*$. Lastly, it should be stressed that, if the rotation axis of the particle is fixed ($\boldsymbol{\omega} = \omega\mathbf{e_x}$), the solution X_4 does not exist and the solutions X_1 and X_2 are both stable. This is reported in Cebers (2000) and studied in detail in a recent paper by Dolinsky and Elperin (2007).

References

Atten, P., C. Boissy, and J. N. Foulc, "The role of conduction in electrorheological fluids: from interaction between particles to structuration of suspensions," J. Electrost. **40-41**, 3–12 (1997).

Bacri, J. C., R. Perzynski, M. I. Shliomis, and G. Burde, "Negative-viscosity effect in a magnetic fluid" Phys. Rev. Lett. **75**, 2128–2131 (1995).

Boissy, C., P. Atten, and J. N. Foulc, "On a negative electrorheological effect," J. Electrost. **35**, 13–20 (1995).

Brenner, H., "Rheology of two-phase systems," Annu. Rev. Fluid Mech. **2**, 137–176 (1970).

Cebers, A., E. Lemaire, and L. Lobry, "Internal rotations in dielectric suspensions," Magnetohydrodynamics (N.Y.) **36**, 347–364 (2000).

Cebers, A., E. Lemaire, and L. Lobry, "Flow modification induced by Quincke rotation in a capillary," Int. J. Mod. Phys. B **16**, 17–18 (2002).

Dolinsky, Y., and T. Elperin "Rotation of the leaky dielectric particle in a rotating electric field," Phys. Rev. E **75**, 066611 (2007).

Jones, T. B., "Quincke rotation of spheres," IEEE Trans. Ind. Appl. **IA-20**, 845–849 (1984).

Lim, S., S. M. Park, and K. I. Kim, "AI vibration control of high-speed rotor systems using electrorheological fluid," J. Sound Vib. **284**, 685–703 (2005).

Lobry, L., and E. Lemaire, "Viscosity decrease induced by a DC electric field in a suspension," J. Electrost. **47**, 61–69 (1999).

Marshall, L., C. F. Zukoski, and J. W. Goodwin, "Effect of electric fields on the rheology of non-aqueous concentrated suspensions," J. Chem. Soc., Faraday Trans. 1 **85**, 2785–2795 (1989).

Melcher, J. R., "Electric field and moving media," IEEE Trans. Educ. **E-17**, 100–110 (1974).

Pannacci, N., E. Lemaire, and L. Lobry, "How insulating particles increase the conductivity of a suspension," Phys. Rev. Lett. **99**, 094503 (2007a).

Pannacci, N., E. Lemaire, and L. Lobry, "Rheology and structure of a suspension of particles subjected to Quincke Rotation," Rheol. Acta **46**, 899–904 (2007b).

Peters, F., L. Lobry, and E. Lemaire, "Experimental observation of Lorenz chaos in the Quincke rotor dynam-

SUSPENSIONS WITH INTERNAL ROTATIONS   783

ics," Chaos **15**, 013102-1–6 (2005).

Phani, A. S., and K. Venkatraman, "Damping characteristics of electro-rheological fluid sandwich beams," Acta Mech. **180**, 195–201 (2005).

Quincke, G., "Ueber rotationen im constanten electrischen felde," Ann. Phys. Chem. **59**, 417–486 (1896).

Rinaldi, C., F. Gutman, X. He, A. D. Rosenthal, and M. Zahn, "Torque measurements on ferrofluid cylinders in rotating magnetic fields," J. Magn. Magn. Mater. **289**, 307–310 (2005).

Tan, K. P., R. Stanway, and W. A. Bullough, "Dynamic velocity response of an electro-rheological (ER) clutch for robotic applications," Mech. Adv. Mater. Struct. **13**, 1–12 (2006).

B.2 Pressure-driven flow of a micro-polar fluid : Measurement of the velocity profile

Pressure-driven flow of a micro-polar fluid: Measurement of the velocity profile

F. Peters, L. Lobry, and E. Lemaire[a]

CNRS, Université de Nice, LPMC-UMR 6622, 06108 Nice Cedex 2, France

Synopsis

The pressure-driven flow of a suspension of spinning particles in a rectangular channel is studied using an acoustic method. The suspension is made of insulating particles [poly(methyl methacrylate)] dispersed in a slightly conducting oil (Ugilec+Dielec) and is subjected to a direct current electric field. In such a case, the particles are polarized in the direction opposite to that of the electric field and begin to rotate in order to flip their dipoles in the field direction. Such a rotation of the particles is known as Quincke rotation and is responsible for an important decrease of the effective viscosity of the suspension. Indeed, due to the electric torque exerted on the particles, the stress tensor in the suspension is not symmetric anymore and a driving effect arises from the anti-symmetric part. When such a suspension flows through a rectangular channel, the velocity profile is expected to deviate from the usual Poiseuille flow. In this paper, the velocity profiles are measured using pulsed ultrasound Doppler velocimetry technique. They compare well to those that are computed from the otherwise measured rheological law. © *2010 The Society of Rheology.* [DOI: 10.1122/1.3302803]

I. INTRODUCTION

In this paper, we are interested in the rheological behavior of a suspension of spheres which experience a torque. In such a case, it is well known that the stress tensor is no longer symmetric but that an anti-symmetric part has to be added to the usual symmetric stress tensor. The role played by this anti-symmetric stress on the mechanical behavior of suspensions has been widely studied both theoretically and experimentally. Such suspensions are known as micro-polar fluids and their theory developed by Eringen (1966) and Dahler, Condiff, and Scriven [Dahler and Scriven (1961); Condiff and Dahler (1964)] around 1960. The mechanical behavior of such fluids is given by two vector fields: the linear velocity field as in the case of non polar fluids and the particle angular velocity field [Lukaszewicz (1999)]. These fields are the solutions of two coupled equations: the linear momentum and internal angular-momentum balance equations. In recent years, the theory of micro-polar fluids has received a new interest with the development of microfluidics and ferrofluid rheology [Rosensweig (2007)]. The ferrofluids submitted to alternating or rotating magnetic fields are undoubtedly the most famous micro-polar suspensions. The external magnetic field exerts a torque on the dipole moments carried by the particles which consequently rotate with an angular velocity different from that of the

---

[a]Author to whom correspondence should be addressed; electronic mail: elemaire@unice.fr

surrounding liquid. Many theoretical [Pérez-Madrid *et al.* (1999); Rinaldi and Zahn (2002); Korlie *et al.* (2008); Shliomis and Konstantin (1994)] and experimental [Bacri *et al.* (1995); Rinaldi *et al.* (2005)] investigations have addressed the role of the magnetic torque on the rheological behavior of ferrofluids. In particular, it has been shown that the application of a fast enough oscillating magnetic field forces the particles to rotate faster than the host fluid leading to a reduction of the apparent viscosity of the ferrofluid [Bacri *et al.* (1995)]. A true apparent "negative" viscosity can be obtained upon submitting the ferrofluid to a rotating magnetic field [Rinaldi *et al.* (2005)].

In this paper, we propose another way to induce a torque on the suspended particles. It consists of applying a dc electric field to a suspension of insulating particles dispersed in a slightly conducting liquid. Indeed, when a non-conducting particle immersed in a semi-insulating liquid is submitted to a sufficiently high amplitude direct current (dc) field, it begins to rotate spontaneously around itself. This instability is known as Quincke rotation [Quincke (1896); Jones (1995)]. When the suspension is motionless and a dc field is applied, the particles start rotating around themselves in any direction perpendicular to the field and the average spin rate of the suspension is zero. But, when a velocity gradient is applied along the E field direction, the particle's rotation axis is favored in the vorticity direction. Therefore, the degeneracy of the rotation direction is eliminated, giving rise to a nonzero spin rate of the ensemble of particles. This macroscopic spin rate may drive the suspending liquid and thus lead to a decrease of the apparent viscosity of the suspension [Lemaire *et al.* (2008)].

We have been working for the last years both on the modeling and on the experimental characterization of the influence of Quincke rotation on the rheological behavior of suspensions. In particular, we have been able to propose a constitutive relation for the rheological behavior of such a suspension of spinning particles. The model predicts that, for low particle concentrations ($\phi < 1/6$), there exists a bistable flow regime and the apparent viscosity of the suspension is negative when it is submitted to a small shear rate. Experimentally, we were not able to show evidence of this negative apparent viscosity but we measured a huge viscosity decrease [Lemaire *et al.* (2008)]. Moreover, we have shown that when an electric field was applied to such a suspension flowing in a rectangular channel, the flow rate could be enhanced. The flow rate increase is expected to be accompanied by a change in the velocity profile shape since, when an electric field is applied, the rheological behavior of the suspension is not Newtonian anymore. The aim of the present paper is to present the direct measurement of the velocity profiles and their modification induced by the electric field. In Sec. II, we present briefly the mechanism involved in the viscosity reduction. Section III is devoted to the description of the experimental set-up and method. The results are presented in Sec. IV and discussed in Sec. V.

II. QUINCKE ROTATION-INDUCED VISCOSITY REDUCTION

All the details concerning the possibility of decreasing the viscosity of a suspension, thanks to dc-electro-rotation, have been previously given [Lemaire *et al.* (2008)]. Here we just mention the starting point of the analysis and the main results.

A. Quincke rotation of a single particle

The electrorotation of a particle induced by a dc electric field is known as Quincke rotation and occurs when an insulating particle immersed into a low conducting liquid is subjected to a sufficiently high dc field. In such a situation, as first observed by Quincke at the end of the 19th century, the particle can rotate spontaneously around itself along

any axis perpendicular to the electric field. A simple physical interpretation was given by Secker and Scialom (1968) and refined by Melcher (1974): during their migration, the free negative and positive charges of the liquid meet the insulating particle and accumulate at its surface. This results in a charge distribution with the particle polarized in a direction opposite to the field. This equilibrium is unstable and when the particle begins to rotate in order to flip the orientation of the induced dipole, it undergoes a driving torque. As stated by Jones (1984), the Quincke rotation may take place only if the charge relaxation time, which is given by the ratio of the dielectric constant to the conductivity, is lower in the liquid than in the particle. In such a case, the retarded part of the dipole, $\mathbf{P}$, which is associated with the charge distribution at the particle-liquid interface, is in the opposite direction from the electric field. Then, if the particle is slightly rotated, the deviation of its dipole moment $\mathbf{P}$ produces a torque, $\Gamma^E = \mathbf{P} \times \mathbf{E_0}$, which tends to increase the angular tilt further.

It has been shown [Cebers (1978); Pannacci et al. (2007a)] that the retarded part of the dipole moment was given by a relaxation equation

$$\frac{\partial \mathbf{P}}{\partial t} = (\boldsymbol{\omega} \times \mathbf{P}) - \frac{1}{\tau_M}(\mathbf{P} - (\chi^0 - \chi^\infty)\mathbf{E_0}), \tag{1}$$

where $\boldsymbol{\omega}$ is the particle angular velocity and τ_M the Maxwell time that is the characteristic relaxation time of the dipole moment

$$\tau_M = \frac{\varepsilon_p + 2\varepsilon_1}{\gamma_p + 2\gamma_1}, \tag{2}$$

with γ_i and ε_i being the electric conductivity and the dielectric permittivity of the liquid ($i=1$) and of the particle ($i=p$).

χ^0 and χ^∞ are the polarizability factors of the particle (radius a) at low and high frequencies, respectively,

$$\chi^0 = 4\pi\varepsilon_1 a^3 \frac{\gamma_p - \gamma_1}{\gamma_p + 2\gamma_1} \quad \text{and} \quad \chi^\infty = 4\pi\varepsilon_1 a^3 \frac{\varepsilon_p - \varepsilon_1}{\varepsilon_p + 2\varepsilon_1}. \tag{3}$$

Besides the electric torque, $\Gamma^E = \mathbf{P} \times \mathbf{E_0}$, the particle is subjected to a viscous torque

$$\Gamma^\eta = -\alpha(\boldsymbol{\omega} - \boldsymbol{\omega}_0), \tag{4}$$

where $\alpha = 8\pi\eta_1 a^3$ is the rotational friction coefficient of the spherical particle, η_1 being the dynamic viscosity of the liquid, and $\boldsymbol{\omega}_0$ being the angular velocity of the surrounding fluid (in a quiescent fluid, $\boldsymbol{\omega}_0 = \mathbf{0}$).
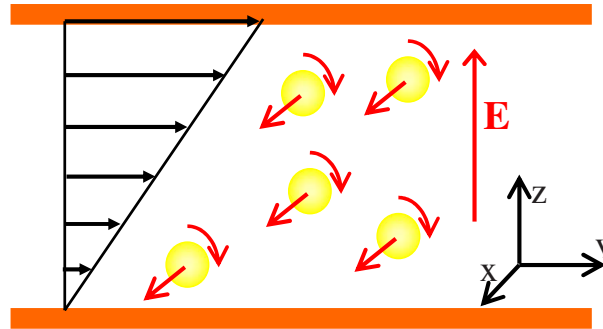
The particle spin rate is obtained upon solving Eq. (1), together with the angular momentum principle

$$I\frac{d\boldsymbol{\omega}}{dt} = \mathbf{P} \times \mathbf{E_0} - \alpha(\boldsymbol{\omega} - \boldsymbol{\omega}_0), \tag{5}$$

where I is the particle moment of inertia.

When $\omega_0 = 0$, the Quincke rotation takes place only if the electric field intensity is high enough for the electric torque to overcome the resistant viscous torque. The threshold intensity is expressed as

$$E_C = \sqrt{\frac{-\alpha}{\tau_M(\chi^0 - \chi^\infty)}}. \tag{6}$$

FIG. 1. The suspension is subjected to both a dc electric field and a simple shear flow. All the particles rotate around themselves with an axis pointing in the vorticity direction. The particles rotate faster than the surrounding liquid, leading to a decrease of the apparent viscosity.

B. Quincke rotation in a suspension

If we are interested in the rotation of an ensemble of particles in a suspension subjected to a constant shear rate $\dot{\gamma}$ (Fig. 1), using a mean field approach, $\boldsymbol{\omega_0}$ is taken as the average angular velocity of the suspending liquid [Brenner (1970)]

$$- \dot{\gamma}\mathbf{e_x} = 2(\phi\boldsymbol{\omega} + (1-\phi)\boldsymbol{\omega_0}), \tag{7}$$

where ϕ is the particle volume fraction. When the applied electric field intensity is higher than a critical value, $E^* = E_c/\sqrt{1-\phi}$, the coupled Eqs. (5) and (7) admit several stationary solutions [Lemaire et al. (2008)]. In the last reference, thanks to a linear stability analysis, we have been able to propose a criterion for the stability of the solutions: if the particles and the surrounding liquid rotate in opposite direction, the solution is unstable.

Once the particle angular velocity is known, it is injected in the model proposed by Brenner (1970) to relate the effective viscosity of a suspension to the particle spin rate

$$\eta_{\text{eff}}(\phi) = \eta(\phi) + \eta_1 \frac{\frac{3}{2}\phi}{1-\phi} \frac{\frac{\dot{\gamma}}{2} + \omega_x}{\frac{\dot{\gamma}}{2}}, \quad \text{with} \quad \eta(\phi) = \eta_1 \frac{1 + \frac{3}{2}\phi}{1-\phi}, \tag{8}$$

where η_1 is the fluid viscosity. From this expression, it is clear that when the particles rotate faster than the liquid ($|\omega_x| > \dot{\gamma}/2$) due to the electric torque, the effective viscosity of the suspension is lowered. It should be noted that the second term of the right hand side of Eq. (8) is related to the anti-symmetric part of the stress tensor which is responsible for the driving effect.

Figure 2(a) shows the expected variation of the normalized viscosity, $\eta_{\text{eff}}(\phi)/\eta(\phi)$, with the reduced shear rate, $\dot{\gamma}\tau_M$, for a suspension whose solid volume fraction is 5%. It should be stressed that when the shear rate is lower than a critical value, $\dot{\gamma}^*$, the effective viscosity, $\eta_{\text{eff}}(\phi)$, is expected to be negative [Lemaire et al. (2008)].

Here we focus our attention on the flow of such a suspension of spinning particles trough a rectangular channel. In such a flow, the control parameter is not the shear rate but the shear stress which is null at the center of the channel and maximum at the walls. The relation between the shear rate and the shear stress is shown in Fig. 2(b). The regions of the rheogram that are explored in a capillary flow are those where the absolute value of the shear rate is larger than $\dot{\gamma}^*$.
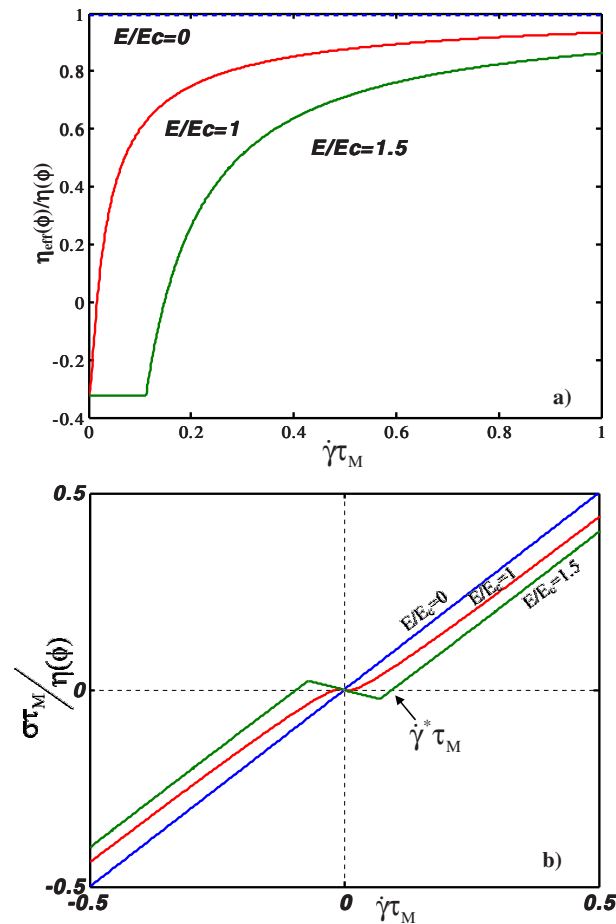
FIG. 2. Predicted rheological behavior of a suspension containing a solid volume fraction of 5% for different electric field strengths. (a) Normalized viscosity, $\eta_{\text{eff}}(\phi)/\eta(\phi)$, versus the reduced shear rate, $\dot{\gamma}\tau_{\text{M}}$. (b) Normalized shear stress, $\sigma\tau_{\text{M}}/\eta(\phi)$, versus the reduced shear rate. It appears that for sufficiently high electric fields, the shear rate can have a finite value, $\dot{\gamma}^*$, while the applied shear stress is zero.

To calculate the velocity profile in the rectangular capillary, we suppose that the capillary width (along x-direction), ℓ, is much larger than its thickness (along z-direction), e, so that the velocity and the stress tensor, except for the pressure terms, depend only on the variable z (see Fig. 3). In that case, the pressure, p, depends only on y.
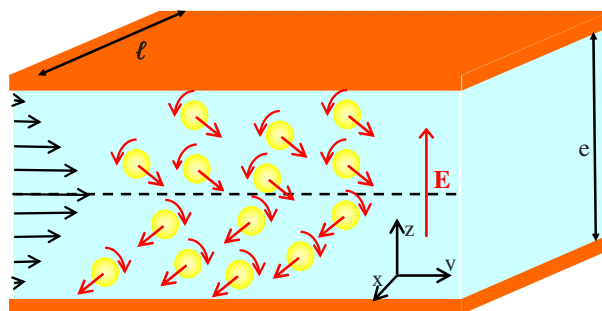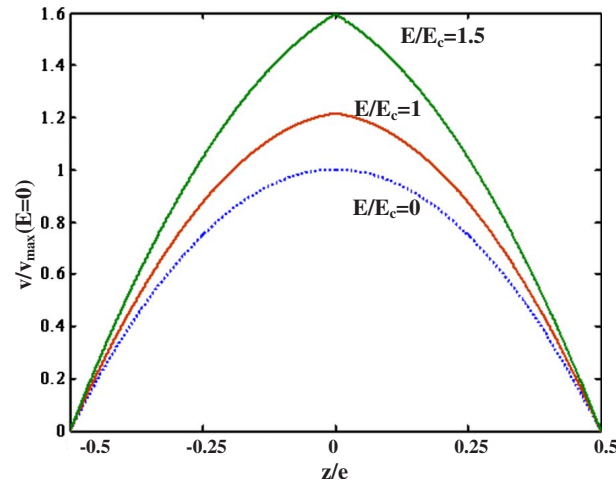

FIG. 3. Flow of a suspension in a rectangular channel.

FIG. 4. Theoretical velocity profiles of a suspension containing a solid volume fraction of 5% and flowing between two plates. The velocities have been normalized by the maximum velocity in absence of an electric field, $v_{max}(E=0)$.

The balance equation for linear momentum reads as

$$-\frac{dp}{dy} + \frac{d\sigma}{dz} = 0, \tag{9}$$

where $\sigma_{yz}(z) = \sigma(z)$ is the shear stress. Equation (9) simplifies by supposing that $\sigma(-z) = -\sigma(z)$,

$$\sigma = \frac{dp}{dy}z. \tag{10}$$

Once the rheological constitutive law which depends on the electric filed intensity, $\dot{\gamma} = f_E(\sigma)$ (a), is deduced from Eq. (7), the velocity profile can be computed,

$$v_y(z) = \int_{e/2}^{z} \dot{\gamma}(z_1)dz_1 = \int_{e/2}^{z} f_E\left(\frac{dp}{dy}z_1\right)dz_1. \tag{11}$$

Figure 4 shows the profiles deduced from the expression (8). As expected, Quincke rotation is responsible for an increase of the suspension linear velocity and as the field intensity increases, the velocity profile becomes sharper. The singular point at $z=0$ originates in the cancellation of the shear stress (or equivalently of the effective viscosity) for a finite shear rate. Indeed, at $z=0$, the shear stress equals zero [see Eq. (10)] while the shear rate is expected to be $+\dot{\gamma}^*$ at $z=0^+$ and $-\dot{\gamma}^*$ at $z=0^-$. This discontinuity in the shear rate is accompanied by an inversion of the particle angular velocity [see Fig. 3 and Eq. (8)]. In the following we present some experiments which have been carried out in order to verify these predictions.

III. EXPERIMENTAL SET-UP

The velocity profile of a suspension flowing through a rectangular capillary is measured thanks to a method of ultrasonic speckle velocimetry. The experimental device is presented in Fig. 5.
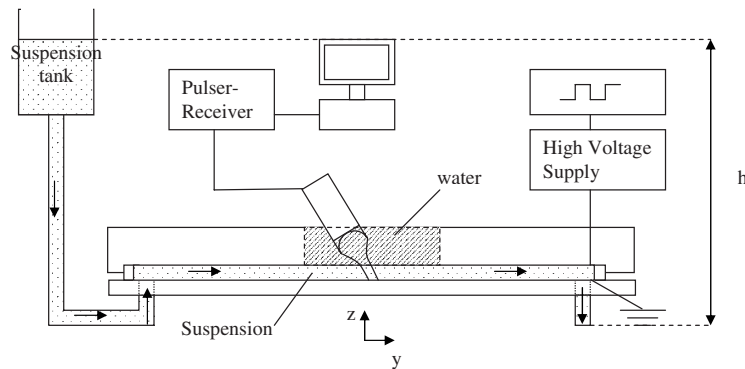
FIG. 5. Experimental device.

A. Materials

The suspensions is made of poly(methyl methacrylate) particles (Microbeads CA6–6) (diameter 6 μm, $\varepsilon_2 = 2.4\varepsilon_0$, density $\rho_p = 1.18 \times 10^3$ kg m^{-3}) dispersed in a mixture of transformer oil (Dielec S, Hafa France) and Ugilec (Elf Atochem). The following properties of the suspending liquid have been measured at T=22 °C: $\varepsilon_1 = 3.7\varepsilon_0$ and η_1 =16.5 mPa s. Its density $\rho_1 = 1.14 \times 10^3$ kg m^{-3} is close to that of the particles. Its conductivity has been raised to $\gamma_1 = 5.4 \times 10^{-8}$ S m^{-1} upon addition of an ionic-surfactant (AOT salt, sodium dioctylsulfosuccinate, Sigma Aldrich). The particle conductivity is small enough ($\gamma_1 \approx 10^{-14}$ S m^{-1}) to consider them as insulating. Accounting for the electric characteristics of the particles and of the suspending liquid, we deduce the values of the critical field and of the Maxwell time: $E_c = 1800$ V/mm and $\tau_M = 1.6$ ms. The volume fraction of the solid particles is $\phi = 5 \times 10^{-2}$ and the viscosity of the suspension, $\eta_s = 19.3$ mPa s, has been measured with a controlled stress rheometer Carrimed CSL 100. The particle volume fraction has been chosen in such a way that the effect of Quincke rotation on the material rheology is sufficiently high without inducing too much ultrasound multiple scattering that would have made the measurement of the velocity profile impossible.

B. Flow geometry

The suspension flows in a rectangular channel, $\ell = 1.5$ cm in width and e=1 mm in thickness. The upper and lower walls of the tube are made of PET films, 175 μm in thickness, coated with a conducting indium tin oxide layer, and glued on a rigid Plexiglas plate. The coated PET films serve also as electrodes so that the electric field is applied along the velocity gradient direction. They are connected to a high voltage supply (Trek 610E) that is fed by a 0.5 Hz square wave signal from a generator (Agilent 33120A). Two holes in one electrode wall, L=22 cm apart, 2 mm in diameter, let the suspension flow in and out of the tube. The pressure drop across the channel is controlled by placing the tank containing the suspension at a height h=17.5 cm above the capillary which lies on a horizontal plane.

C. Pulsed ultrasonic Doppler velocimetry

The velocity profile measurement method is very similar to that precisely described in [Manneville *et al.* (2004)]. The principle of the method is quite simple: a focused ultrasonic transducer emits a pulse wave toward the tube in which the suspension flows [Fig.
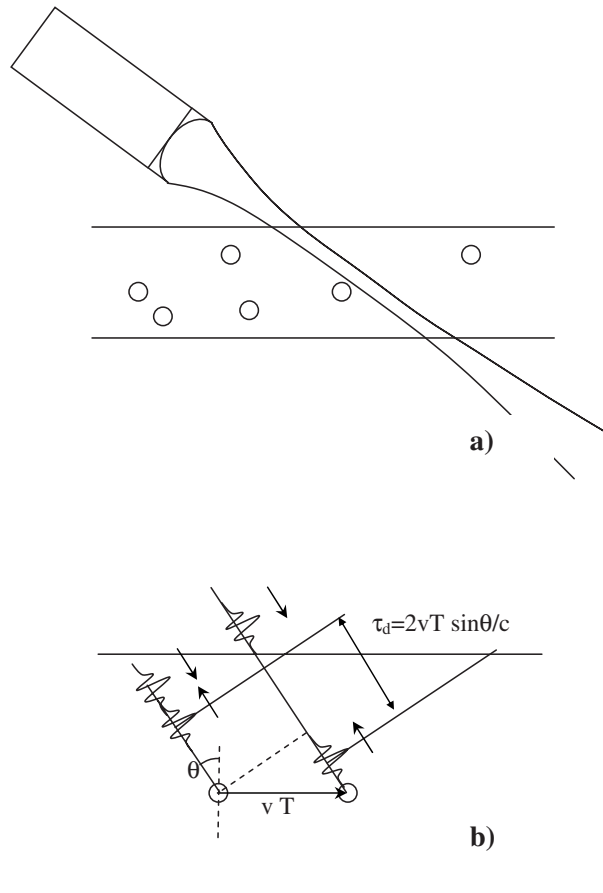
FIG. 6. Principle of pulsed ultrasonic Doppler velocimetry measurement. (a) Focalized ultrasonic beam. (b) Delay time, τ_d, between two successive echoes.

6(a)]. Each particle scatters the wave back to the transducer that works as a receiver as well. As shown in Fig. 6(b), if a particle moves with a velocity v and two pulses are sent at time interval T, their echoes will be received at a time interval $T + \tau_d$, where τ_d is related to the distance traveled by the particle during the time interval T,

$$\tau_d = \frac{2vT \sin \theta}{c},$$ (12)

with θ being the angle between the acoustic wave propagation direction and the normal of the capillary wall and c being the sound velocity in the suspending liquid.

As a consequence, measuring the time delay is equivalent to measure the particle velocity. Moreover, the z-position of the scattering particle in the tube is deduced from the lapse of time between the emitted and received pulses. The measurement of the delay time for all the positions in the tube gives the velocity profile in the medium.

Because a single pulse is scattered by a large number of particles, the received signal is the superposition of all scattered pulses, resulting in a speckle signal, each part of it corresponding to a position in the tube (Fig. 7). In order to process such wave forms and extract the velocity profile, two signals corresponding to two sent pulses are divided in windows of width Δt. If each window from a pulse is labeled by its central time $k\Delta t/2$ (two successive windows overlap), the kth window corresponds to a propagation distance
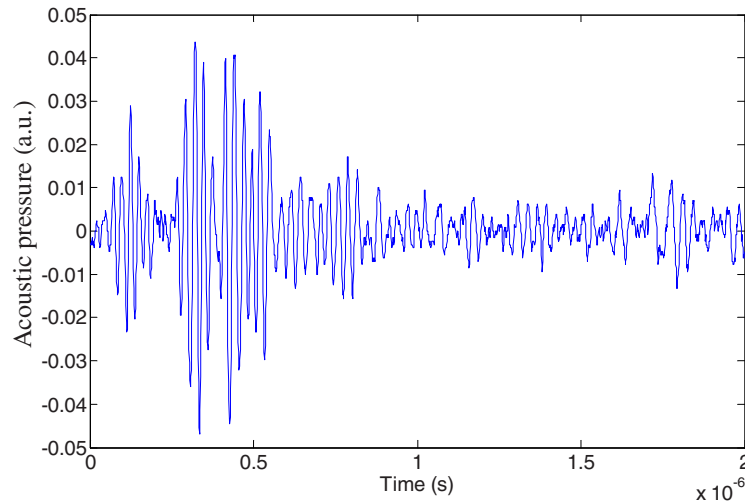
FIG. 7. Typical example of the scattered signal.

in the suspension $ck\Delta t/4$, so that it can be regarded as the signal scattered by the particles that are at a distance $ck\Delta t/4$ from the tube wall. The delay time between the reception of two successive windowed pulses, τ_d, is determined by the maximum of the correlation function of the windowed signals. Thus, only two successive speckle signals are in principle necessary to obtain the complete velocity profile. Actually, the velocity profile is averaged over 400 pairs of pulses.

The spatial resolution along the acoustic beam is given by the time window width $\Delta x = c\Delta t/4$. We chose $\Delta t = 100$ ns $\approx 3.6/f$, where $f = 36$ MHz is the central frequency of the emitted pulse, so that the spatial resolution is approximately the central wavelength of the pulse $\lambda \approx 40$ μm.

As shown in Fig. 5, a hole is made in the upper Plexiglas plate and the transducer is immersed in a water tank in order to avoid any large impedance mismatch. The broadband PVDF ultrasound transducer (Panametrics PI-50-2, actual central frequency 36 MHz) has an active element of 6.35 mm in diameter and a focal length of 12.7 mm, and the focal spot over which the beam has a constant section is approximately 1 mm long in the axial direction and 90 μm in lateral dimension. It is mounted on a precision rotation stage that allows the measurement of the angle θ_0 between the transducer axis and the direction normal to the capillary wall. It can be translated thanks to a linear stage so that the focal spot coincides with the tube gap. The transducer is fed by a high voltage pulse from a pulser-receiver (Panametrics 5073 PR, ultrasonic bandwidth 75 MHz), which amplifies the back-scattered signal and sends it to a high frequency PCI digitizer board (Acqiris DP 235, 1 GS/s, 0.5 GHz, 4 Mb on-board memory). The digital signal is then loaded to the computer for further processing. The repetition frequency $1/T$ varies between 3 and 6 kHz, depending on the highest velocity in the tube.

The sound velocity in the suspending liquid is not known accurately, but it is not really necessary. First, the quantity that allows one to extract the velocity from the delay time, τ_d, is $c/\sin(\theta)$, which is related to the component of the wave vector parallel to the tube wall. It is well known that this quantity is continuous across any interface so that $c/\sin\theta = c_0/\sin\theta_0$, where c_0 is the sound velocity in the water in which the transducer is
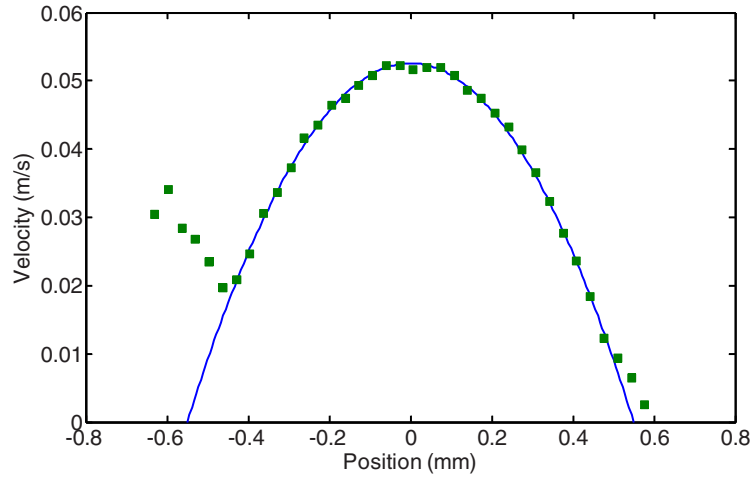
FIG. 8. Velocity profile obtained with a suspension containing a solid volume fraction of 5%. Symbols correspond to the measurements while the solid line is the parabolic fit.

immersed and θ_0 is the angle between the transducer axe and the tube wall on the water side. Both quantities are precisely known: $c_0 = 1488$ m s^{-1} at room temperature, T $= 22$ °C, and all the measurements were performed with $\theta_0 = 18°$.

The z-position of the particles in the capillary is deduced from the delay time between the emission and the reception of a single pulse. We assume that the distance between the upper capillary wall and the scattering particle is proportional to this delay time. As a consequence, only the times at which the pulse enters and exits the channel are to be known. In that purpose, the velocity profile versus delay time is fitted to a parabolic Poiseuille flow, when no electric field is applied, and the times at which the fitting curve cancels give the position of the walls.

IV. EXPERIMENTAL PROCEDURE AND RESULTS

A. Measurement of the profile in the absence of an electric field

During 30 s, the suspension flows in the tube and is collected in a vessel for weighing. The acoustic measurement is performed after 15 s. The level in the tank is controlled and h does not drop below 17 cm (h$= 17.5$ cm at the beginning). The velocity profiles are first measured when no electric field is applied in order to determine the wall position and the hydraulic resistance of the suspension feeding system (tube from the reservoir to the capillary, connection of the tube with the capillary, etc.).

First, the velocity profile measured without applying any electric field is fitted to a parabolic curve and the position of the wall is determined (Fig. 8). It should be stressed that the part of the curve close to the lower wall ($-e/2 < z < 0$) is affected by the sound reflection against the wall.

The viscosity of the suspension, $\eta_s = 19.3 \times 10^{-3}$ Pa s, has been measured with a controlled stress rheometer Carrimed CSL 100. Since for such a low particle volume fraction, $\phi = 5\%$, the suspension exhibits a Newtonian behavior, the velocity profile in the channel is expected to be parabolic

$$v_y = - \frac{e^2}{8\eta} \left(1 - \left(\frac{2z}{e} \right)^2 \right) \frac{dp}{dy}, \tag{13}$$

leading to the flow rate

$$Q = -\frac{\ell e^3}{12\eta}\frac{dp}{dy} = \frac{\ell e^3}{12\eta L}\Delta p, \tag{14}$$

where L is the length of the tube, ℓ is its width, e is its thickness, and Δp is the pressure drop over the length of the capillary. The Reynolds number of the flow is taken as $R_e = \rho Q/(\eta \ell) \approx 2$. The entry length based on the thickness, e, of the pipe is $l_{ent} = R_e e \approx 4$ mm. The entry length based on the width, ℓ, of the channel can be computed as approximately 60 cm. So, the measurement of the velocity profiles 15 cm beyond the capillary entry is meaningful and the hypothesis of a two-dimensional (2D) flow is quite correct.

The flow rate is computed from the velocity profile $Q_{ac} = 5.8 \times 10^{-7}$ m^3 s^{-1} and compares well to the flow measured by weighing $Q = 6.06 \times 10^{-7}$ m^3 s^{-1}. From Q_{ac}, the pressure gradient in the pipe can be evaluated and the hydraulic resistance of the rest of the circuit can be deduced

$$R_h = \frac{\rho gh}{Q} - \frac{12\eta L}{\ell e^3} = 8.2 \times 10^8 \text{ Pa m}^{-3} \text{ s.} \tag{15}$$

R_h is to be compared to the hydraulic resistance of the channel when no electric field is applied

$$R_c = \frac{12\eta L}{\ell e^3} = 2.6 \times 10^9 \text{ Pa m}^{-3} \text{ s.} \tag{16}$$

Since R_h is of the same order of magnitude as R_c, it is necessary to take it into account when the knowledge of the pressure drop across the capillary is needed. In particular, when an electric field is applied in the capillary, its hydraulic resistance is changed since the apparent viscosity of the suspension is reduced while R_h is expected to be almost constant.

B. Measurement of the profile in the presence of an electric field

Rather than a true dc electric voltage, we apply a 0.5 Hz square wave voltage to the electrodes in order to avoid the polarization of the electrodes and the depletion of the electric charges in the tube. The time required to perform one measurement is smaller than 1 s. Thus, it is possible to measure the velocity profile for each polarity of the electric field. No general difference has been noticed between the two polarities, suggesting that no significant migration of the particles under the action of the electric field takes place. The mean profile is then computed. The velocity profiles for different electric field intensities are represented by the symbols in Fig. 9. As expected, the Quincke rotation of the particles results in a decrease of the effective viscosity, i.e., an increase of the flow rate, together with a deviation of the profile from the simple parabolic Poiseuille law.

C. Comparison to rheometric data

To check the consistency of this result with other rheometric experiments, we compute the expected velocity profiles from the relation between shear rate and shear stress that has been measured in a rheometer for a suspension submitted to the same E field intensities. The rheometric measurements were carried out with a controlled stress rheometer, Carrimed CSL 100, in Couette flow geometry. The coaxial cylinders also serve as electrodes so that the electric field is applied along the velocity gradient direction (radial direction). A high voltage is applied to the outer stator while the inner rotor is grounded to the earth through an electrode dipping in a mercury reservoir situated at the top of the
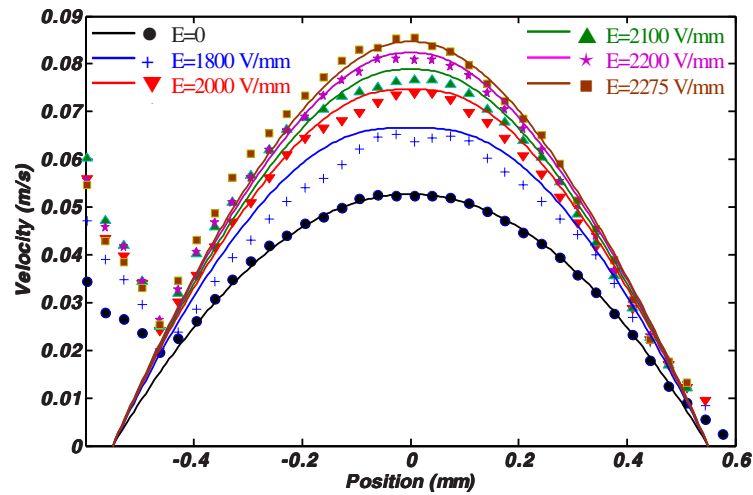
FIG. 9. Velocity profiles obtained for different electric field intensities. Symbols correspond to the acoustic measurements while the lines are the profiles deduced from the rheometric data.

rotation axis of the rheometer. The gap between the two cylinders (1 mm) is narrow compared to their radii (14 and 15 mm) so that the flow can be approximated by a simple shear flow. The variation of the viscosity with the shear rate is shown in Fig. 10 for the different intensities of the electric field. These experimental results agree qualitatively with the predictions of the model [Fig. 2(a)]. In particular, the concordance between experimental data and theoretical values of the viscosity is satisfactory at high shear rates. A discrepancy appears for low values of the shear rate: while the model predicts a negative effective viscosity, the measured viscosity remains positive and even exceeds its zero electric field value for the smallest shear rates. In a previous paper [Pannacci *et al.* (2007b)], we have attributed this behavior to a structuring of the suspension.
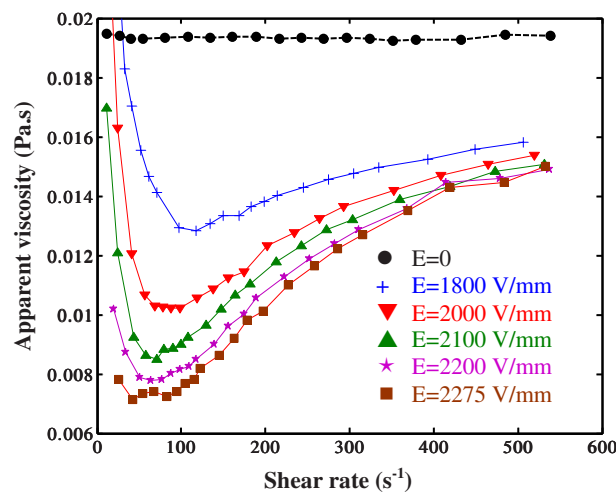

FIG. 10. Variation of the effective viscosity with the shear rate measured with a controlled stress rheometer in Couette geometry for different field intensities.

To compute the expected velocity profiles, we need to know the pressure drop across the channel. Its value is obtained by writing that the total pressure drop is the sum of the pressure drop in the capillary and in the rest of the device

$$\rho gh = L\frac{dp}{dy} + QR_h. \tag{17}$$

Then, using Eq. (11), the flow rate is deduced

$$Q = 2\ell \int_0^{e/2} \left(\int_{e/2}^{z} f_E\left(\frac{dp}{dy}z_1\right)dz_1 \right)dz = \frac{\ell e^2}{2\sigma_w^2} \int_{\sigma_w}^{0} f_E(\sigma)\sigma d\sigma, \tag{18}$$

where $\sigma_w = (e/2)(dp/dy)$ is the wall shear stress. Equations (17) and (18) together lead to the following equation:

$$\int_{\sigma_w}^{0} f_E(\sigma)\sigma d\sigma = \frac{2L}{R_h \ell e^2}\sigma_w^2\left(\frac{2}{e}\sigma_w + \frac{\rho gh}{L}\right). \tag{19}$$

Using the rheometric data, Eq. (19) is solved numerically to obtain the wall shear stress, σ_w. From σ_w, the pressure gradient is deduced and its value is injected in Eq. (11) to compute the expected velocity profiles. They are displayed together with the profiles obtained from acoustic measurement in Fig. 9 where a clear agreement should be noted.

V. DISCUSSION

Thanks to ultrasonic speckle velocimetry, we have been able to measure the flow profiles of a suspension flowing in a rectangular channel and to evidence the role played by the particle electrorotation. The theoretical model predicts that the viscosity is zero when the suspension is subjected to a zero-shear stress at the center of the capillary. This leads to a singular point in the velocity profile. Experimentally, the velocity profiles do not exhibit any singularity but appear to be flatter than the parabola around $z=0$. This is consistent with the rheometric measurements of Fig. 10 which, as noted in Sec. IV C, display a high viscosity value at very low shear rate. Nevertheless, the direct measurement of a negative effective viscosity or zero effective viscosity is difficult because it is supposed to arise when the shear stress is so low that it is hard to control it with a classical rheometer. Consequently, the measurement of the flow profile offers a promising way of measuring such a zero viscosity.

The measurement of the flow profile should also offer information on the possible effects of nonzero spin viscosity on the flow of such a micro-polar fluid. A nonzero spin viscosity introduces a coupling between the linear momentum and internal angular-momentum balance equations [Rosensweig (1997)]

$$-\boldsymbol{\nabla}p + 2\varsigma(\phi)\boldsymbol{\nabla} \times \boldsymbol{\omega} + (\eta(\phi) + \varsigma(\phi))\boldsymbol{\nabla}^2\mathbf{v} = \mathbf{0},$$

$$\tag{20}$$

$$\frac{\phi}{\frac{4}{3}\pi a^3}\mathbf{P} \times \mathbf{E}_0 + 2\varsigma(\phi)(\boldsymbol{\nabla} \times \mathbf{v} - 2\boldsymbol{\omega}) + \eta'(\phi)\boldsymbol{\nabla}^2\boldsymbol{\omega} = \mathbf{0},$$

where ς is the vortex viscosity that actually appears in Eq. (8) to account for the anti-symmetric part of the stress tensor

$$\mathsf{s} = \frac{\frac{3}{2}\phi}{1-\phi}\eta_1.$$ (21)

The spin viscosity η' is expected to be of the functional form: $\eta' = \eta_1 \mathsf{a}^2 \mathsf{f}(\phi)$ [Rosensweig (1997); Feng *et al.* (2006)]. Consequently, the internal angular momentum diffusion term in Eq. (20) depends on the parameter $(\mathsf{a}/\mathsf{e})^2$. In our experiment, the value of this parameter $((\mathsf{a}/\mathsf{e})^2 \approx 10^{-5})$ is 10^6 times larger than in the case of a ferrofluid flow $((\mathsf{a}/\mathsf{e})^2 \approx 10^{-11})$.

Furthermore, according to the theoretical work of Rinaldi and Zahn (2002) or of Lukaszewicz (1999) where Eq. (20) is solved for various values of the ratio $\eta'/\zeta \mathsf{d}^2$, the effect of the spin viscosity should be observable but weak in our experiment. One order of magnitude of this effect can be obtained by comparing the first and the third terms of the second Eq. (20). From Eqs. (1) and (6), the first term scales as $(6\phi\eta_1\omega/[1+(\omega\tau)^2])$ $\times(E/E_c)^2 \sim 6\phi\eta_1\omega$. The third term can be expressed as $\eta_1(\mathsf{a}/\mathsf{e})^2\mathsf{f}(\phi)\omega$, so that the ratio of the spin diffusion term to the volume electric torque is given by $(\mathsf{a}/\mathsf{e})^2(\mathsf{f}(\phi)/6\phi)$. Following Rosensweig (1997), $\mathsf{f}(\phi) \sim 4(\pi/6\phi)^{2/3}$, leading to 10^{-3} for the sought ratio.

To catch such a small effect, the experiment has to be improved. The accuracy of the velocity measurement seems satisfactory although the use of a pulser-receiver with a higher signal to noise ratio would be valuable. We plan also to achieve a better control of the flow parameters. In particular, the true pressure gradient in the channel will be measured thanks a technique that we used previously and that consists in mounting pressure sensors on the capillary walls [Lemaire *et al.* (2006)]. Moreover, in Sec. IV A, the entry length based on the channel width ℓ has been evaluated to be four times the channel length. ℓ should be increased to make this entry length much larger than the capillary length ensuring that the 2D approximation is correct at the channel center. Finally, we plan to use a suspension with a suspending liquid whose conductivity is lower than in the present experiment. Then, the critical electric field intensity, E_c, which varies as the square root of the electrical conductivity (see Sec. II A) will be lowered and the intensities of the electric field we can apply without observing dielectric breakdown would be much higher than E_c that is a condition for a significant change in the rheological behavior of the suspension.

ACKNOWLEDGMENTS

References

Bacri, J. C., R. Perzynski, M. I. Shliomis, and G. I. Burde, "Negative viscosity effect in a magnetic fluid," Phys. Rev. Lett. **75**, 2128–2131 (1995).

Brenner, H., "Rheology of two-phase systems," Annu. Rev. Fluid Mech. **2**, 137–176 (1970).

Cebers, A., "Some peculiarities of the transfer phenomena in suspensions with internal rotations," Prikl. Mat. Mekh. **42**, 673–678 (1978).

Condiff, D. W., and J. S. Dahler, "Fluid mechanical aspects of antisymmetric stress," Phys. Fluids **7**, 842–854 (1964).

Dahler, J. S., and L. E. Scriven, "Angular momentum of continua," Nature (London) **192**, 36–37 (1961).

Eringen, A. C., "Theory of micropolar fluids," J. Math. Mech. **16**, 1–18 (1966).

PRESSURE-DRIVEN FLOW OF A MICRO-POLAR FLUID   325

Feng, S., A. L. Graham, J. R. Abbot, and H. Brenner, "Antisymmetric stresses in suspensions: Vortex viscosity and energy dissipation," J. Fluid Mech. **563**, 97–122 (2006).

Jones, T. B., "Quincke rotation of spheres," IEEE Trans. IAS **IA-20**, 845–849 (1984).

Jones, T. B., *Electromechanics of Particles* (Cambridge University Press, London, 1995).

Korlie, M. S., A. Mulkhrjee, B. G. Nita, J. G. Stevens, A. D. Trubatch, and P. Yecko, "Analysis of flows of ferrofluids under simple shear," Magnetohydrodynamics **44**, 51–59 (2008).

Lemaire, E., L. Lobry, and N. Pannacci, "Flow rate increased by electrorotation in a capillary," J. Electrost. **64**, 586–590 (2006).

Lemaire, E., L. Lobry, N. Pannacci, and F. Peters, "Viscosity of an electro-rheological suspension with internal rotations," J. Rheol. **52**, 769–783 (2008).

Lukaszewicz, G., *Micropolar Fluids* (Birkhauser, Boston, 1999).

Manneville, S., L. Becu, and A. Colin, "High frequency ultrasonic speckle velocimetry in sheared complex fluids," Eur. Phys. J.: Appl. Phys. **28**, 361–373 (2004).

Melcher, J. R., "Electric field and moving media," IEEE Trans. Educ. **17**, 100–110 (1974).

Pannacci, N., E. Lemaire, and L. Lobry, "How insulating particles increase the conductivity of a suspension," Phys. Rev. Lett. **99**, 094503 (2007a).

Pannacci, N., E. Lemaire, and L. Lobry, "Rheology and structure of a suspension of particles subjected to Quincke rotation," Rheol. Acta **46**, 899–904 (2007b).

Pérez-Madrid, A., T. Alarcon, J. M. G. Vilar, and J. M. Rubi, "A mesoscopic approach to the negative viscosity effect in ferrofluids," Physica A **270**, 403–412 (1999).

Quincke, G., "Ueber rotationen im constanten electrischen felde," Ann. Phys. Chem. **295**, 417–486 (1896).

Rinaldi, C., F. Gutman, X. He, A. D. Rosenthal, and M. Zahn, "Torque measurements on ferrofluid cylinders in rotating magnetic fields," J. Magn. Magn. Mater. **289**, 307–310 (2005).

Rinaldi, C., and M. Zahn, "Effects of spin viscosity on ferrofluid flow profiles in alternating and rotating magnetic fields," Phys. Fluids **14**, 2847–2870 (2002).

Rosensweig, R. E., *Ferrohydrodynamics* (Dover, Mineola, 1997).

Rosensweig, R. E., "Stress boundary-conditions in ferrohydrodynamics," Ind. Eng. Chem. Res. **46**, 6113–6117 (2007).

Secker, P. E., and I. N. Scialom, "A simple liquid-immersed dielectric motor," J. Appl. Phys. **39**, 2957–2961 (1968).

Shliomis, M. I., and I. M. Konstantin, "Negative viscosity of ferrofluid under alternating magnetic field," Phys. Fluids **6**, 2855–2861 (1994).

B.3 Size effect in Quincke rotation : A numerical study

Size effect in Quincke rotation: A numerical study

F. Peters, L. Lobry, A. Khayari, and E. Lemaire[a)]
LPMC, CNRS Université de Nice, 06 10/8 Nice Cedex 2, France

This paper deals with the Quincke rotation of small insulating particles. This dc electrorotation of insulating objects immersed in a slightly conducting liquid is usually explained by looking at the action of the free charges present in the liquid. Under the effect of the dc electric field, the charges accumulate at the surface of the insulating particle which, in turn, acquires a dipole moment in the direction opposite to that of the field and begins to rotate in order to flip its dipole moment. In the classical Quincke model, the charge distribution around the rotor is supposed to be purely superficial. A consequence of this assumption is that the angular velocity does not depend on the rotor size. Nevertheless, this hypothesis holds only if the rotor size is much larger than the characteristic ion layer thickness around the particle. In the opposite case, we show thanks to numerical calculations that the bulk charge distribution has to be accounted for to predict the electromechanical behavior of the rotor. We consider the case of an infinite insulating cylinder whose axis is perpendicular to the dc electric field. We use the finite element method to solve the conservation equations for the positive and the negative ions coupled with Navier–Stokes and Poisson equations. Doing so, we compute the bulk charge distribution and the velocity field in the liquid surrounding the cylinder. For sufficiently small cylinders, we show that the smaller the cylinder is, the smaller its angular velocity is when submitted to a dc electric field. This size effect is shown to originate both in ion diffusion and electromigration in the charge layer. At last, we propose a simple analytical model which allows calculating the angular velocity of the rotor when electromigration is present but weak and diffusion can be neglected. © *2009 American Institute of Physics*. [DOI: 10.1063/1.3134046]

I. INTRODUCTION

When a nonconducting particle immersed in a low conducting liquid is submitted to a sufficiently high dc field, it can rotate spontaneously around itself along any axis perpendicular to the electric field. This symmetry break is known as Quincke[1] rotation from the name of the man who first observed it at the end of the 19th century. As explained by Secker and Scialom[2] and later by Melcher,[3] the mechanism responsible for Quincke rotation deals with the action of the free electric charges which are contained in the liquid. Indeed, when the E field E_0 is applied, the charges contained both in the liquid and in the particle migrate under Coulombic force. Then, as stated by Jones,[4] depending on the relative magnitude of the charge relaxation times in the liquid and in the particle, the superficial charge distribution which builds at the particle/liquid interface is equivalent to a dipole P, which is either in the direction of the field or in the opposite direction. In the following, we will call P the retarded dipole moment since, as it is associated with the charge distribution at the particle/liquid interface, it evolves with a finite characteristic time, named Maxwell–Wagner time, τ_{MW}.

The charge relaxation times in the liquid τ_1 and in the particle τ_2 are given by the ratio of the permittivity ε_i to the conductivity σ_i, $i=1,2$ refers to the liquid and the particle, respectively. When $\tau_2 < \tau_1$, the induced dipole is along the E field direction and the configuration is stable. In the opposite

case, i.e, $\tau_2 > \tau_1$ (for instance, when an insulating particle is immersed in a conducting liquid), the dipole P, which has been created by the accumulation of the charges at the particle/liquid interface is opposite to the E field direction [Fig. 1(a)]. In this last case, if the particle is slightly rotated, the deviation of its dipole moment P produces a torque $\Gamma^E = P \times E_0$, which tends to increase the angular tilt further. So, if the E field intensity is high enough for the electric torque to balance the viscous resistant torque exerted by the surrounding liquid on the particle, the particle will rotate continuously around itself with an axis pointing in any direction perpendicular to the dc field [Fig. 1(b)]. A noteworthy feature of Quincke[1] rotation is that the angular velocity of the particle is expected not to depend on its size.

Quincke[1] rotation has many implications on mechanical systems. Dielectric motors consisting of a cylindrical rotor placed between two plane electrodes have been proposed.[2,5] The behavior of an ensemble of particles undergoing Quincke[1] rotation is also of interest. These past few years, we have been working on the consequences of Quincke[1] rotation on the electrical and mechanical behaviors of a suspension. In particular, we have demonstrated that the particle rotation can be responsible for a sensitive increase of the conductivity of a suspension[6] since the particle rotation facilitates the ion migration. On the other hand, the particle rotation causes a substantial decrease of the apparent viscosity of a suspension.[7] These two effects have been both demonstrated with suspensions containing particles whose diam-
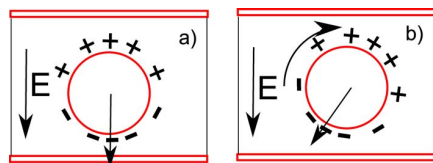
a)Electronic mail: elemaire@unice.fr.

130, 194905-1

FIG. 1. (Color online) If the charge relaxation time is larger in the particle than in the liquid, the superficial charge distribution is equivalent to that of a dipole in the direction opposite to the dc E field (a). The particle starts rotating to flip its dipole in the field direction. In stationary regime, the dipole forms a constant nonzero angle with the field (b).

FIG. 2. An insulating cylinder (symmetry axis along *z*) is submitted to a dc electric field pointing in the (−*x*) direction.

eter is comprised between 50 and 100 μm. It would be interesting to decrease the particle size since the control of the conductivity or of the viscosity of a suspension may have valuable applications in xerography where the pigments are submicronic.[8] Also, it may be of interest to use a single particle as a micromotor in microfluidics devices.[9]

A priori, following the classical model used to predict the electromechanical behavior of a particle undergoing Quinke rotation, the size of the particle does not play any role. Nevertheless, a common hypothesis made in this model consists in assuming that the electric charge distribution created by the field around the particle is purely superficial. One can wonder if this hypothesis remains valid whatever the particle size. Indeed, because of thermal diffusion, the thickness of the charged layer around the particle is *a priori* expected to be of the order of the Debye[10] length $\sqrt{D\tau_1}$ where D is the thermal diffusion coefficient of the ions whose typical value in the nonpolar fluids we study is 2.5×10^{-11} m^2 s^{-1} (typically, the viscosity of the fluid is 10 mPa/s and the ion size 1 nm). Since the order of magnitude of the charge relaxation time is comprised between 1 and 100 ms, the charge layer thickness is expected to be in the range of one tenth of a micron up to 1 μm. As a consequence, one can guess that the rotation of small particles should depend on their size if not much larger than the charge layer thickness. The purpose of the present paper is to study numerically this size effect in Quincke[1] rotation.

While various theoretical and numerical studies deal with the ac electrorotation of colloidal particles dispersed in an aqueous medium,[11–13] the microscopic analysis of a small particle undergoing Quincke[1] rotation has never been addressed. For the sake of simplicity, we will carry out a two-dimensional (2D) numerical study where the rotation of an infinite cylinder whose revolution axis is perpendicular to the applied dc electric field will be considered. Furthermore, only the case of a perfectly insulating cylinder will be considered in the numerical study. In the first part, the usual model of Quincke[1] rotation is reminded. In the second part, we present the electrohydrodynamic equations which have been used to determine the ions distribution around the insulating cylinder and the velocity field in the liquid. The following section is devoted to the presentation of the finite elements method, used to solve the above equations and of the main results concerning the dependence of the cylinder spin rate on its diameter. At last, we propose an analytical extension of the classical Quincke[1] rotation model by accounting for the charge electromigration inside the ionic
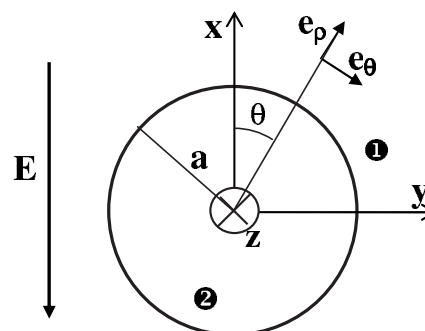
layer around the cylinder and we analyze the numerical results thanks to this modified Quincke[1] rotation model.

II. CLASSICAL TREATMENT OF QUINCKE ROTATION IN TWO DIMENSIONS, MACROSCOPIC DESCRIPTION

We consider an infinite cylinder (radius a, conductivity σ_2, permittivity ε_2) immersed in a dielectric liquid (viscosity η, conductivity σ_1, permittivity ε_1) and subjected to a dc E field perpendicular to its revolution axis: $E_0 = -E_0 e_x$ (Fig. 2). As described in the introduction, the rotation of the cylinder is explained by the action of the electric field on the charges which have accumulated at its surface. The electric field exerts on the charges that are supposed to be stuck on the cylinder an electric torque (per cylinder unit length) that is written as

$$\Gamma^E = a^2 \int_0^{2\pi} \gamma_e(\theta) E_{1\theta}(\rho = a, \theta) d\theta e_z, \tag{1}$$

where γ_e is the surface charge distribution.

A conservation equation for the surface charge can be obtained performing a charge balance on an elementary surface, $dS = adz d\theta$ of the cylinder. The time variation in the charge contained on dS is given by the sum of two terms:

(a) The difference of the conduction currents outside and inside the cylinder, crossing dS: $(\sigma_2 E_2 - \sigma_1 E_1) e_\rho dS$.

(b) The current coming from the displacement of the interfacial charges carried by the rotation of the cylinder: $-\partial/\partial\theta(\gamma_e \Omega a dz) d\theta$ where Ω is the angular velocity of the cylinder around (Oz).

We then obtain

$$\frac{\partial \gamma_e}{\partial t} = \left[\sigma_1 \frac{\partial \Phi_1}{\partial \rho} - \sigma_2 \frac{\partial \Phi_2}{\partial \rho} \right]_{\rho=a} - \Omega \frac{\partial \gamma_e}{\partial \theta}, \tag{2}$$

where Φ_1 and Φ_2 denote the electrostatic potentials outside and inside the cylinder which can be split up into two parts: the instantaneous potential created by the charges that are present on the electrodes surface $\Phi_{1,2}^\infty$ and the electric potential associated with the superficial charge distribution $\Phi_{1,2}^\gamma$.

Assuming that the charge distribution is dipolar, the potentials are written as

$$\Phi_1^\infty = \left(\rho - A \frac{a^2}{\rho} \right) E_0 \cos\theta,$$

$$\Phi_2^\infty = \rho(1 - B) E_0 \cos\theta,$$

$$\Phi_1^\gamma = C \frac{a^2}{\rho} E_0 \cos(\theta - \theta_0),$$

$$\Phi_2^\gamma = D \rho E_0 \cos(\theta - \theta_0),$$
$$(3)$$

where θ_0 is the direction of the dipole moment created by the charge distribution and A, B, C, and D are constants. All these five quantities are determined from Eq. (2) and the boundary conditions

$$\Phi_1^\infty(\rho = a) = \Phi_2^\infty(\rho = a),$$

$$\Phi_1^\gamma(\rho = a) = \Phi_2^\gamma(\rho = a),$$

$$0 = \left[\varepsilon_2 \frac{\partial \Phi_2^\infty}{\partial \rho} - \varepsilon_1 \frac{\partial \Phi_1^\infty}{\partial \rho} \right]_{\rho=a},$$
$$(4)$$

$$\gamma_e = \left[\varepsilon_2 \frac{\partial \Phi_2^\gamma}{\partial \rho} - \varepsilon_1 \frac{\partial \Phi_1^\gamma}{\partial \rho} \right]_{\rho=a}.$$

Finally, in the stationary regime, we obtain

$$A = B = \beta^\infty,$$

$$C = D = -\frac{\beta^0 - \beta^\infty}{\sqrt{1 + \Omega^2 \tau_{\text{MW}}^2}},$$
$$(5)$$

$$\theta_0 = \arctan(\Omega \tau_{\text{MW}}), \quad \text{and} \quad \gamma_e = -(\varepsilon_1 + \varepsilon_2) C E_0 \cos(\theta - \theta_0),$$

where $\tau_{\text{MW}} = \varepsilon_1 + \varepsilon_2 / \sigma_1 + \sigma_2$ is the Maxwell–Wagner time which is the characteristic time for the interfacial charge (or equivalently for the dipole moment) to relax and $\beta^\infty = \varepsilon_2 - \varepsilon_1 / \varepsilon_1 + \varepsilon_2$ and $\beta^0 = \sigma_2 - \sigma_1 / \sigma_1 + \sigma_2$ are the Clausius–Mossotti factors of the cylinder at high and zero frequency, respectively.

In stationary state, the electric torque (Eq. (1)) is balanced by the resistant viscous torque exerted by the fluid on the cylinder

$$\mathbf{\Gamma}^{\mathsf{H}} = -\alpha\Omega,$$
$$(6)$$

where $\alpha = 4\pi\eta a^2$ is the rotational friction coefficient of the cylinder (per unit length), η being the liquid viscosity.

The stationary behavior of such a Quincke[1] rotor has been widely studied and shows some interesting features: the rotation of the cylinder depends on a threshold value of the electric field intensity E_c and, above this critical value, the particle rotates around itself with an axis pointing in any direction perpendicular to the field

$$\Omega = \frac{1}{\tau_{\text{MW}}} \sqrt{\left(\frac{E_0}{E_c} \right)^2 - 1} \quad \text{with} \quad E_c$$

$$= \sqrt{\frac{-2\eta}{\tau_{\text{MW}} \varepsilon_1 (\beta^0 - \beta^\infty)}}.$$
$$(7)$$

Furthermore, as mentioned in the introduction, this model predicts that the angular velocity of the cylinder does not depend on its diameter. In the following, we will show that this model is valid only if the thickness of the charge distribution around the cylinder is thin enough compared to the cylinder diameter and if the ion diffusion and electromigration can be neglected on the cylinder size scale.

III. MICROSCOPIC ANALYSIS

A. Balance equations

Modeling Quincke[1] rotation where electric field and fluid dynamic effects are coupled is based on the combination of continuum equations for the electric and the flow fields in the bulk with balance equations for the ion density.[14] The bulk charge distribution around the cylinder and the fluid velocity field are determined upon solving the charge conservation equations and the Navier–Stokes equation in the liquid. Some simplifying assumptions are made: the conductivity of the cylinder is considered to be much smaller than that of the liquid so that $\sigma_2 \approx 0$ and the dielectric constants of the cylinder and of the liquid are assumed to be equal: $\varepsilon_1 = \varepsilon_2 = \varepsilon$. Furthermore, we will restrict our study to low polar materials for which there exist a dynamical equilibrium between free ions and ionic pairs

$$(A^+ B^-) \underset{k_d}{\overset{k_r}{\rightleftharpoons}} A^+ + B^-,$$
$$(8)$$

where k_r and k_d are, respectively, the recombination and the dissociation constants which, at thermodynamic equilibrium, are related by

$$k_d c_0 = k_r n_0^2,$$
$$(9)$$

where $c_0 = [A^+ B^-]$ and $n_0 = n_+ = n_- = [A^+] = [B^-]$, at thermodynamic equilibrium. Following Debye,[10]

$$k_r = \frac{e_0(K_+ + K_-)}{\varepsilon} (1 - \exp(-l_B/a_i))^{-1}$$

where e_0 is the elementary charge, $l_B = e_0^2 / 8\pi\varepsilon kT$ is the Bjerrum length, and a_i is the distance between ions in an ionic pair (k being the Boltzmann constant and T, the temperature). K_+ and K_- are the electrophoretic mobilities of the positive and negative ions which, in the following, are assumed to be the same: $K_+ = K_- = K$.

In nonpolar fluids, most of the ions are associated in ionic pair ($c_0 \gg n_0$) and $l_B \gg a_i$ so that the recombination constant reduces to the Langevin[15] constant for gases

$$k_r \approx 2 K e_0/\varepsilon.$$
$$(10)$$

The ion conservation equation for the positive and the negative species is written as:[14]

$$\frac{\partial n_{\pm}}{\partial t} + \nabla \cdot [n_{\pm}(v \mp K \nabla \Phi) - D \nabla n_{\pm}] = k_d c - k_r n_+ n_-.$$
(11)

In this equation, v is the velocity of the fluid and D is the ionic diffusion coefficient which has been chosen equal for both the positive and the negative ions. c is the concentration of the neutral species. In the following, it will be considered that, everywhere, the ion concentration c is equal to c_0 and also to the initial concentration of electrolyte added to the liquid, since, as usual in low polar liquids, the dissociation coefficient is supposed to be small.

The charge density and the electric potential must satisfy Poisson's equation

$$\nabla \cdot (\varepsilon \nabla \Phi) = - e_0(n_+ - n_-).$$
(12)

At last, the fluid flow is governed by the Navier–Stokes equation and the continuity equation for an incompressible fluid

$$\rho_f \frac{\partial v}{\partial t} + \rho_f(v \cdot \nabla)v = -\nabla p + \eta \nabla^2 v - e_0(n_+ - n_-) \nabla \Phi,$$
(13)

$$\nabla \cdot v = 0,$$
(14)

where p is the pressure and ρ_f, the fluid density.

In a nondimensional form, Eqs. (11)–(14) become

$$\Omega \tau_r \frac{\partial \tilde{n}_{\pm}}{\partial \tilde{t}} + \Omega \tau_r \tilde{\nabla} \cdot (\tilde{n}_{\pm} \tilde{v}) \mp \frac{\tau_r}{\tau_m} \tilde{\nabla} \cdot (\tilde{n}_{\pm} \tilde{\nabla} \tilde{\Phi}) - \frac{\tau_r}{\tau_D} \tilde{\nabla}^2 \tilde{n}_{\pm}$$

$$= 1 - \tilde{n}_+ \tilde{n}_-,$$
(15)

$$\tilde{\nabla}^2 \tilde{\Phi} = - \frac{\tau_m}{2\tau_r}(\tilde{n}_+ - \tilde{n}_-),$$
(16)

$$\mathcal{R}e\left(\frac{\partial \tilde{v}}{\partial \tilde{t}} + (\tilde{v} \cdot \tilde{\nabla})\tilde{v}\right) = -\tilde{\nabla}\tilde{p} + \tilde{\nabla}^2 \tilde{v} - \frac{r\tau_m}{2\Omega \tau_r^2}(\tilde{n}_+ - \tilde{n}_-)\tilde{\nabla}\tilde{\Phi},$$
(17)

$$\tilde{\nabla} \cdot \tilde{v} = 0,$$
(18)

where the dimensionless variables are: $\tilde{t} = \Omega t$, $\tilde{\rho} = \rho/a$, $\tilde{v} = v/a\Omega$, $\tilde{n}_{\pm} = n_{\pm}/n_0$, $\tilde{\Phi} = \Phi/aE_0$, and $\tilde{p} = p/\eta\Omega$. $\mathcal{R}e = \rho_f \Omega a^2/\eta$ is the Reynolds number, $r = (E_0/E_c)^2$ where E_c is the threshold field defined in Eq. (7). Beside $1/\Omega$, 3 time scales appear in Eqs. (15)–(17). $\tau_r = \varepsilon/\sigma_1 = \tau_{\mathrm{MW}}/2$ is the charge relaxation time, $\tau_D = a^2/D$ is the characteristic time for the tangential diffusion around the cylinder. At last, $\tau_m = a/KE_0$ is the characteristic time for ion electromigration around the cylinder.

Considering Eqs. (15)–(17), it is worth noting that $1/\tau_m$ and $1/\tau_D$ represent the magnitude of the electromigration flux and of the tangential diffusion flux, respectively.

B. Orders of magnitude

Now we shall see how the above characteristic times compare to each other for different cylinder sizes. Besides the cylinder size, various physical parameters of the liquid

TABLE I. Variation in the three characteristic times with the radius of the rotor. The electric field intensity is 10^6 V/m and the physical parameters used to calculate these times are: $\varepsilon_1 = \varepsilon_2 \approx 2\varepsilon_0$, $\sigma_1 \approx 10^{-8}$ S/m, $\eta \approx 10^{-2}$ Pa s, $K \approx 10^{-9}$ m^2 V^{-1} s^{-1} and $D \approx 2.5 \times 10^{-11}$ m^2 s^{-1}.

Cylinder radius (μm)	1	2.5	10	100
$\tau_r = \dfrac{\varepsilon}{\sigma}(s)$	1.8×10^{-3}	1.8×10^{-3}	1.8×10^{-3}	1.8×10^{-3}
$\tau_m = \dfrac{a}{KE_0}(s)$	10^{-3}	2.5×10^{-3}	10^{-2}	10^{-1}
$\tau_D = \dfrac{a^2}{D}(s)$	4×10^{-2}	0.25	4	400

appear in these characteristic times. In the following, we will fix them to the typical values they have in the systems we use to study experimentally:[6,7] $\varepsilon \approx 2\varepsilon_0$, $\sigma_1 \approx 10^{-8}$ S/m, $\eta \approx 10^{-2}$ Pa s, $K \approx 10^{-9}$ m^2 V^{-1} s^{-1} and $D \approx 2.5 \times 10^{-11}$ m^2 s^{-1}. Using these values we get the intensity of the critical field, $Ec = 5.7 \times 10^5$ V/m and the orders of magnitude of the characteristic times which are reported in Table I for different cylinder radii. It should be noted that whatever the size of the cylinder (comprised between 1 and 100 μm), the diffusion time is always larger than the other ones. But, when the radius of the cylinder becomes as small as 1 μm, the electromigration time and the charge relaxation time are of the same order of magnitude and the diffusion time is only 40 times larger than them. So we expect diffusion to play a role for particles smaller than a few microns and electromigration for particles smaller than a few tens of microns.

C. Numerical study

In this section, we will show how the relative magnitude of the different characteristic times influences the cylinder angular velocity.

1. Numerical technique

The equations have been solved with the software COMSOL MULTIPHYSICS™ for an infinite cylinder. The solutions are supposed to be invariant under translation along the cylinder axis (2D approximation). Using the nondimensional variables of Eq. (15)–(18), the cylinder radius equals 1, and the velocity of the fluid at the surface is purely tangential and equals 1 too. The cylinder is placed at the center of a square box with edge length 40. The boundary conditions in the nondimensional variables are displayed in Fig. 3. J_{n+} and J_{n-} are the components of the flux density of ions normal to the boundary. We note that when the characteristic times are varied, the geometry and the boundary conditions are kept unchanged, while the equations are modified.

The mesh is automatically generated by the software. The number of nodes on the cylinder boundary (circle) is fixed, so as to impose the typical size on an element at this position. We usually work with 4000 nodes on the cylinder boundary. As already mentioned, the smaller length of the problem is the charge layer thickness. With 4000 nodes on the boundary, the typical size of an element is 1.5×10^{-3}, so that, as it will be shown in Sec. IV, the dense layer is always
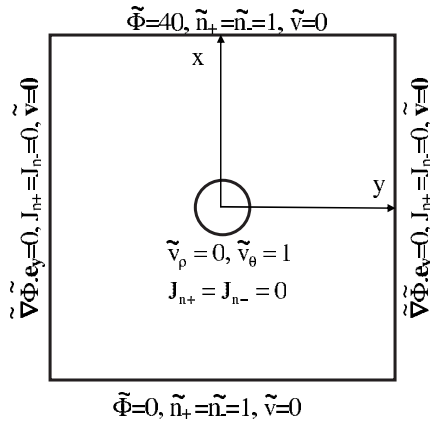
FIG. 3. Boundary conditions for the normalized equations. An insulating cylinder (normalized radius, 1) is placed in a square box (normalized edge length, 40).

FIG. 5. Squared normalized spin rate vs $r=(E_0/E_C)^2$ for different values of τ_m/τ_r and τ_D/τ_r: solid lines: $\tau_D/\tau_r=2000$, dashed lines: $\tau_D/\tau_r=200$, dotted lines: $\tau_D/\tau_r=20$, circles: $\tau_m/\tau_r=20$, triangles: $\tau_m/\tau_r=2$, squares: $\tau_m/\tau_r=0.8$. The thick line corresponds to the predictions of the classical Quincke rotation model.

larger than three or four times this length. Furthermore, we have checked that the mesh density was sufficient to ensure that the result did not depend on the mesh size.

The nonlinear solver performs iterative computation, until the relative error estimate was lower than 10^{-3}, but usually, the final error estimate is lower than 10^{-6}.

2. Numerical procedure

For each set of parameters $\{(E_0/E_c)^2, \tau_m/\tau_r, \tau_D/\tau_r\}$, the angular velocity Ω is increased from zero, and for each value of Ω the solution of Eqs. (15)–(18) is sought and the viscous torque exerted on the cylinder is computed from the fluid velocity field. If the electric field is large enough (higher than a critical value), the viscous torque is positive for low values of Ω, which means that the fluid drives the cylinder (Fig. 4). For increasing values of Ω, the viscous torque cancels and then becomes negative. The spontaneous rotation velocity is the value of Ω for which the viscous torque cancels.

3. Numerical results

As already mentioned, the purpose of the present paper is to evaluate the effect of the rotor size on its angular ve-
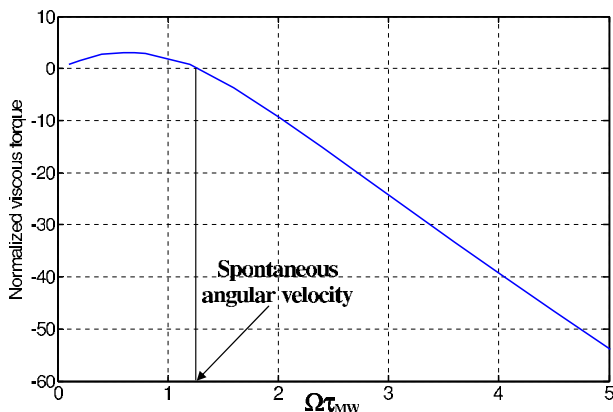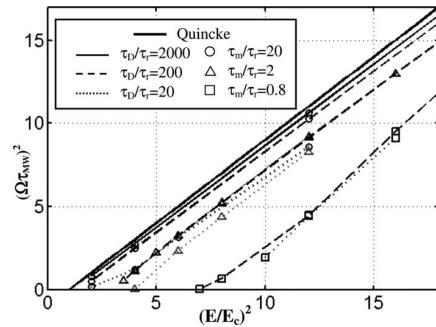

FIG. 4. (Color online) Normalized viscous torque of the cylinder vs its angular velocity. This curve has been obtained for $(E_0/E_c)^2=4$, $\tau_m/\tau_r=2.5$, and $\tau_D/\tau_r=564$.

locity. Nevertheless, as it can be seen in Eq. (15)–(17), the control parameters of the system are the field intensity and the ratios of the electromigration time and of the diffusion time to the charge relaxation time. As a consequence, in a first step, we shall present an analysis of the electromechanical behavior of the cylinder in terms of the characteristic times. After that, we shall focus on the variation in the cylinder spin rate with its diameter, all other parameters being fixed.

First, we examine the variation in the cylinder spin rate as a function of the squared E field intensity for various values of the migration time and of the diffusion time (Fig. 5). One can observe a strong dependence of the angular velocity on both the migration time τ_m and the diffusion time τ_D. The dependence is particularly significant when these two characteristic times are not very large compared to the relaxation time. When it is not the case (i.e., when $\tau_D \gg \tau_r$ and $\tau_m \gg \tau_r$), as expected, the rotor behavior is very close from that predicted by the Quincke[1] rotation model. At constant τ_D, when the migration time decreases, the rotor spin rate is reduced. The same observation can be made when the diffusion time is decreased at constant τ_m (and when τ_D is not much larger than τ_m). The qualitative interpretation to these two observations is straightforward since the tangential diffusion is expected to smooth the angular dependence of the charge density profile and since the ion electromigration around the cylinder will decrease the local charge density. Both effects lead to a decrease of the torque exerted by the E field on the ion distribution.

Since the purpose of this paper is to estimate the influence of the rotor size on the Quincke[1] rotation, let us fix all other parameters: $\eta=10^{-2}$ Pa s, $\varepsilon_1=\varepsilon_2=2\varepsilon_0$, $\sigma_1=10^{-8}$ S/m, $K=10^{-9}$ m^2 V^{-1} s^{-1}, and $D=2.5\times10^{-11}$ m^2 s^{-1} ($E_c \approx 570$ V/mm and $\tau_r \approx 1.8$ ms) and let us vary the cylinder radius. The dependence of the cylinder squared spin rate as a function of the normalized squared electric field intensity for different cylinder sizes ($a=2.5, 3, 5$ and 10 μm) is shown by the symbols (the meaning of the lines will be given in the next section) in Fig. 6. In this representation, the control parameters which are kept constant along each curve of the Fig. 6 are τ_D and the product $r\tau_m^2$.

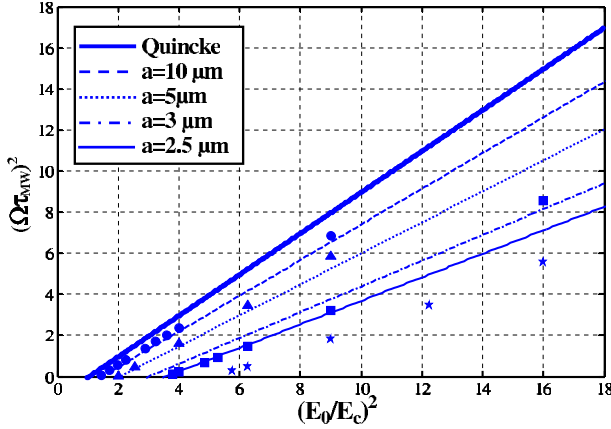An interesting feature to note on this figure is that, what-

FIG. 6. (Color online) Squared normalized spin rate vs $r=(E_0/E_C)^2$ for different values of the cylinder radius. The lines correspond to the predictions of the model and the symbols to the numerical computations: circles, dashed line: $a=10$ μm $(r(\tau_m/\tau_r)^2=100)$; triangles, dotted line: $a=5$ μm $(r(\tau_m/\tau_r)^2=25)$; squares, dot-dashed line: $a=3$ μm $(r(\tau_m/\tau_r)^2=11)$; stars, solid line: $a=2.5$ μm $(r(\tau_m/\tau_r)^2=6.25)$. The thick line corresponds to the predictions of the classical Quincke rotation model.

ever the size of the rotor, the qualitative dependence of the angular velocity on the field intensity is the same as in the classical Quincke[1] model

$$\Omega = \frac{1}{\tau^*_{\mathrm{MW}}} \sqrt{\left(\frac{E_0}{E^*_c}\right)^2 - 1}$$

where E^*_c and τ^*_{MW} are function of the parameters $r\tau^2_m$ and τ_D or equivalently of the cylinder radius but do not depend on the electric field intensity. The smaller the cylinder radius is, the lower its angular velocity: the critical field increases and the slope of the curves decreases when the size decreases.

Besides this qualitative description, it should be stressed that, in the parameter range we have considered, the tangential diffusion time is always much higher than both the charge relaxation and electromigration times (for $a=2.5$ μm, $\tau_D/\tau_r=140$ and $57<\tau_D/\tau_m<228$ for $E_c<E_0<4E_c$; for $a=10$ μm, $\tau_D/\tau_r=2200$ and $228<\tau_D/\tau_m<912$). Therefore, consistently with Fig. 5, the tangential diffusion is not expected to play a significant role. On the opposite, τ_m is of the same order of magnitude as τ_r ($0.4<\tau_m/\tau_r<1.7$ for $a=2.5$ μm and $1.7<\tau_m/\tau_r<6.9$ for $a=10$ μm). As a consequence, one can guess that the rotor angular velocity is mainly controlled by the electromigration. In the following section we show how to account for the tangential electromigration flux in the prediction of the cylinder angular velocity.

IV. DISCUSSION

In this section, we propose a simple analytical model which holds in the case of negligible tangential diffusion. We show that the migration flux results in an equivalent surface conductivity which can be included in the classical Quincke[1] model. Let us suppose that the surface charge is distributed in a thin layer around the cylinder so that the ion density is much higher in the layer than in the bulk liquid.

The charge carriers present in this layer are responsible for a local increase of the conductivity. We take it into account by integrating the tangential migration flux over the layer thickness, δ

$$J_S = \int_a^{a+\delta} (n_+ + n_-)eKE_\theta d\rho. \tag{19}$$

This expression is further simplified upon supposing that the tangential electric field is constant within the layer and that, whatever the angular position, one type of charge carrier is predominant so that $n_+ + n_- \approx |n_+ - n_-|$. The migration flux is given by

$$J_S = E_\theta \int_a^{a+\delta} |n_+ - n_-|eKd\rho \approx |\gamma_e(\theta)|KE_\theta, \tag{20}$$

where the second approximate equality assumes that the layer is thin ($\delta \ll a$).

Equation (20) defines a surface conductivity, $\sigma_\Sigma(\theta) = |\gamma_e(\theta)|K$. For the sake of simplicity, we introduce the average surface conductivity

$$\sigma_\Sigma = \sqrt{\langle \gamma_e^2 \rangle_\theta} K. \tag{21}$$

Taking into account this surface conductivity and assuming as in Sec. III that the cylinder is perfectly insulating, Eq. (2) becomes

$$\frac{\partial \gamma_e}{\partial t} = \left[\sigma_1 \frac{\partial \Phi_1}{\partial \rho} \right]_{\rho=a} - \Omega \frac{\partial \gamma_e}{\partial \theta} + \frac{\sigma_\Sigma}{a^2} \left[\frac{\partial^2 \Phi_1}{\partial \theta^2} \right]_{\rho=a}. \tag{22}$$

Looking for a dipolar solution $\Phi_2 \sim \rho \cos(\theta - \theta_0)$, and using the continuity of the electrostatic potential at the cylinder surface, it follows:

$$\frac{1}{a} \frac{\partial^2 \Phi_1}{\partial \theta^2} = -\left[\frac{\partial \Phi_2}{\partial \rho} \right]_{\rho=a}, \tag{23}$$

so that Eq. (22) becomes

$$\frac{\partial \gamma_e}{\partial t} = \left[\sigma_1 \frac{\partial \Phi_1}{\partial \rho} - \frac{\sigma_\Sigma}{a} \frac{\partial \Phi_2}{\partial \rho} \right]_{\rho=a} - \Omega \frac{\partial \gamma_e}{\partial \theta}. \tag{24}$$

Comparing Eqs. (2) and (24), we note that the surface conductivity is equivalent to a bulk conductivity in the cylinder $\sigma_2 = \sigma_\Sigma/a$.[16] Supposing $\varepsilon_1 = \varepsilon_2$ as in Sec. III, Eqs. (5) and (7) together with Eqs. (21) and (24) result in a self-consistent determination of σ_2

$$\frac{\sigma_2}{\sigma_1} = R(\Omega) = \sqrt{2} \frac{\tau_r}{\tau_m} \frac{1-R}{1+R} \frac{1}{\sqrt{1+\left(\frac{\Omega\tau_{\mathrm{MW}}}{1+R}\right)^2}} \left(\frac{\Omega\tau_{\mathrm{MW}}}{1+R}\right)^2$$

$$= r \frac{1-R}{(1+R)^2} - 1. \tag{25}$$

Eliminating Ω in the Eqs. (25), the expression of the normalized equivalent bulk conductivity in the cylinder is obtained
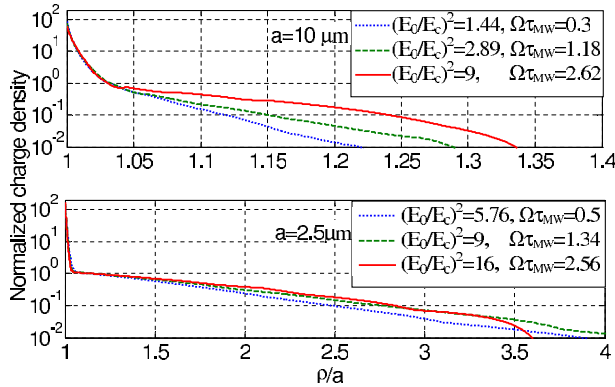
FIG. 7. (Color online) Normalized charge density profile for two values of the cylinder radius. The diffuse layer normalized thickness is far larger in the case of the smallest cylinder.

$$\frac{\sigma_2}{\sigma_1} = \frac{1}{r\left(\frac{\tau_m}{\tau_r}\right)^2}\left(\sqrt{1 + 2r\left(\frac{\tau_m}{\tau_r}\right)^2} - 1 \right). \tag{26}$$

This expression deserves one important remark: the equivalent bulk conductivity is a function of the single parameter $r(\tau_m/\tau_r)^2$. In particular, turning to the physical parameters, $r(\tau_m/\tau_r)^2 = \sigma_1/4\eta K^2 a^2$ so that σ_2/σ_1 does not depend on the electric field intensity, but on the cylinder radius. Thus, for a given rotor size, the angular velocity obeys Eq. (7) with the constant cylinder conductivity (26). We note that τ_D does not appear in Eq. (26). Indeed, the tangential diffusion flux has been neglected.

The results of this model together with the numerical computation are displayed on Fig. 6. First, concerning the intermediate sizes 10 and 5 μm, corresponding to values of $r(\tau_m/\tau_r)^2$ equal to 100 and 25, respectively, the surface conduction model agrees quite convincingly with the fem computation, even as the latter differs sensibly from the Quincke[1] model. However, for high field intensities, we note a slight deviation from the linear behavior. When $r(\tau_m/\tau_r)^2$ decreases and becomes smaller than a typical value of 10, the discrepancies grow up, and the model turns out to be inadequate.

To try to better understand this discrepancy, we can examine the numerical results concerning the radial charge distribution that are displayed in Fig. 7 for two values of the cylinder radius ($a = 10$ μm and $a = 2.5$ μm). It appears clearly that, whatever the angular velocity of the cylinder, the ionic cloud is much more extended when the cylinder is small. More precisely, apart from the very dense and thin layer close to the surface, there exists a diffuse layer which can be much thicker. For instance, the normalized charge density has decayed to about one-thousandth of its surface value at a typical normalized distance of 0.15 for $a = 10$ μm and 1.5 for $a = 2.5$ μm. Furthermore, for this last rotor size, in the direction where the charge density is maximum, only approximately half the charge is contained in the dense layer. In that case, the thin layer approximation may be very crude. In particular, the velocity field of the liquid around the particle, which is coupled to the charge distribution, will be quite different from the $1/\rho$ velocity profile that is supposed to take place in the Quincke[1] rotation model and those results in the viscous torque expression (6). More generally, all the fluxes may play a role in the building of the charge layer. For that reason, it seems difficult to give an analytical description of the system, and even to evaluate the thickness of the layer. Anyway, we have checked that it could be as large as ten times the Debye[10] length ($\sqrt{D\tau_r} = a\sqrt{\tau_r/\tau_D}$).

However, an order of magnitude of the dense layer thickness δ may be obtained by equating the radial diffusion and migration ion fluxes at the insulating cylinder surface

$$Kn_\pm E_0 \sim Dn_\pm/\delta, \tag{27}$$

$$\frac{\delta}{a} \sim \frac{\tau_m}{\tau_D}. \tag{28}$$

Analyzing the numerical computation of the charge profiles, we have been able to confirm that Eq. (28) gives the right order of magnitude for the dense layer thickness. Indeed, in Table II, one can see a comparison between the results provided on one hand by the expression (28) and on the other hand by the analysis of the numerical charge profiles in the direction where the charge density is maximum, for different values of r and a. From a numerical point of view, the layer thickness is evaluated by assuming that the charge density

TABLE II. Thin layer thickness around the rotating cylinder for various cylinder radii and various field intensities: a comparison between the layer thickness obtained thanks to the numerical computation (δ/a) and the order of magnitude resulting from the balance of the radial diffusion and the tangential electromigration fluxes (τ_m/τ_D).

	$r=2$	$r=4$	$r=9$	$r=16$	
$a=10$ μm	2.4×10^{-3}	2.8×10^{-3}	3.6×10^{-3}		δ/a
	3.2×10^{-3}	2.2×10^{-3}	1.5×10^{-3}		τ_m/τ_d
$a=5$ μm	4.8×10^{-3}	4×10^{-3}	4×10^{-3}		δ/a
	6.3×10^{-3}	4.4×10^{-3}	2.9×10^{-3}		τ_m/τ_d
$a=3$ μm		5.6×10^{-3}	4.4×10^{-3}	3.2×10^{-3}	δ/a
		7.4×10^{-3}	4.9×10^{-3}	3.7×10^{-3}	τ_m/τ_d
$a=2.5$ μm			5.2×10^{-3}	4.4×10^{-3}	δ/a
			5.9×10^{-3}	4.4×10^{-3}	τ_m/τ_d

profile is exponential and by dividing its value at the cylinder surface by e, the Euler's number.

Again, for cylinder sizes larger than typically 5 μm, the charge is mainly contained in the thin layer, and the thin layer hypothesis holds. On the opposite, for smaller sizes, both thick and thin layer have to be considered, and the electromechanical behavior of the system has to be studied numerically.

V. CONCLUSION

Using a finite element method, a numerical study of Quincke[1] rotation has been performed in order to evaluate the influence of the rotor size on its angular velocity when subjected to a dc electric field. To solve this problem, the charge conservation equations and the Navier–Stokes and Poisson equations have been written in a nondimensional form where, beside the inverse of the cylinder spin rate, three characteristic times appear: the diffusion time and the ion electromigration time over the rotor radius, and the charge relaxation time. A study of the influence of the magnitude of these different characteristic times has been addressed and it has been shown that both electromigration and diffusion result in a decrease of the angular velocity of the cylinder and an increase of the threshold field. A modified Quincke[1] model has been proposed to calculate analytically the rotor spin rate. This model accounts for the electromigration inside the charge layer which is present around the rotor thanks to an equivalent surface conductivity. Its results agree with the numerical ones if the charge layer thickness is small compared to the cylinder radius. The numerical computation shows that it is the case if the cylinder radius is larger than typically five microns. For smaller particles, the estimation

of the charge thickness may be difficult due to the large number of coupled parameters that play a role (electromigration, diffusion, convection). However, we have shown that the charge layer consists in a dense and thin layer at the cylinder surface surrounded by a diffuse layer whose thickness can be as large as ten times the Debye[10] length.

[1] G. Quincke, Ann. Phys. Chem. **59**, 417 (1896).
[2] P. E. Secker and I. N. Scialom, J. Appl. Phys. **39**, 2957 (1968).
[3] J. R. Melcher, IEEE Trans. Educ. **E-17**, 100 (1974).
[4] T. B. Jones, IEEE Trans. Ind. Appl. **IA-20**, 845 (1984).
[5] T. Coddington, A. F. Pollard, and H. House, J. Phys. D: Appl. Phys. **4**, 1212 (1970).
[6] N. Pannacci, E. Lemaire, and L. Lobry, Phys. Rev. Lett. **99**, 094503 (2007a).
[7] E. Lemaire, L. Lobry, N. Pannacci, and F. Peters, J. Rheol. **52**, 769 (2008).
[8] R. H. Leach, R. J. Pierce, E. P. Hickman, M. J. Mackenzie, and H. G. Smith, *The Printing Ink Manual* (Springer, Netherlands, 2007), Chap. 12.
[9] C. F. Wilson, M. I. Wallace, K. Morishima, G. J. Simpson, and R. N. Zare, Anal. Chem. **74**, 5099 (2002)
[10] P. Debye, Trans. Electrochem. Soc. **82**, 262 (1942).
[11] J. P. Huang, K. W. Yu, G. Q. Gu, Phys. Lett. A **300**, 385 (2002).
[12] H. Zhou, M. A. Preston, R. D. Tilton, and L. R. White, J. Colloid Interface Sci. **285**, 845 (2005).
[13] V. Zimmerman, V. N. Shilov, J. J. Lopez-Garcia, and C. Grosse, J. Phys. Chem. **<**, 13384 (2002).
[14] A. Castellanos, A. I. Zhakin, P. K. Watson, P. Atten, and J. S. Chang, *Electrohydrodynamics* (Springer-Verlag, New York, 1998).
[15] P. Langevin, Ann. Chim. Phys. **28**, 433 (1903).
[16] T. B. Jones, *Electromechanics of Particles* (Cambridge University Press, New York, 1995).

B.4 Experimental observation of Lorenz chaos in the Quincke rotor dynamics

Experimental observation of Lorenz chaos in the Quincke rotor dynamics

François Peters, Laurent Lobry, and Elisabeth Lemaire
Laboratoire de Physique de la Matière Condensée, UMR 6622, Université de Nice-Sophia Antipolis,
06108 Nice Cedex 2, France

In this paper, we report experimental evidence of Lorenz chaos for the Quincke rotor dynamics. We study the angular motion of an insulating cylinder immersed in slightly conducting oil and submitted to a direct current electric field. The simple equations which describe the dynamics of the rotor are shown to be equivalent to the Lorenz equations. In particular, we observe two bifurcations in our experimental system. Above a critical value of the electric field, the cylinder rotates at a constant rate. At a second bifurcation, the system becomes chaotic. The characteristic shape of the experimental first return map provides strong evidence for Lorenz-type chaos. © *2005 American Institute of Physics.* [DOI: 10.1063/1.1827411]

The Quincke rotor experiment consists in studying the rotation of an insulating cylinder immersed in a low conducting liquid and submitted to a dc electric field. This is a classical experiment to illustrate the relaxation of the electric polarization with a finite characteristic time. Until now, only a steady rotation of the Quincke rotor has been predicted and observed. Nevertheless, if the inertia of the rotor is accounted for, its dynamics is governed by two times: In addition to the relaxation time of the polarization, there is a characteristic mechanical time related to the relaxation of the angular velocity. Here we show that the competition of these two characteristic times leads to a complex dynamics of the rotor whose behavior obeys exactly the Lorenz equations. This theoretical assertion is experimentally verified. Indeed, we present the experimental bifurcation diagram of the angular velocity versus the electric field, which exhibits two bifurcations. After the second bifurcation, a chaotic regime takes place. The characteristic shape of the first return map that we build is evidence of Lorenz-type chaos.

I. INTRODUCTION

The spontaneous rotation of an insulating particle immersed in a low conducting liquid and submitted to a high dc electric field was observed as early as 1896 by Quincke.[1] Although this observation is old, an exact interpretation and a quantitative prediction of the angular velocity of the Quincke rotation have only been given in the 1970's.[2,3] The mechanism involved is the following: During their migration from one electrode to the other, the free charges (ions) of the liquid accumulate at the surface of the particle, inducing a dipole moment P. If the charge relaxation time of the liquid is shorter than that of the solid, the direction of P is opposite to that of the field [Fig. 1(a)]. Then, for a field intensity high enough, this configuration is unstable and the particle begins to rotate in order to flip the orientation of the induced dipole along the field direction. The system reaches a stationary state where the electric torque $\Gamma^E = P \times E$ is balanced by the viscous one $\Gamma^v \propto -\Omega$ where Ω is the angular velocity [Fig. 1(b)]. A noticeable property of the Quincke rotation is that the angular velocity does not depend on the particle size. This feature allows one to study either microscopic or macroscopic objects.

The Quincke rotation has recently found a new interest, due to its applications in the field of suspensions. Indeed, this phenomenon has important consequences on the electrical and rheological behavior of suspensions. In recent experiments, we have shown that the spontaneous rotation of the particles makes it easier for the ions to migrate through the suspension, leading to an increase of the apparent conductivity.[4,5] Moreover, if the suspension flows, the collective movement of the particles drives the surrounding liquid and then leads to an important reduction of the apparent viscosity of the suspension.[5–7]

In all these experiments, the rotation of the particles is supposed to be steady. But we have shown recently that the stationary rotation of one isolated particle was not the only possible dynamics. Until now, none of the models of the Quincke rotation has taken into account the inertia of the particle. If it is accounted for, the dynamics of the particle obeys nonlinear equations which are strictly equivalent to the Lorenz equations.[8] So, the Quincke rotation is a very suitable system for the experimental study of the Lorenz chaos. Indeed, only few systems are directly represented by the Lorenz equations. The most famous examples are Rayleigh–Bénard convection[9] and laser dynamics.[10] In both cases, hypotheses on the fields spatial structure are necessary to reduce the number of degrees of freedom of the system. Moreover, the experimental studies on these systems show much richer dynamics than predicted by the Lorenz equations.[11]

In this paper, we present the experimental study of the dynamic behavior of a macroscopic rotor: An insulating cylinder which is free to rotate around its axis of revolution and immersed into a low conducting dielectric liquid. A dc electric field is applied perpendicularly to the axis of the cylinder. Above a threshold value E_c of the electric field, the cylinder rotates at constant velocity either in clockwise or counter-clockwise direction depending on the initial conditions. For even larger field intensities, the angular velocity is
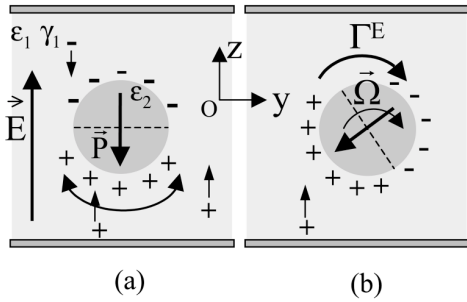
FIG. 1. Illustration of the Quincke rotation: (a) Unstable equilibrium before the rotation starts. The charge accumulation at the surface of the particle induces a dipole P in the direction opposite to the electric field E. (b) Particle in steady rotation. The induced dipole P is no longer aligned along the electric field direction so that the particle undergoes a driving torque.

no longer constant and the rotation direction changes randomly.

In the first part, we establish the dynamic equations for the Quincke rotor. Then, we present the experimental device we have used to study the dynamics of the rotor. Finally, we report the experimental results which unambiguously show that the Quincke rotor dynamics exhibits Lorenz-type chaos.

II. THE ROTOR'S DYNAMICS

We consider the angular motion of a cylinder (radius R, length L) submitted to a dc electric field E perpendicular to its axis. The dynamics of the cylinder can be described by two coupled equations. First, the dipole moment of the cylinder is split into two parts $P_{\text{total}} = \chi_\infty E + P$:

- $\chi_\infty E = 2\pi\varepsilon_1 R^2 L[(\varepsilon_2 - \varepsilon_1)/(\varepsilon_2 + \varepsilon_1)]E$ is the high-frequency polarization of the cylinder that comes from the permittivity mismatch between the cylinder (ε_2) and the liquid (ε_1).
- P is the retarding part of the polarization that comes from the free charge accumulation on the liquid–solid boundary. It obeys a relaxation equation that originates in the conservation of charge at the surface of the cylinder[12]

$$\frac{dP}{dt} = (\Omega \times P) - \frac{1}{\tau_M}(P - (\chi_0 - \chi_\infty)E), \qquad (1)$$

where $\chi_0 E = 2\pi\varepsilon_1 R^2 L[(\gamma_2 - \gamma_1)/(\gamma_2 + \gamma_1)]E$ is the total dipole moment when the system is at rest, γ_1 and γ_2 being the conductivities.

The first term of the right-hand side of Eq. (1) corresponds to the charge convection due to the rotation of the cylinder. The second term is the relaxation of the dipole moment towards its equilibrium value. The characteristic relaxation time for the dipole moment is the Maxwell time

$$\tau_M = \frac{\varepsilon_1 + \varepsilon_2}{\gamma_1 + \gamma_2}. \qquad (2)$$

In the following, we suppose $\chi_0 - \chi_\infty < 0$ (i.e., $\varepsilon_1/\gamma_1 < \varepsilon_2/\gamma_2$). This is the necessary condition for the induced dipole to be opposite to the field direction and for the spontaneous rotation to occur.

The dynamics is also determined by the conservation of the angular momentum which yields the following mechanical equation:

$$I\frac{d\Omega}{dt} = -\alpha\Omega + P \times E, \qquad (3)$$

where I is the inertial moment of the cylinder and $\alpha = 4\pi\eta R^2 L$ its coefficient of viscous friction. This expression of the stationary viscous torque is valid only if the characteristic time τ associated with the angular velocity dynamics is large enough for the liquid velocity to diffuse over a length larger than the cylinder radius[13]

$$\tau \gg \frac{a^2}{\nu}, \qquad (4)$$

where ν is the cinematic viscosity of the liquid.

Let (Ox) be the angular velocity axis, (Oy) and (Oz) the axes perpendicular and along the field direction, respectively (Fig. 1). The projection of Eqs. (1) and (3) on the axes Ox, Oy and Oz gives the following equations:

$$\frac{dP_y}{dt} = -\Omega P_z - \frac{1}{\tau_M}P_y,$$

$$\frac{dP_z}{dt} = \Omega P_y - \frac{1}{\tau_M}(P_z - (\chi_0 - \chi_\infty)E),$$

$$I\frac{d\Omega}{dt} = -\alpha\Omega + P_y E.$$

Introducing the dimensionless variables

$$t^* = \frac{t}{\tau_M}; \quad X = \Omega\tau_M; \quad Y = \frac{\tau_M}{\alpha}P_y E;$$

$$Z = \frac{\tau_M}{\alpha}(P_z - (\chi_0 - \chi_\infty)E)E,$$

we obtain exactly the Lorenz equations

$$\frac{dX}{dt^*} = Pr(Y - X), \qquad (5a)$$

$$\frac{dY}{dt^*} = -XZ + rX - Y, \qquad (5b)$$

$$\frac{dZ}{dt^*} = XY - bZ, \qquad (5c)$$

with the parameters Pr, r and b given by

$$Pr = \alpha\tau_M/I, \quad r = (E/E_c)^2$$
$$\text{with } E_c^2 = -\alpha/(\tau_M(\chi_0 - \chi_\infty)) \text{ and } b = 1. \qquad (6)$$

For this value of the parameter $b = 1$, the Lorenz equations have been studied numerically before. Indeed the dynamic behavior of a chaotic waterwheel (Malkus wheel) is simply described by this set of equations.[14] Consequently, we will not linger over a numerical study but we will only recall the main properties of the solutions of this set of equations[14,15]
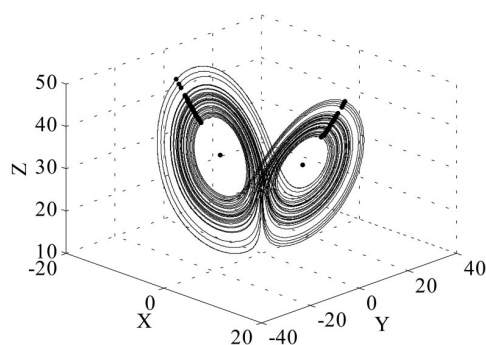
FIG. 2. Phase portrait in the 3D space of the Lorenz system [Eq. (5)] at $Pr=2.5$, $r=33$, and $b=1$.

FIG. 3. The Lorenz system [Eq. (5)] at $Pr=2.5$, $r=33$, and $b=1$. (a) is the Poincaré section deduced from the intersection between the trajectory and the plane $X=Y$ where only the points that verify $|X|>\sqrt{r-1}$ have been represented. (b) is the first return map plotted with each maximum in X verifying $|X|>\sqrt{r-1}$ vs the previous one. (c) is the first return map $|X_{k+1}|=f(|X_k|)$. (d) shows a phase portrait projected onto the X-Z plane. The solid circle is a maximum of X, the open circle is the maximum of Z on the same loop.

and relate them to the physical behavior of the Quincke rotor.

For $r<1$, the origin $(X,Y,Z)=(0,0,0)$ is the only fixed point. It is stable and globally attracting. The cylinder is at rest and the dipole moment P is in the direction opposite to the external field direction. At $r=1$ (i.e., $E=E_c$), the system undergoes a pitchfork bifurcation: The origin becomes unstable and two stable fixed points appear C_+ and C_- whose coordinates are given by

$$(X,Y,Z)_\pm = (\pm\sqrt{r-1}, \pm\sqrt{r-1}, r-1). \tag{7}$$

The angular velocity of the cylinder is constant, and the dipole moment is stationary and tilted away from the field direction. The electric torque is balanced by the viscous torque.

A linear stability analysis of the stationary solutions shows that if $Pr\leqslant 2$, both points C_+ and C_- are stable for any value of r, while if $Pr>2$, C_+ and C_- become unstable for

$$r > r_b = Pr\frac{Pr+4}{Pr-2}. \tag{8}$$

Above this critical value, a chaotic regime occurs. Actually, it is well known that the chaos appears for lower values of r if the initial conditions are far away from the fixed points C_+ and C_- (see Ref. 13 for a detailed numerical study).

On Fig. 2 we display a numerical trajectory of the system in the three-dimensional (3D) phase space for $Pr=2.5$ and $r=33$. This trajectory is typical of the Lorenz attractor: The system cannot reach any steady state but oscillates alternatively around the stationary points C_+ and C_-, without any periodicity. The representation of the trajectory is simplified by the choice of a Poincaré section: The intersection between the trajectory and a particular surface is displayed instead of the trajectory itself. Very often in the literature, the Poincaré section is obtained from the intersection of the trajectory with the surface $XY=Z$ corresponding to the maxima of the variable Z [see Eq. (5c)]. Then, the flow is reduced to the first return map $Z_{k+1}=f(Z_k)$ where Z_k is the Kth maximum of the variable Z.

In this experimental study of the Quincke rotor dynamics, only the first variable X (related to the angular velocity) can be measured. For that reason, we have chosen another Poincaré section that is built from the intersection between the trajectory and the plane $X=Y$ (black points in Fig. 2).
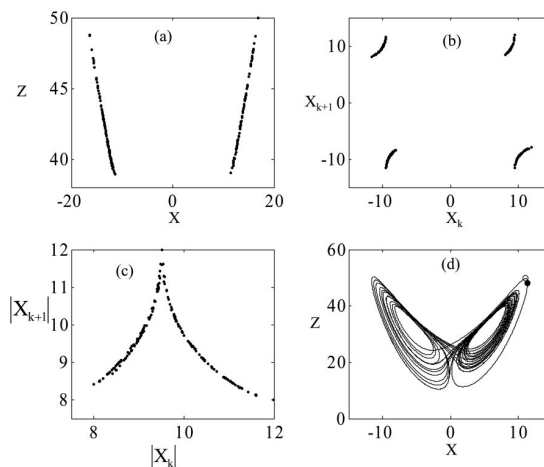
Equation (5a) shows that the points $X=Y$ correspond to the extrema of X. In order to account for only one intersection point per orbit, the Poincaré section is drawn with the ensemble of the extrema of X that verify $|X|>X_c=\sqrt{r-1}$. Figure 3(a) shows this numerical Poincaré section for the trajectory of Fig. 2. The points seem to gather along a one-dimensional curve. It is not completely true, since a finite thickness can be seen if the plot is enlarged. Nevertheless, a point of the section is well defined by the corresponding value of X. From these points, we draw the first return map $X_{k+1}=f(X_k)$ where X_k is the abscissa of the Kth point of the section [Fig. 3(b)]. If rather than $X_{k+1}=f(X_k)$, we plot $|X_{k+1}|=f(|X_k|)$ [Fig. 3(c)], we obtain a first return map which is very similar in shape to the usual map $Z_{k+1}=f(Z_k)$. The similarity of these two mappings is not surprising if one considers the position of the maximum of X (solid circle) or of Z (open circle) on the projection of the trajectory on the plane (X,Z) [Fig. 3(d)]. Both points are visibly associated to the same loop.

III. EXPERIMENTAL SETUP

The rotor is a glass capillary tube (length $L=5$ cm, outer radius $a=1$ mm, inner radius $b=0.5$ mm) mounted on two needle points (Fig. 4). The cylinder is supported by a frame that contains two cavities in which the needle points fit. This mounting allows the cylinder to rotate almost freely around its axis with a very low precession. We have noted that the use of a cylindrical tube rather than a solid cylinder significantly reduces the friction on the bottom (thanks to Archimedes' force which reduces the apparent weight). Furthermore, using a tube reduces the inertia which, as we will see below, allows one to have a value of Pr larger than 2 which is a necessary condition to observe chaos.
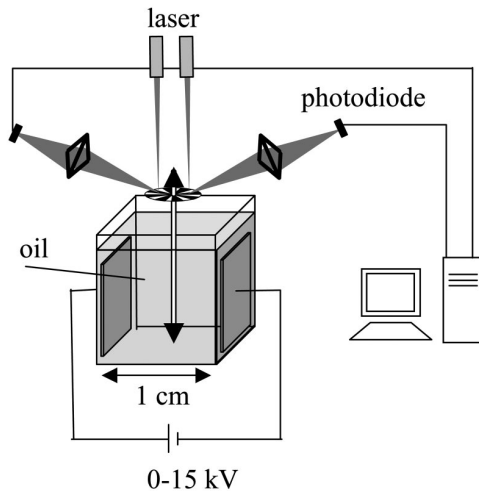
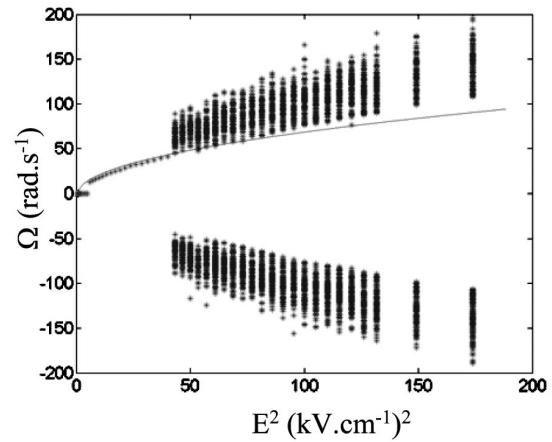FIG. 4. Schematic representation of the experimental setup.

FIG. 5. Bifurcation diagram: For the stationary regime, the angular velocity Ω is plotted vs the square of the electric field intensity. For the chaotic regime, we have reported the maxima of Ω verifying $|\Omega| > \Omega_{st}$. The solid line represents the predicted stationary angular velocity.

The rotor is immersed in transformer oil whose viscosity is $\eta = 14$ mPa s and placed between two square stainless steel electrodes (4 cm long) separated by a 1 cm gap.

In the absence of rotation, the expression of the dipole moment of a tube in an electric field is well known.[16] Identifying the expression of χ_∞ for a tube to that of a solid cylinder, one obtains the effective permittivity of the rotor

$$\varepsilon_2' = \varepsilon_2 \frac{1 + \Delta \dfrac{b^2}{a^2}}{1 - \Delta \dfrac{b^2}{a^2}} \quad \text{with } \Delta = \frac{\varepsilon_0 - \varepsilon_2}{\varepsilon_0 + \varepsilon_2}.$$

Taking 3.8 for the glass permittivity, one obtains $\varepsilon_2' = 2.44$.

To measure the mechanical relaxation time of the rotor, $\tau_{mech} = I/\alpha$, we have applied a mechanical torque and measured the stop-time after the torque is switched off. We have obtained $\tau_{mech} = 60$ ms.

The liquid conductivity is controlled by adding AOT salt [di(2-ethylhexyl sulfosuccinate sodium, Fluka] and has been measured to be $\gamma_1 = 2.65 \times 10^{-10}$ S m^{-1}, the cylinder is supposed to be a perfect insulator ($\gamma_2 = 0$).

To measure the angular position of the rotor, we have used an encoder. A small disc (radius 3 mm, thickness 0.5 mm) with 16 black and white sectors is mounted on the rotor. Two focused lasers provide two light points on the disc. The image of one point on a photodiode detects the crossing of the sectors edges and gives the rotor position. The second light point provides a signal in quadrature phase with the first one, so that the direction of rotation is determined. Consequently, the angular position is coded on 16 values. The signal is sampled at the rate 5 ksample s^{-1} and downloaded to a computer for signal processing. The angular velocity is then evaluated in the following way: For each point, a third degree polynomial fit is performed with six neighboring points. The analytical derivative is then deduced from the resulting polynomial coefficients.

IV. RESULTS AND DISCUSSION

In order to obtain the bifurcation diagram, we proceed as follows: The intensity of the electric field is increased from zero to 13 kV cm^{-1} by step of 250 V cm^{-1}. For each field intensity, we wait during one minute before we record the signals from the photodiodes. The bifurcation diagram is plotted on Fig. 5.

A. First bifurcation

After the first bifurcation, the zero-velocity state becomes unstable and a stable stationary state appears, characterized by an angular velocity that grows up with the field intensity. Due to our experimental procedure (the field is not switched off between two measurement points), the figure shows only one rotation direction. Nevertheless, we have checked that, for repeated experiments, both directions appear with equal probabilities. From Eq. (7), we expect the following expression for the velocity versus the field intensity:

$$\Omega_{st} = \frac{1}{\tau_M} \sqrt{\left(\frac{E}{E_c}\right)^2 - 1}.$$

The corresponding theoretical curve is plotted on the bifurcation diagram (solid line). The parameters τ_M and E_C have been calculated from their theoretical expressions [Eqs. (2) and (6)] which give $\tau_M = 150$ ms and $E_C = 0.97$ kV cm^{-1}. The qualitative behavior is satisfactory although the measured angular velocity is slightly lower than the predictions. Furthermore, the critical field above which the rotation takes place is higher than the predicted one ($E_{C\ exp} = 2.4$ kV cm^{-1}). We impute this discrepancy to the residual solid friction whose effect cannot be neglected for low angular velocities.

B. Second bifurcation

When the field intensity is increased above 6.5 kV cm^{-1}, the angular velocity is no longer constant but, as shown on Fig. 6, becomes erratic: The trajectory consists of loops
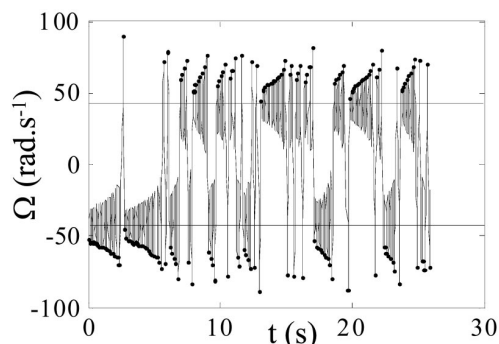
FIG. 6. Angular velocity of the rotor vs time for $E = 6.6$ kV.cm^{-1}. The solid circles correspond to the maxima in Ω that we have used to build the first return map.

around the unstable fixed points ($|\Omega| \approx 45$ rad s^{-1}). The amplitude of the winding around one point grows up until the system starts winding around the other point. On the bifurcation diagram (Fig. 5) we have plotted the maxima of the angular velocity whose absolute value is higher than the stationary value Ω_{st}. The corresponding points are displayed on Fig. 6 (symbols). As explained in Sec. II, these maxima allow us to build the first return map represented on Fig. 7.

This first return map has been obtained for a value of the field intensity just above the second bifurcation: $E = 6.6$ kV cm^{-1}. In spite of the presence of some noise, there is a clear qualitative agreement between the experimental first return map and that obtained by numerically solving the Lorenz equations [Fig. 3(c)]. This gives a rather strong support in favor of Lorenz-type chaos for the Quincke rotor.

Again, the second bifurcation takes place for an electric field a little higher than the predicted one. Indeed, using Eq. (8) with $Pr = \tau_M / \tau_{mecha} = 2.5$, chaos is expected to appear for a critical parameter $r_b = 32.5$ which corresponds to an electric field of 5.5 kV cm^{-1} while its experimental value is 6.5 kV cm^{-1}. Apart from solid friction, these quantitative discrepancies could originate in the nonstationary flow
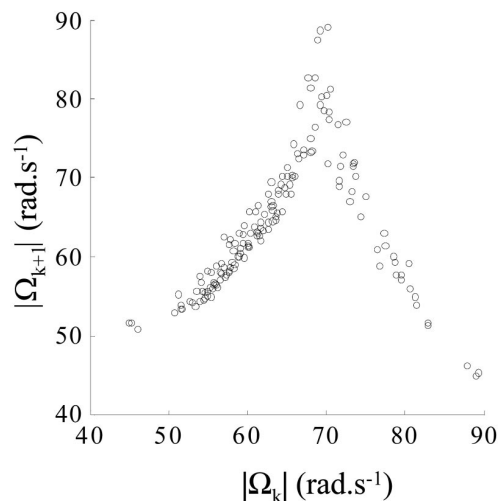
around the cylinder. Indeed, the characteristic time for the velocity to diffuse over a length equal to the cylinder radius is approximately $a^2 / \nu \approx 70$ ms. The characteristic time τ of the cylinder dynamics is estimated from Fig. 6: $\tau = 150$ ms (approximately the Maxwell time). Thus, the condition in Eq. (4) is not completely true.

V. CONCLUSION AND OUTLOOK

The dynamics of the Quincke rotor are qualitatively well described by the Lorenz equations. In particular, in the chaotic regime, we have been able to obtain an experimental first return map which is very similar to the numerical one. The quantitative discrepancies between the experimental and expected critical fields may be explained by residual solid friction and some nonstationary effects in the viscous torque. To overcome this last problem, we project to use more viscous oil in further experiments.

To our knowledge, only few experimental systems display a dynamical behavior that is accurately described by the Lorenz equations without any strong approximation. Furthermore, in the case of the Quincke rotor, the parameters r and Pr can easily be varied, so an important portion of the plane (Pr, r) can be explored. Indeed, in a forthcoming study, we will change the inertia of the rotor, and the viscosity of the liquid in order to vary Pr. We hope to observe other regimes of the dynamics (periodic windows and intermittency). We also plan to study more precisely the second bifurcation, especially by considering the influence of the initial conditions (hysteresis), and of the time variation of the parameter r (bifurcation delay).

Moreover, we will study the influence of the chaotic dynamics on the rheological behavior of a suspension of rotating particles. From a rheological point of view, the mechanical properties of a suspension is expected to depend drastically on the angular motion of the particles. In that case, the shear must be taken into account in the dynamics of one particle, which amounts to breaking the symmetry between clockwise and counterclockwise rotation. Preliminary numerical studies show that chaos appears for larger fields intensity than in the case of an unsheared suspension and that the effective viscosity is enhanced when chaos takes place.

ACKNOWLEDGMENTS

[1] G. Quincke, Annu. Rev. Phys. Chem. **59**, 417 (1896).
[2] J. R. Melcher, IEEE Trans. Educ. **E-17**, 100 (1974).
[3] T. B. Jones, IEEE Trans. IAS **IA-20**, 845 (1984).
[4] A. Cebers, E. Lemaire, and L. Lobry, *2nd International Workshop on Electrical Conduction, Convection and Breakdown in Fluids*, Grenoble, France, edited by P. Atten and A. Denat (2000), pp. 206–208.
[5] A. Cebers, E. Lemaire, and L. Lobry, Magnetohydrodynamics (N.Y.) **36**, 347 (2000).
[6] L. Lobry and E. Lemaire, J. Electrost. **47**, 61 (1999).
[7] A. Cebers, E. Lemaire, and L. Lobry, Int. J. Mod. Phys. B **16**, 2603 (2002).
[8] E. Lemaire and L. Lobry, Physica A **314**, 663 (2002).
[9] P. Bergé, Y. Pomeau, and C. Vidal, *Order within Chaos: Towards a Deterministic Approach to Turbulence* (Wiley, New York, 1986).

FIG. 7. Experimental first return map plotted from the maxima of Ω (solid circles on Fig. 6).

[10]H. Haken, Phys. Lett. **53A**, 77 (1975).
[11]C. P. Smith and R. Dykstra, Opt. Commun. **129**, 69 (1996).
[12]A. Cebers, Mechanics of Liquid and Gas (in Russian) **2**, 86 (1980).
[13]L. D. Landau and E. M. Lifshitz, *Fluid Mechanics* (Butterworth-Heinemann, London, 1987), Sec. 24.

[14]M. Kolar and G. Gumbs, Phys. Rev. A **45**, 626 (1992).
[15]C. Sparrow, *The Lorenz Equations: Bifurcations, Chaos, and Strange Attractors, Applied Mathematical Sciences*, Vol. 41 (Springer-Verlag, Berlin, 1985).
[16]E. Durand, *Electrostatique* (Masson, Paris, 1966), Tome III, p. 247.

Annexe C

Electrophorèse

C.1   Electrophoretic Mobility of Silica Particles in a Mixture of Toluene and Ethanol at Different Particle Concentrations

Electrophoretic Mobility of Silica Particles in a Mixture of Toluene and Ethanol at Different Particle Concentrations

M. Medrano,[†] A. T. Pérez,*,[†] L. Lobry,[‡] and F. Peters[‡]

[†]*Departamento de Electrónica y Electromagnetismo, Universidad de Sevilla, Spain, and*
[‡]*Laboratoire de Physique de la Matière Condensée, CNRS-Université de Nice, France*

In this paper we present measurements of the electrophoretic mobility of colloidal particles by using heterodyne detection of light scattering. The measurements have been made up to concentrations of 5.4% silica nanoparticles, with a diameter on the order of 80 nm, in a mixture of 70% toluene and 30% ethanol. To make possible the measurements at these concentrations, the liquid mixture is chosen so as to match the index of refraction of the particles, thus resulting in a transparent suspension.

Introduction

Particles of various sorts often acquire charge when they are immersed in low conducting liquids. The electric repulsion between the particles contributes to stabilize the suspension. Although this stabilization is in general weaker than for aqueous media, it is important in some industrial areas, such as printing and xerography, and from a fundamental point of view.

The charge on the particle surface induces the accumulation of ions of opposite sign around the particle. This gives rise to a structure known as the double layer. When an electric field is applied to a suspension of charged particles, a force appears on both parts of the double layer. This force moves the particles with respect to the liquid with a velocity proportional to the applied field. The coefficient of proportionality is referred to as the electrophoretic mobility. This phenomenon was observed for the first time by Reuss in 1809. Smoluchowski developed the first theory of electrophoresis for one insulated particle when the zeta potential is small and the particle radius is much larger than the Debye length, $\kappa a \gg 1$ (a is the particle radius and κ^{-1} is the Debye length). His well-known solution for the electrophoretic mobility is

$$\mu_E = \frac{\varepsilon_r \varepsilon_0 \zeta}{\eta} \qquad (1)$$

where μ_E is the electrophoretic mobility, ε_r is the relative permittivity of the liquid, ε_0 is the dielectric permittivity of the vacuum, ζ is the zeta potential, and η is the viscosity of the liquid. However, Hückel obtained the expression for the mobility of particles with a thick double layer ($\kappa a \ll 1$)

$$\mu_E = \frac{2}{3} \frac{\varepsilon_r \varepsilon_0 \zeta}{\eta} \qquad (2)$$

Later, Henry joined both electrophoresis relations within an analytical expression that is valid for a single sphere with small zeta potentials and arbitrary double-layer width. He included the function $f(\kappa a)$ in the Smoluchowski expression $\mu_{Henry} = \mu_{Smol} f(\kappa a)$. Function $f(\kappa a)$ is known as the Henry function, which is 1 when $\kappa a \to \infty$ (Smoluchowski approximation) and $^2/_3$ when

$\kappa a \to 0$ (Hückel approximation). For thick double layers ($\kappa a < 5$), the Henry function is[1]

$$f(\kappa a) = \frac{2}{3} + \frac{(\kappa a)^2}{24} - \frac{5(\kappa a)^3}{72} - \frac{(\kappa a)^4}{144} + \frac{(\kappa a)^5}{144}$$
$$+ \left[\frac{(\kappa a)^4}{12} - \frac{(\kappa a)^6}{144} \right] e^{\kappa a} \int_\infty^{\kappa a} \frac{e^{-x}}{x}\, dx... \qquad (3)$$

Neither the Smoluchowski nor Henry solution includes hydrodynamic interactions between neighboring particles.

For a finite volume fraction, even without taking into account hydrodynamic interactions or double-layer overlap, the electrophoretic mobility depends on the volume fraction for the following reason: when the particle moves in one direction, the same volume of liquid has to move in the opposite direction. This back flow results in a dependence of the mobility on the particle concentration as[2−5]

$$\mu_E(\varphi) = \mu_E(0)[1-\varphi] \qquad (4)$$

where φ is the particle solid fraction.

Additionally, the presence of particles alters the distribution of the applied electric field.[5] In the case of insulating particles, this fact contributes $-^{\varphi}/_2$ to the expression of μ_E

$$\mu_E(\varphi) = \mu_E(0)\left[1 - \frac{3}{2}\varphi + O(\varphi^2)\right] \qquad (5)$$

where $O(\varphi^2)$ denotes terms of order φ^2 and smaller.

Reed and Morrison[6] studied the hydrodynamic interactions for pairs of particles with a thin double layer as a function of the interparticle distance. They showed that hydrodynamic and electric interactions cancel each other when the particles are weakly charged and have the same zeta potential. In that case, eq 5 is expected to describe the electrophoretic mobility.

However, when the particles have a thick double layer, the interaction between them becomes more complex. As a consequence

---

(1) Henry, D. C. *Proc. R. Soc. London, Ser. A* **1931**, *133*, 106.
(2) Anderson, J. L. *J. Colloid Interface Sci.* **1981**, *82*, 248.
(3) Zukoski, C. F., IV; Saville, D. A. *J. Colloid Interface Sci.* **1987**, *115*, 422.
(4) Pérez, A. T.; Lemaire, E. *J. Colloid Interface Sci.* **2004**, *279*, 259.
(5) Ahualli, S.; Delgado, A. V.; Grosse, C. *J. Colloid Interface Sci.* **2006**, *301*, 660.
(6) Reed, L. D.; Morrison, F. A. *J. Colloid Interface Sci.* **1975**, *54*, 117.

*Corresponding author. E-mail: alberto@us.es.

of the interactions, the electrophoretic mobility decreases as φ increases more quickly than predicted by eq 5. In this case, the mobility is[7,8]

$$\mu_E(\varphi) = \mu_E(0)[1 + S\varphi + O(\varphi^2)] \tag{6}$$

where the coefficient S depends on the parameter κa. When κa is smaller than 20, this coefficient decreases quickly. The case of κa as low as 1 has been numerically addressed in Shugai's work.[8] For $\kappa a = 1$, the calculated value of S is much less than $-{}^3/_2$, between -6 and -9, depending on some model details.

For the case of aqueous media, there are some experimental electrophoretic studies where the effect of the particle concentration on the mobility is measured.[3,9] In our work, we focus on nonaqueous systems.

For concentrated suspensions, the use of the electrokinetic sonic amplitude (ESA) effect is a suitable measurement technique.[10] However, ESA works in the MHz range, and the results rely on some theoretical assumptions concerning the generation of sonic waves. Optical techniques are still applicable to concentrated suspensions if the liquid is chosen to match the index of refraction of the particles, rendering the suspension transparent.

We study suspensions of silica in a mixture of ethanol and toluene with the technique of photon correlation spectroscopy (PCS). In spite of the fact that there are some commercial apparatuses available, we have used our own system for two reasons. First, we can apply higher electrical voltages. Second, we have better control of the data analysis.

We will first recall the theoretical background concerning the PCS technique. Then we present the materials and the experimental setup, followed by the experimental results. In the last section, we discuss the results in light of the existing theoretical model and numerical computation based on hydrodynamic interactions and double-layer overlap.

Theoretical Background

Photon correlation spectroscopy (PCS) is a useful method of characterizing colloidal suspensions, micellar systems, and biological materials. In PCS, a light beam is directed toward the sample, and the scattered light is detected with an appropriate device, usually a photomultiplier.

There are two different PCS methods: homodyne and heterodyne. In the homodyne method, only the scattered light impinges on the photocathode. In the heterodyne method, a portion of the unscattered light is mixed with the scattered light on the photomultiplier cathode.

For a set of uncorrelated particles, the autocorrelation function of the light intensity measured by the photomultiplier in heterodyne detection is (see the Appendix for details)

$$C_2(\tau) = 1 + \alpha_2 e^{-\Gamma\tau} \cos(\omega_D\tau) \tag{7}$$

where α_2 is a constant that depends on some experimental parameters, the constant Γ is the product Dq^2, and the Doppler frequency ω_D is defined as

$$\omega_D = \vec{q} \cdot \vec{v} = vq \cos\alpha \tag{8}$$

(7) Ennis, J.; White, L. R. *J. Colloid Interface Sci.* **1996**, *185*, 157.
(8) Shugai, A. A.; Carnie, S. L.; Chan, D. Y. C.; Anderson, J. L. *J. Colloid Interface Sci.* **1997**, *191*, 357.
(9) Reiber, H.; Köller, T.; Palberg, T.; Carrique, F.; Ruiz-Reina, E.; Piazza, R. *J. Colloid Interface Sci.* **2007**, *309*, 315.
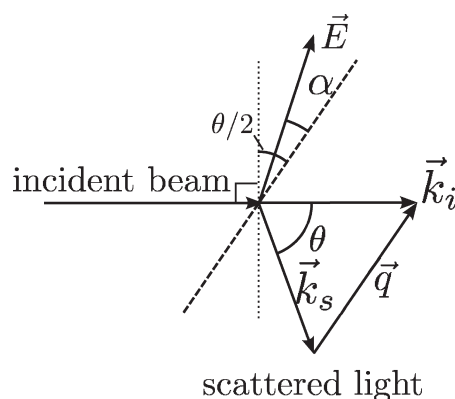(10) Hunter, R. J. *Colloids Surf., A* **1998**, *141*, 37.

Figure 1. Geometry of an electrophoretic light-scattering experiment.
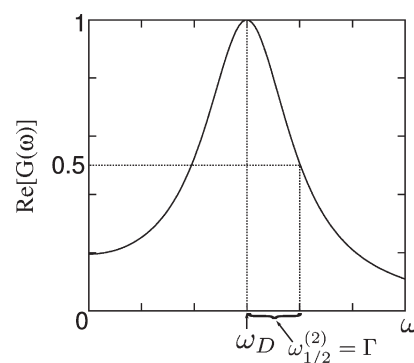

Figure 2. Normalized Fourier transform of the heterodyne correlation function, $C_2(t) - 1$, which shows a peak at the Doppler frequency.

where α is the angle between the scattering vector $\vec{q}$ and the particle velocity $\vec{v}$.

When particles move by electrophoresis, their velocity is $\vec{v} = \mu_E\vec{E}$. If the applied electric field is perpendicular to the incoming beam, then the angle α is $^\theta/_2$ (Figure 1). Then the Doppler frequency is

$$\omega_D = \frac{2\pi n}{\lambda_0}\mu_E E \sin\theta \tag{9}$$

where E is the modulus of the electric field and θ is the angle between the incoming and scattered beams. Here, we have assumed that $|\vec{k}_i| \approx |\vec{k}_s|$; therefore, the scattering vector module is $|\vec{q}| = (4\pi n/\lambda_0)\sin(^\theta/_2)$, where λ_0 is the wavelength in the vacuum of the incoming beam and n is the refraction index of the scattering medium.

To obtain Γ and ω_D, we study the real part of the Fourier transform $G_2(\omega)$ of the correlation function $C_2(\tau) - 1$:

$$\mathrm{Re}[G_2(\omega)] = \alpha_2\left(\frac{\Gamma}{\Gamma^2 + (\omega - \omega_D)^2} + \frac{\Gamma}{\Gamma^2 + (\omega + \omega_D)^2}\right) \tag{10}$$

This function is Lorentzian with the peak placed at ω_D.

If we define the width at midheight, $\omega_{1/2}^{(2)}$, as the frequency at which the value of $\mathrm{Re}[G_2(\omega)]$ is half the maximum value, then eq 10 implies that $\omega_{1/2}^{(2)} = \Gamma$.
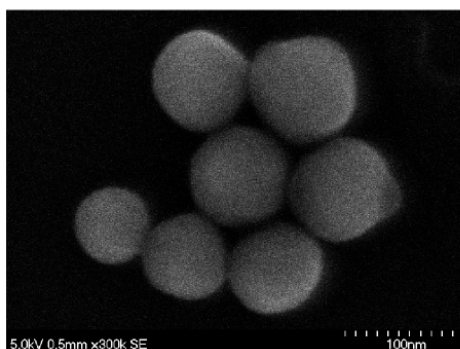
Experiment

Materials. It is often assumed that optical methods are useful only for dilute suspensions, when the sample is transparent. However, it is possible to have a concentrated yet transparent

Article *Medrano et al.*

Figure 3. Micrograph of the particles.

suspension. The requirement is that the refraction index of the liquid matches that of the particle.[11]
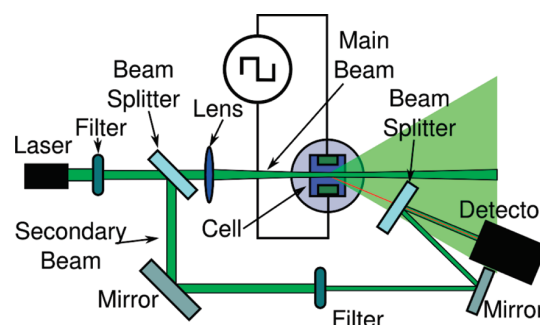
We have synthesized spherical and monodisperse silica nanoparticles by the Stöber method,[12] which consist of hydrolyzed tetraethyl-orthosilicate (TEOS) in ethanol, by using ammonia as a catalyst. The final product is a suspension of silica particles in a solution of ethanol, water, and ammonia. This suspension is called alcosol. The proportion of reactants that we used was 0.5 M TEOS (supplied by Fluka), 0.1 M distilled water, and 0.2 M NH_3 (30%) in absolute ethanol. Ammonia and ethanol were supplied by Panreac.

To prepare the alcosol, we made two different solutions. The first contained 539 mL of ethanol, 22 mL of NH_3, and 31 mL of water. The second had 461 mL of ethanol and 130 mL of TEOS. The second solution was added to the first one while it was being stirred with a magnetic stirrer. The final mixture was stirred for 3.5 h. The reaction yields 0.31 g of silica from 10 mL of alcosol. In the second step, the particle surface was modified with phenyl groups to improve the suspension stability and to increase the hydrophobity of the particle surface.[13] Specifically, we added 2.75 mL of phenyltriethoxysilane supplied by Fluka. We let the reaction stir for 1 day. The polymer forms a layer on the particle surface, providing steric stabilization.

To increase the particle concentration, the suspension is centrifuged at 2000 rpm and the supernatant is removed. After each centrifugation, the suspension was redispersed by sonicating for several minutes. It is important to prevent the particles from forming a compact layer at the bottom of the centrifuge tube because redispersion would be almost impossible to achieve. The next step is to change the remnant liquid by absolute ethanol. To this end, we centrifuged the suspension and replaced the supernatant by ethanol. The solid fraction of silica in absolute ethanol was measured by evaporating a known volume of suspension and by weighing the dried residue. With this procedure, the particle concentration obtained was 18% by volume, where we have taken a silica density of 2.0 g/cm^3.[14]

The particle size was determined by analyzing a set of scanning electron microscopy (SEM) photographs. Figure 3 shows one of these photographs. The diameter obtained was (88 ± 8) nm. The refractive index of the particles is 1.46, and the density is 2.0 g/cm^3.

The suspension of silica in ethanol is completely opaque. This is due to the difference between the particle and the liquid refractive indexes, 1.46 and 1.36, respectively.[14] To match the refractive indexes, the suspending liquid was chosen to be a mixture of toluene (70%) and ethanol (30%).[15] For such a liquid, we did not observe multiple scattering, and the scattering intensity was high enough for measurements to be performed. The conductivity of this mixture was measured to be 6.7 ± 0.3 μS/m, and the relative

(11) Phalakornkul, J. K.; Gast, A. P.; Pecora, R. *Phys. Rev. E* **1996**, *54*, 661.
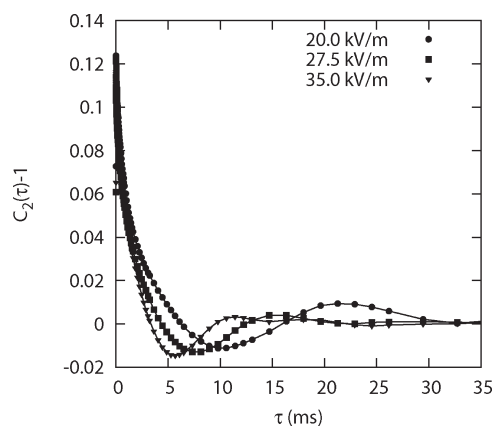(12) Stöber, W.; Fink, A. *J. Colloid Interface Sci.* **1968**, *26*, 62.
(13) Wu, Z.; Xiang, H.; Kim, T.; Chun, M. S.; Lee, K. *J. Colloid Interface Sci.* **2006**, *304*, 119.
(14) Robert, C. W. *Handbook of Chemistry and Physics*; CRC Press: Cleveland, OH, 1974.
(15) Philipse, A. P.; Vrij, A. *J. Colloid Interface Sci.* **1989**, *128*, 121.

Figure 4. Diagram of the experimental setup used for heterodyne detection.

permittivity was 6.8 ± 0.5. Both parameters were measured with a device designed and built by the authors.[16,17]

Experimental Setup. Figure 4 shows a diagram of the experimental setup. The main laser beam is divided into two beams by means of a beam splitter. The first beam comes to the measurement cell, and a lens focuses it at a mid-distance between the cell electrodes. The second beam is led directly to the photomultiplier with the help of two mirrors. On the photomultiplier, the second beam and the light scattered by the sample are mixed together. The electric signal produced by the photomultiplier is sent to the correlator board inside the computer. The correlator counts the number of pulses and computes the autocorrelation function.

A set of diaphragms and lens are used to focus the scattered light onto the photomultiplier window and to choose the scattering volume of the cell.

The light intensity is regulated with two filters: one is in front of the laser, and the other is placed on the secondary beam path. These filters allow us to choose the intensity ratio between the scattered light and the secondary light beam. In heterodyne detection, the intensity of the scattered beam must be at least 10 times lower than the secondary beam. Thus, the filters have to be changed for each sample because the scattered light intensity varies with particle concentration.

The measurement cell is a dip cell suitable for organic liquids supplied by Malvern. It has a square section with a 1 cm side and an electrode gap of 2 mm. This cell design has the advantage that the measurement zone is far enough from the lateral walls as to avoid any significant electroosmotic flow.

To minimize light refraction, the cell is placed into the center of a cylindrical ethanol bath. It would have been best to use a bath with the same solution, toluene−ethanol, but we came up against serious difficulties with the toluene vapor because it dissolves some plastic pieces that support the measurement cell. We control the angle of the scattered light with the help of a goniometer; in our case, we use an angle of 25°. For the calculations, it is necessary to correct the scattering angle due to the refraction between the sample ($n = 1.46$) and the ethanol bath ($n = 1.36$). The corrected scattering angle is 23.18°.

We applied a symmetric square signal with a frequency of 1 Hz for 50 s. The temperature is measured and monitored for each measurement, which has always been between 18 and 20 °C.

Results and Discussion

Doppler Frequency Measurement. Figure 5 shows several heterodyne correlation functions computed by the correlator, when the particles are undergoing electrophoresis. To obtain the Doppler frequency from the data set, we compute the Fourier transform of the heterodyne correlation function. According to

(16) Medrano, M.; Pérez, A. T.; Soria-Hoyo, C. *J. Phys. D* **2007**, *40*, 1477.
(17) Medrano, M.; Pérez, A. T.; Soria-Hoyo, C. *IEEE Trans. Dielectr. Electr. Insul.* **2009**, *16*, 404.

Figure 5. Example of some heterodyne correlation functions when the particles are undergoing electrophoresis. In this case, the suspension has a concentration of particles of 4.5% by volume. The electrical signal is square symmetric with a frequency of 1 Hz and an amplitude of 20.0, 27.5, and 35.0 kV/m.
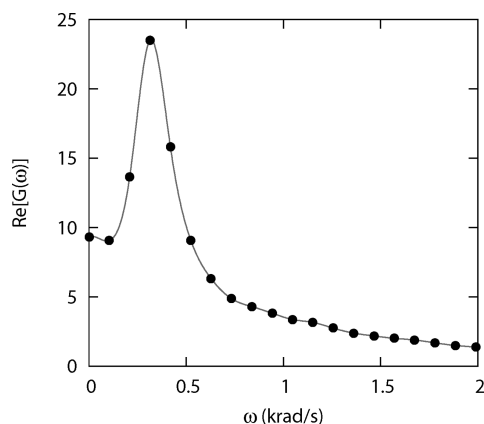
Figure 6. Function $G(\omega)$ is the Fourier transform of $C_2(\tau) - 1$. This figure corresponds to the data obtained for an applied electrical field of 25 kV/m to our suspension. The particle concentration is 4.5% by volume. It shows a peak at the Doppler frequency.

eq 10, we identify the frequency of the maximum with the Doppler frequency. Figure 6 shows the spectrum of the correlation function for a voltage of 50 V between the electrodes (25 kV/m).

Mobility Measurement. To determine the electrophoretic mobility, we measure the Doppler frequency for several electric fields. Figure 7 plots the Doppler frequencies versus the applied electric field for a suspension with a particle concentration of 4.5% by volume. The frequency values have a linear relation with the applied voltage, as relation 9 predicts. The electrophoretic mobility is obtained from the slope of this straight line.

By using this method, we have obtained the electrophoretic mobility for several particle concentrations. Specifically, the particle concentrations was varied from 0.32 to 5.4% by volume.

The values of the mobility measurements with their error bars are shown in Figure 8. For certain values of the electric field, we have also measured the mobility of the samples using a nano zetasizer by Malvern. The results are compatible with values obtained by PCS method. The zetasizer allows us to determine the sign of the particle charge, which is negative.

Figure 8 shows how the electrophoretic mobility decreases with the particle concentration. Because we worked with semidilute
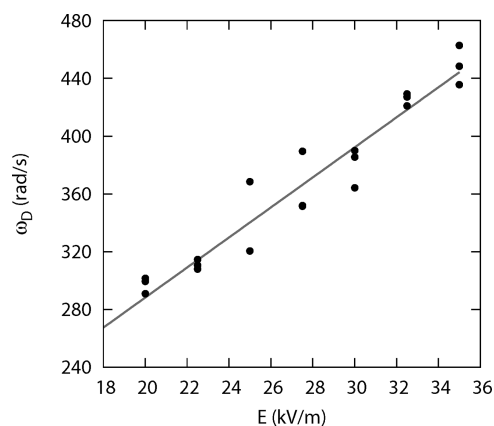
Figure 7. Doppler frequency versus applied electric field between the electrodes. The particle concentration is 4.5% by volume. The straight line is the least-squares fit to the data. We have taken several measurements of ω_D for each value of the electric field.
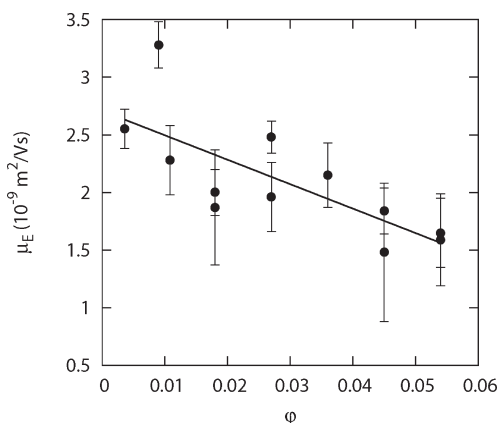
Figure 8. Electrophoretic mobility versus solid fraction. Each point in the plot corresponds to a different sample.

suspensions ($\varphi < 0.06$), the values of the electrophoretic mobility can be fitted to relation 6 by discarding the term $O(\varphi^2)$:

$$|\mu_E(0)| = (2.7 \pm 0.2) \times 10^{-9} \text{ m}^2/\text{Vs}$$

$$S = -8 \pm 2$$

This shows that μ_E decreases with particle concentration faster than predicted by relation 5, which corresponds to $\kappa a \gg 1$.

Mobility Polydispersity. When the applied electric field increases, the Doppler frequency also increases. At first sight and because the factor $e^{-\Gamma\tau}$ in eq 7 does not depend on the electric field, the heterodyne autocorrelation function should have more visible oscillations as the electric field increases. Therefore, for higher electric field, we expect that the spectrum peaks will lie farther from the origin and be better resolved. But Figure 5 shows that the number of visible oscillations in the correlation function does not increase with the electric field. In fact, this Figure shows that the amplitude of the correlation function decreases faster for larger fields. Moreover, what is observed experimentally is a broadening of the peaks in the Fourier transform of the correlation function as the electric field increases (Figure 9). Besides, a decrease in the maximum value is found.

This effect was noticed in other work,[9,18] where it is attributed to a diffusion coefficient dependence on the electric field. Effectively, accordingly to eq 10, the Γ coefficient increases apparently with the applied voltage. Furthermore, eq 10 implies that the broadening of the peaks is due to increased Γ. However, this is not physically sound because the diffusion coefficient is directly related to the particle size.

Wu[19] suggests that a broadening of the peaks in heterodyne spectra is due to a mobility polydispersity. In fact, eq 26 is valid only if the particles have the same electrophoretic velocity, but if there is an electrophoretic velocity distribution or, in other words, a Doppler frequency distribution, then the effect of this polydispersity will affect the correlation functions.

To analyze the effect, let us assume a Gaussian distribution of Doppler frequencies

$$P(\omega_{\mathrm{D}}) = \frac{1}{\sqrt{2\pi}\sigma_\omega}\mathrm{e}^{-(\omega_{\mathrm{D}}-\omega_{\mathrm{D}_0})^2/2\sigma_\omega^2} \tag{11}$$

where ω_{D_0} is the average Doppler frequency and σ_ω is its dispersion. The new correlation function of the electric field is

$$g(t) = \int_{-\infty}^{+\infty} \frac{1}{\sqrt{2\pi}\sigma_\omega}\mathrm{e}^{-(\omega_{\mathrm{D}}-\omega_{\mathrm{D}_0})^2/2\sigma_\omega^2}\,\mathrm{e}^{(-\Gamma+i\omega_{\mathrm{D}})t}\,\mathrm{d}\omega_{\mathrm{D}}$$

$$= \mathrm{e}^{-\Gamma t}\mathrm{e}^{-\sigma_\omega^2 t^2}\mathrm{e}^{i\omega_{\mathrm{D}_0}t} \tag{12}$$

With this new expression of the correlation function of the light electric field and eq 23, the expression of the correlation function for heterodyne detection is

$$C_2(t) = 1+\alpha_2\mathrm{Re}[g(t)] = 1+\alpha_2\mathrm{e}^{-\Gamma t-\sigma_\omega^2 t^2}\cos(\omega_{\mathrm{D}_0}t) \tag{13}$$

This expression shows that the relaxation time of the correlation functions depends on the Doppler frequency dispersion.

The Fourier transform of correlation function 13 does not have an analytical expression, but we can calculate the limits when $\sigma_\omega \ll \Gamma$ and $\sigma_\omega \gg \Gamma$. For the first case, we can take $\sigma_\omega \rightarrow 0$, and then the Fourier transform will be relation 10. In the second case, where the frequency dispersion dominates, we can take the limit $\Gamma \rightarrow 0$, and then the Fourier transform of eq 13 is

$$\mathrm{Re}[G_2(\omega)] = \frac{1}{2}\frac{\sqrt{2\pi}}{\sigma_\omega}\left[\exp\left(-\frac{(\omega-\omega_{\mathrm{D}_0})^2}{2\sigma_\omega^2}\right)+\exp\left(-\frac{(\omega+\omega_{\mathrm{D}_0})^2}{2\sigma_\omega^2}\right)\right] \tag{14}$$
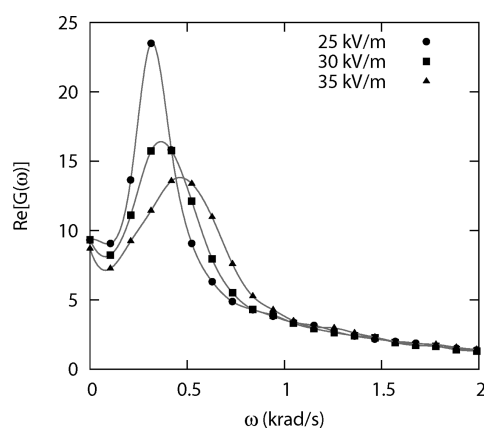
For high electric fields, where we can neglect the diffusion term in the autocorrelation functions, the frequency $\omega_{1/2}^{(2)}$ is determined by the frequency dispersion

$$\omega_{1/2}^{(2)} = \sigma_\omega\sqrt{2\ln 2} \tag{15}$$

The interesting point is that σ_ω depends on the electric field because

$$\omega_D = \frac{2\pi n}{\lambda}\sin(\theta)\mu_{\mathrm{E}}E$$

$$\sigma_\omega = \frac{2\pi n}{\lambda}\sin(\theta)\sigma_\mu E \tag{16}$$

where μ_{E} is the electrophoretic mobility and σ_μ is its dispersion. Therefore, $\omega_{1/2}^{(2)}$ increases linearly with E.

(18) Palberg, T.; Versmold, H. *J. Phys. Chem.* **1989**, *93*, 5296.
(19) Xu, R. *Langmuir* **1993**, *9*, 2955.

Figure 9. Fourier transform of the heterodyne correlation function for three values of the electric field. The Doppler frequency increases with the electric field, and the peaks become smaller and wider.

Relation 16 explains the peak broadening in the heterodyne autocorrelation function (Figure 9). In short, for small electric fields, the relaxation time of the correlation functions is dominated by the diffusion coefficient, whereas for high electric fields the frequency dispersion dominates. Another important conclusion is that mobility polydispersity affects only the width of the peaks, whereas the average Doppler frequency does not vary.

However, because of mobility polydispersity the autocorrelation function decays over time on the order of σ_ω^{-1}. The period of oscillations of the same function is ω_{D}^{-1}. Both quantities depend on the electric field, as eq 16 shows, but their ratio is independent of it. However, we can not measure σ_ω directly but only the value of $\omega_{1/2}^{(2)}$. In fact

$$\frac{1/\omega_{1/2}^{(2)}}{1/\omega_{\mathrm{D}}} = \frac{\mu_{\mathrm{E}}}{\sigma_\mu\sqrt{2\ln 2}} \tag{17}$$

which can be used to calculate σ_μ.

Although we have assumed a Gaussian distribution of Doppler frequencies, this will not be so in general. However, the main conclusion that the value $\omega_{1/2}^{(2)}$ increases with the electric field as a result of the mobility polydispersity will remain true. Even more, eq 17 can be used at least as an estimation of the mobility polydispersity σ_μ.

Table 1 shows how the ratio between the Doppler frequency and $\omega_{1/2}^{(2)}$ does not change with the electric field when this is high enough. From the data of Table 1, we can estimate experimentally the mobility dispersion σ_μ if we take $\omega_{1/2}^{(2)}/\omega_{\mathrm{D}} \approx \sigma_\mu/\mu_{\mathrm{E}}$. The mobility dispersion is on the order of $0.6\mu_{\mathrm{E}}$.

Discussion

First, the double-layer thickness is worth evaluating. We did not add electrolyte to the suspension; therefore, the double layer is formed from solvent molecules, impurities, and ions brought together with the particles. To estimate the Debye length, we use the expression

$$\kappa^{-1} = \sqrt{\frac{D\varepsilon_{\mathrm{r}}\varepsilon_0}{\sigma}} \tag{18}$$

where ε_0 is the dielectric permittivity of vacuum, ε_{r} is the relative permittivity of the toluene−ethanol mixture, D is the diffusion coefficient of the ions, and σ is the electrical conductivity of the liquid.

Medrano et al.   *Article*

Table 1. Ratio between the Doppler Frequency, ω_D, and $\omega_{1/2}^{(2)}$ [a]

E (kV/m)	ω_D (rad/s)	$\omega_{1/2}^{(2)}$ (rad/s)	$\omega^{(2)}{}_{1/2}/\omega_D$
25.0	320	63	0.20
27.5	352	214	0.61
30.0	364	238	0.66
32.5	434	251	0.58
35.0	439	283	0.64

[a] It tends to a constant value close to 0.6. The concentration of particles is 4.5% in volume.

Considering a typical value for the diffusion coefficient on the order of 10^{-9} m^2/s and the measured value for the conductivity, we obtain $\kappa^{-1} \approx 90$ nm and $\kappa a \approx 0.44$. Under these conditions, particle–particle forces cannot be neglected. In fact, the typical distance between particles varies from 500 nm for a concentration of 0.36% to less than 200 nm for concentrations higher than 4.5%; this leads to overlap of the double layers.

In Shugai's work,[8] the mobility of suspensions with thick double layers is numerically studied. In addition to κ^{-1}, another characteristic length enters the pair correlations functions $g(r)$. This is the Bjerrum length

$$\lambda_B = \frac{e^2}{4\pi\varepsilon_0\varepsilon_r k_B T} \tag{19}$$

In our case, $a\lambda_B^{-1} \approx 5$. Shugai et al.,[8] for $\kappa a = 1$ and $a\lambda_B^{-1} = 10$, obtained for the parameters of eq 6 $S \approx -6$. The experimental measurement that we have performed is thus in quite good agreement with this numerical result. In any case, it is worthwhile to note that those models that lead to either constant mobility or weakly decreasing mobility with the volume fraction, as $1 - \phi$ or $1 - (^3/_2)\phi$, are clearly excluded by our measurements.

Another important point discussed by Ennis[7] and Shugai[8] is the following: because of hydrodynamic interactions between a pair of particles, the mobility in a direction parallel to the line of their centers is different from the mobility in the transverse direction. As a consequence, in suspension, the particle velocity has fluctuating components, leading to mobility dispersion. For $a\lambda_B^{-1} = 10$ and $\kappa a = 1$, Shungai et al. computes the fluctuation in particle mobility to be $\sigma_\mu/\mu_E \approx 7 \times 10^{-2}$.

For smaller values of $a\lambda_B^{-1}$ and κa, Shugai et al. show that a larger value of $\sigma_\mu\mu_E^{-1}$ is expected. Therefore, our measurements are in qualitative agreement with the numerical computation.

Other sources of mobility dispersion should be taken in account. First, the 10% size polydispersity could have implications in the mobility dispersion. Unfortunately, this has not been numerically explored in the work by Shugai et al. Another factor is the surface charge polydispersity. When $\varphi \rightarrow 0$, the electrophoretic mobility must agree with Henry's equation. In our case, where $\kappa a \approx 0.44$, Hückel's equation (eq 2) is precise enough to give the zeta potential from the mobility at $\varphi = 0$:

$$\zeta = (47 \pm 3) \text{ mV}$$

Assuming that the zeta potential is the potential at the particle surface, the total charge over each particle can be estimated from the expression

$$Q = 4\pi\varepsilon_0\varepsilon_r a\zeta \tag{20}$$

We estimate that the number of elementary charges is approximately 10. This small quantity implies that any variation of the electrical charge produces a large dispersion in the zeta potential and hence in the mobility.

Conclusions

The technique of refractive index matching has allowed us to study the electrophoretic mobility of concentrated suspension by PCS. It has been found that the mobility of the particles decreases with concentration faster than $1 - 1.5\varphi$, which indicates that the interactions between the particles are important. The measured mean mobility is in good agreement with the numerical computation by Shugai et al. This experimental technique enabled us to measure the mobility polydispersity as well. This polydispersity has been seldom measured in the past. We think that this is a useful method to gain insight into the velocity fluctuations in electrophoresis.

Appendix

The autocorrelation function is defined as

$$C(\tau) = \frac{\langle I(t)\, I(t+\tau)\rangle}{\langle I(t)\rangle^2} \tag{21}$$

where $I(t)$ is the light intensity at initial time t and τ is the time lag. Symbols $\langle\rangle$ denote the temporal average.

The correlation function (eq 21) may be expressed in terms of the correlation function of the electric field of the scattered light $g(\tau)$.

For homodyne detection, the correlation function is[20]

$$C_1(\tau) = 1 + \alpha_1 |g(\tau)|^2 \tag{22}$$

and for heterodyne detection it is

$$C_2(\tau) = 1 + \alpha_2 \text{Re}[g(\tau)] \tag{23}$$

where α_1 and α_2 are constants depending on experimental parameters such as the coherence area and the ratio between the scattered light and the direct beam intensity for the heterodyne case. The symbol Re denotes the real part of the complex function $g(\tau)$.

The correlation function of the electric field of the scattered light is

$$g(\tau) = \frac{\langle \vec{E}(t)\cdot\vec{E}*(t+\tau)\rangle}{\langle \vec{E}(t)\cdot\vec{E}*(t)\rangle} \tag{24}$$

where $\vec{E}$ is the electric field of the light scattered by the scattering volume and $\vec{E}*$ denotes its complex conjugate.

For uncorrelated particles, eq 24 becomes[20]

$$g(\vec{q},\tau) = e^{-\Gamma\tau}e^{i\omega_D\tau} \tag{25}$$

where Γ is the product Dq^2, $\vec{q}$ is the scattering vector ($\vec{q} = \vec{k}_i - \vec{k}_s$), D is the diffusion coefficient, and ω_D is the Doppler frequency.

Using eq 25, the correlation functions (eqs 22 and 23) take the form

$$C_1(\tau) = 1 + \alpha_1 e^{-2\Gamma\tau} \tag{26}$$

and

$$C_2(\tau) = 1 + \alpha_2 e^{-\Gamma\tau}\cos(\omega_D\tau) \tag{27}$$

(20) Berne, B.; Pecora, R. *Dynamic Light Scattering*; Wiley: New York, 1976.

Annexe D

Rhéologie des suspensions concentrées

D.1   Particle Image Velocimetry in Concentrated Suspensions : Application to Local Rheometry

Particle Image Velocimetry in Concentrated Suspensions: Application to Local Rheometry

Frédéric Blanc, François Peters, Elisabeth Lemaire*

CNRS, Université de Nice, LPMC-UMR 6622, 06108 Nice Cedex 2, France

*Corresponding author: elisabeth.lemaire@unice.fr
Fax: x33.4.92076754

Abstract:

This paper presents an experimental facility that allows simultaneous viscosimetric and Particle Image Velocimetry measurements on concentrated suspensions in a wide-gap Couette rheometer. The experimental procedure is detailed: the optical characteristics of the index-matched suspension are carefully studied, the bottom end effect on both the viscosimetric measurements and the recorded velocity profiles are analysed. First the experimental procedure is tested on a Newtonian fluid whose viscosity is known. The spatial and time resolutions of our device are shown to be 200 μm and 100 ms. The precision of the local viscosity measurement is evaluated to better than 4 %. Then we show that the device can be used to characterize the rheological behaviour of a 47 %-concentrated suspension of 30 μm spheres. According to the particles large size, the Brownian motion can be neglected. However, colloidal interaction are still noticeable.

Zusammenfassung:

In dieser Arbeit wird ein experimenteller Aufbau vorgestellt, mit dem gleichzeitig viskosimetrische und sogenannte Particle-Image-Velocimetry (PIV)-Messungen an konzentrierten Suspensionen in einem Couette-Rheometer mit einem großen Spaltabstand durchgeführt werden können. Das experimentelle Verfahren wird im Detail beschrieben: Die optischen Eigenschaften der Suspension mit dem angepassten Brechungsindex werden genau gemessen, und die Randeffekte werden sowohl bei den viskosimetrischen Messungen und den aufgenommenen Geschwindigkeitsprofilen analysiert. Zuerst wird das experimentelle Verfahren anhand eines Newtonschen Fluids getestet, dessen Viskosität bekannt ist. Die räumliche und zeitliche Auflösung unserer Apparatur betragen 200 μm bzw. 100 ms. Es wurde festegestellt, dass die Genauigkeit der lokalen Viskositätsmessungen größer als 4% ist. Darüber hinaus zeigen wir, dass die Apparatur benutzt werden kann, um das rheologische Verhalten einer Suspension mit einer Kugel-Konzentration von 47% Kugeldurchmesser 30 μm) bestimmt werden kann. Aufgrund des großen Partikeldurchmessers kann die Brownsche Bewegung vernachlässigt werden. Jedoch sind kolloidale Wechselwirkungen erkennbar.

Résumé:

Nous présentons ici un dispositif expérimental permettant de coupler des mesures rhéologiques macroscopiques à des mesures de champ de vitesse par PIV, dans des suspensions concentrées cisaillées dans une cellule de Couette cylindrique large entrefer. Nous présentons la méthode d'analyse d'images que nous avons choisie et la procédure expérimentale que nous avons suivie en insistant sur la façon dont l'adaptation d'indice entre les particules et le fluide est réalisée et sur l'influence du fond de la cellule de Couette sur les profils de vitesse et le couple visqueux exercé sur le rotor. La méthode proposée est d'abord validée sur un liquide simple, newtonien, dont la viscosité est connue. Sur ce liquide, il est montré que la résolution spatiale est de l'ordre de 200 μm, la résolution temporelle, de 10 ms et que l'incertitude de mesure sur la viscosité est inférieure à 4 %. Ensuite, le dispositif expérimental est utilisé pour caractériser la réponse visqueuse d'une suspension concentrée (ϕ = 47 %) de sphères non-browniennes.

Key words: particle image velocimetry, concentrated suspension, viscosity, local rheometry

1   INTRODUCTION

The knowledge of the rheological behaviour of concentrated suspensions of solid particles is an important issue since suspensions are involved in many domains like industrial processes or geophysical phenomena. A theoretical understanding of the mechanical behaviour of concentrated suspensions is difficult because of the particle interactions and its experimental characterization is complicated by numerous disturbing effects such as shear induced particle migration or wall slip. During these last decades, a significant effort has been made to develop non-invasive techniques that ensure that the measured properties are actually the bulk properties of the suspensions. Among these techniques, we may cite the Ultrasound
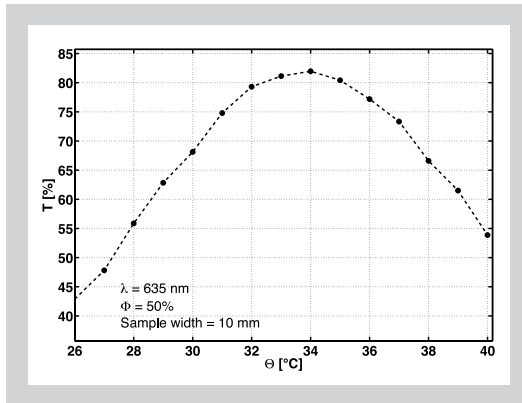
Figure 1:
Spectrophotometer measurement of the transmittance of a $\phi = 50$ % suspension of $31\,\mu m$ PMMA particles in Cargille mineral oil versus temperature. The particle liquid index matching is thus found to be optimal for a temperature $T = 34$°C and $\lambda = 635$ nm.

Doppler Velocimetry (UDV) [1], the Laser Doppler Velocimetry (LDV)[2][3][4], the Magnetic Resonance Imaging (MRI) [5 – 7], the Particle Tracking Velocimetry (PTV) [8, 9] and the Particle Image Velocimetry (PIV) [10 – 13]. UDV use is restricted to rather low concentrated suspensions especially when the particle size is not very small compared to the acoustic wavelength. MRI is a very powerful technique [14] that allows measuring both the particle concentration and the velocity profiles. Unfortunately, the MRI technique does not allow carrying out the measurements directly inside a commercial viscometer and, usually, the rheological measurements have to be made separately. If one wants to compare simultaneously macroscopic and local rheological measurements, the LDV or PIV techniques are suitable since they are easily implemented on a rheometer but they require to use an index-matched suspension (for a recent review, see [15]). The LDV allows very accurate measurements of the mean and fluctuating parts of the velocity [4] but, since it is a pointwise method, the instantaneous velocity profile cannot be determined. The PIV and PTV are now broadly used techniques in flow measurements [10] but they remain challenging techniques in concentrated heterogeneous media [8, 16]. Nevertheless they have been successfully employed to measure velocity fields in concentrated suspensions [11, 12, 17, 18].

In this paper we describe the PIV facility that we have developed in order to study the rheological behaviour of concentrated suspensions in a wide-gap Couette viscosimeter. We first present the suspension characteristics and detail the experimental device. Then, we validate our experimental procedure with a Newtonian liquid whose viscosity is known and, at last, we present the local rheological measurements performed on a concentrated suspension ($\phi = 47$ %).

2 MATERIALS AND METHODS

2.1 TRANSPARENT CONCENTRATED SUSPENSION

The suspensions that we study here are composed of monodisperse spherical PMMA particles (diameter $31 \pm 4\,\mu m$, density 1.178) immersed in a mineral oil (Cargille, $\eta_o = 1.03 \pm 0.01$ Pa·s at 34°C)

which is Newtonian. We have prepared suspensions of various concentrations between 30 and 50 %. The fluid is chosen to match both the refractive index and density of the particles. At 25°C, its refractive index n = 1.4900 ± 0.0005, its density is 1.18 and its thermal expansion is $3.6 \cdot 10^{-3}$/°C. Thus no sedimentation is observed in the suspensions which are almost transparent, as required by the PIV measurements.

In order to improve the transparency of the suspensions we have to match as closely as possible the refractive index of the particles and of the suspending liquid. This is achieved by controlling the temperature of the suspensions thanks to the Christiansen effect [19, 20]. Indeed, the refractive indices of the particles and of the host liquid do not vary in the same way with the temperature. Thus it is possible to improve the index matching at a given wavelength upon varying the temperature. The optimal temperature has been determined by measuring the transmittance of a $\phi = 50$ % suspension as a function of the temperature. Figure 1 shows the results obtained with a spectrophotometer (Varian Cary 500). The transmittance is therefore maximum for a temperature T = 34°C. All the PIV measurements will be performed at this temperature.

At last, a small amount of the particles (between 0.15 and 0.25 %) from the same batch are tagged with a fluorescent dye (Nile Blue A) and serve as PIV-tracers. To dye the particles, we disperse them in a dye-saturated ethanol solution which is heated at 50°C during one hour. The particles are then rinsed in ethanol until the liquid is clear. They are dried and sieved to eliminate possible clusters. The procedure of immersing the particles in ethanol was not found to have any discernible effect on the PMMA particles. Using Scanning Electron Microscopy, we have been able to observe that their size and surface have not been modified. We have checked that at T = 34°C no sedimentation was observed for several tens of hours. To this purpose, the positions of the fluorescent particles in the laser sheet have been recorded and no displacement was observed.

2.2 DESCRIPTION OF THE FLOW CELL

The rheology of the suspensions is studied in a wide-gap Couette geometry mounted on a controlled-stress rheometer Mars II (Haake). The particles and the fluid are mixed together in the vis-

cosimeter cup which is removable. During the mixing, many air bubbles are trapped in the suspension. They are removed by vacuum degassing after the mixing has stopped. The outer cylinder is then fixed on the reference plane of the rheometer with four screws. The inner cylinder is then slowly moved down until it is located 1 mm above the bottom of the cup. We have chosen such a small distance between the bob and the cup to limit the particle migration from or toward the region situated below the rotor [21]. In turn, we expect to observe significant end effects even though the rotor has been specially designed to reduce the bottom viscous friction. A cavity has been made in the lower part of the rotor so that an air bubble is trapped between the rotor and the cup and the wall around the bubble has been bevelled (see Figure 2). The inner rotating cylinder ($2R_{in}$ = 28 mm in diameter, 60 mm in height) and the outer stationary cup ($2R_{out}$ = 48 mm in diameter, 60 mm in height) are made of PMMA, so that their refractive index is approximately matched with the suspension one. The front face has been polished in the form of a rectangular window that lets the laser sheet enter the gap between the cylinders almost without refraction. The inner cylindrical walls have been roughened (except the cup bottom which, on the contrary, has been polished) to minimize the suspension slip.

2.3 DESCRIPTION OF THE OPTICAL DEVICE

Figure 3 offers a schematic view of the device. An externally triggered horizontal laser sheet (Lasiris TEC Laser, Stockeryale, 635 nm, 35 mW), roughly 100 μm thick, illuminates the transparent suspension located in the wide-gap Couette cell. A camera (PLB 741 U, Pixelink, 1280 x 1024 pixel) records successive images of the fluorescent tagged particles. The laser sheet and the camera are fixed on an arc which can be vertically translated. We can thus measure the particles displacement at any height in the suspension.

The laser light excites the dyed tracers which emit isotropically around 650 nm. A high pass filter in front of the camera allows only the fluorescent light to be detected. Thus the scattered and refractive light from the laser is cut off. Linear and tilt stages (Newport) allow positioning the camera and setting the laser sheet horizontally. In order to control the temperature, the

device is placed in an isothermal box made of wood covered with 2 cm thick polyurethane sheets. The box is heated by a radiator connected to an heating circulator bath, which is controlled by a Pt 100 resistance thermometer located near the Couette cell. To improve the homogeneity of the temperature in the box, a fan is placed behind the radiator. The temperature is set to 34 ± 0.1°C. Figure 4 shows a typical picture (inverted contrast) taken 14 mm above the bottom of the cup in a ϕ = 40 % suspension.

3 PIV PROCEDURE

The image processing is performed by the open source software DPIVsoft (*https://www.irphe.fr/meunier/*) developed under Matlab environment. PIV is a technique for measuring velocity fields in a plane. Each image is first divided into overlapping subsets named correlation windows. The cross correlation function of the corresponding windows from two successive images is computed (see Figure 5). The mean displacement in this window is given by the location of the maximum of the cross-correlation function. The same procedure performed on all windows gives the displacement field in the illuminated plane. The FFT-based correlation func-
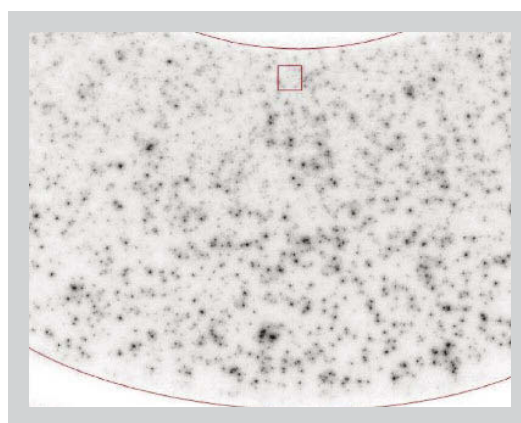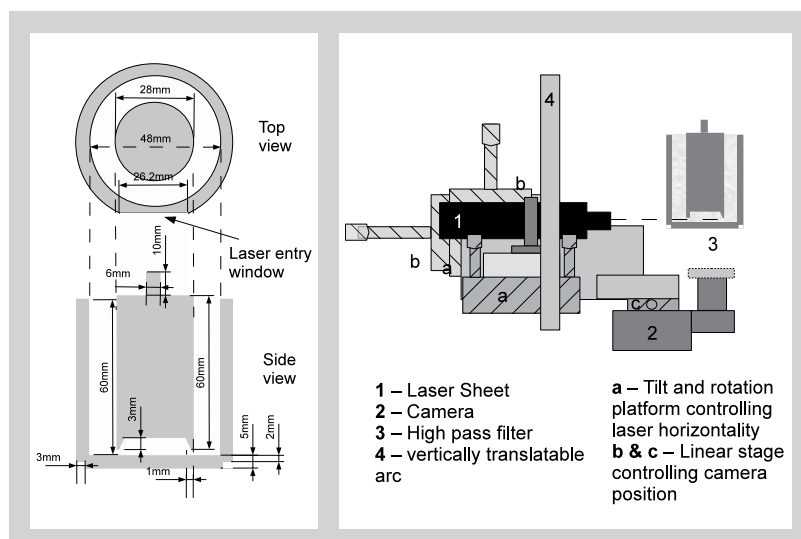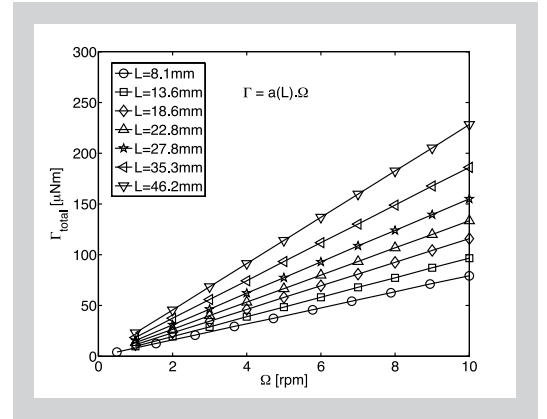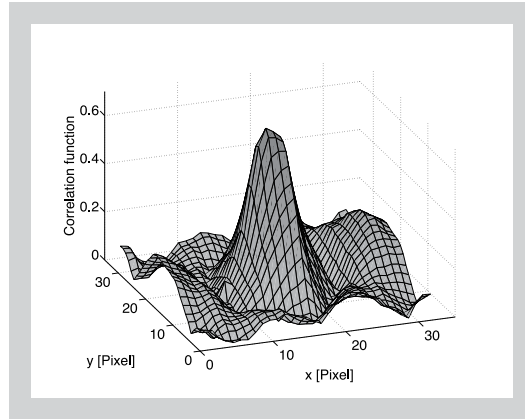
Figure 2 (left above): Schematic drawing of the Couette geometry that is used for the PIV measurements. Both cylinders are made of plexiglas. Their surfaces in contact with the suspension have been roughened to minimize wall slip when the suspension is sheared.

Figure 3 (right above): PIV set-up: A laser sheet (Lasiris TEC Laser, Stockeryale, 635 nm, 35 mW), roughly 100 μm thick, illuminates an horizontal plane of the transparent suspension located in the wide-gap Couette cell. A camera (PLB 741 U, Pixelink, 1280 x 1024 pixel) situated under the bottom of the cup records successive images of the fluorescent tagged particles. The laser sheet and the camera are both fixed on an arc which can be vertically translated.

Figure 4 (below): Typical image (inverted contrast) obtained 14 mm from the bottom of the geometry in a 40 % suspension (Rotor and stator are fitted with two circles, Square: correlation window).

tion algorithm is performed in two steps [22]. A first displacement field is computed, making it possible to compute the local 2D displacement gradient in the suspension. During the second run, the windows are first deformed according to the previously computed displacement gradient, before the definitive displacement field to be determined. The size B of the correlation window for the first run plays an important role in the issue of the velocity field calculation. It should fit two criteria : the number of particles in the window has to be larger than typically 4 and the larger particle displacement should be lower than $B/3$ [22]. The former is necessary to obtain a sufficiently peaked correlation function, while the latter avoids that too many particles exit the window. The first criterion gives the amount of dyed tracers. A quantity of 0.25 % of dyed particles experimentally corresponds to around 5 particles in a $B = 64$ pixels correlation window and allows measurement to be performed high enough above the bottom of the geometry. A larger amount of dyed tracers increases light absorption and degrades the velocity measurement accuracy. The length scale on our image is about 1000 pixels/cm. We can thus rewrite the second criterion evaluated at the inner cylinder surface in terms of rotation speed Ω (in rpm) and frame rate f (in Hz): $\Omega/f \lesssim 10^{-1}$ rpm/Hz. As the faster rate of our camera is 10 Hz, the rotor speed should be smaller than 1 rpm. Finally,
we obtain a 60 x 60 Cartesian velocity field, i.e. a spatial resolution around 200 μm. The time resolution is given by the camera frame rate, at most 10 Hz in our case.

3.1 LOCAL MEASUREMENT

3.1.1 Determination of the Local Shear Rate

We calibrate our image plane by fitting two circles to the cylinders surfaces and then find the center of the geometry and the length scale factor from the known gap value. It is thus possible to deduce the velocity components in the cylindrical coordinate system (r, θ), that are then aver-

aged over the azimuthal angle θ. The mean radial velocity is always very close to zero, and the local shear rate is computed from the mean azimuthal velocity $V_\theta(r, t)$ by $\dot{\gamma}(r) = r\partial/\partial r V_\theta/r$. To avoid numerical fluctuations of the spatial derivative, a function is fitted to the experimental velocity profile $V_\theta(r, t)$:

$$V_{fit}(r) = V_{Newtonian} + f(r) = ar + \frac{b}{r} + \frac{c}{r^2} \tag{1}$$

where a, b and c are free parameters. The shear rate is deduced from the differentiation of the fitting function.

3.1.2 Determination of the Local Shear Stress

In the hypothesis of an infinitely high cylinder it is possible to deduce the shear stress $\sigma_{r\theta}(r, t)$ from the torque on the rotating cylinder $\Gamma_{inf}(t)$ by

$$\sigma_{r\theta}(r, t) = \frac{\Gamma_{inf}(t)}{2\pi r^2 L} \tag{2}$$

where L is the height of the sheared fluid. This hypothesis does not hold since L is not very large compared to the gap width. A significant bottom end effect exists and has to be accounted for. To this purpose, we perform experiments on the suspending liquid alone. We measure the torque Γ_{total} and the rotor angular velocity Ω for different values of the sheared liquid height. All results are displayed in Figure 6. It shows a linear behaviour for each height L of sheared Newtonian liquid in the gap. This linear behaviour can also be seen in Figure 7 where Γ_{total} / Ω is plotted versus L. In this representation, all data collapse in a single linear curve. We deduce:

$$\frac{\Gamma_{total}}{\Omega} = a_1 L + a_2 \tag{3}$$

with a_1 = 0.397 μNm/(rpm·mm) and a_2 = 4.44 μNm/rpm. Γ_{total} is the sum of two terms, Γ_{inf} =
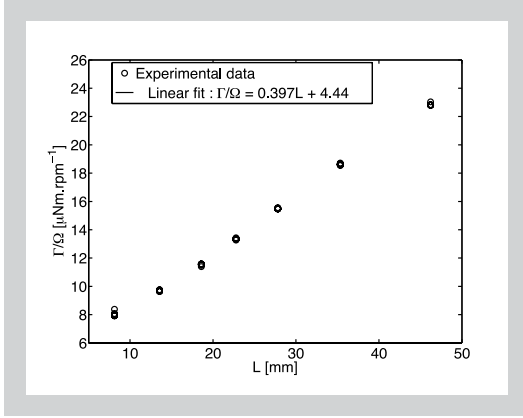
$a_1 L\Omega$ which corresponds to the torque when $L \longrightarrow \infty$ and $\Gamma_{bottom} = a_2\Omega$ which can be interpreted as the bottom contribution to the torque. In particular, we can deduce the viscosity from the value of a_1. Indeed, for Newtonian liquid sheared between two infinite cylinders, the relation between the torque on the inner rotating cylinder and its angular velocity reads:

$$\frac{\Gamma_{inf}}{\Omega L} = \frac{4\pi R_{in}^2 R_{out}^2}{R_{out}^2 - R_{in}^2}\eta$$

(4)

From the value of a_1 together with Equation 4, the viscosity is measured to be $\eta_o = 1.02$ Pa·s. Concerning the bottom end correction we can write

$$\frac{\Gamma_{bottom}}{\Gamma_{total}} = \frac{1}{1+\dfrac{\Gamma_{inf}}{\Gamma_{bottom}}} = \frac{1}{1+8.96\cdot10^{-2}L(mm)}$$

(5)

In a typical experiment L is equal to 50 mm, so that $\Gamma_{bottom}/\Gamma_{total} = 18.2\,\%$ meaning that the bottom end influence should not be neglected in this geometry. In the following, this bottom contribution is subtracted from the total torque, in order the shear stress to be computed from Equation 2.

3.2   VALIDATION OF THE PROCEDURE

First we want to check the validity of the local PIV measurement for a Newtonian liquid, namely the host liquid of the suspension. It is seeded with some fluorescent PMMA particles ($2a = 31\,\mu$m) that amount to 0.25 % of the total volume. Figure 8 shows the azimuthal velocity profile in the gap at different heights z above the bottom of the outer cylinder in the pure suspending liquid. The velocity is normalized by the inner cylinder velocity. The experimental data (symbols) are compared to finite element (FEM) computations performed by Comsol Software (solid lines) and to the expected Newtonian flow profile between infinite cylinders (dashed line). This last (non-
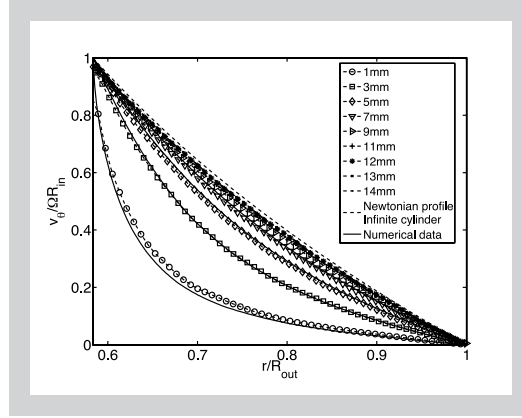
normalized) profile has the well known expression:

$$V_{inf} = \Omega\left(\frac{R_{in}^2 R_{out}^2}{R_{out}^2 - R_{in}^2}\frac{1}{r} - \frac{R_{in}^2}{R_{out}^2 - R_{in}^2}r\right)$$

(6)

and the corresponding shear rate is given by:

$$\left|\dot\gamma\right| = 2\Omega\frac{R_{in}^2 R_{out}^2}{R_{out}^2 - R_{in}^2}\frac{1}{r^2}$$

(7)

Experimental and numerical data are in very good agreement. As expected, the end effect is noticeable up to an height of $z \cong 10$ mm, which is the gap width. This is obviously the origin of the bottom end effect displayed in Figures 6 and 7. Above 10 mm, the relative discrepancy from a Newtonian profile calculated for infinite cylinders is less than 4 %.

The normalized velocity profile measured at a height $z = 14$ mm above the bottom is plotted on Figure 9. The height of liquid in the gap is $h = 26.4$ mm (the sum of $L = 25.4$ mm and 1 mm which is the distance between the bob and the cup). Also displayed is the fitting function (Equation 1) and the infinite cylinder theoretical profile (Equation 6). The shear rate profile from the velocity fit is shown on Figure 10 together with the expected profile from Equation 7. Again the agreement is very good. The viscosity profile calculated from one single shear rate profile $\eta(r) = \sigma(r)/\dot\gamma(r)$, that is displayed on Figure 11, is clearly characteristic of a Newtonian liquid. The dashed lines take into account the standard error calculated from 80 profiles. The overall mean viscosity value $\eta_{micro} = 1.07 \pm 0.01$ Pa·s is in good agreement with the value $\eta_o = 1.02$ Pa·s that has been deduced from the macroscopic measurement shown in the previous section. Both values are consistent with the measurement carried out with the Mars II equipped with a narrow-gap cylinder geometry Z20 DIN Ti: $\eta_o = 1.03 \pm 0.01$ Pa·s.

Figure 9 (left above): Velocity profile in the Newtonian liquid (Height of liquid: h = 26.4 mm, Laser position: z = 14 mm above the bottom, also represented: fitting function and infinite cylinder profile).
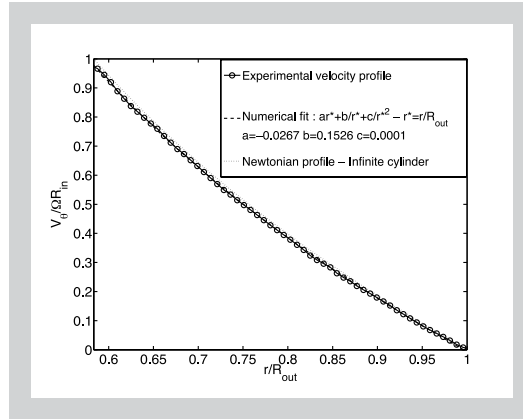
Figure 10 (right above): Shear rate profile in the Newtonian liquid (Height of liquid: h = 26.4 mm, Laser position: z = 14 mm above the bottom, also represented: infinite cylinder profile).
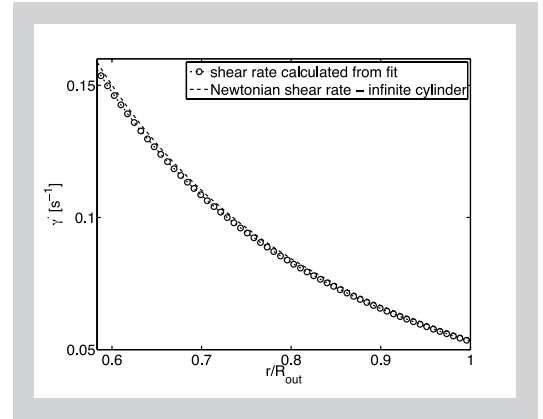
Figure 11 (left below): Viscosity profile in the Newtonian liquid-The dashed lines represent the standard error over 80 profiles that is about 1 %.
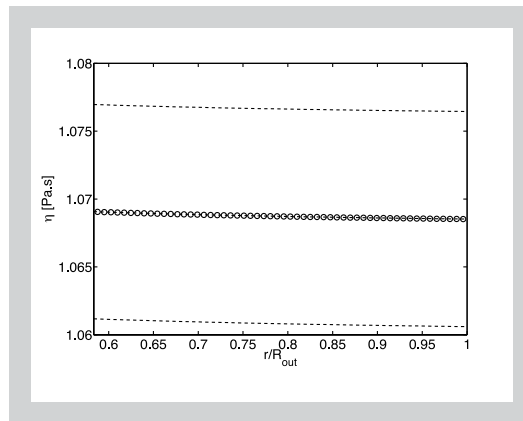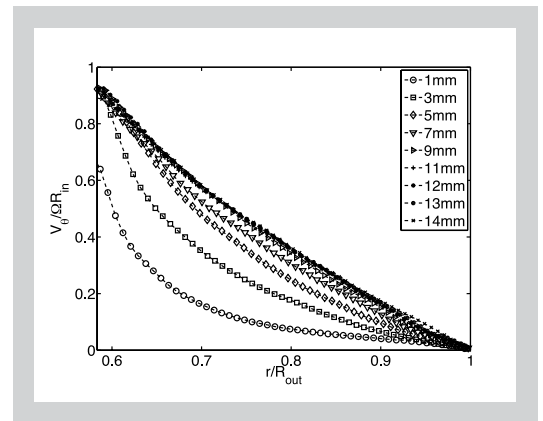
Figure 12 (right below): Dimensionless azimuthal velocity profile in a 47 % concentrated suspension-The different profiles are determined at different heights from the bottom of the cup. Each profile is the result of an average over 100 instantaneous profiles. Height of the suspension: h= 20.1 mm.

4   RESULTS AND DISCUSSION

4.1   VISCOUS BEHAVIOUR OF A 47 % CONCENTRATED SUSPENSION

Now that we have validated the experimental apparatus for pure liquid measurements, we test it in the field of concentrated suspensions. We mainly perform local measurements on a $\phi = 47\%$ suspension. This volume fraction seems moderate. Actually, as shown below the packing fraction ϕ^* of the suspensions is around 0.53 and not $0.61 - 0.63$ as usual, so that $\phi \sim 0.9\phi^*$.

First, we have measured the flow curve of the suspension in a narrow-gap Couette cell Z20 DIN Ti (inner radius 10 mm, outer radius 10.85 mm) in the range $2 \cdot 10^{-2} < \dot{\gamma} < 2.5$ s⁻¹. It fits well to a power law:

$$\sigma_{r\theta} = 40\dot{\gamma}^{0.875} \tag{8}$$

The shear-thinning behaviour is classically observed in such non-Brownian suspensions and the value of the exponent is consistent with that found by Gadala-Maria and Acrivos [23] or by Narumi et al. [24]. Concerning the local measurements, we have performed the same experiment as in the case of the pure suspending liquid to check the influence of the vertical position on the velocity profile. The results are shown in

Figure 12. As in the previous section, the bottom influence on the velocity profiles is negligible above 10 mm. In the following, all local measurements are performed 14 mm above the bottom.

The measurement of the suspension viscosity are performed just after the shear flow has begun without any pre-shear. Thus no or very weak migration is expected to have occurred. Nevertheless, since there is no real consensus about the characteristic time of the shear-induced migration the assumption of a homogeneous suspension has to be checked. To this purpose, we have measured the time evolution of the instantaneous velocity at different locations in the gap. As it can be seen in Figure 13, after a transient decrease the velocity stabilizes to a plateau value and does not change anymore at the time scale of our experiment. Such a transient has already been related in previous papers [23, 25] and is supposed to be due to the formation of a shear-induced microstructure [23]. In particular, Gadala-Maria and Acrivos [23] showed that the steady viscosity is reached after a characteristic strain of about 1. This is consistent with our measurements: taking $V_m = 1$ cm/s for the mean bob velocity during the transient, and $\tau = 10$ s for the typical transient time, we deduce the characteristic strain $\gamma = V_m\tau/(R_{out} - R_{in}) \sim 1$. The velocity profiles that are presented in the following are the result of a time average over
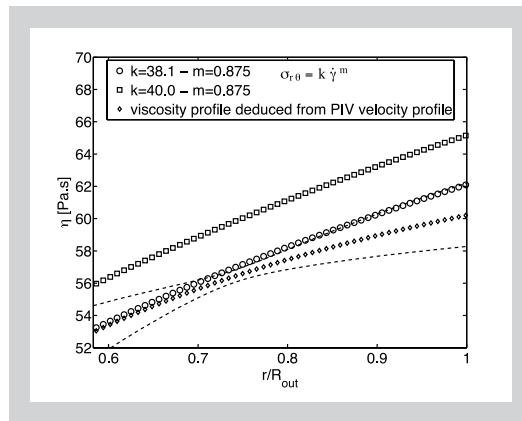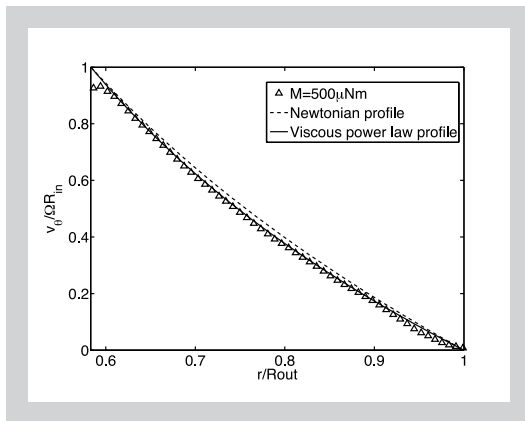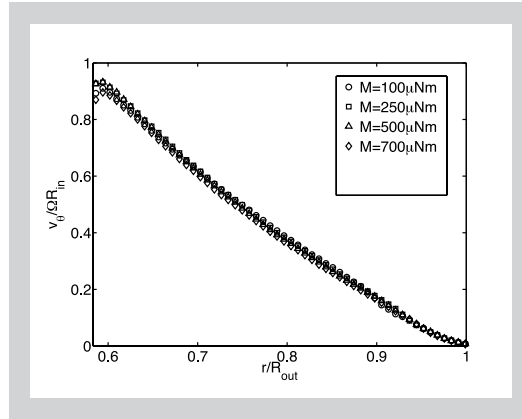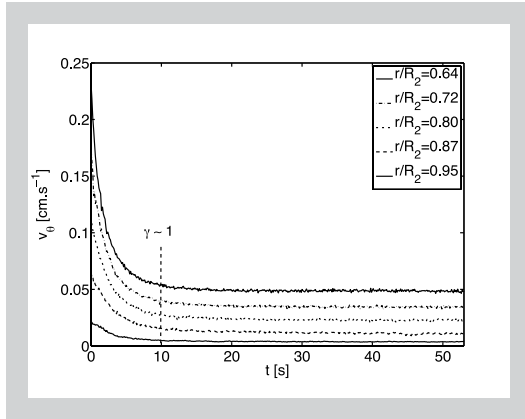
Figure 13 (left above): Time evolution of the velocity at various locations in the gap for a 47 % concentrated suspension (Height of the suspension: h = 45 mm. The imposed torque on the inner cylinder is 500 μNm and the plateau angular velocity of the bob is 4.4·10⁻² rad/s.

Figure 14 (right above): Velocity profiles for different values of the torque for a 47 % concentrated suspension. Each profile is the result of an average over 100 instantaneous profiles (Height of the suspension: h = 45 mm).

Figure 15 (left below): Normalized time averaged azimuthal velocity profile in a 47 % concentrated suspension (h = 45 mm, Dashed line: velocity profile expected for a Newtonian liquid sheared between infinite cylinders, Solid Line: velocity profile deduced from the power law $\sigma_{r\theta} = 40\dot{\gamma}^{0.875}$).

Figure 16 (right below): Viscosity profile in a 47 % concentrated suspension (Laser position above the bottom of the cup: z = 14 mm, Height of the suspension h = 45 mm). The dashed lines represent the standard error over 100 profiles that is at most 4 %. $\sigma_{r\theta} = 40\dot{\gamma}^{0.875}$ is the fitting curve to the macroscopic flow curve.

approximately 12 s once the plateau has been reached. Thus no significant migration is expected to take place at the time scale of one experiment. It should be stressed that at longer times, a significant variation of the velocity is measured, which should be related to a change in the particle concentration profile. The velocity change is typically 1 % per revolution of the bob. However, in the experiments reported in this paper, a suspension was never sheared for more than 4 revolutions before it was completely mixed again, so that it can be considered homogeneous.

We have measured the velocity profiles for the ϕ = 47 % suspension for several values of the torque applied on the bob. The bob angular velocity was also recorded. Since the constitutive law of the suspension has been determined as a power law, we expect the normalized velocity profiles $v_\theta/\Omega R_{in}$ obtained for different torques to collapse onto a single curve:

$$\frac{V_\theta}{\Omega R_{in}} = \frac{\left(\dfrac{R_{out}}{r}\right)^{\frac{m}{2-m}} - \dfrac{r}{R_{out}}}{\left(\dfrac{R_{out}}{R_{in}}\right)^{\frac{m}{2-m}} - \dfrac{R_{in}}{R_{out}}} \qquad (9)$$

This is observed in Figure 14, where the normalized velocity profiles obtained for the torque val-

ues Γ = 100, 250, 500, and 700 μNm are displayed. The experimental normalized velocity profile measured for a torque Γ = 500 μNm is displayed on Figure 15 together with the expected profile from Equation 8. For comparison, the Newtonian profile has also been plotted. The agreement is fairly good, except close to the inner and outer cylinders. The discrepancy observed near the outer cylinder originates in the fact that the PIV software can not measure displacements smaller than approximately 0.5 pixel, due to the middling quality of the images and to the small number of particles in a correlation window. In addition, near the inner cylinder, the first two velocity values are underestimated due to the overlapping of the correlation windows with the inner cylinder that lacks tracers. As a consequence, our PIV device does not allow for an accurate determination of the wall slip.

From the velocity profile, the viscosity profile is computed and compared to the expected profile from Equations 2, 5, and 8 in Figure 16. Since no significant migration has occurred during the experiment time, and since the viscosity variation across the gap is weak, the bottom end correction (Equation 5) which has been determined for a Newtonian fluid should be still valid. The agreement is quite good again, especially if we keep in mind that macroscopic rheometric measurements suffer some uncertainty. Measuring the absolute viscosity of a liquid with a

Figure 17:
Variation of the relative viscosity deduced from PIV measurements with the particle volume fraction. The measurement has been performed at r = 0.77 R_{out} and the applied torque has been controlled for the bob angular velocity to be approximately 0.4 rpm (Laser position above the bottom of the cup: z = 14 mm. Height of the suspension h = 45 mm).
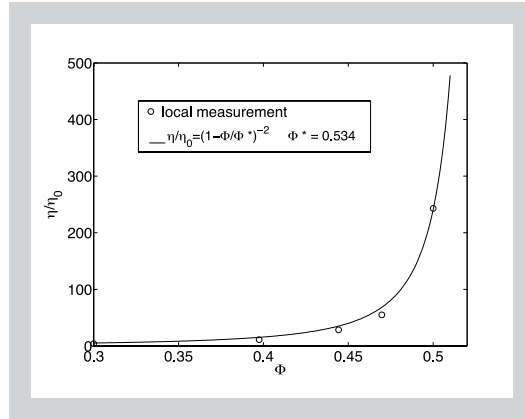
precision higher than a few percents is a hard task. The case of concentrated suspensions is even more tricky due to a possible wall slip at the interface between the suspension and the container. As shown on Figure 16, a minute change in the parameter *k* substantially reduces the 5 % gap between experimental and expected profiles. By the way, the PIV bulk measurement of the viscosity is not altered by the wall slip, except near the walls.

Finally, we measure the viscosity profile of the suspension for different values of the solid volume fraction. The mean shear rate was kept approximately constant whatever the volume fraction by adjusting the torque on the bob in such a way that $\Omega \sim 0.4$ rpm, resulting in $\dot{\gamma} \sim 5 \cdot 10^{-2}$ s^{-1}. Figure 17 displays the relative viscosity measured at the position $r/R_{out} = 0.77$ as a function of the solid volume fraction. The experimental points are fitted to a Maron-Pierce law [26]:

$$\frac{\eta}{\eta_o} = \frac{1}{\left(1 - \dfrac{\phi}{\phi^*}\right)^2}$$

(10)

which gives the packing volume fraction $\phi^* = 0.534$. This seems lower than the usual values measured for non-colloidal suspensions around 0.6. We conjecture some residual colloidal interactions between the particles. As a consequence, the volume fraction that we chose for most of the local measurements displayed in this paper namely $\phi = 0.47$ corresponds to a fairly concentrated suspension. We can note the exponent 2 in Equation 10 is well appropriate to our experimental data. However, more experimental points in particular close to ϕ^* would be necessary to be more conclusive.

5 CONCLUSION

We have presented an experimental protocol that allows for determining simultaneously the macroscopic and the local rheological properties of a concentrated suspension. A $\phi = 47$ % suspen -

sion is sheared in a wide-gap Couette cell ($R_{in} = 14$ mm and $R_{out} = 24$ mm) mounted on controlled shear stress rheometer. The average viscosity of the suspension is determined from the variation of the rotor spin rate with the applied torque while the local viscosity is deduced from the PIV measurement of the velocity profile in the flowing suspension together with the torque data. The PIV measurement in such a concentrated suspension has been made possible by a close index-matching of the particles and host liquid, that allows to record satisfactory images 1.5 cm deep in the suspension.

First we have checked the validity of the experimental procedure with a Newtonian simple liquid. The influence of the bottom end on both the velocity profiles and the macroscopic measurements has been carefully studied. Upon varying the liquid height, the torque correction that is to be introduced to account for the bottom friction has been determined. The bottom end effect on the velocity profiles has been analysed upon measuring the flow profiles at different positions above the cup bottom. We noted that above roughly 10 mm, i.e. the gap thickness, the velocity profiles only slightly depend on the vertical position. The local viscosity can be deduced from the velocity profiles measured at heights larger than 10 mm together with the torque data, corrected for the bottom end effect. Its value agrees within 4 % with the macroscopic viscosity. The spatial and time resolution for the determination of the velocity profiles have been evaluated to respectively 200 μm and 100 ms, and the statistical precision of the viscosity measurement, about 1 %.

Once the procedure had been checked with a Newtonian liquid, local measurements on concentrated suspensions have been performed. We have been able to measure viscosity profiles over the 1 cm gap with a 4 % statistical resolution. These local measurements are in good agreement with the macroscopic measurements. In particular, the shear-thinning behaviour of the suspension evidenced by the macroscopic flow curve has been observed and the expected 10% variation of the viscosity over the gap has been measured.

The experimental facility that we have presented here allows to measure the variation of the viscosity with the particle concentration. Since the divergence law of the viscosity near the

packing volume fraction is still an open problem, we plan to perform some more measurements in this concentration range.

Finally, one difficult but interesting and open problem that arises in such measurements of suspension properties in a wide-gap Couette cell is the shear-induced migration (for a recent review, see [27]). Thanks to the good time resolution of our apparatus, we have been able to check that the migration was sufficiently slow in our case to induce only weak variations of the velocity profiles at the time scale of one experiment. However, we clearly understand that the main drawback of our experimental device is the lack of a quantitative concentration profile measurement, that will be necessary in order to deal with the open question of the shear-induced migration models [28 – 32]. At this time, we were not able to measure concentration profiles due to the large uncertainties linked with the small concentration of tracers, but some experiments are in progress, with particles larger than the laser sheet thickness, where we try to slightly tag the host liquid in place of some tracer particles.

ACKNOWLEDGMENTS

REFERENCES

[1]   Manneville S, Bécu L, Colin A: High-frequency ultrasonic speckle velocimetry in sheared complex fluids, Eur. Phys. J. App. Phys. 28 (2004) 361 – 373.

[2]   Muller S: Velocity measurements in complex flows of non-newtonian fluids, Korea-Aust. Rheo. J. 14 (2002) 93 – 105.

[3]   Jana S, Kapoor B, Acrivos A: Apparent wall slip velocity coefficients in concentrated suspensions of noncolloidal particles, J. Rheol. 39 (1995) 1123 – 1132.

[4]   Shapley N, Armstrong R, Brown R: Laser doppler velocimetry measurements of particle velocity fluctuations in a concentrated suspension, J. Rheol. 46 (2002) 241 – 272.

[5]   Abbott J, Tetlow N, Graham A, Altobelli S, Fukushima E, Mondy L, Stephens T: Experimental observations of particle migration in concentrated suspensions: Couette flow, J. Rheol. 35 (1991) 773 – 795.

[6]   Raynaud J, Moucheront P, Baudez J, Bertrand F, Guilbaud J, Coussot P: Direct determination by nuclear magnetic resonance of the thixotropic and yielding behavior of suspensions, J. Rheol. 46 (2002) 709 – 732.

[7]   Ovarlez G, Bertrand F, Rodts S: Local determination of the constitutive law of a dense suspension of noncolloidal particles through magnetic resonance imaging, J. Rheol. 50 (2006) 259 – 292.

[8]   Breedveld V, van den Ende D, Bosscher M, Jongschaap R, Mellema J: Measurement of the full shear-induced self-diffusion tensor of noncolloidal suspensions, J. Chem. Phys. 116 (2002) 10529 – 10535.

[9]   Nicolai H, Herzhaft B, Hinch E, Oger L, Guazzelli E: Particle velocity fluctuations and hydrodynamic self-diffusion of sedimenting non-brownian spheres, Phys. Fluids 7 (1995) 12 – 23.

[10] Adrian R: Twenty years of particle image velocimetry, Exp. Fluids 39 (2005) 159 – 169.

[11] Lenoble M, Snabre P, Pouligny B: The flow of a very concentrated slurry in a parallel-plate device: Influence of gravity, Phys. Fluids 17 (2005) 073303.

[12] Wiederseiner S, Ancey C, Rentschler M, Andreini N: Rheophysics of highly concentrated coarse-particle suspensions in a wide-gap Couette rheometer, AIP Conf. Proceed. 1145 (2009) 1063 – 1066.

[13] Zachos A, Kaiser M, Merzkirch W: PIV measurements in multiphase flow with nominally high concentration of the solid phase, Exp. Fluids 20 (1996) 229 – 231.

[14] Huang N, Ovarlez G, Bertrand F, Rodts S, Coussot P, Bonn D: Flow of wet granular materials, Phys. Rev. Lett. 94 (2005) 4 – 7.

[15] Wiederseiner S, Andreini N, Epely-Chauvin G, Ancey C: Refractive-index and density matching in concentrated particle suspensions: A review, Exp. Fluids. 10.1007/s00348-010-0996-8.

[16] Hassan Y, Dominguez-Ontiveros E: Flow visualization in a pebble bed reactor experiment using piv and refractive index matching techniques, Nucl. Eng. and Des. 238 (2008) 3080 – 3085.

[17] Lenoble M: Écoulement et ségrégation dans des pâtes granulaires modèle, Ph.D. thesis, Université Bordeaux I (2005).

[18] Wiederseiner S: Rheophysics of Concentrated Particle Suspensions in a Couette Cell using a Refractive Index Matching Technique, Ph.D. thesis, Ecole Polytechnique Fédérale de Lausanne (2010).

[19] Christiansen C: Untersuchungen über die optischen Eigenschaften von fein verteilten Körpern, Ann. Phys. 260 (1885) 439 – 446.

[20] Christiansen C: Untersuchungen über die optischen Eigenschaften von fein verteilten Körpern, Ann. Phys. 259 (1884) 298 – 306

[21] Leighton D, Acrivos A: The shear-induced migration of particles in concentrated suspensions, J. Fluid Mech. 181 (2006) 415 – 439.

[22] Meunier P, Leweke T: Analysis and treatment of errors due to high velocity gradients in particle image velocimetry, Exp. Fluids 35 (2003) 408−421.

[23] Gadala-Maria F, Acrivos A: Shear-induced structure in a concentrated suspension of solid spheres, J. Rheol. 24 (1980) 799.

[24] Narumi T, See H, Suzuki A, Hasegawa T: Response of concentrated suspensions under large amplitude oscillatory shear flow, J. Rheol. 49 (2005) 71−85.

[25] Narumi T, See H, Honma Y, Hasegawa T, Takahashi T, Phan-Thien N: Transient response of concentrated suspensions after shear reversal, J. Rheol. 46 (2002) 295−305.

[26] Maron S, Pierce P: Application of ree-eyring generalized flow theory to suspensions of spherical particles, J. Coll. Sci. 11 (1956) 80−95.

[27] Morris J F: A review of microstructure in concentrated suspensions and its implications for rheology and bulk flow, Rheol. Acta 48 (2009) 909−923.

[28] Phillips R, Armstrong R, Brown R, Graham A: A constitutive equation for concentrated suspensions that accounts for shear-induced particle migration, Phys. Fluids A 4 (1992) 30−40.

[29] Nott P, Brady J: Pressure-driven flow of suspensions: simulation and theory, J. Fluid Mech. 275 (1994) 157−199.

[30] Mills P, Snabre P: Rheology and structure of concentrated suspensions of hard spheres. shear induced particle migration, J. Phys. II 5 (1995) 1597−1608.

[31] Buyevich Y: Particle distribution in suspension shear flow, Chem. Eng. Sci. 51 (1996) 635−647.

[32] Morris J, Boulay F: Curvilinear flows of noncolloidal suspensions: The role of normal stresses, J. Rheol. 43 (1999) 1213−1237.

D.2 Local transient rheological behavior of concentrated suspensions

Local transient rheological behavior of concentrated suspensions

F. Blanc, F. Peters, and E. Lemaire[a]

*CNRS, Université de Nice LPMC, UMR 6622,
Parc Valrose 06108, Nice Cedex 2, France*

Synopsis

This paper reports experiments on the shear transient response of concentrated non-Brownian suspensions. The shear viscosity of the suspensions is measured using a wide-gap Couette rheometer equipped with a particle image velocimetry device that allows measuring the velocity field. The suspensions made of PMMA particles (31 μm in diameter) suspended in a Newtonian index- and density-matched liquid are transparent enough to allow an accurate measurement of the local velocity for particle concentrations as high as 50%. In the wide-gap Couette cell, the shear induced particle migration is evidenced by the measurement of the time evolution of the flow profile. A peculiar radial zone in the gap is identified where the viscosity remains constant. At this special location, the local particle volume fraction is taken to be the mean particle concentration. The local shear transient response of the suspensions when the shear flow is reversed is measured at this point where the particle volume fraction is well defined. The local rheological measurements presented here confirm the macroscopic measurements of Gadala-Maria and Acrivos [J. Rheol. **24**, 799–814 (1980)]. After shear reversal, the viscosity undergoes a steplike reduction, decreases slower, and passes through a minimum before increasing again to reach a plateau. Upon varying the particle concentration, we have been able to show that the minimum and the plateau viscosities do not obey the same scaling law with respect to the particle volume fraction. These experimental results are consistent with the scaling predicted by Mills and Snabre [Eur. Phys. J. E **30**(3), 309–316 (2009)] and with the results of numerical simulation performed on random suspensions [Sierou and Brady, J. Fluid Mech. **448**, 115–146 (2001)]. The minimum seems to be associated with the viscosity of an isotropic suspension or at least of a suspension whose particles do not interact through non-hydrodynamic forces, while the plateau value would correspond to the viscosity of a suspension structured by the shear where the non-hydrodynamic forces play a crucial role. © *2011 The Society of Rheology.* [DOI: 10.1122/1.3582848]

I. INTRODUCTION

Concentrated suspensions are very common in several engineering fields such as civil engineering, food or pharmaceutical industry, or geophysical situations such as debris flows, sediment transport, and submarine avalanches. In order to understand their flowing behavior, it is desirable to know their response to imposed forces and motions at their boundary. A broad variety of complex rheological behaviors such as shear thinning or shear thickening, yield stress, normal stress differences, or shear banding are exhibited.

---

[a]Electronic mail: elemaire@unice.fr

This diversity issues from the diversity of the interactions (Brownian, van der Waals, steric, and electrostatic) and of the particles properties (size, shape, and polydispersity) that are possibly involved in the flow behavior. Nevertheless even a suspension whose physicochemical characteristics are very simple (non-Brownian spherical particles, negligible colloidal interactions, and Newtonian suspending liquid) can exhibit a complex rheological behavior. For instance, non-Brownian concentrated suspensions are usually shear thinning [Stickel and Powell (2005)] and, if the particle and fluid density are not carefully matched, a yield stress has been shown to develop [Fall *et al.* (2009)]. The transient response of such suspensions is also of interest as reported by Gadala-Maria and Acrivos (1980), Kolli *et al.* (2002), and Narumi *et al.* (2002). As emphasized by Stickel and Powell (2005) and Morris (2009) in their review articles on the rheology of dense suspensions, such a complexity of the rheological behavior is most likely due to the formation of a microstructure induced by the shear flow together with the non-hydrodynamic forces and the key problem is to understand the relationship between the macroscopic or bulk properties of the medium and its microscopic structure.

The first direct experimental evidence of the shear-induced anisotropic microstructure has been provided by Parsi and Gadala-Maria (1987) who measured the pair distribution function for a suspension whose particle volume fraction was 0.4. They note a maximum of the pair distribution function in a direction, which is roughly that of the compression axis. Furthermore, they show that when the direction of the shear is reversed, the particles rearrange into the mirror image of the structure. This direct observation of the microstructure confirms the hypothesis advanced by Gadala-Maria and Acrivos (1980), a few years before, to explain the transient shear stress response of a suspension when it undergoes a shear reversal. The suspension viscosity was shown to depend only on the strain after the shear reversal. In 2002, these results were supplemented by the measurement of the transient normal stresses [Kolli *et al.* (2002); Narumi *et al.* (2002)] which present the same kind of behavior, i.e., a collapse of the recovery normal stresses if plotted against the strain, whatever the shear rate step magnitude.

The characterization of the microstructure has also motivated a lot of numerical studies based on various numerical techniques such as Stokesian dynamics [Singh and Nott (2000); Sierou and Brady (2002); Drazer *et al.* (2004); Bricker and Buttler (2007)] or force coupling method [Yeo and Maxey (2010); Abbas *et al.* (2007)] which all conclude to the formation of an anisotropic shear-induced microstructure.

Achieving accurate rheological measurements with a non-colloidal suspension is quite challenging because perturbative effects such as wall slip [Jana *et al.* (1995)], shear localization [Huang *et al.* (2005)], or particle migration [Leighton and Acrivos (1987); Chow *et al.* (1994)] can arise during the experiment. The local rheological measurements have been shown to be very powerful to measure the true rheological response of a dense suspension.

For instance, Shapley *et al.* (2002) used laser Doppler velocimetry to measure particle velocity fluctuations and velocity profiles in concentrated suspensions sheared in a narrow-gap Couette cell. Another powerful technique to visualize both the velocity and the concentration profiles in suspensions is the magnetic resonance imaging (MRI). In 2006, Ovarlez *et al.* (2006) used such MRI techniques to perform local measurements on very concentrated suspensions sheared in a wide-gap Couette viscosimeter. They have been able to measure both the velocity and the particle concentration profiles in the suspension sheared between two concentric cylinders. They have obtained very impressive results on the stationary behavior of suspensions with particle concentration as high as 60%. One of their main results is that contrarily to what is observed with macroscopic rheological measurements, i.e., a pseudo-yield stress, suspensions have a purely viscous

behavior. Furthermore, they measured the particle concentration profiles and showed that for such high concentrated suspensions, the migration is almost instantaneous. It should be stressed that all their measurements have been performed after a period of pre-shear.

On the opposite, the present paper is focused on the transient shear rate response of rather concentrated suspensions $(0.3 < \phi < 0.5)$ of non-Brownian spheres (diameter 31 μm) when a shear stress is suddenly applied or reversed. Suspensions of various concentrations are sheared between two concentric cylinders so that the shear stress field is controlled in the gap. The suspensions are designed to be almost transparent allowing to determine the velocity field in the gap using particle image velocimetry (PIV) measurements. The local transient response of the suspension is then deduced from the local shear stress and shear rate. The main characteristics of the suspensions are presented in Sec. II. Section III is devoted to the description of the experimental procedure. The results are displayed in Sec. IV where two transient regimes with two different characteristic times are studied. The long time variation of the velocity profile coming from the shear induced particle migration is presented in Sec. IV A, while the rapid changes happening after the shear reversal are described in Sec. IV B. All these results are discussed in Sec. V.

II. SUSPENSION CHARACTERISTICS

The suspension is made of monodisperse spherical PMMA particles (Microbeads CA30), 31 μm in diameter, dispersed in a Newtonian fluid that has been specially designed for our application (Cargille Laboratories, Immersion Liquid Code 11295101160). The fluid has both the same density (d=1.18) and the same refractive index (n=1.49) as the PMMA particles in order to perform the PIV measurements detailed below. To improve the index matching, the temperature is controlled and the best matching is obtained for T=34 °C. At this temperature, the suspending fluid has been found to be fully Newtonian and its viscosity has been measured to be η_0=1.02 Pa s [Blanc *et al.* (2011)]. The particle volume fraction varies from 0.3 to 0.5. The shear viscosity measurements have been performed for shear rates, $\dot{\gamma}$, between 10^{-2} and 1 s^{-1}. Therefore, given the above characteristics of the suspension, the Peclet number that measures the ratio of convection to thermal diffusion is very large:

$$\mathrm{Pe} = \frac{6\pi\eta_0 a^3 \dot{\gamma}}{kT} \sim 10^5 - 10^7$$

and the Reynolds number based on the particle size is very small:

$$\mathrm{Re_p} = \frac{\rho \dot{\gamma} a^2}{\eta_0} \sim 10^{-9} - 10^{-7},$$

where ρ is the density of the suspending fluid and a is the radius of the suspended particles. Thus, our measurements were carried out in the creeping flow regime with negligible Brownian motion.

The viscosity of the suspensions has been studied either in a narrow- or in a wide-gap Couette geometry mounted on a rheometer Mars II (Haake, Thermofisher). The possible variation of the viscosity of the suspension with the shear rate was first studied in a narrow-gap Couette cell (inner radius of 10 mm and outer radius of 10.85 mm). After the suspension had been poured in the cup and degassed, the shear stress was increased step by step. At each step, the steady value of the shear rate was recorded and the value of the viscosity deduced. The measurements have then been performed upon increasing or decreasing the stress, and gave the same results, suggesting that no migration had occurred.
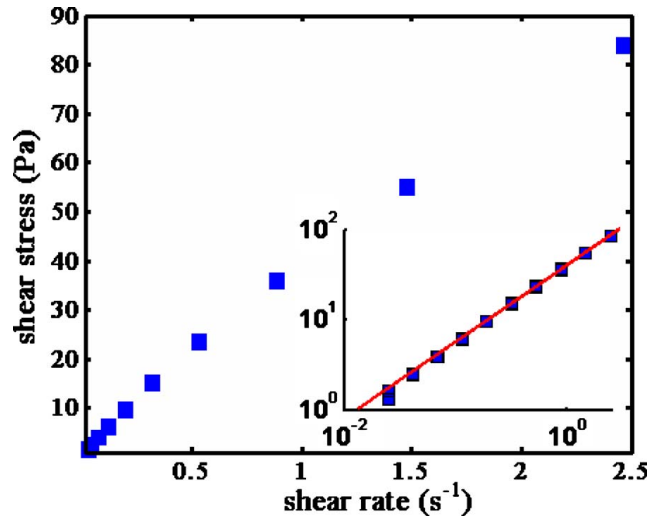
FIG. 1. Flow curve of a $\phi=0.47$ suspension obtained in a narrow-gap Couette rheometer. Inset: power-law fit: $\ln(\sigma(\mathrm{Pa}))=0.88.\ln(\dot{\gamma}(\mathrm{s}^{-1}))+3.7$.

Figure 1 shows the flow curve obtained for a $\phi=0.47$ suspension. The data are well fitted by a power law: $\sigma=40\dot{\gamma}^{0.88}$, where σ and $\dot{\gamma}$ are measured in Pa and s^{-1}, respectively. Such a slight shear thinning behavior is often observed in concentrated non-Brownian suspensions [Gadala-Maria and Acrivos (1980); Zarraga et al. (2000)]. Acrivos et al. (1994) showed that such a shear thinning could occur when the host liquid and the particles do not have the same density, due to the viscous resuspension of the particles. Nevertheless we never noticed any evidence for sedimentation in our experiments and the origin of the low shear thinning observed in our experiments remains unclear.

As it is well known [Jana et al. (1995)] and shown again in Appendix B, the viscosity measurements are difficult to perform in a narrow-gap Couette cell because of the wall slip that significantly changes the value of the apparent viscosity. For that reason and since the observed shear thinning is rather weak (when the shear stress is multiplied by two, the viscosity decreases by only 9%), we decided to perform the further viscosity measurements in the wide-gap Couette cell that will be used for the PIV experiments even though the shear stress is not constant in the gap.

The inner and outer cylinder radii are $R_{in}=14$ mm and $R_{out}=24$ mm, respectively, and their height is 60 mm. The rotor basis is hollowed out and is positioned 1 mm above the cup (Fig. 2). We have chosen to set the rotor close to the cup in order to limit shear-induced migration from or toward the bottom [Leighton and Acrivos (1987)]. Nevertheless, since the rotor is close to the cup and its immersed height is not very large compared to the gap between the coaxial cylinders, the usual relation between the torque and the shear stress does not hold and a correction has to be introduced:

$$\Gamma = 2\pi r^2 L \sigma(r) + \Gamma^{\mathrm{bot}}. \tag{1}$$

Upon varying the height L of the sheared liquid, we measure Γ^{bot}, the torque that results from the presence of the bottom [Blanc et al. (2011)] and we deduce the shear stress field in the gap between the coaxial cylinders:
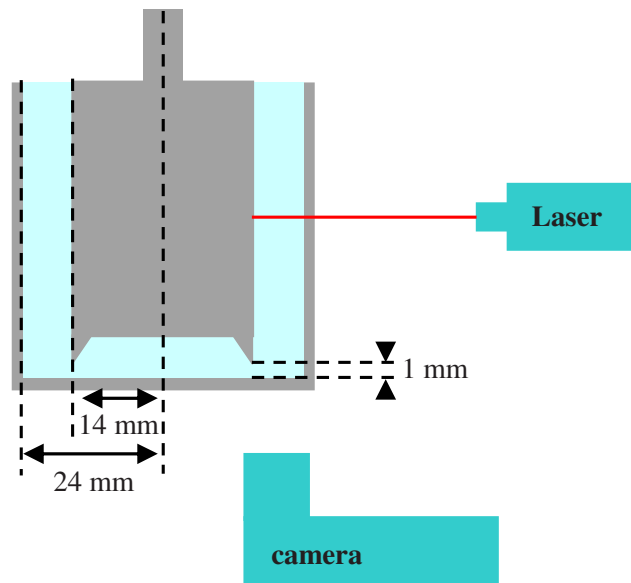
FIG. 2. Experimental set-up.

$$\sigma(r) = \frac{\Gamma - \Gamma^{\text{bot}}}{2\pi L r^2} = \frac{\Gamma^{\text{cor}}}{2\pi L r^2}. \tag{2}$$

Neglecting the slight shear thinning behavior of the suspension, the shear rate in the gap is obtained from the spin rate of the inner cylinder, Ω:

$$\dot{\gamma}(r) = 2\Omega \frac{R_{\text{in}}^2 R_{\text{out}}^2}{R_{\text{out}}^2 - R_{\text{in}}^2} \frac{1}{r^2}. \tag{3}$$

And the viscosity is given by the ratio of the shear stress to the shear rate:

$$\eta_{\text{app}} = \frac{\Gamma^{\text{cor}}}{4\pi\Omega L} \frac{R_{\text{in}}^2 - R_{\text{out}}^2}{R_{\text{in}}^2 R_{\text{out}}^2}. \tag{4}$$

The variation of the apparent viscosity as a function of the particle volume fraction is shown on Fig. 3. These measurements have been performed for an average shear rate, $\langle \dot{\gamma} \rangle = (\dot{\gamma}(R_{\text{in}}) + \dot{\gamma}(R_{\text{out}}))/2$, of about 0.02 s^{-1}.

The data represented in Fig. 3 are fitted to a Krieger–Dougherty law (solid line) with a maximum packing fraction $\phi^* = 0.536$ and an exponent n = 2:

$$\eta = \eta_0 \frac{1}{\left(1 - \dfrac{\phi}{\phi^*}\right)^{\text{n}}}. \tag{5}$$

This value of ϕ^* is very small compared to the values usually found in the literature [Ovarlez et al.(2006); Stickel and Powell (2005)] that are around 0.60–0.63. It should be mentioned that Zarraga et al. (2000) also found a rather low value for the packing fraction ($\phi^* = 0.58$). As discussed in Appendix A, we attribute this low value to polymeric forces between particles. Indeed, we noticed a viscoelastic behavior of the suspensions, which is not expected for a suspension of truly hard, non-Brownian spherical particles.
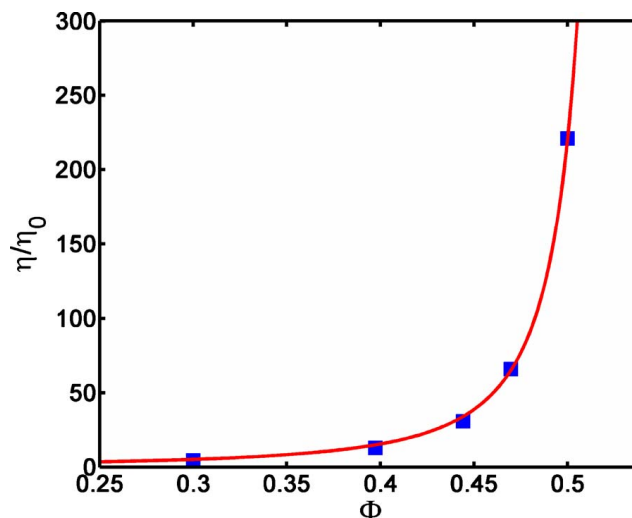
FIG. 3. Steady relative viscosity of the suspension versus the particle volume fraction. These measurements have been performed in the wide-gap Couette cell for an average shear rate of 0.02 s^{-1}.

III. EXPERIMENTAL PROCEDURE

PIV is a now widespread non-invasive technique that allows for flow profile measurements (see Adrian (2005) for a review). However, even if it has been already used in the field of concentrated suspensions [Lenoble *et al.* (2005); Wiederseiner *et al.* (2009)], PIV is still a challenging technique in such heterogeneous media. The experimental facility and methods are described in detail elsewhere [Blanc *et al.* (2011)]. The present section summarizes the main information.

A transparent wide-gap Couette cell is mounted on a controlled-stress rheometer (Haake Mars II, Thermo Scientific). The measurement of the rotor spin rate provides macroscopic rheometric data, while the velocity profile in the gap between the cylinders is deduced from PIV analysis. A schematic drawing of the setup is shown in Fig. 2. The inner rotating cylinder (28 mm in diameter and 60 mm in height) and the outer stationary cup (48 mm in diameter and 60 mm in height) are made of PMMA, in order that their refractive index is approximately matched with the index of the suspension. The front face has been polished in the form of a rectangular window that lets the horizontal laser sheet (Lasiris TEC Laser 635 nm, 35mW, Stockeryale) enter the gap between the cylinders. The inner cylindrical walls have been roughened to minimize the suspension slip. The whole apparatus is placed in a thermostated box, and the temperature is set to T=34 °C.

A small quantity of the particles, which amounts to 0.25% of the whole suspension in volume, is colored with a fluorescent dye, the Nile Blue A (excitation peak at 635 nm and broad emission peak at 650 nm). Those particles serve as flow tracers. A CCD USB camera (Pixelink PLB 741 U, 1280×1024 pixels) is placed under the cup and records sequential images of the illuminated part of the suspension through the polished bottom of the cup. The laser sheet and the camera are trigged by an external oscillator. In order to enhance the contrast of the images, the reflected and scattered light is filtered out by an optical high pass filter (λ_{HP}=650 nm) placed in front of the camera, so that only the fluorescing light is detected. The laser sheet illuminates the horizontal plane 14 mm above the bottom of the cup, where it has been shown [Blanc *et al.* (2011)] that the
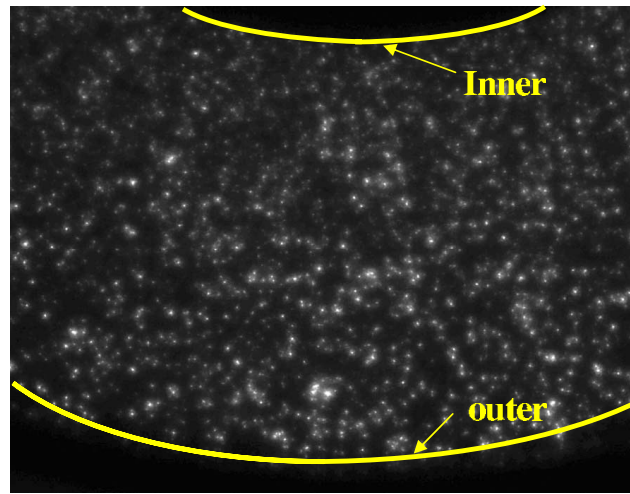
FIG. 4. Typical image of a $\phi=0.444$ suspension recorded 14 mm above the cup bottom.

influence of the bottom on the velocity profile could be neglected. Figure 4 displays a typical image of the illuminated plane obtained with a $\phi=44.4\%$ suspension.

The image processing is performed using an open source software DPIV SOFT available on the web (https://www.irphe.fr/~meunier/). Each image is divided into overlapping subsets named correlation windows (64×64 pixels). The cross correlation of the corresponding windows from two successive images yields the mean velocity of the particles in the window. The same procedure performed on all windows gives the velocity field (60×30 2D vectors) in the illuminated plane. The concentration of colored particles has been chosen such that the number of particles in a window is sufficient (approximately 5), while keeping acceptable light absorption. Given the size of the image plane (approximately 1×1.5 cm^2), the spatial resolution is around 200 μm. The camera acquires frames at a maximum rate of 10 Hz, resulting in a temporal resolution of 100 ms.

The radial and azimuthal components of the velocity are then computed and averaged over the azimuthal angle θ. The mean radial velocity $v_r(r,t)$ is always very close to zero $[v_r/v_\theta\sim O(10^{-2})]$. The local shear rate is extracted from the mean azimuthal velocity $v_\theta(r,t)$: the best fit of the function $f(r,t)=a(t)r+[b(t)/r]+[c(t)/r^2]$ to the velocity data is sought and the shear rate is deduced from the well-known expression:

$$\dot{\gamma}=r\frac{\partial}{\partial r}\left(\frac{f(r,t)}{r}\right). \tag{6}$$

As explained previously, the local shear stress is deduced from the torque on the rotating cylinder [Eq. (2)] that is corrected for the influence of the bottom of the cup [Blanc *et al.* (2011)] and the viscosity profile is computed:

$$\eta(r,t)=\frac{\sigma(r,t)}{\dot{\gamma}(r,t)}. \tag{7}$$

The statistical error in the viscosity measurement has been estimated lower than 4% [Blanc *et al.* (2011)] and the uncertainty in the determination of the bulk volume fraction is less than 0.1%.
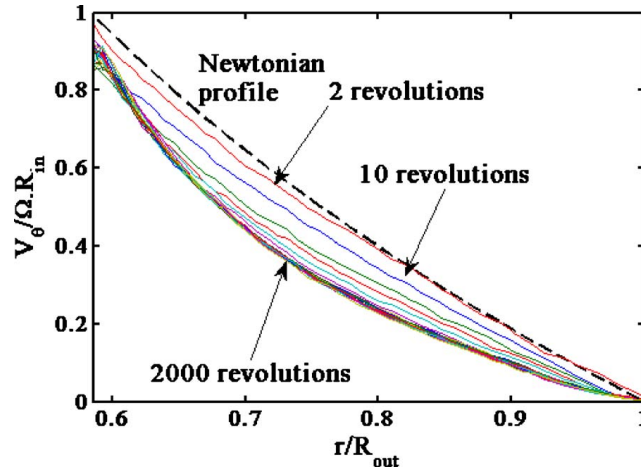
FIG. 5. Long time evolution of the velocity profile in a $\phi = 0.444$ suspension sheared in a wide-gap Couette cell (inner radius 14 mm and outer radius 24 mm). The bob spin rate is set to 1 rpm.

IV. TRANSIENT RESPONSE

A. Long time migration

The main goal of this paper is the measurement of the local transient response of a concentrated suspension to a shear reversal. One parameter plays a major role in this mechanical response, namely, the particle volume fraction. As a consequence, we need to efficiently control this parameter. However, it is well known that the particles in a sheared suspension tend to migrate toward regions where the shear rate is lower [Phillips *et al.* (1992)]. This migration is all the more rapid as the particle concentration is higher and can have significant effects after even a few revolutions of the bob. For example, the velocity profile change obtained for a continuously sheared suspension whose mean volume fraction is $\phi_{\mathrm{mean}} = 0.444$ is displayed in Fig. 5. This curve has been obtained upon controlling the rotor spin rate at a value 1 rpm, which corresponds to an average shear rate of 2 s^{-1}. Figure 5 suggests that wall slip is present near the inner cylinder but, due to the finite size of the correlation windows, we are not able to measure accurately the velocity close to the boundaries. Thus, we cannot conclude anything about the wall slip velocity. After ten revolutions, the velocity profile has changed significantly due to outward migration. From Eqs. (2), (6), and (7), we can compute the time evolution of the viscosity profile that is shown in Fig. 6. We note that around a special value of $r = r_c$, the viscosity remains approximately constant. We have chosen $r_c / R_{\mathrm{out}} = 0.77$, which is the position where the viscosity variation is the lowest at the beginning of the migration, even though in Fig. 6, where very long time variation are displayed, a higher value seems more appropriate. Since the viscosity mostly depends on the particle volume fraction through a monotonic increasing function, the volume fraction around the position $r = r_c$ should also be constant. The existence of this radial zone where the particle concentration varies slightly throughout the migration process was observed experimentally by Phillips *et al.* (1992) and is predicted either by the suspension balance model [Morris and Boulay (1999)] or by the diffusive flux model [Phillips *et al.* (1992)]. We have observed that the value of r_c depends only very weakly on the mean volume fraction. As a consequence, in the following, all local measurements are performed at this particular radial position in the gap, giving the properties of the suspension at the volume fraction ϕ_{mean}.
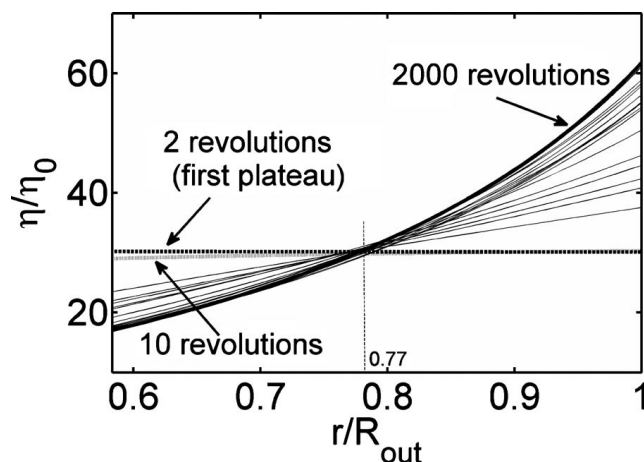
FIG. 6. Long time evolution of the normalized viscosity profile for the $\phi=0.444$ suspension.

B. Transient response after shear reversal

Besides this long time evolution of the velocity profiles, we have observed a fast transient response of the suspension when the shear is reversed. Figure 7 shows the evolution of the normalized velocity profiles in a suspension with $\phi=44.4\%$ when the direction of the torque applied on the inner cylinder is reversed. The measurement has been performed right after that the suspension had been mixed and poured in the Couette cell, so that an approximately homogeneous spatial distribution of the particles was expected at the beginning of the experiment. A negative torque of 250 μN m is applied to the inner cylinder until it has rotated quarter turn, which corresponds to a mean deformation of 3.5 in the suspension. At time zero, the magnitude of the torque passes from -250 μN m to 250 μN m which, according to expression (2) corresponds to a shear stress of 2 Pa at the bob. In Fig. 7, the dashed line represents the velocity profile expected for a Newtonian fluid. The solid lines are the measured profiles at various times, t, after the torque reversal. The very first ones are nearly Newtonian, and the next profiles
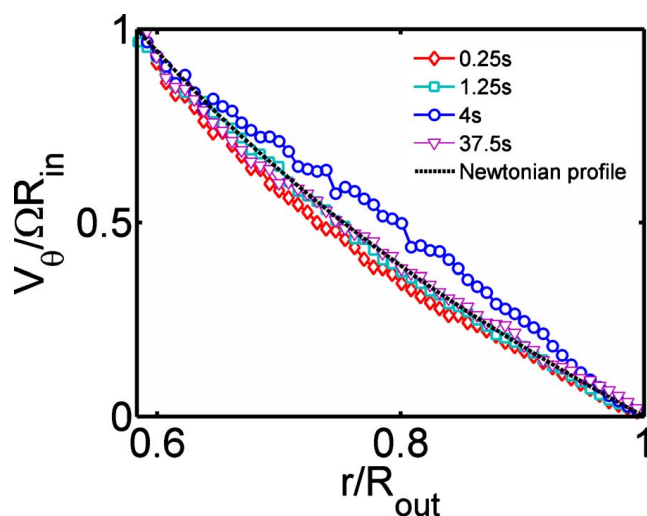

FIG. 7. Transient velocity profiles after shear-reversal (at t=0 the applied torque passes from -250 to $+250$ μN m) at different times (0.25, 1.25, 4, and 37.5 s). The dashed line represents the Newtonian profile. $\phi=0.444$.
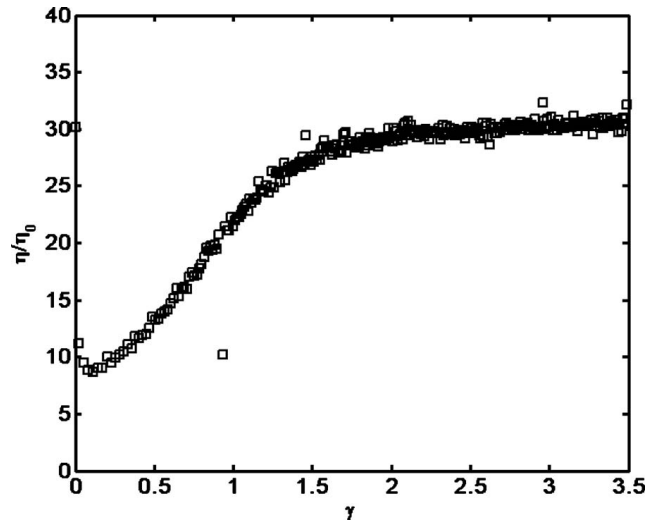
FIG. 8. Transient reduced viscosity after shear reversal versus local strain measured at $r/R_{out}=0.77$, $\phi=0.444$.

deviate from this Newtonian curve before returning to it for longer times. From each curve, following the procedure described in Sec. III, we can deduce the viscosity profiles $[\eta(r,t)]$ as well as the total strain $[\gamma(r,t)]$:

$$\gamma(r,t) = \int_0^t \dot{\gamma}(r,t')dt'. \tag{8}$$

In particular, we can measure the viscosity and the strain at the special point $r=r_c$ where we are assured that the particle volume fraction has almost not changed.

If we plot the viscosity $\eta(r_c,t)$ as a function of the strain, $\gamma(r_c,t)$, we obtain the curve that is shown on Fig. 8. Just after the shear reversal, the viscosity undergoes a step-like decrease. When the strain increases further, the viscosity first decreases, passes through a minimum, and increases again to reach a plateau value.

First, we can note that such a strain-dependent viscosity is consistent with the time evolution of the normalized velocity profile shown in Fig. 7 since, in a wide-gap Couette cell, the shear rate is larger close to the bob and so is the strain. Thus as long as the plateau viscosity has not been reached everywhere in the gap, the viscosity is not uniform and the velocity profile is not Newtonian.

Second, it should be stressed that the characteristic total strain for such an experiment is 3.5, which corresponds to approximately 1/4 revolution of the bob. According to Fig. 6, for such a strain, the effect of the particle migration on the viscosity profile is negligible. All further experiments were conducted for an accumulated strain lower than 50 (corresponding to 4 revolutions of the bob) so that the particle migration was weak. Moreover, to minimize further the effect of migration, all viscosity measurements were performed at the radial position $r=r_c$.

The shear reversal experiment is repeated for other values of the applied torque corresponding to shear stresses of 0.85, 2.12, 4.25, and 5.95 Pa and the results obtained with a $\phi=0.47$ suspension are presented in Fig. 9. The first observation is that the viscosity mainly depends on the strain amplitude even though, in accordance with the slight shear
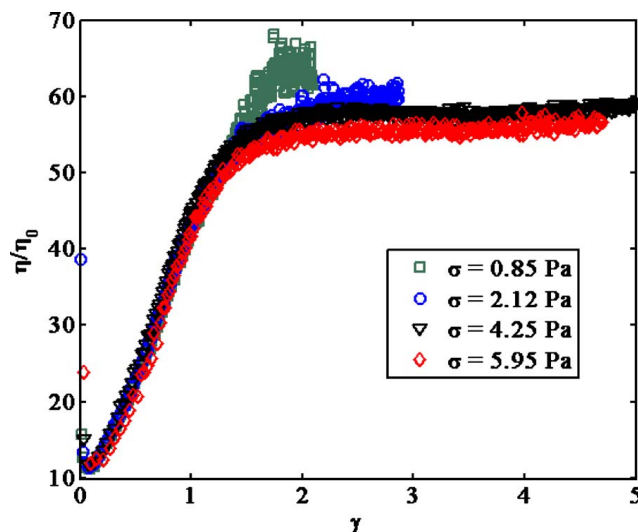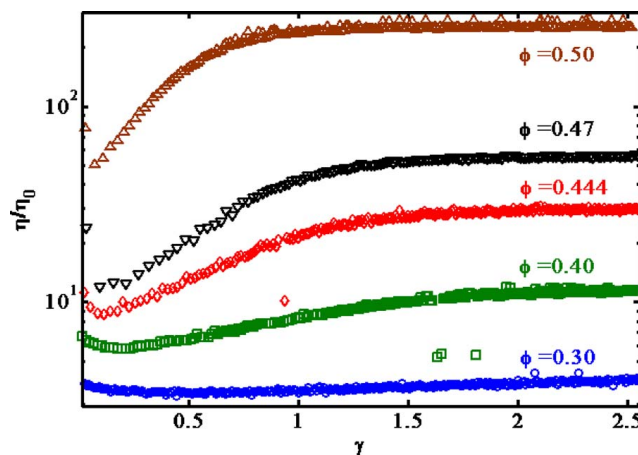
FIG. 9. Transient reduced viscosity after shear reversal versus local strain. The experiment has been performed for different applied torques that correspond to different shear stresses at the bob (σ=0.85, 2.12, 4.25, and 5.95 Pa), ϕ=0.47.

thinning behavior of the suspension (Fig. 1), the value of the plateau decreases as the shear rate increases. On the contrary, the value of the minimum of the viscosity seems not to depend on the value of the applied torque.

The same experiment is carried out for other values of the particle concentration and the results are displayed on Fig. 10. For each particle volume fraction, the value of the applied torque is chosen in order that the angular velocity of the internal cylinder at the plateau is roughly the same (around 0.5 rpm which corresponds to an average shear rate of 0.1 s^{-1}). As the particle concentration increases, the minimum is more pronounced and the strain necessary to reach the plateau value of the viscosity decreases.

A striking result shown in Fig. 11 is that the minimum of the viscosity scales as $(\phi_m^* - \phi)^{-1}$ with ϕ_m^*=0.537, while the plateau viscosity scales as $(\phi_p^* - \phi)^{-2}$ with ϕ_p^*=0.534. This result is discussed in Sec. V.

FIG. 10. Transient viscosity after shear reversal for different particle volume fractions vs local strain. $\langle \dot{\gamma} \rangle_{\text{plateau}} \approx 0.1$ s^{-1}. The applied torque values have been chosen in order the bob angular spin rate to be roughly 0.5 rpm at the plateau whatever the particle volume fraction and thus the viscosity.
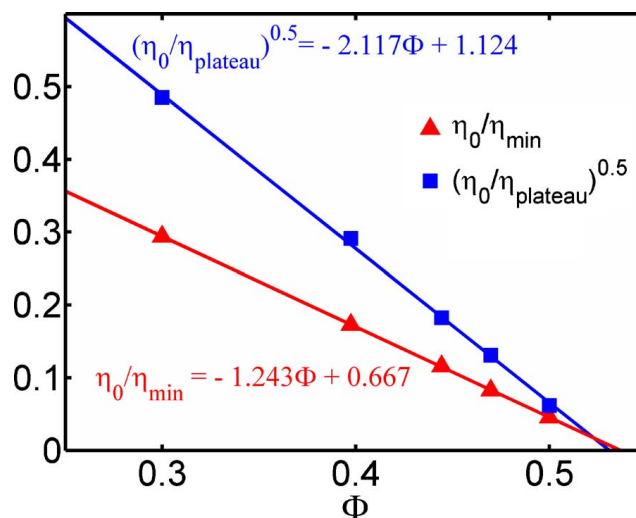
FIG. 11. Scaling law for the plateau viscosity and the minimum viscosity. The applied torque values have been chosen in order the bob angular spin rate to be roughly 0.5 rpm whatever the particle volume fraction and thus the viscosity.

V. DISCUSSION

The transient response of a concentrated suspension after shear reversal has already been studied through macroscopic rheological measurements either in narrow-gap Couette [Gadala-Maria and Acrivos (1980)] or in parallel plate geometry [Kolli *et al.* (2002); Narumi *et al.* (2002)]. In particular, it has been shown that the transient viscosity is a function of the strain only. Gadala-Maria and Acrivos (1980) proposed to explain the transient response by the development of a shear-induced microstructure. This microstructure has been observed by Parsi and Gadala-Maria (1987) and is characterized by the asymmetry of the pair distribution function with an excess of particles in the compressional quadrant. When the direction of the shear is reversed, the microstructure is broken and the particles rearrange into the mirror image of this microstructure.

In 2002, Kolli *et al.* (2002) studied the transient shear and normal force response to a shear reversal in non-Brownian suspensions in an annular plate-plate geometry. They observed that the normal force exhibited a transient behavior too. It abruptly went to a negative small value before increasing again to its positive value. They connected the initial value of both shear and normal stresses with the hydrodynamic contribution (in a structured state) and the plateau value with a mixed contribution of hydrodynamic and contact forces. They noted that the hydrodynamic contribution compared to the plateau value decreased as the concentration increased. Haan and Steif (1998) found previously the same type of behavior for the particle pressure in numerical simulations of two-dimensional suspensions of cylinders.

Thus both shear-induced microstructure and relative contributions of the hydrodynamic and non-hydrodynamic effects are presumably involved in the transient rheological response of non-Brownian suspensions.

Basically, the local response of the suspension presented in the current paper displays the same features as those obtained through conventional viscosimetric measurements. The main contribution of our work is to confirm that the transient response is actually a bulk property of the flowing suspension and cannot originate from a boundary problem such as the development of a Vand zone [Vand (1948)] or of a slip layer [Jana *et al.* (1995)].

A more precise comparison between our results and those obtained by Gadala-Maria and Acrivos (1980) reveals a small difference: while all their results collapse into a single curve when the viscosity divided by its plateau value is plotted versus the strain, our results are slightly different. Indeed, Fig. 9 shows that, as the applied torque increases, the plateau viscosity decreases while the minimum remains almost unchanged. This effect is rather weak so we do not want to give too much importance to this observation but it would mean that the shear thinning behavior of the suspension is related to a change of its microstructure together with the non-hydrodynamic interactions with the magnitude of the shear rate. Indeed, we speculate that the viscosity passes through the minimum when the microstructure has disappeared and the suspension is almost isotropic before the particles have rearranged into the steady-state structure when the viscosity plateau is reached again. In this latter state, the particles are very close together along the compression axis and it is plausible that their arrangement and the non-hydrodynamic interactions depend slightly on the value of the shear rate that causes the plateau viscosity to vary. On the opposite, if the minimum viscosity is reached when the suspension is unstructured and when non-hydrodynamic forces have relaxed, the value of the minimum should not depend on the shear rate magnitude. The results reported in Fig. 11 are more pronounced and have more implications. The minimum viscosity and the plateau value do not scale in the same way with the particle concentration. Both diverge when the particle concentration approaches approximately the same value, $\phi^*=0.535$ but with different power laws of $(\phi^*-\phi)$. The minimum viscosity diverges when ϕ tends to ϕ^* with an exponent (-1) while the plateau viscosity follows a (-2) power law. Following our speculation that the suspension is almost isotropic when the viscosity is minimum and that an anisotropic structure has formed at the plateau, two different behaviors were indeed expected. As for the plateau, the (-2) power law is usually observed both in experiments and in numerical simulations. From a theoretical point of view, Mills and Snabre (2009) proposed to explain this scaling with a model that accounts for the solid friction between particles in dynamic clusters. In the same paper, they also provide a scaling of the viscosity with the solid volume fraction for an isotropic random suspension where the dissipation is purely hydrodynamic. The viscosity is shown to scale as $\phi^{4/3} \cdot (\phi^*-\phi)^{-1}$. Thus, they predict the same divergence of the viscosity with the particle concentration as that we measured although we have not observed the $\phi^{4/3}$-dependence.

In the particle concentration range that we consider here, our results are in close agreement with Stokesian dynamics simulation of unstructured non-Brownian suspensions [Sierou and Brady (2001)]. Their results together with our experimental data are displayed in Fig. 12 where the inverse of the minimum reduced viscosity, η_0/η_{min}, is plotted versus the reduced particle volume fraction, ϕ/ϕ^* (in our case, $\phi^*=0.535$ and in the case of Stokesian dynamics results, $\phi^*=0.64$). For relatively moderate solid volume fractions $(0.55<\phi/\phi^*<0.93)$, the linear scaling is satisfactory for both results, even though the simulation results show a clear curvature. For higher particle concentrations, Sierou and Brady proposed a different scaling of the viscosity with the reduced volume fraction that fits well to their simulations for this higher range of volume fractions. Unfortunately, we did not perform measurements at so high concentrations.

We note that in the work of Sierou and Brady (2001), the particles are homogeneously and isotropically distributed, whereas Kolli et al. (2002) considered the initial values of the shear and normal stresses after shear reversal, which correspond to a structured state where the non-hydrodynamic interactions have relaxed. As for our study, we consider the minimum of the viscosity that should be obtained for the less structured state of the
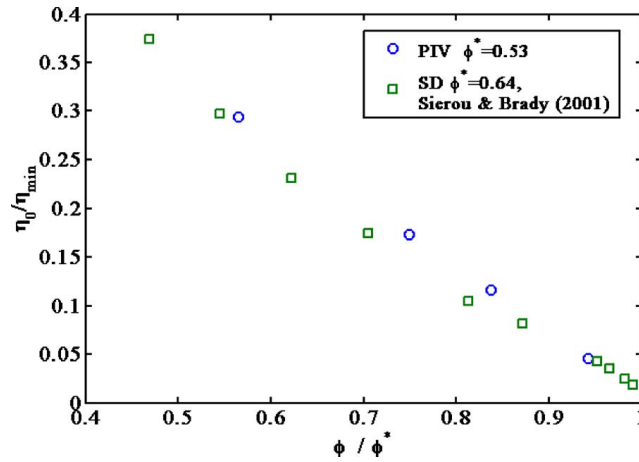
FIG. 12. Inverse of the relative viscosity η_0/η versus ϕ/ϕ^*: (○) minimum viscosity from PIV measurement. (□) High-frequency viscosity from Stokesian dynamics [Sierou and Brady (2001)].

sheared suspension, and our results compare well to the simulations of Sierou and Brady (2001). However, it is not clear to us whether the point is the isotropic structure or the lack of non-hydrodynamic interactions.

VI. CONCLUSION

We have been able to characterize the bulk transient response of concentrated non-Brownian suspensions of various particle volume fractions after shear reversal, using a PIV technique. Our measurements confirm those previously obtained using classical viscosimetry [Gadala-Maria and Acrivos (1980)][Kolli *et al.* (2002)][Narumi *et al.* (2002)]: the transient viscosity mostly depends on the strain. After shear reversal, the viscosity undergoes a step-like reduction, decreases slower, passes through a minimum, and increases again to reach a plateau value. The plateau viscosity obeys the classical Krieger–Dougherty law with an exponent n=2 and a packing concentration $\phi^*=0.535$ whose low value could be explained by interparticle forces. As for the minimum viscosity, its values compare well with the results of numerical simulation performed on random suspensions [Sierou and Brady (2001)] and is consistent with the predictions of Mills and Snabre (2009): in the range of particle volume fractions that we have studied ($0.55 < \phi/\phi^* < 0.93$), the minimum viscosity diverges as $(\phi^*-\phi)^{-1}$, suggesting that the suspension passes through an almost isotropic structure where the non-hydrodynamic forces have relaxed.

ACKNOWLEDGMENT

APPENDIX A: A POSSIBLE EXPLANATION FOR THE LOW VALUE OF THE PACKING FRACTION

Upon fitting the data of Fig. 3 with the Krieger–Dougherty law, the particle packing fraction, ϕ^*, is found to be around 0.536. This value is much smaller than the usual values obtained for non-colloidal suspensions, $\phi_{nc} \approx 0.61$. We speculate that even though the particles are as large as 31 μm in diameter, they undergo soft interactions. One can
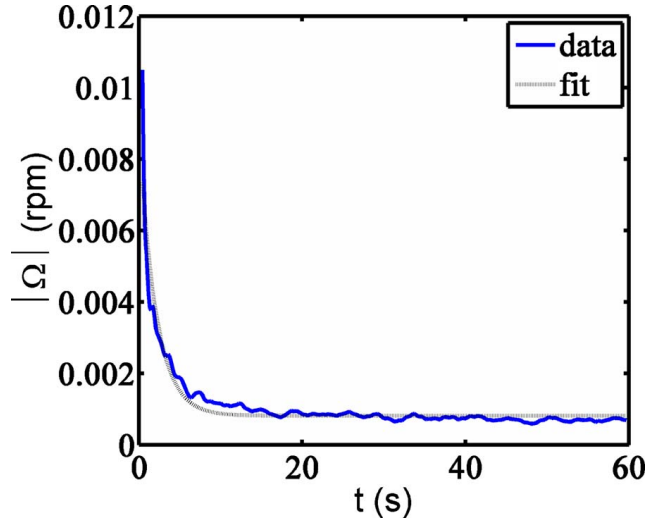
**FIG. 13.** Recovery test after shear stress cancellation, $\phi=0.444$.

wonder about the nature of the inferred interactions. We can rule out the electrostatic interactions since we have measured the same value of ϕ^* when the particles were dispersed in an aqueous solution whose polarity is of course very different from that of the mineral oil used in the present experiment. The van der Waals forces should also be discarded as their interaction range is too short for explaining the low value of the packing volume fraction. Furthermore, they should be weak since the refractive indices of the particles and of the liquid are matched. Finally, polymeric forces remain the only possible interaction between particles. We have to mention that we have attempted to wash the particles with de-ionized water and with ethanol without noting any change on the suspension rheology. According to the constructor (Microbeads AS), it is plausible that the particles are covered by polymer chains (cellulose) that served as surfactant during the manufacturing of the particles.

We can estimate the characteristic interaction length, δ, by considering the excluded volume arising from the repulsion between particles:

$$\left(\frac{a + \delta}{a}\right)^3 \approx \frac{\phi_{nc}}{\phi^*} = \frac{0.61}{0.535}, \tag{A1}$$

where a is the particle radius. Equation (A1) leads to $\delta \approx 1$ μm.

Moreover, the presence of repulsive forces between particles is corroborated by the observation of an elastic behavior of the suspension which is illustrated in Fig. 13. This recovery test has been carried out on a $\phi=0.444$ suspension. The recovery curve (solid line) is almost well fitted by an exponential function (dashed line) with a Maxwell time, τ, of about 2 s, which corresponds to an elastic modulus of approximately $\eta/\tau \approx 70$ Pa. Furthermore, we speculate that the repulsive forces between particles are responsible for a perturbation of the shear-induced microstructure. This has been observed during transient tests where shear stress steps have been applied always in the same direction after rest periods of different durations. The protocol is represented in Fig. 14(a) and the bob angular velocity response is plotted in Fig. 14(b). The longer the rest period is, the higher the angular velocity overshoot (or lower the viscosity) is. This would mean that, during shear periods, the particles are forced to approach each other in the compression direction and, when the shear is stopped, the particles move away one from each other under the
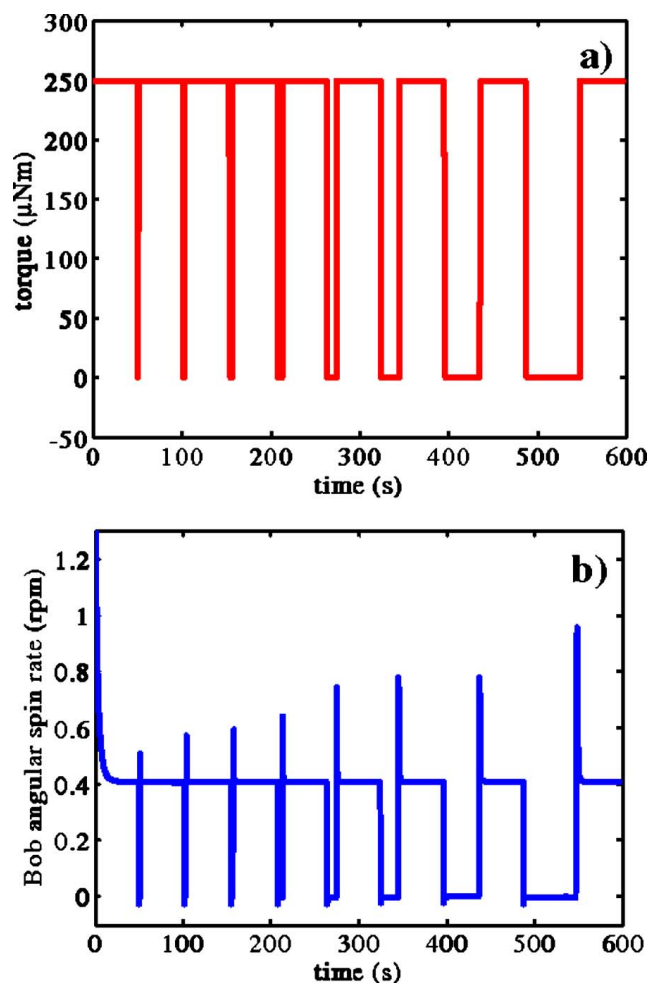
FIG. 14. Sequence of shearing and shear stress break with increasing of the break duration. (a) Applied torque. (b) Bob angular velocity response. The velocity overshoot amplitude increases with the break duration, ϕ=0.444.

repulsive interactions. Thus, after a sufficiently long rest time, the shear-induced structure of the suspension tends to disappear and its viscosity approaches the minimum viscosity recorded during shear reversal. Again, this elastic behavior together with the small value of ϕ^* suggests that some polymer molecules at the surface of the particles give rise to soft steric repulsion.

APPENDIX B: COMPARISON WITH MACROSCOPIC NARROW-GAP MEASUREMENTS

In this section, we perform classical rheometric measurements in a narrow-gap Couette geometry Z40Ti mounted on the rheometer Mars II (Haake, Thermofisher). The bob diameter is $2R_i$=41.42 mm, the gap is $g=R_o-R_i$=0.99 mm, and its height is L=55 mm. The transient viscosity of the ϕ=47% suspension is measured. After it had been poured in the cup, the suspension was shortly pre-sheared (total strain around 365) in order to obtain a well defined structure in the suspension. Then the shear reversal measurements were performed.
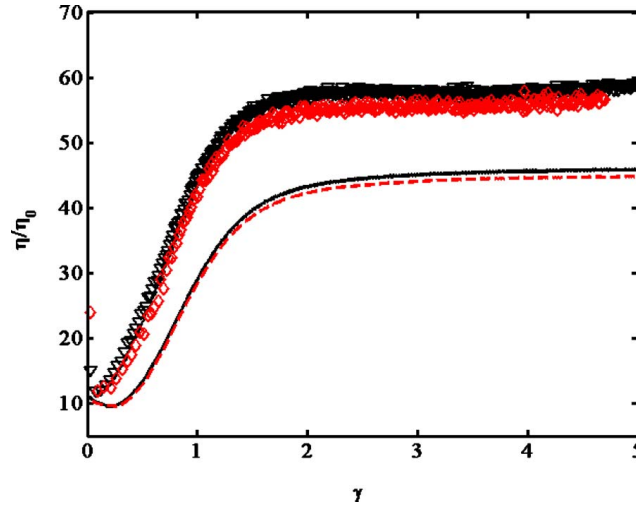
FIG. 15. Viscosity response to a shear stress reversal for a $\phi=0.47$ suspension. Wide-gap +PIV measurements: $\sigma=4.25$ Pa ($\triangledown$) and $\sigma=5.95$ Pa ($\diamond$). Narrow-gap measurements: $\sigma=4.25$ Pa (—) and $\sigma=5.95$ Pa (—-).

The raw viscosity measured for two values of the imposed shear stress (4.25 and 5.95 Pa) is displayed in Fig. 15, together with the corresponding wide-gap local measurements. The apparent viscosity is significantly lower in the narrow-gap cell, suggesting that wall slip occurs at the boundaries.

Jana et al. (1995) performed local measurements in a narrow-gap geometry to determine the slip length at the wall. They used a laser Doppler velocimetry technique to measure the velocity profile across the gap. In this paper, they sheared the suspensions for 2 days before they acquired the velocity profile, so that they had to take the radial migration into account. The wall slip was characterized by an apparent slip velocity, i.e., the difference between the velocity of the walls and the velocity of the suspension at the same position. They showed that the slip velocity u_s was related to the local shear rate $\dot{\gamma}$ and the local volume fraction ϕ by

$$u_s = \frac{\eta_r}{q} \dot{\gamma} a, \tag{B1}$$

where a is the radius of the particles and η_r is the relative viscosity of the suspension. q is a constant that is determined experimentally: in Jana et al. (1995), q=8.

In our work, the total strain during pre-shear is small, so that we can neglect migration. For comparison, Gadala-Maria and Acrivos (1980), in similar conditions, measured a characteristic strain for migration of around 4.32×10^4. Following Jana et al. (1995), we introduce a slip velocity at the bob u_{si} and at the cup u_{so}. In the case of a purely viscous homogeneous liquid, the velocity profile is given by

$$\frac{u}{r} = \frac{R_o^2 - r^2}{R_o^2 - R_i^2} \left(\frac{R_i}{r}\right)^2 \left(\Omega - \left(\frac{u_{si}}{R_i} - \frac{u_{so}}{R_o}\right)\right) + \frac{u_{so}}{R_o} \tag{B2}$$

and the shear rate

$$|\dot{\gamma}| = \left| r \frac{d}{dr}\left(\frac{u}{r}\right) \right| = \left(2 \frac{R_o^2}{R_o^2 - R_i^2} \left(\frac{R_i}{r}\right)^2\right)\left(\Omega - \left(\frac{u_{si}}{R_i} - \frac{u_{so}}{R_o}\right)\right), \tag{B3}$$

where Ω is the bob angular velocity.
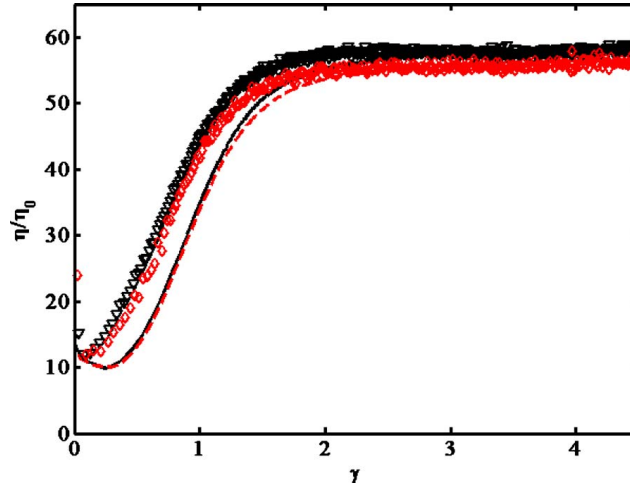
FIG. 16. Viscosity response to a shear stress reversal for a $\phi=0.47$ suspension. Wide-gap +PIV measurements: $\sigma=4.25$ Pa ($\triangledown$) and $\sigma=5.95$ Pa ($\diamond$). Narrow-gap measurements corrected for the wall slip: $\sigma=4.25$ Pa (—) and $\sigma=5.95$ Pa (—-).

From Eqs. (B1)–(B3), the slip velocity is found at the boundaries, and the velocity profile can be computed.

$$\dot{\gamma}(R_i) = \frac{2R_o^2\Omega}{R_o^2-R_i^2} \frac{\dfrac{q}{\eta_r a}}{\dfrac{q}{\eta_r a} + \dfrac{2}{R_o^2-R_i^2}\left(\dfrac{R_o^2}{R_i} + \dfrac{R_i^2}{R_o}\right)} = \dot{\gamma}_{app} \frac{\dfrac{q}{\eta_r a}}{\dfrac{q}{\eta_r a} + \dfrac{2}{R_o^2-R_i^2}\left(\dfrac{R_o^2}{R_i} + \dfrac{R_i^2}{R_o}\right)} \quad \text{(B4)}$$

with $\dot{\gamma}_{app}$ the apparent shear rate, at the bob.

Using Eq. (B4) and setting that the stress is controlled:

$$\sigma = \eta_r\dot{\gamma} = \eta_r^{app}\dot{\gamma}^{app} \quad \text{(B5)}$$

we obtain the expressions of the bulk shear rate $\dot{\gamma}$ and relative viscosity η_r versus their apparent values $\dot{\gamma}^{app}$ and η_r^{app}:

$$\dot{\gamma} = \dot{\gamma}^{app}\left(1 - \frac{2\eta_r^{app}}{q}\frac{a}{R_o^2-R_i^2}\left(\frac{R_o^2}{R_i} + \frac{R_i^2}{R_o}\right)\right),$$

$$\eta_r = \frac{\eta_r^{app}}{1 - \dfrac{2\eta_r^{app}}{q}\dfrac{a}{R_o^2-R_i^2}\left(\dfrac{R_o^2}{R_i} + \dfrac{R_i^2}{R_o}\right)} \quad \text{(B6)}$$

as well as the expression of the bulk strain:

$$\gamma = \int_0^{\gamma^{app}}\left(1 - \frac{2\eta_r^{app}(u)}{q}\frac{a}{R_o^2-R_i^2}\left(\frac{R_o^2}{R_i} + \frac{R_i^2}{R_o}\right)\right)du. \quad \text{(B7)}$$

Figure 16 displays the PIV measurements together with the viscosity measured in the narrow-gap Couette rheometer after slip correction. The wall slip-corrected viscosity has been computed with q=6.8 that is the optimal value to match the plateau viscosity measured using PIV. If, like Jana *et al.*, we take q=8, the plateau viscosity values are slightly smaller ($\eta_{plateau}=56$ Pa s for $\sigma=4.25$ Pa and $\eta_{plateau}=54$ Pa s for $\sigma=5.95$ Pa),
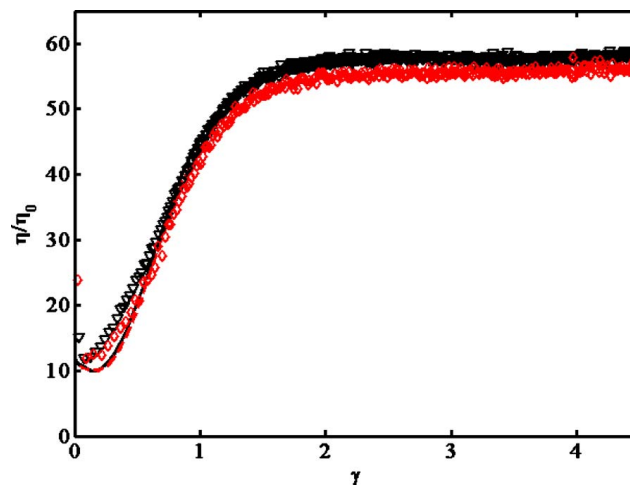
FIG. 17. Viscosity response to a shear stress reversal for a $\phi=0.47$ suspension. Wide-gap +PIV measurements: $\sigma=4.25$ Pa ($\triangledown$), $\sigma=5.95$ Pa ($\diamond$). Narrow-gap measurements corrected for the wall slip: $\sigma=4.25$ Pa (—), $\sigma=5.95$ Pa (—-). The wall slip correction is calculated using the plateau viscosity in Eq. (B1).

but it is reasonable to expect that the q value depends on the particles and on the wall roughness and the wall-slip correction proposed by Jana *et al.* reconciles the narrow-gap and the PIV measurements at the plateau. However, the beginnings of the transients are quite different, suggesting that the slip velocity (B1) is only valid when the sheared suspension has reached its steady state. According to Fig. 16, during the transient, Eq. (B1) underestimates the slip velocity.

At last, we would like to mention a striking result shown in Fig. 17 where the slip correction has been calculated upon replacing $\eta_r(\gamma)$ with its plateau value $[\eta_r(\gamma->\infty)]$, in Eq. (B1). Although we do not have any explanation for it, it appears clearly that the agreement is far better when Eq. (B1) is solved with $\eta_r(\gamma->\infty)$ rather than with $\eta_r(\gamma)$.

References

Abbas, M., E. Climent, and O. Simonin, "Fully coupled simulations of non-colloidal monodisperse sheared suspensions," Chem. Eng. Res. Des. **85**(6), 778–791 (2007).

Acrivos, A., X. Fan, and R. Mauri, "On the measurement of the relative viscosity of suspensions," J. Rheol. **38**, 1285–1296 (1994).

Adrian, R. J., "Twenty years of particle image velocimetry," Exp. Fluids **39**(2), 159–169 (2005).

Blanc, F., F. Peters, and E. Lemaire, "Particle Image Velocimetry in concentrated suspensions: application to local rheometry," Appl. Rheol. **21**, 23735–23744 (2011).

Bricker, J. M., and J. E. Buttler, "Correlation between stresses and microstructure in concentrated suspensions of non-Brownian spheres subject to unsteady shear flows," J. Rheol. **51**, 735–759 (2007).

Chow, A. W., S. W. Sinton, J. H. Iwamiya, and T. S. Stephens, "Shear-induced migration in Couette and parallel-plate viscosimeters: NMR imaging and stress measurements," Phys. Fluids A **6**, 2565–2576 (1994).

Drazer, G., J. Koplik, B. Khusid, and A. Acrivos, "Microstructure and velocity fluctuations in sheared suspensions," J. Fluid Mech. **511**, 237–263 (2004).

Fall, A., F. Bertrand, G. Ovarlez, and D. Bonn, "Yield stress and shear banding in granular suspensions," Phys. Rev. Lett. **103**, 178301 (2009).

Gadala-Maria, F., and A. Acrivos, "Shear-induced structure in a concentrated suspension of solid spheres," J. Rheol. **24**, 799–814 (1980).

Haan, J. J., and P. S. Steif, "Particle-phase pressure in a slow shearing flow based on the numerical simulation of a planar suspension of rough contacting cylinders," J. Rheol. **42**, 891–916 (1998).

Huang, N., G. Ovarlez, F. Bertrand, S. Rodts, P. Coussot, and D. Bonn, "Flow of wet granular materials," Phys. Rev. Lett. **94**(2), 028301 (2005).

Jana, S. C., B. Kapoor, and A. Acrivos, "Apparent wall slip velocity coefficients in concentrated suspensions of non colloidal particles," J. Rheol. **39**, 1123–1132 (1995).

Kolli, V. G., E. J. Pollauf, and F. Gadala-Maria, "Transient normal stress response in a concentrated suspension of spherical particles," J. Rheol. **46**, 321–333 (2002).

Leighton, D., and A. Acrivos, "The shear-induced migration of particles in concentrated suspensions," J. Fluid Mech. **181**, 415–439 (1987).

Lenoble, M., P. Snabre, and B. Pouligny, "The flow of a very concentrated slurry in a parallel-plate device: Influence of gravity," Phys. Fluids **17**, 073303 (2005).

Mills, P., and P. Snabre, "Apparent viscosity and particle pressure of a concentrated suspension of non-Brownian hard spheres near the jamming transition," Eur. Phys. J. E **30**(3), 309–316 (2009).

Morris, J. F., "A review of microstructure in concentrated suspensions and its implications for rheology and bulk flow," Rheol. Acta **48**, 909–923 (2009).

Morris, J. F., and F. Boulay, "Curvilinear flows of noncolloidal suspensions: The role of normal stresses," J. Rheol. **43**, 1213 (1999).

Narumi, T., H. See, Y. Honma, T. Hasegawa, T. Takahashi, and N. Phan-Thien, "Transient response of concentrated suspensions after shear reversal," J. Rheol. **46**, 295–305 (2002).

Ovarlez, G., F. Bertrand, and S. Rodts, "Local determination of the constitutive law of a dense suspension of noncolloidal particles through magnetic resonance imaging," J. Rheol. **50**, 259–292 (2006).

Parsi, F., and F. Gadala-Maria, "Fore-and-aft asymmetry in a concentrated suspension of solid spheres," J. Rheol. **31**, 725–732 (1987).

Phillips, R. J., R. C. Armstrong, R. A. Brown, A. L. Graham, and J. R. Abbott, "A constitutive equation for concentrated suspensions that accounts for shear-induced particle migration," Phys. Fluids A **4**, 30–40 (1992).

Shapley, N. C., R. C. Armstrong, and R. A. Brown, "Laser Doppler velocimetry measurements of particle velocity fluctuations in a concentrated suspension," J. Rheol. **46**, 241–272 (2002).

Sierou, A., and J. F. Brady, "Accelerated Stokesian dynamics simulations," J. Fluid Mech. **448**, 115–146 (2001).

Sierou, A., and J. F. Brady, "Rheology and microstructure in concentrated noncolloidal suspensions," J. Rheol. **46**, 1031–1056 (2002).

Singh, A., and P. R. Nott, "Normal stresses and microstructure in bounded sheared suspensions via Stokesian dynamics simulations," J. Fluid Mech. **412**, 279–301 (2000).

Stickel, J. J., and R. L. Powell, "Fluid mechanics and rheology of dense suspensions," Annu. Rev. Fluid Mech. **37**, 129–149 (2005).

Vand, V., "Viscosity of solutions and suspensions. I Theory," J. Phys. Colloid Chem. **52**, 277–299 (1948).

Wiederseiner, S., C. Ancey, M. Rentschler, and N. Andreini, "Rheophysics of highly concentrated coarse-particle suspensions in a wide-gap Couette rheometer," AIP Conf. Proc. **1145**(1), 1063–1066 (2009).

Yeo, K., and M. R. Maxey, "Dynamics of concentrated suspensions of non-colloidal suspensions," J. Fluid Mech. **649**, 205–231 (2010).

Zarraga, I. E., D. A. Hill, and D. T. Leighton, "The characterization of the total stress of concentrated suspensions of noncolloidal spheres in Newtonian fluids," J. Rheol. **44**, 185–220 (2000).

D.3 Experimental Signature of the Pair Trajectories of Rough Spheres in the Shear-Induced Microstructure in Noncolloidal Suspensions

Experimental Signature of the Pair Trajectories of Rough Spheres in the Shear-Induced Microstructure in Noncolloidal Suspensions

Frédéric Blanc, François Peters, and Elisabeth Lemaire

CNRS, Université de Nice, LPMC-UMR 6622, 06108 Nice Cedex 2, France

(Received 23 August 2011; published 8 November 2011)

The shear-induced microstructure in a semidilute noncolloidal suspension is studied. A high-resolution pair distribution function in the plane of shear is experimentally determined. It is shown to be anisotropic, with a depleted direction close to the velocity axis in the recession quadrant. The influence of roughness on the interaction between particles is quantitatively evidenced. The experimental results compare well with a model from particle pair trajectories.

The influence of the particle interactions on the rheology of non-Brownian suspensions, such as normal stress differences and shear-induced migration, and their link with the shear-induced microstructure, are questions of central interest and remain an experimental challenge. A quantitative measurement of the microstructure is provided by the pair distribution function (PDF). Since the pioneering work of Bossis and Brady [1], in Stokesian dynamics, the PDF of an unbounded suspension of interacting spheres undergoing a simple shear flow is known to have an angular dependence. In a semidilute suspension, experimental [2], numerical [3,4], and analytical [5] studies have shown the existence of a particle depleted area along the velocity direction. In their numerical work, Drazer *et al.* [4] showed that, besides this anisotropy, a fore-aft asymmetry appears in the presence of strong enough nonhydrodynamic forces acting between the spheres. Repulsion forces between particles eliminate closed orbit trajectories and the particles that were close from each other in the approach quadrant are redistributed in the recession quadrant, leading downstream to a tilt of the depleted area away from the velocity direction. Though only a few experimental measurements of PDF have been performed in non-Brownian suspensions [6,7], the depleted area close to the velocity direction in a simple shear flow has already been accurately studied by Rampall *et al.* in semidilute suspensions ($\phi = 0.10$–0.15). They explain their experimental results by a model that computes the PDF from the trajectories of two colliding rough spheres. Besides the depleted area, their theoretical PDF shows fore-aft asymmetry. These predictions are in qualitative agreement with their experimental results. However, these early measurements suffer from a quite low resolution that precludes a fully quantitative comparison.

In this Letter, we report the measurement of a high-resolution PDF in a semidilute sheared suspension. The results are in qualitative agreement with the works mentioned above but demonstrate a new property: in the recession quadrant, right above the depleted zone, a tail-like high particle concentration zone is apparent, that is not present in the approach quadrant. A trajectory-based model shows that this tail is a direct signature of the pair trajectories of rough spheres in the shear-induced microstructure.

This has been observed with a suspension of PMMA particles (Arkema BS510) dispersed in a Newtonian liquid ($\eta_0 = 0.85$ Pa $\cdot$ s) designed by Cargille Laboratories (Immersion liquid Code 11295101160) in order to match both the density ($d = 1180$ kg $\cdot$ m^{-3}) and the refractive index ($n = 1.49$) of the particles. To improve the index matching, the temperature is controlled ($T = 37°$ C). The particles are sieved to reduce the initially large size distribution. The final size distribution is determined by direct microscope observation over several hundreds of particles. The particles diameter is $2a = 170 \pm 12$ μm. The suspension is sheared in a cylindrical Couette cell, $R_i = 19$ mm in inner radius, $R_o = 24$ mm in outer radius and 60 mm in height. The whole apparatus design is precisely described in [8,9]. Some fluorescent dye (Nile Blue A) is dissolved in the host liquid and a thin laser sheet (635 nm, 30 μm in thickness), perpendicular to the cell axis, illuminates the suspension. The position of the laser sheet, 11 mm above the bottom of the cell, allows to neglect the bottom end effect on the flow [8]. A CCD camera positioned under the cell and equipped with a long pass filter (650 nm) images the interstitial fluid, showing the particles in negative (Fig. 1).

The particle positions and radii are detected using an open source MATLAB procedure based on the Circular Hough Transform [10,11]. The position of the particle centers is determined with a subpixel resolution. For the sake of comparison, the mean particle radius $a = 85$ μm corresponds to 14.7 pixels on the frame. The inner cylinder angular velocity is controlled by a rheometer (Mars II, Thermofisher) and set to the value $\Omega = 1$ rpm. The Reynolds number Re $= (a^2 d/\eta_0)\Omega R_i/(R_o - R_i) \approx 4 \times 10^{-6}$ and the Péclet number Pe $= (\eta_0 a^3/k_B T)\Omega R_i/(R_0 - R_i) \approx 6 \times 10^7$ allow to neglect inertia and Brownian motion. The shear rate $\dot{\gamma} = 2\Omega R_i^2 R_o^2/((R_o^2 - R_i^2)R^2)$ depends on the distance to the
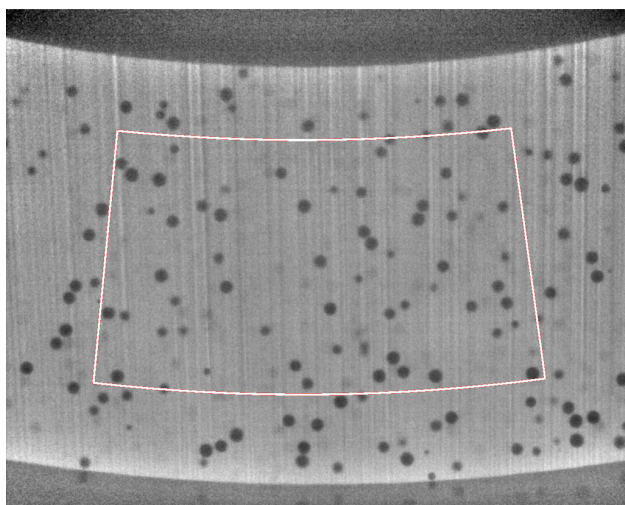
FIG. 1 (color online). Typical image. $\phi = 5\%$. Only the origin particles in the white box are considered.

cylinders center R, and its variation across the gap is approximately 50%. This is not a problem, however, since at low concentration, the non-Brownian suspension rheology does not depend on the shear rate.

For each frame, a 2D PDF is built in the following way. First, for each particle pair, the relative position vector of the pair in the local flow direction frame of particle 1 is determined [see Fig. 2(a)]. The plane of the particles relative position $\vec{r}_{12}$ (ρ, θ) is evenly sampled ($\Delta\rho =$ 1 pixel, $\Delta\theta = 2\pi/80$ rad), and the number of particle pairs (1,2) corresponding to a particular sample $N(\rho, \theta)$ is normalized by the total number of origin particles N_1, by the sample surface, and by the mean surface density of particles n_{0S}.

$$g(\rho, \theta) = \frac{1}{n_{0S}} \frac{N(\rho, \theta)}{N_1 \rho \Delta\rho \Delta\theta}. \qquad (1)$$

The PDF is then averaged over all images. $g(\rho, \theta)$ is thus a surface distribution function, that is related to the real 3D PDF through the integration over an interval $[-2\Delta z_{max}, 2\Delta z_{max}]$ in the z direction, as explained in [2] and shown in Fig. 2(b). To reduce this interval, an histogram of the apparent radii of the detected particles is built, and only
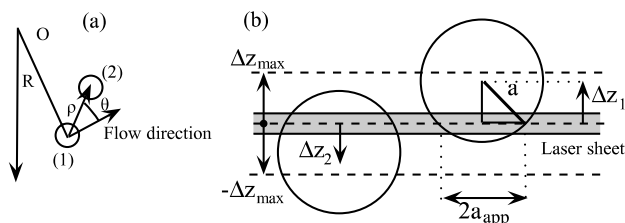
particles greater than or equal to 13 pixels ($0.88a$) are taken into account. From this, we evaluate Δz_{max} to approximately $0.5a$ (Fig. 2). To avoid frame boundary effects on the large ρ limit of $g(\rho, \theta)$, all origin particles (1) outside a central area are rejected (Fig. 1). The distance of the box edges to the frame edges is larger than $11a$. In addition, in order to reduce the hydrodynamic wall effects, no particle (2) closer than an arbitrary distance of $3a$ to the inner or outer cylinder is considered. Thus, the PDF should not suffer any frame boundary induced spurious decrease for interparticle distances smaller than $8a$.

We turn now to the PDF measured for a $\phi = 5\%$ suspension. 50 000 frames are recorded at the rate 0.33 fps during more than 41 hours. We have checked that the PDF computed using the frames 1 to 10 000 was not different from the PDF shown here, except for statistical noise, suggesting that any transient state can be neglected. Actually, we evaluate the transient time to the time necessary to break the closed orbits, i.e., the collision time $1/\dot{\gamma} \approx 3$ s that is much smaller than the experiment duration. Figure 3 displays the measured PDF. As already shown by Rampall et al. [2], the PDF is anisotropic, with a depleted area in the approximate direction of the flow velocity. To be specific, as shown in Fig. 4, the depleted direction is situated around the angle $\theta \approx 6°$ in the recession quadrant. This slight tilt angle away from the velocity axis suggests some particle roughness. Away from this depleted direction, at large distance from the origin, the PDF is quite isotropic, with a value close to 1, as expected from the normalization in Eq. (1). We note in passing that any strong influence of the walls or of a possible

FIG. 2 (color online). (a) Pair position vector relative to the local azimuthal flow direction (b) a_{app} is the apparent radius of the particle.
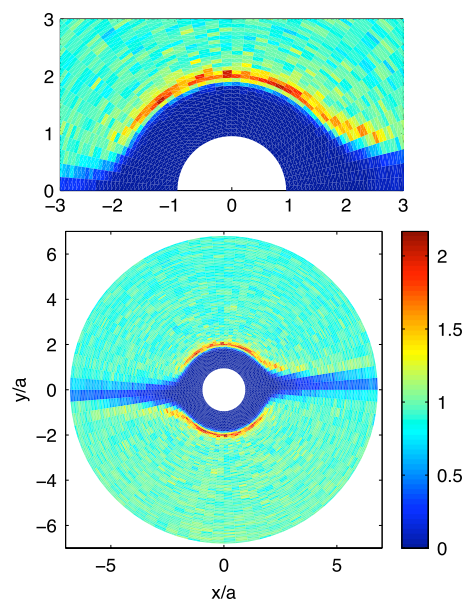

FIG. 3 (color online). Pair distribution function in the plane $(\vec{v}, \vec{\nabla}v)$. $\phi = 5\%$. The approach quadrants are defined by $xy < 0$. Up: magnification of the central region.
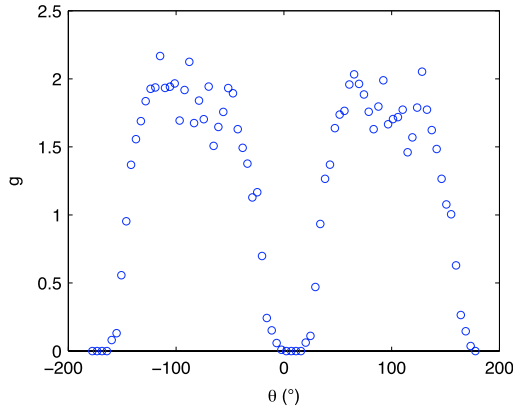
FIG. 4 (color online).   PDF averaged over the ρ interval [1.97a 2.04a]. The approach quadrant is $\theta \in [90°, 180°]$.

concentration gradient, that would destroy this symmetry, can be ruled out. Another classical property is the large increase of the PDF near the surface $\rho = 2a$. Moreover, thanks to the large number of frames that leads to a high-resolution PDF, we observe for the first time a tail-like high particle concentration zone in the recession quadrant, that is not present in the approach quadrant.

This high concentration tail clearly recalls the relative trajectory of two rough particles in a simple shear flow (Fig. 5). As we will show in the following, this tail allows a good estimation of the particles roughness. Indeed, such roughness-modified trajectories have already been used to compute the shear-induced diffusivity in a dilute suspension [12]. In their paper, a roughness length ϵa is defined. When the distance between the particles equals $(2 + \epsilon)a$, the relative radial velocity is cancelled, preventing the particles to get closer from each other. This results in a break of the fore-aft symmetry, the spheres separating on streamlines further apart than on their approach (Fig. 5). Following the idea of Rampall *et al.* [2], we use the roughness-modified trajectories to compute the PDF. For
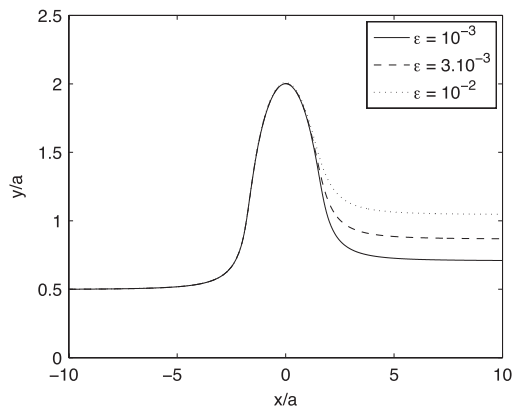

FIG. 5.   Trajectory from the point $x/a = -10$, $y/a = 0.5$, $z/a = 0$ for different values of the roughness ϵa.

an introductory purpose, we recall here the classical isotropic expression obtained by Batchelor and Green for the PDF from the motion of two smooth particles in an ambient linear flow [13,14].

$$g_{\text{BG}}(r) = \frac{1}{1 - A(r)} \exp\left(\int_r^\infty \frac{3}{s} \frac{B(s) - A(s)}{1 - A(s)} ds\right), \quad (2)$$

where A and B are mobility functions that depend only on the interparticle distance r, and whose expressions can be found in [12]. Equation (2) applies everywhere a trajectory comes from infinity. In a simple shear flow however, there exists an infinite region of closed trajectories in which it is impossible to predict the PDF values. In the plane of shear, the particles that undergo such closed orbits approach each other at a distance smaller than approximately $2.00004a$ [12,15]. Following Rampall *et al.* [2], and in agreement with the numerical work of Drazer *et al.* [3], we suppose that, owing to the roughness that prevents particles to come too close to each other, the bound pairs are eliminated. Thus, only the trajectories from infinity will be taken into account.

We use the expression of the mobility functions $A(r)$ and $B(r)$ given in [12] to compute the relative velocity $\vec{V}$ of two particles in a simple shear flow $\vec{V}_\infty = \dot{\gamma} y \vec{e}_x$, together with their relative trajectory. $A(r)$ is set to 1 when contact occurs at $r = (2 + \epsilon)a$. The integration scheme, namely, a variable order Adams-Bashforth-Moulton predictor-corrector solver, was tested as in [12] for $\epsilon = 0$ and provided the same results. Figure 5 displays trajectories in the plane of shear for different values of the roughness length. For a given value of ϵ, all trajectories that drive the particles in contact concentrate downstream on a single trajectory. Thus, downstream, no particle can locate between the x axis and this trajectory. We note that the displacement of the trajectories depends strongly on ϵ. To determine the PDF, we compute the trajectories from evenly spaced origins in the plane ($x_0 = -10a$), with a sample time $\Delta t = 0.01/\dot{\gamma}$. The set of trajectories forms a distribution of particle positions $\vec{r}$ in the probability space, and each point has a velocity $\vec{V}$. Since the number of particles is conserved, this distribution is a discrete form of a function $p(\vec{r})$ that obeys Eq. (3):

$$\frac{\partial p}{\partial t} + \vec{\nabla} \cdot (p\vec{V}) = \vec{\nabla} \cdot (p\vec{V}) = 0. \quad (3)$$

We recall [3,14] here that the PDF $g(\vec{r})$ is related to the conditional probability $P(\vec{r}|\vec{r}_0 = 0)$ of finding a sphere with its center at $\vec{r}$ given that there is a sphere with its center at $\vec{r}_0 = 0$ and the bulk density of particles n_0 through the equation $g(\vec{r}) = P(\vec{r}|\vec{r}_0 = 0)/n_0$. Since $P(\vec{r}|\vec{r}_0 = 0)$ obeys Eq. (3) too [14], it is sufficient to impose the limit $p \to 1$ as $r \to \infty$ to set $p(\vec{r}) = g(\vec{r})$. To this purpose, each trajectory is weighted by the inverse of the density in the plane $x = x_0$, namely $L_y L_z V_x(x_0)\Delta t$, where L_y and L_z are the distances between the trajectories origins
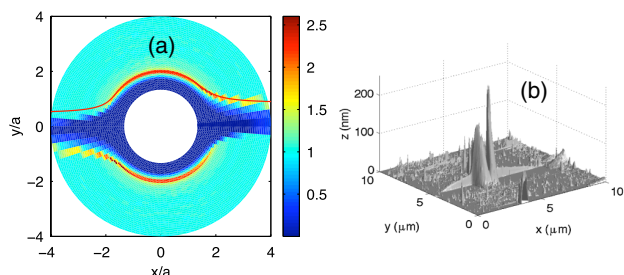
FIG. 6 (color online). (a) PDF from particle trajectories. The roughness is $\epsilon = 3 \times 10^{-3}$. Red line: a trajectory in the plane of shear for which contact occurs. (b) AFM image of the particle surface.

in that plane along the directions y and z. From this set of points, we compute the relevant 2D PDF that could be compared to our experimental results. The region of interest is defined by $z \in [-2\Delta z_{\max}, 2\Delta z_{\max}]$, $\rho = \sqrt{x^2 + y^2} \in [2a, R_{\max}]$ where we chose $R_{\max} = 4a$. This region is sampled in polar coordinates with the sampling periods $\Delta \rho = a/15$, $\Delta \theta = \pi/40$, and the number of points in each cell divided by its volume $4\Delta z_{\max}\Delta(\rho^2)/2\Delta\theta$ gives the sought PDF.

We restrict the plane ($x = x_0 = -10a$) of trajectory origins outside the closed orbits region. In order the PDF to be smooth enough, the value of the sampling period in the plane $x = x_0$ have been chosen: $L_z/(2\Delta z_{\max}) = 1/20$, $L_y/a = 1/50$. $\Delta z_{\max} = 0.5a$ has been manually adjusted to fit the experimental data at best. We note that this value corresponds also to the estimation of $\Delta z_{\max}$ from the distribution of particle radii [Fig. 2(b)]. We have checked that this method yield the isotropic distribution of Eq. (2) in the case of a pure strain flow. Concerning the simple shear flow, we obtain the PDF in Fig. 6(a) for a roughness $\epsilon a = 3 \times 10^{-3}a = 255$ nm. A trajectory in the plane of shear for which contact occurs is also shown for the same roughness. It is centered on the tail in the recession quadrant. We have checked that away from the depleted area and the tail, the PDF is identical to the isotropic g_{BG} of Eq. (2), in agreement with [3]. Figure 7(a) displays the experimental and computed PDF $g(\rho, \theta)$ as a function of θ for two values of the distance ρ. The agreement is very good, especially concerning the position of the tail that appears clearly on the experimental curve. The radial profiles can be compared on Fig. 7(b) for three different angles. The model describes accurately the experimental PDF, both in the direction of the velocity gradient ($85.5° < \theta < 90°$) and near the depleted direction ($18° < \theta < 22.5°$). However, in the depleted direction ($0° < \theta < 4.5°$), the model predicts the total lack of particles in contrast to the experimental results. As already mentioned in [2], this is probably the consequence of multibody effects. Finally, we have performed surface roughness measurements on the particles using an atomic force microscope. The main roughness height is small (≈ 20 nm), with isolated bumps,
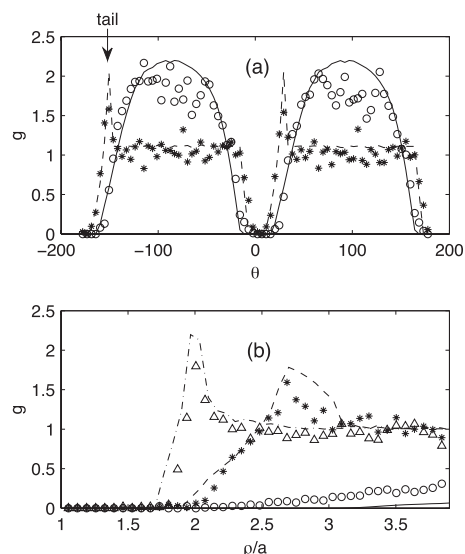

FIG. 7. Experimental (symbols) and computed (lines) PDF. (a) $g(\rho, \theta)$ vs θ ($\circ$) $1.97 < \rho < 2.04$; ($*$) $2.31 < \rho < 2.38$; ($-$) $1.93 < \rho < 2.00$; ($- -$) $2.33 < \rho < 2.40$; (b) $g(\rho, \theta)$ vs ρ/a ($\circ$) $0 < \theta < 4.5$; ($*$) $18° < \theta < 22.5°$; ($\triangle$) $85.5° < \theta < 90°$; ($-$) $0 < \theta < 4.5°$; ($- -$) $18° < \theta < 22.5°$; ($- \cdot$) $85.5° < \theta < 90°$.

approximately 200 nm in height, as shown on Fig. 6(b). Those bumps are frequent, even if we did not perform any extensive statistical study. These direct measurements are fully consistent with the experimental PDF.

In conclusion, we have measured a high-resolution PDF in a sheared dilute suspension. Its fore-aft asymmetry is quantitatively explained by the particle roughness as modeled by a minimum approach distance between particles ϵa [12], which can be determined with reasonable accuracy. Some experiments are currently performed on more concentrated suspensions ($\phi = 0.10$–0.55). In the semidilute regime, we observe that the tilt angle from the velocity axis hardly depends on the volume fraction. For volume fractions higher than 0.2, the tilt angle increases with the particle concentration, as already reported by Drazer et al. [3]. In addition, the tail turns blurred, partly due to poorer statistics (1000 frames per PDF), but also to increasingly large multibody effects, that modify the pair trajectories.

[1] G. Bossis and J. Brady, J. Chem. Phys. **80**, 5141 (1984).
[2] I. Rampall, J. Smart, and D. Leighton, J. Fluid Mech. **339**, 1 (1997).
[3] G. Drazer, J. Koplik, B. Khusid, and A. Acrivos, J. Fluid Mech. **511**, 237 (2004).

[4] G. Drazer, J. Koplik, B. Khusid and A. Acrivos., J. Fluid Mech. **460**, 307 (2002).

[5] H. J. Wilson and R. H. Davis. J. Fluid Mech. **421**, 339 (2000).

[6] D. Husband and F. Gadala-Maria, J. Rheol. **31**, 95 (1987).

[7] F. Parsi and F. Gadala-Maria, J. Rheol. **31**, 725 (1987).

[8] F. Blanc, F. Peters, and E. Lemaire, Applied Rheology **21**, 23 735 (2011).

[9] F. Blanc, F. Peters, and E. Lemaire, J. Rheol. **55**, 835 (2011).

[10] T. Peng, http://www.mathworks.com/matlabcentral/fileexchange/9168.

[11] C. Kimme, D. Ballard, and J. Sklansky, Commun. ACM **18**, 120 (1975).

[12] F. Da Cunha and E. Hinch, J. Fluid Mech. **309**, 211 (1996).

[13] G. Batchelor and J. Green, J. Fluid Mech. **56**, 375 (1972).

[14] G. K. Batchelor and J. T. Green, J. Fluid Mech. **56**, 401 (1972).

[15] P. Arp and S. Mason, J. Colloid Interface Sci. **61**, 21 (1977).

Bibliographie

[1] F. Peters and L. Petit. A broad band spectroscopy method for ultrasound wave velocity and attenuation measurement in dispersive media. *Ultrasonics*, 41(5) :357–363, 2003.

[2] F. Peters and L. Petit. Propagation of ultrasound waves in concentrated suspensions. *Acta Acustica united with Acustica*, 86(5) :838–846, 2000.

[3] F. Peters and E. Lemaire. Cohesion induced by a rotating magnetic field in a granular material. *Physical Review E*, 69(6) :061302, 2004.

[4] G. Quincke. Ueber rotationen im constanten electrischen felde. *Annalen der Physik*, 295(11) :417–486, 1896.

[5] J.R. Melcher. Electric fields and moving media. *Education, IEEE Transactions on*, 17(2) :100–110, 1974.

[6] T.B. Jones. Quincke rotation of spheres. *Industry Applications, IEEE Transactions on*, IA-20(4) :845–849, 1984.

[7] L. Lobry and E. Lemaire. Viscosity decrease induced by a dc electric field in a suspension. *Journal of electrostatics*, 47(1-2) :61–69, 1999.

[8] A. Cebers, E. Lemaire, and L. Lobry. Internal rotations in dielectric suspensions. *Magnetohydrodynamics*, 36(4) :282–299, 2000.

[9] A. Cebers, E. Lemaire, and L. Lobry. Flow modification induced by quincke rotation in a capillary. *International Journal of Modern Physics B*, 16 :2603–2609, 2002.

[10] E. Lemaire and L. Lobry. Chaotic behavior in electro-rotation. *Physica A : Statistical Mechanics and its Applications*, 314(1-4) :663–671, 2002.

[11] E. Lemaire, L. Lobry, and N. Pannacci. Flow rate increased by electrorotation in a capillary. *Journal of electrostatics*, 64(7-9) :586–590, 2006.

[12] N. Pannacci, E. Lemaire, and L. Lobry. Rheology and structure of a suspension of particles subjected to quincke rotation. *Rheologica acta*, 46(7) :899–904, 2007.

[13] N. Pannacci, E. Lemaire, and L. Lobry. Dc conductivity of a suspension of insulating particles with internal rotation. *The European Physical Journal E : Soft Matter and Biological Physics*, 28(4) :411–417, 2009.

[14] T.C. Halsey. Electrorheological fluids. *Science*, 258(5083) :761, 1992.

[15] F. Peters, L. Lobry, and E. Lemaire. Experimental observation of lorenz chaos in the quincke rotor dynamics. *Chaos : An Interdisciplinary Journal of Nonlinear Science*, 15 :013102, 2005.

[16] P. Kuzhir, G. Bossis, and V. Bashtovoi. Effect of the orientation of the magnetic field on the flow of a magnetorheological fluid. i. plane channel. *Journal of Rheology*, 47 :1373, 2003.

[17] A Cebers. Internal rotation in hydrodynamics of low conducting dielectric suspensions. *Mehanica Zhidkosti i Gaza,*, 2 :86–90, 1980. (en russe).

[18] E. Lemaire, L. Lobry, N. Pannacci, and F. Peters. Viscosity of an electro-rheological suspension with internal rotations. *Journal of Rheology*, 52 :769, 2008.

[19] A. Einstein. Eine neue bestimmung der moleküldimensionen. *Annalen der Physik*, 324(2) :289–306, 1906.

[20] GK Batchelor. The stress system in a suspension of force-free particles. *J. Fluid Mech*, 41(3) :545–570, 1970.

[21] GK Batchelor and JT Green. The determination of the bulk stress in a suspension of spherical particles to order c2. *Journal of Fluid Mechanics*, 56(03) :401–427, 1972.

[22] R.E. Rosensweig. *Ferrohydrodynamics*. Dover Pubns, 1997.

[23] H. Brenner. Rheology of two-phase systems. *Annual Review of Fluid Mechanics*, 2(1) :137–176, 1970.

[24] S. Manneville, L. Bécu, and A. Colin. High-frequency ultrasonic speckle velocimetry in sheared complex fluids. *European Physical Journal Applied Physics*, 28 :361–373, 2004.

[25] W.B. Russel, WB Russel, DA Saville, and W.R. Schowalter. *Colloidal dispersions*. Cambridge Univ Press, 1992.

[26] F. Peters, L. Lobry, A. Khayari, and E. Lemaire. Size effect in quincke rotation : a numerical study. *The Journal of chemical physics*, 130 :194905, 2009.

[27] P. Bergé, Y. Pomeau, C. Vidal, and D. Ruelle. *L'ordre dans le chaos : vers une approche déterministe de la turbulence*, volume 33. Hermann, 1984.

[28] M. von Smoluchowski. Electrische endosmose und strömungsströme. *Handbuch der Elektrizität und des Magnetismus*, 2, 1921.

[29] R.W. O'Brien and L.R. White. Electrophoretic mobility of a spherical colloidal particle. *J. Chem. Soc., Faraday Trans. 2*, 74 :1607–1626, 1978.

[30] B.J. Berne and R. Pecora. *Dynamic light scattering : with applications to chemistry, biology, and physics*. Dover Pubns, 2000.

[31] M. Medrano, AT Perez, L. Lobry, and F. Peters. Electrophoretic mobility of silica particles in a mixture of toluene and ethanol at different particle concentrations. *Langmuir*, 25(20) :12034–12039, 2009.

[32] LD Reed, FA Morrison, et al. Hydrodynamic interactions in electrophoresis. *Journal of Colloid and Interface Science*, 54(1) :117–133, 1976.

[33] A.A. Shugai, S.L. Carnie, D.Y.C. Chan, and J.L. Anderson. Electrophoretic motion of two spherical particles with thick double layers. *Journal of colloid and interface science*, 191(2) :357–371, 1997.

[34] G. Ovarlez, F. Bertrand, and S. Rodts. Local determination of the constitutive law of a dense suspension of noncolloidal particles through magnetic resonance imaging. *Journal of Rheology*, 50 :259, 2006.

[35] S.H. Maron and P.E. Pierce. Application of ree-eyring generalized flow theory to suspensions of spherical particles. *Journal of colloid science*, 11(1) :80–95, 1956.

[36] IM Krieger and TJ Dougherty. A mechanism for non-newtonian flow in suspensions of rigid particles. *Trans. Soc. Rheol*, 3 :137, 1959.

[37] I.E. Zarraga, D.A. Hill, and D.T. Leighton Jr. The characterization of the total stress of concentrated suspensions of noncolloidal spheres in newtonian fluids. *Journal of Rheology*, 44 :185, 2000.

[38] A. Singh and P.R. Nott. Experimental measurements of the normal stresses in sheared stokesian suspensions. *Journal of Fluid Mechanics*, 490 :293–320, 2003.

[39] F. Boyer, O. Pouliquen, and É. Guazzelli. Suspensions in a tilted trough : second normal stress difference. *J. Fluid Mech.*, 686 :5, 2011.

[40] É. Couturier, F. Boyer, O. Pouliquen, and É. Guazzelli. Suspensions in a tilted trough : second normal stress difference. *J. Fluid Mech*, 686 :26, 2011.

[41] JR Abbott, N. Tetlow, AL Graham, SA Altobelli, E. Fukushima, LA Mondy, and TS Stephens. Experimental observations of particle migration in concentrated suspensions : Couette flow. *Journal of rheology*, 35 :773, 1991.

[42] A.W. Chow, S.W. Sinton, J.H. Iwamiya, and T.S. Stephens. Shear-induced particle migration in couette and parallel-plate viscometers : Nmr imaging and stress measurements. *Physics of Fluids*, 6 :2561, 1994.

[43] P.R. Nott and J.F. Brady. Pressure-driven flow of suspensions : simulation and theory. *Journal of Fluid Mechanics*, 275 :157–200, 1994.

[44] J.F. Morris and F. Boulay. Curvilinear flows of noncolloidal suspensions : The role of normal stresses. *Journal of rheology*, 43 :1213, 1999.

[45] P.R. Nott, E. Guazzelli, and O. Pouliquen. The suspension balance model revisited. *Physics of Fluids*, 23 :043304, 2011.

[46] V. Breedveld, D. van den Ende, A. Tripathi, and A. Acrivos. The measurement of the shear-induced particle and fluid tracer diffusivities in concentrated suspensions by a novel method. *Journal of Fluid Mechanics*, 375(1) :297–318, 1998.

[47] DJ Pine, JP Gollub, JF Brady, and AM Leshansky. Chaos and threshold for irreversibility in sheared suspensions. *Nature*, 438(7070) :997–1000, 2005.

[48] S. Kim and S.J. Karrila. *Microhydrodynamics : principles and selected applications*. Butterworth-Heinemann Boston, 1991.

[49] FR Da Cunha and EJ Hinch. Shear-induced dispersion in a dilute suspension of rough spheres. *Journal of Fluid Mechanics*, 309(1) :211–223, 1996.

[50] J.F. Brady and G. Bossis. Rheology of concentrated suspensions of spheres in simple shear flow by numerical simulation. *Journal of Fluid Mechanics*, 155 :105–29, 1985.

[51] J.F. Brady and J.F. Morris. Microstructure of strongly sheared suspensions and its impact on rheology and diffusion. *Journal of Fluid Mechanics*, 348 :103–139, 1997.

[52] A. Meunier and G. Bossis. The influence of surface forces on shear-induced tracer diffusion in mono and bidisperse suspensions. *The European Physical Journal E : Soft Matter and Biological Physics*, 25(2) :187–199, 2008.

[53] A. Sierou and JF Brady. Rheology and microstructure in concentrated noncolloidal suspensions. *Journal of Rheology*, 46 :1031, 2002.

[54] G. Drazer, J. Koplik, B. Khusid, and A. Acrivos. Deterministic and stochastic behaviour of non-brownian spheres in sheared suspensions. *Journal of Fluid Mechanics*, 460 :307–335, 2002.

[55] G. Drazer, J. Koplik, B. Khusid, and A. Acrivos. Microstructure and velocity fluctuations in sheared suspensions. *Journal of Fluid Mechanics*, 511 :237–263, 2004.

[56] H.J. Wilson and R.H. Davis. The viscosity of a dilute suspension of rough spheres. *Journal of Fluid Mechanics*, 421 :339–367, 2000.

[57] H.J. Wilson and R.H. Davis. Shear stress of a monolayer of rough spheres. *Journal of Fluid Mechanics*, 452 :425–441, 2002.

[58] I.E. Zarraga and D.T. Leighton Jr. Normal stress and diffusion in a dilute suspension of hard spheres undergoing simple shear. *Physics of Fluids*, 13 :565, 2001.

[59] F. Gadala-Maria and A. Acrivos. Shear-induced structure in a concentrated suspension of solid spheres. *Journal of Rheology*, 24 :799, 1980.

[60] T. Narumi, H. See, Y. Honma, T. Hasegawa, T. Takahashi, and N. Phan-Thien. Transient response of concentrated suspensions after shear reversal. *Journal of Rheology*, 46 :295, 2002.

[61] V.G. Kolli, E.J. Pollauf, and F. Gadala-Maria. Transient normal stress response in a concentrated suspension of spherical particles. *Journal of Rheology*, 46 :321, 2002.

[62] N. Phan-Thien, X.J. Fan, and B.C. Khoo. A new constitutive model for monodispersed suspensions of spheres at high concentrations. *Rheologica acta*, 38(4) :297–304, 1999.

[63] J.J. Stickel, R.J. Phillips, and R.L. Powell. A constitutive model for microstructure and total stress in particulate suspensions. *Journal of Rheology*, 50 :379, 2006.

[64] JD Goddard. A dissipative anisotropic fluid model for non-colloidal particle dispersions. *Journal of Fluid Mechanics*, 568 :1–18, 2006.

[65] DM Husband and F. Gadala-Maria. Anisotropic particle distribution in dilute suspensions of solid spheres in cylindrical couette flow. *J. Rheol.*, 31 :95, 1987.

[66] F. Parsi and F. Gadala-Maria. Fore-and-aft asymmetry in a concentrated suspension of solid spheres. *J. Rheol.*, 31(8) :725–32, 1987.

[67] I. Rampall, J.R. Smart, and D.T. Leighton. The influence of surface roughness on the particle-pair distribution function of dilute suspensions of non-colloidal spheres in simple shear flow. *J. Fluid Mech.*, 339(-1) :1–24, 1997.

[68] SC Jana, B. Kapoor, and A. Acrivos. Apparent wall slip velocity coefficients in concentrated suspensions of noncolloidal particles. *Journal of Rheology*, 39 :1123, 1995.

[69] F. Blanc. *Rheologie et microstucture des suspensions concentrées non-browniennes*. PhD thesis, Université de Nice-Sophia Antipolis, 2011.

[70] A. Sierou and J.F. Brady. Accelerated stokesian dynamics simulations. *Journal of Fluid Mechanics*, 448 :115–146, 2001.

[71] F. Blanc, F. Peters, and E. Lemaire. Experimental signature of the pair trajectories of rough spheres in the shear-induced microstructure in noncolloidal suspensions. *Physical Review Letters*, 107(20) :208302, 2011.

[72] F. Blanc, F. Peters, and E. Lemaire. Particle image velocimetry in concentrated suspensions : Application to local rheometry. *Applied Rheology*, 21 :23735, 2011.

[73] R.J. Phillips, R.C. Armstrong, R.A. Brown, A.L. Graham, and J.R. Abbott. A constitutive equation for concentrated suspensions that accounts for shear-induced particle migration. *Physics of Fluids A : Fluid Dynamics*, 4 :30, 1992.

[74] JC Van der Werff and CG De Kruif. Hard-sphere colloidal dispersions : the scaling of rheological properties with particle size, volume fraction, and shear rate. *Journal of Rheology*, 33 :421, 1989.

[75] P. Mills and P. Snabre. Apparent viscosity and particle pressure of a concentrated suspension of non-brownian hard spheres near the jamming transition. *The European Physical Journal E : Soft Matter and Biological Physics*, 30(3) :309–316, 2009.

[76] J.M. Bricker and J.E. Butler. Correlation between stresses and microstructure in concentrated suspensions of non-brownian spheres subject to unsteady shear flows. *Journal of rheology*, 51 :735, 2007.

[77] T. Dbouk. *Rheology of concentrated suspensions and shear-induced migration*. PhD thesis, Université de Nice-Sophia Antipolis, 2011.

[78] F. Boyer, É. Guazzelli, and O. Pouliquen. Unifying suspension and granular rheology. *Physical Review Letters*, 107(18) :188301, 2011.

[79] J.F. Morris and B. Katyal. Microstructure from simulated brownian suspension flows at large shear rate. *Physics of Fluids*, 14 :1920, 2002.

[80] K. Yeo and M.R. Maxey. Dynamics of concentrated suspensions of non-colloidal particles in couette flow. *Journal of Fluid Mechanics*, 649(1) :205–231, 2010.

[81] G. Bossis and JF Brady. Self-diffusion of brownian particles in concentrated suspensions under shear. *The Journal of chemical physics*, 87 :5437, 1987.

[82] PG De Gennes. Conjectures on the transition from poiseuille to plug flow in suspensions. *Journal de Physique*, 40(8) :783–787, 1979.